Doctoral Dissertation

博士論文

Study of disk winds in low mass X-ray binaries to determine their driving mechanisms

(低質量X線連星における円盤風駆動機構の解明)

A Dissertation Submitted for Degree of Doctor of Philosophy

December 2019

Department of Physics, Graduate School of Science,
The University of Tokyo

令和元年12月（理学）申請

東京大学大学院理学系研究科物理学専攻

Ryota Tomaru

都丸亮太

Abstract

Winds are ubiquitous in accreting systems, seen as blueshifted absorption lines in protostars, white dwarfs, neutron stars and black hole binaries as well as in the much more massive black hole accretion flows which power the Active Galactic Nuclei (AGN) and quasars. Understanding how these winds are driven is important in order to be able to calculate how much mass, momentum and energy they carry. In all systems the winds probably control the material available for accretion.

The winds are most easily studied in the low mass X-ray binary (LMXB) systems, where blueshifted highly ionized absorption lines are seen in the X-ray spectra of high inclination systems. Potential launch mechanisms for these equatorial disk winds are gas pressure (thermal driving), radiation forces (radiation driving) or Lorentz forces (magnetic driving). However, up till now it is not clear which one of these mechanisms dominates.

Thermal (or thermal-radiative) winds are driven by strong X-ray irradiation from the inner regions of the accretion flow. This heats the surface of the disk to the radiation temperature, and the resulting gas velocity exceeds the escape velocity at large radii where the gravitational potential has decreased sufficiently for this material to be unbound. This matches well to the observed properties of LMXB winds, as these are preferentially seen in large disk systems, and have low velocity indicative of a large launch radius. However, no quantitative models of thermal-radiative winds had ever been fit to the data.

This thesis develops the first self consistent simulation framework which can calculate the full spectra of thermal-radiative winds. This chains together a radiation hydrodynamic (RHD) code which uses the observed spectrum to calculate self consistently the heating/cooling rates and radiation forces, including bound-bound, bound-free, free-free and Compton processes. This resulting density and velocity structure is used as input to a fully 3D Monte-Carlo radiation transfer code to simulate the detailed spectra of the absorption and emission lines to compare with the observational data.

Using this framework, we show that the observed ion columns and velocities in the black hole binary H1743-322 can be described by the thermal-radiative wind predictions when the source is bright with a soft, disk dominated spectrum. We highlight the importance of radiation forces on both bound-free and bound-bound transitions as well as electron scattering in reproducing the observed velocity. We suggest winds are more accurately described as thermal-radiative rather than simply thermal. We also highlight the importance of the static X-ray heated atmosphere which forms at smaller radii as this can cast a shadow over the outer disk where the wind is launched. Our simulated spectrum fits well to the observed line profiles. This shows that our thermal-radiative wind model can be the origin of the observed absorption features, rather than requiring a magnetically driven wind. We also show how the velocity structure is key observable to discriminate between magnetic and thermal-radiative winds. Magnetic winds from the entire disk domain are faster at smaller radii because of large escape velocity, whereas thermal-radiative winds transition to a static atmosphere at smaller radii due to large gravity. New data from the next generation X-ray observatory *XRISM* (due for launch Jan 2022) will give an unprecedented view of the physics of the wind launch and acceleration processes, but the existence of static atmospheres in small disk systems already rules out magnetic winds which assume self-similar magnetic fields from the entire disk as the origin of the observed absorption features.

We also calculate the thermal-radiative winds expected from H1743-322 in lower luminosity states, where a much harder spectrum is seen. These simulations show that the absorption lines disappear, as observed, because the wind becomes overionized as well as weaker due to increased shadowing of the outer disk by the inner heated disk atmosphere.

We also apply this framework to bright neutron star LMXB GX 13+1 which has the largest disk known. We run the RHD simulation using the observed luminosity, spectral shape, and the estimated disk size. We show that our RHD gives a good overall match the observed ion column and velocity without any additional parameters. The full simulated spectrum also matches fairly well with even the highest resolution data currently available although there is some uncertainty in the level of turbulence present. We conclude that thermal-radiative winds are the origin of the observed absorption lines in LMXB systems.

Contents

1 Introduction **1**

2 X-ray binaries and its observational features **5**

2.1 X-ray binaries 5
2.2 Acccretion efficiency and Eddington luminosity 6
2.3 Observed spectra and its interpretation of BH XRBs 7
  2.3.1 Radiation from accretion disk 9
  2.3.2 The origin of power-law component 10
  2.3.3 Additional components 11
  2.3.4 X-ray light curve 12
2.4 Neutron star LMXBs 15
  2.4.1 Z source 16
  2.4.2 Atoll source 17
2.5 Outflow from compact objects 18
  2.5.1 Radio jets 18
  2.5.2 Accretion disk winds 21
  2.5.3 Jet driving mechanisms 26
  2.5.4 Wind driving mechanisms 28
2.6 Radiative process in accretion disk winds 33
  2.6.1 Photoinozed plasma 33
  2.6.2 Interactions between X-ray and photoionized plasma 33

3 Formation of thermal winds **41**

3.1 Thermal wind models 41
  3.1.1 Thermal instability of photoionized plasma 41
  3.1.2 Features of thermal winds 42
3.2 Highly simplified model for observable 46
3.3 Evolution of the wind with $L/L_{\rm Edd}$ 48
3.4 Radiation pressure correction 51

3.5 Predicted absorption features . . . 53
3.5.1 Behavior at the transition . . . 53
3.5.2 Comparison to observations across the transition . . . 54
3.5.3 High luminosities and the wind in GRO J1655-40 . . . 56
3.6 Summary . . . 58

4 Framework for constructing comprehensive models 61
4.1 Definition of framework . . . 61
4.2 Radiation hydrodynamics code . . . 62
4.2.1 Basic equations . . . 62
4.2.2 Integration method of energy equation . . . 64
4.3 Numerical test; comparison with previous work . . . 65
4.3.1 The test of energy equation . . . 65
4.3.2 Hydrodynamic simulation of thermal winds . . . 66
4.4 Radiation transfer based on the Monte-Carlo method . . . 69

5 Spectral modeling of thermal winds by Monte Carlo method 73
5.1 Radial streamlines . . . 73
5.1.1 Geometry and Parameters . . . 73
5.1.2 Result of radiation transfer . . . 74
5.2 Diverging wind . . . 76
5.2.1 Geometry and Parameters . . . 77
5.2.2 Result of radiation transfer . . . 79
5.3 Comparison with GX13+1 . . . 81
5.3.1 Observational data . . . 81
5.3.2 Model of GX 13+1 . . . 83

6 Hydrodynamic model of H 1743–322 87
6.1 BH LMXB H 1743-322 . . . 87
6.2 Simulation setup . . . 89
6.3 Ionization state calculations . . . 90
6.4 Inner corona . . . 92
6.5 Results for fiducial soft state spectral energy distribution . . . 94
6.5.1 Fiducial simulations: effect of radiation force . . . 96
6.5.2 Changing the disk size . . . 97
6.5.3 Changing luminosity:$L/L_{\rm Edd} = 0.5$ and 0.1 . . . 99
6.5.4 Changing the extent of the shadow from the inner attenuation zone . . . 103

6.6 Result for the hard state spectral energy distribution 105
6.7 Discussion 108

7 Iron line prediction for H1743-322 111
7.1 Monte-Carlo radiation transfer 111
7.2 Iron line Emission and Absorption line Profiles 113
7.3 Fitting to current and future high resolution data 116
  7.3.1 *Chandra*/HETGS 116
  7.3.2 Simulated *XRISM*/Resolve observations 117
7.4 Discussion: distinguishing between thermal-radiative and magnetic winds 120

8 The comprehensive model for GX 13+1 123
8.1 The NS LMXB GX 13+1: system parameters 123
8.2 Observational data 124
8.3 Radiation hydrodynamic simulation 125
  8.3.1 Fiducial model: $L/L_{\rm Edd} = 0.5$ 125
  8.3.2 Changing luminosity: $L/L_{\rm Edd} = 0.7$ 128
  8.3.3 Changing disk size: $R/R_{\rm IC} = 1.0$ 130
8.4 Monte Carlo radiation transfer 132
  8.4.1 Calculation setup 132
  8.4.2 The effect of additional turbulent velocity 133
  8.4.3 Fitting to *Chandra*/HETG first and third order spectra 137

9 Summary and Discussion 139
9.1 Summary 139
  9.1.1 Radiation transfer through a phenomenological biconical wind model for GX13+1 139
  9.1.2 Radiation transfer through a radiation hydrodynamic wind model for H1743-322 140
  9.1.3 Radiation transfer through a radiation hydrodynamic wind model for GX 13+1 143
9.2 Discussion 144

10 Conclusion 147

A Appendix 161
A.1 Geometry of thermal wind models 161
  A.1.1 The rotation velocity for radial streamlines 161

A.1.2 Density and velocity structure for the diverging streamlines . . 161
A.2 Numerical test II; the number of grid 163

List of Figures

2.1 Schematic view of stellar wind accretion (left) and Roche-lobe overflow (right) taken from Shapiro & Teukolsky (1983). Solid line shows Roche-lobe. . . . 6

2.2 Spectra of the BH HMXB Cygnus X-1 taken from Gierliński et al. (1999) . . . 8

2.3 Spectra of the BH LMXB GRO J1655-40 taken from Done et al. (2007). Colors show very high state (black), soft state (green), ultra soft state (red), and hard state (blue), respectively. . . . 8

2.4 Schematic view of geometry of accretion flow of hard state (a) and soft state (b) taken from by Zdziarski & Gierliński (2004) . . . 9

2.5 The X and γ-ray spectrum of GX 339-4 taken from Zdziarski et al. (1998) The data is fitted by a model consisting of black body radiation (dot-dashed line) providing seeds for thermal Comptonization in a hot plasma (dashed line). The hard radiation of the hot plasma is Compton-reflected from some cold medium also shown by the dotted line. . . . 12

2.6 X-ray light curves of X-ray binaries taken from Done et al. (2007). These show the outburst. Color points show spectral hardness corresponding to the hard (blue), very high (green) and soft (red) state, while black points show unclear hardness because of large uncertainties to the assign state. Grey points show non-detections (3σ). . . . 13

2.7 Hardness intensity diagram (HID) of X-ray binaries taken from Muñoz-Darias et al. (2013). The vertical axis shows X-ray luminosity and horizontal axis shows hardness ratio $6-10$keV to $2-6$keV obtained by *RXTE*. Left panels show low inclination systems, whereas right panels show high inclination systems. Grey marks the X-ray color-luminosity region reached solely by low inclination systems. This is explained by considering inclination-dependent relativistic effects on accretion disks. . . . 14

2.8 Light curves of some dippers taken from Diaz Trigo et al. (2005) . . 15

2.9 The classification of LMXBs by observational inclination angle taken from Frank et al. (1987) The solid line shows the Roche-lobe and left side is the companion. 16

2.10 CDs and HIDs of Z sources from *RXTE*/PCA taken from (Lin et al., 2009). The soft color means the ratio of count rates in the (3.6–5.0)/(2.2–3.6) keV band and the hard color means that in (8.6–18.0)/(5.0–8.6) keV. 17

2.11 *RXTE*/PCA spectra of GX 340+0 and GX 17+2. The solid, dashed, dotted, and dot-dashed lines correspond to labels "A"-"D" in Fig.2.10, respectively. Bottom panels show the ratios. This figure taken from (Lin et al., 2009) 18

2.12 CD of atoll source 4U 1608-52 from *RXTE* taken from (Gierliński & Done, 2002). Top regions 1-3 are island (hard) state and bottom regions 4-8 shows banana (soft) state. 19

2.13 Spectra of 4U 1608-52 from *RXTE* taken by Gierliński & Done (2002). Labels correspond to the position in Fig.2.12. The mass accretion rate increases from S1 to S8. Each panel shows the unfolded data and models, as well as the residuals. Colors show disk blackbody (red), thermal Comptonization (cyan), and its reflection (green). . . . 19

2.14 Direct image of jets from BH XRB in the hard state of 1E 1740.7-2942, taken from Mirabel & Rodríguez (1999). At a distance of 8 kpc the length of the jet structure would be ~ 5 pc. 20

2.15 HID of H 1743-322 taken from Miller-Jones et al. (2012) Circles indicate radio detections and open triangles indicate non-detections. Radio emission from the jet is observed in the hard state. 21

2.16 The schematic view of P-Cygni profile 22

2.17 Bule shifted absorption lines in LMXB GX 13+1 taken from Ueda et al. (2004) 22

2.18 The schematic of disk winds taken from Ponti et al. (2012). 23

2.19 Spectra of GRO J1655–40 taken from Higginbottom et al. (2018). The two spectra are offset by a factor 3 for clarity. They are actually very similar in observed continuum luminosity and shape, with the red spectrum being only marginally softer than the black (Fig.2.20). 23

2.20 Multi-wavelength SEDs of GRO J1655–40 during the 2005 ourburst taken Shidatsu et al. (2016) (top). Colors show hypersoft state (red) in April, and normal soft state (black) in March. The bottom show ratio of the two SEDs. The former data (red) are divided by the latter (black). 24

2.21 The relation between absorption lines and spectral state taken from Ponti et al. (2012). The left panel shows HID taken from *RXTE* overplotting absorption equivalent widths by simultaneous *Chandra*/HEG in dipping sources. Absorption lines are only seen in soft state. The right panel shows the same as left but non-dippig source. They are not observed in non-dipping source. 24

2.22 The results of Radiation Magneto Hydrodynamic (RMHD) simulations near the black hole for models slim disk (Super-Eddington accrtion), standard disk, and hot accretion flow (ADAF), from left to right, taken from Ohsuga & Mineshige (2011). Upper panels: Normalized density distributions (color) are overlaid with isosurfaces, at which the outward velocity equals to the escape velocity. The model of hot accretion flow is optically thin. Lower panels: The distributions of the normalized radiation energy density (color) is overlaid with the magnetic field lines. 27

2.23 The simulated density distribution of super-Eddington accretion flow taken from Ohsuga et al. (2005). The arrows show velocity fields. The input mass accretion rate is $1000 L_{\rm Edd}/c^2$ with $M_c = 10 M_\odot$. . . . 29

2.24 The result of radiation hydrodynamic simulaton taken from Proga et al. (2000). Panels show density distribution (top left), temperature (top right), ionization parameter ξ (bottom left), and velocity (bottom right). Materials accelerate at ionization region. 30

2.25 A schematic of the MHD wind taken from Fukumura et al. (2017). Poloidal two-dimensional wind streamlines (thick solid grey lines), the decreasing velocity ($V_0 \sim c$) and ionization parameter ξ with radius are illustrated. The hatched region represents the absorbing region with velocity 100–1000 km/s. The red arrows indicate possible lines of sight, with the green arrow believed to be the true line of sight based on published binary solutions. 31

2.26 The *Chandra*/HETG spectrum of GRO J1655–40 overlaid on the global MHD wind model taken from Fukumura et al. (2017) 32

2.27 Ion fractions vs. ionization parameter ξ with an $F_E \propto E^{-1}$ ionizing continuum taken from Kallman et al. (2004) 34

3.1 Schematic diagram of thermal equilibrium curve of photoionized plasma taken from Jimenez-Garate et al. (2002) 42

3.2 Input spectra and their thermal equilibrium curves taken from Woods et al. (1996). 45

3.3 Left: The mass flux density from a $10^8 M_\odot$ BH per unit area of disk at a scaled radius $\zeta = R/R_{\rm IC}$ for $\log L/L_{\rm Edd}$ =-3 (black) -2 (red), -1 (green), 0 (blue) and 1 (cyan), as in Woods et al. (1996). These correspond to $L/L_{\rm crit} = 0.0125$–125 for the assumed constant $T_{\rm IC,\,8} = 0.13$. Right: The corresponding cumulative mass-loss rate from the disk at $R_{\rm disk} < 5\ R_{\rm IC}$. 46

3.4 The effect of disk size on the efficiency of wind production per unit mass accretion rate taken from Done, Tomaru, & Takahashi (2018). The vertical axis shows $\dot{M}_{\rm w}/\dot{M}_{\rm a}$ ($\dot{M}_{\rm a} = L/(0.1c^2)$). The horizontal axis shows the luminosity normalized by the critical luminosity $L_{\rm crit} = 0.08 L_{\rm Edd}$ with $T_{\rm IC} = 1.3 \times 10^7$K. The disk size $R_{\rm disk}/R_{\rm IC} = 0.1$ (black), 0.3 (red), 1 (green), 3 (blue) and 10 (cyan). All disk show that disk is increasingly efficient at producing a wind with increasing mass accretion rate for $L/L_{\rm crit} \to 1$ but the efficiency stabilized to a constant for $L/L_{\rm crit} \gg 1$ 47

3.5 Column densities of Woods et al. (1996) (doted line) and Done, Tomaru, & Takahashi (2018) (solid line). Colors show $L/L_{\rm Edd} = 0.3$ (green), 0.08 (red) and 0.01 (black), respectively. 47

3.6 The upper panel shows the assumed change in $T_{\rm IC}$ with $L/L_{\rm Edd}$ (red). The power-law spectral index softens with increasing luminosity in the hard state, so the inverse Compton temperature drops. The abrupt drop at $L/L_{\rm Edd} = 0.02$ marks the transition to the disk dominated state, where the Compton temperature increases with luminosity. The second panel shows the effect of this on $R_{\rm IC}$ (green). A higher Compton temperature means that the wind can escape from smaller radii. The third panel shows how $L/L_{\rm crit}$ changes (blue). An increase in Compton temperature means that the radiation heats the gas faster, so it can drive the temperature up to $T_{\rm IC}$ at $R_{\rm IC}$ at a lower luminosity. The assumed $L/L_{\rm Edd} - T_{\rm IC}$ behavior means that the luminosity is only above the critical luminosity for $L > 0.1L_{\rm Edd}$. Thus the wind is lauched from $R_{\rm in} = 0.2R_{\rm IC}$ only for $L > 0.1L_{\rm Edd}$. Below this, the wind instead is launched from $R_{\rm in} = 0.2R_{\rm IC}/(L/L_{\rm crit})$, so the wind launch radius (cyan) decreases with increasing $L/L_{\rm Edd}$ in the hard state, as the increase in $L/L_{\rm crit}$ more than offsets the increase in $R_{\rm IC}$. The lower panel (magenta) shows the wind efficiency (mass outflow rate in terms of the mass accretion rate). This is fairly constant at $\sim 5\times$ the mass accretion rate required to produce the luminosity, except for more complex behavior around the transition. The dotted lines on all panels show the effect of including a simple radiation pressure term to reduce the effective gravity. The wind can be launched from progressively smaller radii, and the mass loss rates increase. 49

3.7 The upper panel (red) shows the column density at $\cos\theta = 0.25$ i.e. an inclination angle of $\sim 75°$. This is roughly proportional to the mass accretion rate, but with a dip at the spectral transition due to the lower Compton temperature of the dimmest soft states. The second panel (green) shows the ionization state calculated from the total bolometric flux, $\xi = L_{\rm bol}/nR^2$. This is fairly constant, as the increase in luminosity is mostly balanced by an increase in density of the wind. The third panel shows the fraction of bolometric flux which is emitted in the 8.8-30 keV high energy band pass (blue). These are the photons which are most effective in photoionizing He- and H-like iron, and this shows a dramatic dip around the spectral transition, even including a power-law to higher energies which carries 5% of the total disk luminosity. The fourth panel shows the high energy ionization parameter, $\xi_H = f_H L_{\rm bol}/nR^2$ (cyan). This is almost completely constant in the hard state, but dips dramatically in the soft state due to the much softer spectra, and only recovers to the same value as seen in the hard state at the highest luminosities. The bottom panel shows the outflow velocity. This mirrors the behavior of the launch radius of the wind shown in Fig.3.6d. The dashed lines show the effect of including a simple radiation pressure correction. The wind becomes optically thick. 52

3.8 The hard (black) and soft (red) spectra from *RXTE* data on H 1743−322, with the inset showing the simultaneous Chandra data, with a clear difference in wind absorption features taken from Done et al. (2018). The high energy 8.8– 30 keV photoionizing flux is quite similar between the two data sets, but the overall luminosity is quite different. If the wind stayed constant, responding only to the high energy photoionizing flux, then the difference in wind properties would require a change in the wind structure, potentially linked to the appearance of the jet. However, thermal winds respond to the overall flux, as well as to the high energy part, and this predicts that the column should be smaller by a factor of ˜5 in the low/hard state, consistent with the observations. 55

4.1 The outline of our numerical simulations 62

4.2 The net heating/cooling rate ($\log |\Gamma - \Lambda|$) (left), and Force multiplier $M(\xi, T)$ (right) with the irradiation spectrum of BH XRB H1743-322 in soft state. The spectrum itself is taken from Shidatsu & Done (2019). 64

4.3 thermal equilibrium curve obtained by CLOUDY C17.01 (red) and that of Woods et al. (1996) (black) which use old version CLOUDY 65

4.4 The net heating/cooling rate $\log_{10} |\Gamma(\xi, T) - \Lambda(\xi, T)|$ (left). The numerical test for thermal equilibrium temperature (right). The black line show thermal equilibrium temperature from CLOUDY calculation. The red dashed line shows our thermal equilibrium using our root finder. 67

4.5 The time evolution of energy equation with $\xi_0 = 10^6, T^0 = 10^6$K. Colors show $\rho_0 = 10^{-13}$g cm^{-3} (blue) and 10^{-12}g cm^{-3} (orange). . . 67

4.6 Distributions of density (left) and temperature (right). The temperature is heated up to the Compton temperature. 68

4.7 The comparison with the column density Woods et al. (1996). Colors show the column density of our simulation (red) and that of Woods et al. (1996) (black). The large column at a high inclination angle means the disk surface. 68

4.8 Schematic diagram of Monte Carlo simulation taken from Odaka et al. (2011). 69

5.1 Distribution of density (left) and mean Fe ionization state (right) for the radial streamline model 74

5.2 Spectra computed for the radial streamline model with 1 eV resolution for different lines of sight. Each panel shows the spectrum in a different inclination angle bin (the angular bin sizes are indicated the top of each panel). The total spectrum is shown in black (top), the spectrum direct photons in red and scattered/reprocessed spectrum is blue (bottom). Note that the vertical axis is plotted linearly in the top panels but logarithmically in the bottom panels. Lines are Fe XXV (6.668 keV for Heα y and 6.700 keV for Heα w) and Fe XXVI (6.952 keV for Lyα_2 and 6.973 keV for Lyα_1). The equatorial density structure of the wind means that the absorption is much stronger at high inclination angles. The emission is more isotropic, so it can clearly be seen at low inclination angles, but is absorbed by the wind at high inclinations. 75

5.3 Left panel: EW of the absorption lines as a function of inclination angle, Fe XXV (Heα w, red) and Fe XXVI (Lyα_2, green and Lyα_1, blue). The EW of all absorption lines increases strongly at higher inclination, showing the assumed equatorial disk wind geometry. The Doppler wings (with width set by turbulent velocity) of the two H-like absorption lines start to merge for inclinations above 70° so above this we show the total EW of the two lines. Right panel: the blue shifted absorption line velocity for each ion species. This clearly shows the assumed constant velocity structure of the radial streamline. 76

5.4 The geometry of the diverging biconical wind model. 78

5.5 The solid lines show column density as a function of the cosine of the inclination angle through the wind resulting from the hydrodynamic simulations of Woods et al. (1996) for $L/L_{\rm Edd} = 0.01$(green), 0.08 (red), 0.3 (black). The filled circles show that resulting from the diverging biconical wind (Section 4) while the open circles show the radial streamline model of Done et al. (2018)(Section 3). 78

5.6 Distribution of density (left) and Fe ionization state (right) for the diverging wind geometry. The accelerating flow gives higher density material close to the disk compared to the constant velocity outflow model in Fig. 5.1, giving lower mean ionization state. 79

5.7 As in Fig 5.2, but for the diverging biconical wind geometry. 80

5.8 As in Fig. 5.3, but for the diverging wind model. The lower The lower ionization state means that there is also a contribution from the intercombination line of Fe XXV Heα y (black) at the highest inclinations. 80

5.9 HEG spectra of GX 13+1 from 1st order (black) and 3rd order (red) by stacking 4 dataset (OBSID:11814-11817). 82

5.10 The column density as a function of the cosine of the inclination angle for the diverging biconical wind calculated for the system parameters of GX13+1. The blue line shows the predictions for a purely thermal wind, while the red includes a very simple treatment of radiation pressure. The source has $L/L_{\rm Edd} \sim 0.5$, so the thermal wind can be launched from closer in due to the lower effective gravity. This effect has a large impact on the predicted column, so the details of how this radiation pressure correction affects the velocity and density structure will be important in determining the line profiles. 84

5.11 The model (red) and HEG 3rd order spectrum (black). The best fit inclination angle is $i = 80°$. This gives roughly the correct column of Fe XXV and XXVI at low velocity, but fails to match the observed higher velocity blue wing to the absorption features. 85

5.12 As in Fig. 5.8, but with the system parameters of GX 13+1 and the simplest radiation pressure correction to make a hybrid thermal/radiative wind. 86

6.1 Line spectra from soft state (black) and hard state (red) *Chandra*/HETGS observations of H 1743-322 taken from Miller et al. (2012). 89

6.2 a) The energy flux of H 1743-322 which consists of a disk-blackbody plus Comptonized power-law (DISKBB+DISKBB*SIMPLE in XSPEC). b) The heating and cooling function ($\Gamma - \Lambda$). The black curve shows the thermal equilibrium ($\Gamma - \Lambda = 0$), the right colour bar shows the absolute logarithm value of heating minus cooling function ($\log|\Gamma - \Lambda|$). The Compton temperature of this spectrum is $T_{\rm IC} = 1.0 \times 10^7$ K. c)The zooming figure of b) surrounding by white dashed line. The vertical lines show the instability points. Red vertical lines is $\Xi_{\rm h,min} = 100$. 91

6.3 a)Thermal equilibrium curve of $\log \xi$vs $\log T$. b): Force multiplier of continuum process(bound-free plus scattering, red), line (green) and total (black) at the thermal equilibrium state. The vertical dashed line shows $\xi_{\rm H,min} = 1.7 \times 10^2$ which is the ionization parameter of disk surface. 92

6.4 schematic view of geometry of our hydrodynamic simulation 92

6.5 Hydrogen column density of all simulations in Tab.6.1. 94

6.6 Top : the inclination dependence of column densities of Fe XXVI (solid line) and Fe XXV (dashed line). Bottom: the inclination dependence of column weighted mean velocities of Fe XXVI (solid line) and Fe XXV (dashed line). The colours show the thermal-radiative wind of $L/L_{\rm Edd} = 0.3$, $R_{\rm IS}/R_{\rm IC} = 0.18$(black) and the thermal wind (red). . 95

6.7 Distributions of density (top) and temperature (bottom), the solid white lines show Mach 1 surface of radial velocity and black arrows show velocity. 98

6.8 The distribution of density (left) and temperature (right) of small disk simulation. 99

6.9 As in Fig. 6.6 but $R_{\rm disk}/R_{\rm IC} = 1.0$ (black) and 0.18 (blue). 100

6.10 As Fig.6.6 but for $L = 0.5L_{\rm Ldd}$. 101

6.11 As in Fig.6.6 but for $L/L_{\rm Edd} = 0.1$ (violet), 0.3 (black), 0.5 (green) . . 102

6.12 As in Fig.6.6 but for $L/L_{\rm Edd} = 0.3$, $R_{\rm IS}/R_{\rm IC} = 0.18$ (black), $L/L_{\rm Edd} = 0.5$, $R_{\rm IS}/R_{\rm IC} = 0.22$ (green), $L/L_{\rm Edd} = 0.3$, $R_{\rm IS}/R_{\rm IC} = 1.0$ (orange), and $L/L_{\rm Edd} = 0.5$, $R_{\rm IS}/R_{\rm IC} = 1.0$ (magenta). 104

6.13 a) Spectra of soft state(black) and hard state (blue). b) The thermal equilibrium curves. colours correspond to input spectra of a) 105

6.14 The distribution of density (left) and temperature (right) of hard state105

6.15 The angular dependence of column densities Fe XXVI (black solid line), Fe XXV (black dashed line) and those of column weighted velocities (bottom) of hard state. Cyan shows the observational upper limit calculated from Miller et al. (2012) 106

7.1 Distribution of the density (left), outflow velocity (middle), and rotation velocity (right). The dark blue region of outflow velocity map means negative velocity. 112

7.2 Distributions of ion density Fe XXVI (left), Fe XXV (middle) and temperature (right) calculated by CLOUDY 112

7.3 The results using the density/velocity structure from the hydrodynamic simulations (i.e. no additional turbulent velocity). Each panel shows the calculated spectra (black) seen at inclination of $45°, 60°$ and 75°, normalised by the incident spectrum. The transmitted (red) and scattered (green) components are also shown. 113

7.4 As in Fig.7.3 but including additional saturated turbulent velocity ($v_{\rm turb} = v_R$) 113

7.5 The radial profile of velocity (top) and ratios of local ion column density to that of total at $i = 75°$ (bottom). Colours show Fe XXVI (red) and Fe XXV (green), respectively, ... 114

7.6 The angular dependence of equivalent width Fe XXVI (Lyα_1: 6.953 keV + Lyα_2: 6.973 keV, red) and Fe XXV (Heα y: 6.668 keV + Heα w: 6.700 keV, black) with $v_{\rm turb} = 0$ (left) and $v_{\rm turb} = v_R$ (left). Error bars are calculated from Poisson noise. 116

7.7 *Chandra*/HETGS data with best fit model of $v_{\rm turb} = 0$ (left) and $v_{\rm turb} = v_R$ (right). Best fit inclination angle is 81° and 78° respectively. The data is taken from HEG +1 (Black) and -1 (red). 118

7.8 Simulated spectrum of a 30ks *XRISM* observation (live time fraction of 0.1) for the model with no additional turbulence (left), and $v_{\rm turb} = v_R$ (right) around the Fe XXVI Kα doublet line energy. The absorption is modelled using a single KABS component (red). The lower panel shows the residuals as a ratio between the data and model at each energy. Clearly Resolve can determine the velocity structure in the lines even at these low velocities. 118

7.9 As Fig. 7.8 but fitted by double KABS model 119

8.1 The SED of GX 13+1 (left) and its thermal equilibrium curve (right) 125

8.2 The distribution of density (left) and temperature (right) 126

8.3 The angular dependence of ion columns (top) and ion column weighted mean velocities (bottom). Color show Fe XXVI (red), Fe XXV (green), S XVI (blue), and Si XIV (magenta). Solid lines show simulation of $L/L_{\rm Edd} = 0.5$ whereas Dashdotted lines show that of $L/L_{\rm Edd} = 0.7$. Dashed crosses show the observational values. 127

8.4 The angular dependence of hydrogen column density with $(L/L_{\rm Edd}, R_{\rm disk}/R_{\rm IC}) = (0.5, 10.0)$ (solid line), $(0.7, 10.0)$ (dashed-dot line), and $(0.5, 1.0)$ (dotted line). 129

8.5 As in Fig.8.3 but the $R_{\rm disk}/R_{\rm IC}$ =10.0 (solid lines) and 1.0 (dotted lines). 131

8.6 Top: The distribution of density (left), radial velocity (middle), and rotation velocity (right) extracted radiation hydrodynamic simulation Bottom: The CLOUDY output as the input MONACO. 133

8.7 Radial profile of ion column densities (top) and velocities (bottom) at 65°. Color show Fe XXVI (red) and Fe XXV (green). The solid line shows radial velocity and the dashed line shows rotation velocity. . . 134

8.8 The angluar dependence of line profiles for $v_{\rm turb} = 0$ (top), v_R (middle), and v_ϕ (bottom). 135

8.9 The inclination dependence of EWs for $v_{\rm turb} = 0$ (left), v_R (middle) and v_ϕ (right) Colors show Fe XXV Heα y+w (green), Fe XXVI Lyα_1+α_2 (red), Ni XXVII Heα $y + w$ (blue), Fe XXV Heβ w (orange), Ni XXVIII Ly$\alpha_1 + \alpha_2$ (magenta), and Fe XXVI Ly$\beta_1 + \beta_2$ + Fe XXV Heγ w (cyan). 135

8.10 The comparison with our line profile and observed spectrum taken from HEG 1st order (OBSID: 11818). Models are $v_{\rm turb} = 0$(left), v_R (middle), and v_ϕ (right). Inclination angles are $\cos\theta = 0.29, 0.47, 0.33$ 136

8.11 The comparison with our line profile and observed spectrum taken from *Chandra*/HEG 3rd order. Models are $v_{\rm turb} = 0$ (left), v_R (right), and v_ϕ (right) Inclination angles are $\cos\theta = 0.35, 0.47, 0.37$ 136

9.1 The schematic diagram of inflow-outflow geometry in soft (top) and hard state (bottom) suggested by our work. 142

A.1 Details of the model geometry for the diverging wind streamlines. . . 163
A.2 The distribution of density 164
A.3 Comparison of number of grid 164

List of Tables

2.1 List of low-mass X-ray binaries for which a photoionized plasma local to the source has been detected in the absorption spectrum taken from Díaz Trigo & Boirin (2016). The first columns indicate the source name, the orbital period, the galactic column density towards the source after Kalberla et al. (2005), type of the compact object, whether it shows dips (D), and, if not, the source inclination (i). (See Liu et al. (2007) for the references on the period and inclination, unless otherwhise noted.) The last column indicates if the degree of ionization of the photoionised absorber(s) detected during persistent intervals (outside dips) is < 3 or ≥ 3 in $\log \xi$, whether the absorber seems to flow outwards (out), inwards (in) or to be bound as an atmosphere (atm), based on the velocity shifts of the absorption lines detected with *Chandra*/HETGS or *XMM-Newton*/RGS. "no grat." means that no contraints were published on the velocity shifts from these gratings. 25

4.1 Detailed parameters for each line included in these MONACO simulations. Note that we list only lines which have larger oscillator strength than 10^{-3}. These are listed from the lowest energy. 71

5.1 List of the *Chandra*/HETGS observations 82

6.1 The summary of simulations and inner corona parameters 94

7.1 Single KABS fits to the simulated XRISM Resolve data 119

7.2 Double KABS fits to the simulated XRISM Resolve data 119

8.1 Fits to the absorption lines of OBSID: 11818 using KABS. Errors are calculated by 90% confidence level. 124

8.2 The summary of simulations and inner corona parameters for GX 13+1125

8.3 Fitting results 137

Chapter 1

Introduction

Outflowing gas is ubiquitous in accreting systems across he mass scale from protostars (e.g Bachiller, 1996; Carrasco-González et al., 2010) through to stellar mass compact objects, including white dwarfs, neutron stars and black hole binaries, all the way to the supermassive black holes in active galactic nuclei (AGN) at the center of galaxies (e.g. Heckman et al., 1990; Hagino et al., 2016) These outflows exist as either highly collimated jets (e.g. Burrows et al., 1996; Mirabel & Rodríguez, 1999; Remillard & McClintock, 2006) or as wider angle winds (e.g. Tombesi, 2010; Ueda et al., 2009; Bjerkeli et al., 2016). The interesting open questions in the field are how these outflows are driven, whether there are common processes across these very different objects, and whether there is a causal relation between jets and winds. Jets are almost certainly magnetic (Blandford & Znajek, 1977) but winds can be powered by radiation forces (Ohsuga et al., 2005; Proga et al., 2000), or thermal gas pressure (Begelman et al., 1983; Woods et al., 1996), as well as magnetic fields (Blandford & Payne, 1982; Fukumura et al., 2010). It is important to know the physical mechanisms in order to understand these outflows as they can carry away a large fraction of the accreting mass and/or kinetic power so they can have a significant impact on the accretion environment.

In super-massive black hole these outflows connect the accretion flow to the much wider scale of the host galaxy, controlling its star formation powered growth via AGN feedback. However, the environment in AGN is complex, making it difficult to isolate the effect of the accretion disk outflows. Instead, Low mass X-ray binaries (LMXBs) are simpler systems on which to start to develop an understanding of these issues. The low mass of the companion star means mass transfer occurs though Roche lobe overflow. Thus we observe the accretion flow and its winds/jet directly, without the complications from absorption from surrounding material which can be present in AGNs and in the high mass binary systems. LMXBs also have the advantage that they are typically bright and vary on easily observed timescales of days/weeks/months, so we can directly observe the response of the winds and jet to changes in the mass accretion rate through the disk.

Jets in LMXBs are seen by their radio emission. However, this is only seen when the X-ray spectrum from the accretion flow is hard, dominated by Compton scattering, very unlike the simple disk model predictions. The jet emission collapses when the flow makes an abrupt transition to a soft disk dominated state at higher luminosities (Ponti et al., 2012; Ponti et al., 2014). The spectral change can be explained as a transition between a disk and hot accretion flow, where the collapse of the larger scale height hot flow into a geometrically thin disk also triggers the collapse of the steady compact radio jet (see e.g. the review by Done et al. 2007). Instead, disk winds, seen by the presence of blueshifted absorption lines from highly ionized material in high inclination sources (e.g. the compilation by Ponti et al. 2012), are present only in the disk dominated states. This observed anti correlation of jet and disk wind led to the suggestion that the same magnetic field responsible for the jet in the hard state underwent a reconfiguration to power a wind by Lorentz force (magnetic wind) in the soft state (Neilsen & Lee, 2009; Miller et al., 2012). However, the observed wind velocities are rather slow, less than 1000 km/s (Miller et al., 2015), which indicates that the wind arises from large radii on the disk. This is also shown by the fact that winds are seen preferentially in systems with large disks (e.g. Díaz Trigo & Boirin, 2016). Jets are clearly launched from small radii, so there is a disconnect between the scales of the jet and of the wind. There are magnetic field configurations which could produce this behavior (Fukumura et al., 2010; Fukumura et al., 2017) but these configurations cannot be calculated from first principles so have to be assumed.

Instead, thermal winds driven by gas pressure have a clear link to both disk size and illuminating spectrum and luminosity. The pioneering work by (Begelman et al., 1983) showed that bright X-ray emission from the inner disk and corona heats the surface of the disk at larger radii to the Compton temperature, $T_{\rm IC}$. This temperature depends only on the spectrum of the radiation, so the entire disk surface has a heated atmosphere at this temperature, which is unbound at radii $R_{\rm IC}$ where this temperature means that particles have enough energy to escape i.e. $kT_{\rm IC} = GM_c\mu m_p/R_{\rm IC}$ where where μ is the mean molecular weight, set to 0.61. This launches a thermal wind at radii larger than the inverse Compton radius, $R_{\rm IC} \sim (6.4 \times 10^4/T_{\rm IC,8})R_g(R_g = GM_c/c^2, T_{\rm IC,8} = T_{\rm IC}/10^8$ K), giving a clear dependence on both the spectrum (through $T_{\rm IC}$) and the disk size, as observed.

In this thesis, in order to explain observed features such as observed spectra and absorption visibility of spectral state transition, we firstly build a highly simplified analytic predictive model for the mass loss rate of thermal winds based on Begelman et al. (1983); Woods et al. (1996). We take a physically realistic wind geometry from hydrodynamic simulations Woods et al. (1996) and input this into a Monte-Carlo radiation transfer (MCRT) code to directly compare to observed spectra. We then use modern, state of the art radiation hydrodynamic (RHD) simulations to make more physical models of thermal-radiative winds, and show how these can explain the observed properties of the winds, specifically how they change as the source switches from soft to hard. We use these as input to the MCRT to compute the detailed line profiles resulting from these winds. We clearly show how the observed spectra are consistent with thermal-radiative winds and large scale ordered magnetic fields are not required.

This thesis is organized in the following order. In Chapter 2, we review the current understanding of accretion disk winds and their possible driving mechanisms in LMXB and important physical processes. In Chapter 3 we introduce the previous model of thermal winds (Begelman et al., 1983; Woods et al., 1996) and build the highly simplified model for observable such as column density and velocity using previous model. In Chapter 4 we build the spectral model for direct comparison with observed spectrum by MCRT. We adapt this model to bright neutron star GX 13+1. Chapter 5 describes our RHD simulation code. In Chapter 6 and 7, we build more realistic model by RHD and MCRT simulations and compare that with observed spectra in BH LMXB H1743-322. Chapter 8 describe the comparison our comprehensive model of RHD and MCRT with GX 13+1. After we describe the summary and discussion in Chapter 9, finally, in Chapter 10, our conclusions are stated.

Chapter 2

X-ray binaries and its observational features

In this chapter, we review the current observational features such as spectra, light curves and, outflows in XRBs (especially LMXBs). We also review the current theoretical interpretation of these features. Results presented in this chapter are obtained by X-ray observatories such as *Rossi X-ray Timing Explorer (RXTE), Chandra, XMM-Newton*, and *Suzaku*.

2.1 X-ray binaries

XRBs consist of a compact object such as a black hole (BH) or a neutron star (NS), and a normal companion star. These systems are luminous in X-ray by converting gravitational energy of infalling material from the companion to the compact object to X-ray. X-ray is emitted from the inner part of the accretion disk around the compact object. These systems are generally divided into two classes; high-mass X-ray binaries (HMXBs) and Low-mass X-ray binaries (LMXBs). HMXBs normally have the massive stars which are O or B type companion stars and the mass transfer is carried by the stellar wind accretion (left in Fig. 2.1). LMXBs have low mass companions with $\sim M_\odot$, K or M type stars and the mass transfer is carried by the Roche-lobe overflow (right in Fig.2.1).

LMXBs are the best target to study accretion physics. They are highly time variable systems, and its time scale is from a few days to a few months ,which is easy to observe (Done et al., 2007). Because there are no stellar winds from its companion, we can directly observe this time variations and the intrinsic X-ray radiation from accretion disk without the reprocessed X-ray from the stellar wind. In this thesis, we treat only LMXBs. In this chapter, we briefly summarize observational spectral features of LMXBs and their current theoretical interpretation.

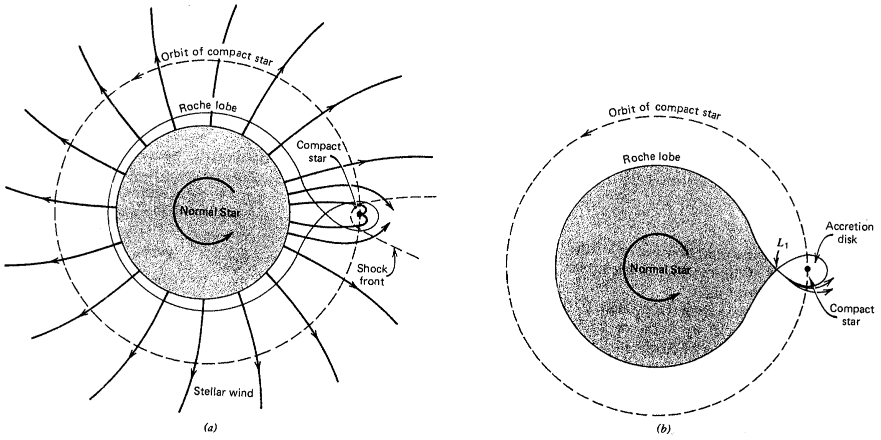

Figure 2.1: Schematic view of stellar wind accretion (left) and Roche-lobe overflow (right) taken from Shapiro & Teukolsky (1983). Solid line shows Roche-lobe.

2.2 Acccretion efficiency and Eddington luminosity

When materials accrete onto compact objects, the gravitational potential of these materials is released. The released energy heats the gas. As a result, these materials generate radiation. When gas accretes with a rate $\dot{M}$ onto a central object of mass M_{c} and radius R_{m} of the central object with spherical accretion, the emergent luminosity L_{acc} is

$$L_{\mathrm{acc}} = \frac{GM_{\mathrm{c}}\dot{M}}{R_m} \tag{2.1}$$

where G is the gravitational constant. The efficiency of radiative emission in this process is $\eta = \dot{M}c^2/L_{\mathrm{acc}} = GM/(R_m c^2)$. For typical BHs or NSs, this efficiency is quite high, at a value of $\eta = 0.1$ because the R_m is quite small. We use $\eta = 0.1$ in this thesis. (In reality, accretion material forms a disk around the central object because they have angular momentum and this value is variable with the innermost stable circular orbit $(0.06 < \eta < 0.4)$).

For accretion to occur, gravity must exceed the radiation force from accretion luminosity. The luminosity which is equal to the gravity is called Eddington luminosity, and it is used as the criteria for maximum luminosity. The radiation pressure from this luminosity at radius R from the central object is $p_{\mathrm{rad}} = L_{\mathrm{acc}}/(4\pi c R^2)$. Thus the radiation force via electron scattering is $F_{\mathrm{rad}} = p_{\mathrm{rad}}\sigma_T$. The gravity of the accretion material is $GM_{\mathrm{c}}m_i/R^2$, where $m_i = 1.2m_p$ is the mean ion mass per electron. Therefore Eddington luminosity is given by

$$L_{\mathrm{Edd}} = \frac{4\pi G M_c m_i c}{\sigma_T} \tag{2.2}$$

$$= 1.5 \times 10^{38} (M_c/M_\odot) \ \mathrm{erg/s} \tag{2.3}$$

If we use the proton mass instead of m_i, then the coefficient is 1.3. The mass accretion rate of the Eddington Luminosity is

$$\dot{M}_{\mathrm{Edd}} = \frac{L_{\mathrm{Edd}}}{0.1c^2} \tag{2.4}$$

$$= 2.0 \times 10^{18} \left(\frac{M_c}{M_\odot}\right) \ \mathrm{g/s} \tag{2.5}$$

2.3 Observed spectra and its interpretation of BH XRBs

The spectra of black hole X-ray binaries (both LMXBs and HMXBs) generally show two types spectral states; a high/soft (thermal dominated) state and a low/hard (Compton dominated) state (Zdziarski & Gierliński, 2004; Remillard & McClintock, 2006; Done et al., 2007, etc). Soft state shows the intense blackbody radiation from an accretion disk with a temperature of ~ 1 keV plus a weak high energy power-law component called the hard-tail with spectral photon index between $2.1 < \Gamma < 2.4$ from non-thermal electrons, accelerated to high energy. On the other hand, hard state (Fig. 2.2 blue) shows weak disk radiation and strong hard X-ray which can be modelled by the power-law distribution of $1.4 < \Gamma < 2.1$ with a cut-off energy of ~ 100 keV via the inverse Compton scattering by high energy electrons in a hot flow near the compact objects. Fig. 2.4 shows a schematic of the accretion flow in the soft state and hard state.

In reality, BH XRBs show other spectral types (Fig.2.3). The figure is a selection of spectra seen in the BH LMXB GRO J1655-40, which shows the spectral transition of these states (hard, soft, soft with extremely weak tail, sometimes called ultrasoft, and an extreme example of the very high state). The very high state shows strong and steeper power-law than that of soft state $\Gamma > 2.4$, in addition to disk blackbody. Although these states are not a unique function of mass accretion rate onto BHs measured by luminosity, the general picture is clear that soft and very high state are typically high luminosity state, while the hard state is often seen in low luminosity.

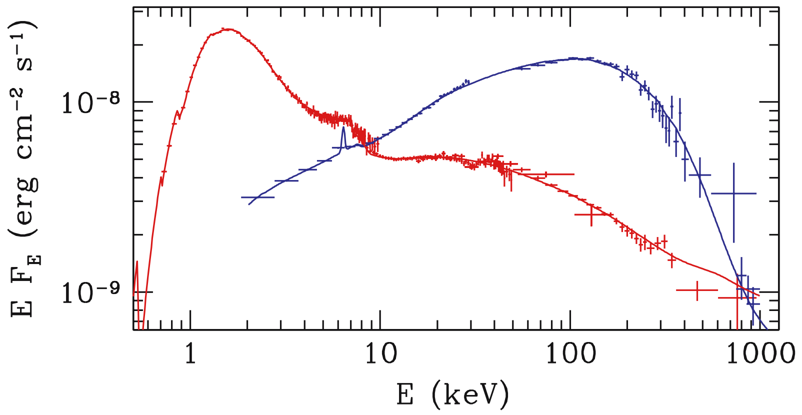

Figure 2.2: Spectra of the BH HMXB Cygnus X-1 taken from Gierliński et al. (1999)

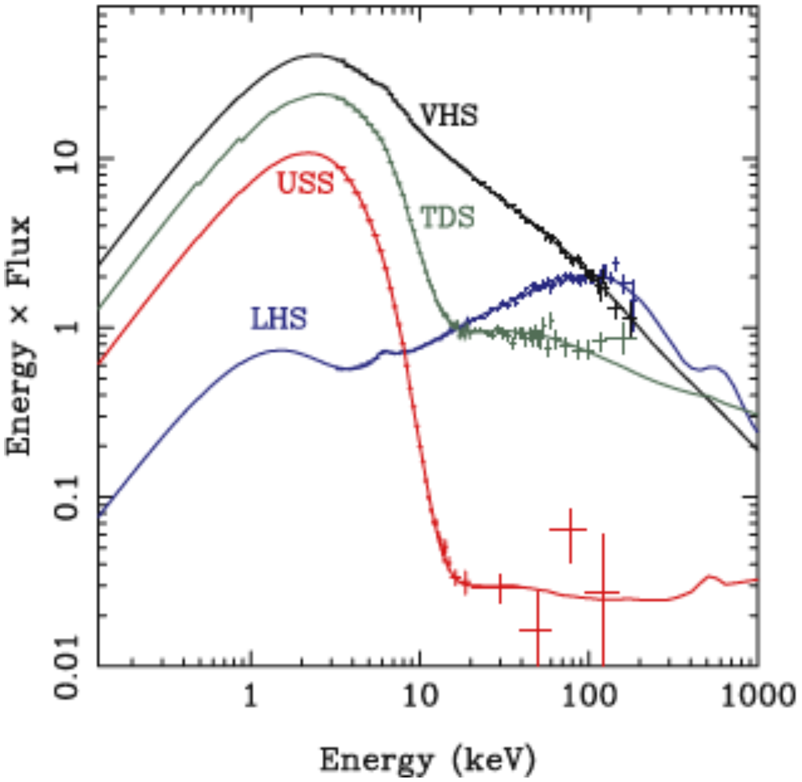

Figure 2.3: Spectra of the BH LMXB GRO J1655-40 taken from Done et al. (2007). Colors show very high state (black), soft state (green), ultra soft state (red), and hard state (blue), respectively.

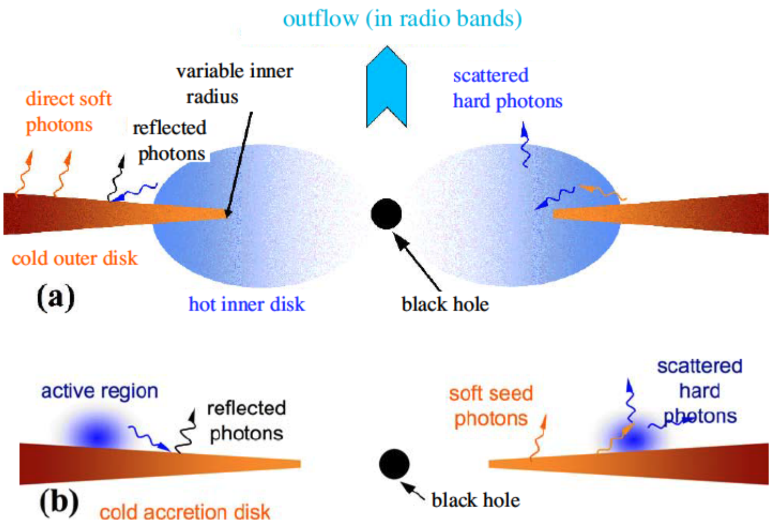
outflow (in radio bands)
variable inner radius
direct soft photons
reflected photons
scattered hard photons
cold outer disk
(a)
hot inner disk
black hole
active region
reflected photons
soft seed photons
scattered hard photons
(b)
cold accretion disk
black hole

Figure 2.4: Schematic view of geometry of accretion flow of hard state (a) and soft state (b) taken from by Zdziarski & Gierliński (2004)

2.3.1 Radiation from accretion disk

When material accretes onto the central object, these material forms an accretion disk around the central object. In the disk, the material has to lose its angular momentum to accrete inwards. Shakura & Sunyaev (1973) first proposed the accretion disk model (standard disk, or disk), in which the material loses angular momentum in the disk (Fig. 2.4). They assume that the disk is axisymetric, geometrically thin, optically thick (radiation is blackbody) and have nearly Keplerian rotation. They also assume that the mass accretion rate at a given radius is constant. They introduce the dimensionless angular momentum transportation efficiency $\alpha < 1$ and solve the stationary solution of the accretion disk. The mechanism of angular transport is likely magnetorotational instability (MRI) in the disk (Balbus & Hawley, 1998; Stone & Norman, 1992)

The temperature of blackbody radiation from the disk can be estimated by using the virial theorem. Half of the gravitational energy in the range of R to $R + \delta R$ equals to radiation energy from the disk such that

$$\frac{1}{2}\frac{GM_c\dot{M}}{R^2}\delta R = 2 \times 2\pi R\delta R\sigma_{SB}T^4 \tag{2.6}$$

where σ_{SB} is Stefan-Boltzmann constant, and $2 \times R\delta R$ is the area of the disk. Thus, the temperature of blackbody radiation at radius R is

$$T(R) = \left(\frac{GM_c\dot{M}}{8\pi\sigma_{SB}R^3}\right)^{1/4} \tag{2.7}$$

More accurately, considering the effect at the inner boundary of the disk, is

$$T(R) = \left[\frac{3GM_c\dot{M}}{8\pi\sigma_{SB}R^3}\left(1-\sqrt{\frac{R_{\rm in}}{R}}\right)\right]^{1/4} \tag{2.8}$$

$$= T_0\, r^{-3/4}(1-r^{-1/2})^{-1/4}, \quad \left(T_0 = \left[\frac{3GM_c\dot{M}}{8\pi\sigma_{SB}R_{\rm in}^3}\right]^{1/4}\right) \tag{2.9}$$

$$= 2\times 10^7 \dot{m}^{1/4} m^{-1/4} r^{-3/4}(1-r^{-1/2})^{-1/4}\ \mathrm{K} \tag{2.10}$$

where $\dot{m} = \dot{M}/\dot{M}_{\rm Edd}, m = M/M_\odot, r = R/R_{\rm in}$ and $R_{\rm in} = 3R_s$ respectively. This function has a maximum value $T_{\rm max} = 0.488T_0$ at $R = (49/36)R_{\rm in}$. Thus the temperature of the disk of XRBs is $T \sim 10^7$ K and this temperature corresponds to a X-ray emitting region 10^7 K ~ 1 keV .

2.3.2 The origin of power-law component

The spectrum of hard state (Fig.2.2 blue) is fitted well by a cut-off power-law distribution.

$$N(E) = N_0 E^{-\Gamma}\exp\left(-\frac{E}{E_c}\right) \tag{2.11}$$

The typical cut-off energy is $E_c = 50 - 100$ keV and the typical photon index is $\Gamma \sim 1.7$. When the soft X-ray seed photons from the disk enter a high energy electron region with temperature T_e, they gain energies by inverse Compton scattering, which can produce a power-law spectrum (Sunyaev & Truemper, 1979). Photons cannot receive much higher energy than kT_e, so cut-off is produced. When we consider a seed photon with an energy of $E_0(\ll kT_e)$, where k is Boltzman constant, is scattered off a non-relativistic high energy electron with thermal distribution, the photon's energy increases by $\Delta E = 4kT_e/(m_ec^2)E_0$ in a single scattering event, where m_e is the electron mass. When the photon is scattered N times, the resultant photon energy is written as

$$E \sim E_0 \exp\left[N(\frac{4kT_e}{m_ec^2})\right] \tag{2.12}$$

Because the number N can be described using optical depth $\tau_{\rm es}$ as $\max(\tau_{\rm es}, \tau_{\rm es}^2)$,thus

$$E = E_0\exp(y) \tag{2.13}$$

$$y = \max(\tau_{\rm es}, \tau_{\rm es}^2)\frac{4kT_e}{m_ec^2} \tag{2.14}$$

where y is called as Compton y-parameter. The photon index Γ is written as

$$\Gamma = -\frac{3}{2} \pm \sqrt{\frac{9}{4}+\frac{4}{y}} \tag{2.15}$$

These high energy thermal electrons are understood as a different type of accretion flow than standard accretion disk. This hot flow is geometrically thick and optically thin. This flow is called an ADAF (Advection dominant accretion flow) (Ichimaru, 1977; Narayan & Yi, 1994) (the hot inner disk of (a) in Fig.2.4) or more generally RIAF (Radiatively inefficient accretion flow). Because of its quite small mass accretion rate, the density of the ADAF is very small as a result radiative cooling and Coulomb interaction is inefficient. Therefore the protons in the ADAF lose little energy and its temperature is almost virial.

$$kT \approx \frac{GM_c m_p}{R} \sim 10^{12}(R/R_s)\mathrm{K} \tag{2.16}$$

The electrons gain only a small amount of energy via Coulomb collisions and lose most of it by radiating. Because the flow is optically thin, this radiation is in the form of Comptonization, bremsstrahlung and/or synchrotron. The radiation efficiencies of these processes are much smaller than blackbody. Thus the luminosity of this hot flow is much lower than that of a standard disk. Because of the high virial temperature, this hot flow is geometrically thick: $H/R \sim 0.5$ (where H is the scale height of this hot flow). The radial velocity is much larger than in the standard disk, and the angular velocity is sub-Keplerian because the pressure is much larger due to high temperature. Therefore gravity is partially balanced by the radial pressure gradient. Because both disk blackbody and Comptonized spectra are sometimes observed in the hard state, it is believed that inner standard disk is truncated at large radii and being replaced by a hot inner flow (e.g. Done et al. 2007; Yuan & Narayan 2014).

In the soft state (2.2 red), we can observe not only blackbody radiation from the accretion disk but also a power-law component whose photon index is $\Gamma > 2.0$. In this component, there is no observable (as yet) high-energy cutoff in the spectrum. The highest energy of this spectrum is $\sim$ 10 MeV. Thus this radiation seems to come from a power-law (non-thermal) distribution of electrons via inverse Compton scattering. However, the origin of these electrons is not yet understood.

2.3.3 Additional components

We observe not only the direct radiation from the accretion flow but also reprocess emission. There is reprocessed X-ray from ionized or neutral material (George & Fabian, 1991) The most prominent component is the reflection from the accretion disk and absorption from an ionized absorber around the accretion disk. The reflection component shows a typical shape called Compton hump around $20-50$ keV, which comes from Compton scattering by electrons in the accretion disk (Fig.2.5).

This hump is produced as a high energy X-rays incident on the disc lose energy by Compton down scattering in reflection, while low energy X-rays are strongly absorbed by the photo-electric effect. In addition to the Compton hump, fluorescence lines are also produced after the resulting photo-electric absorption. The most prominent line is Kα from neutral iron at 6.4 keV

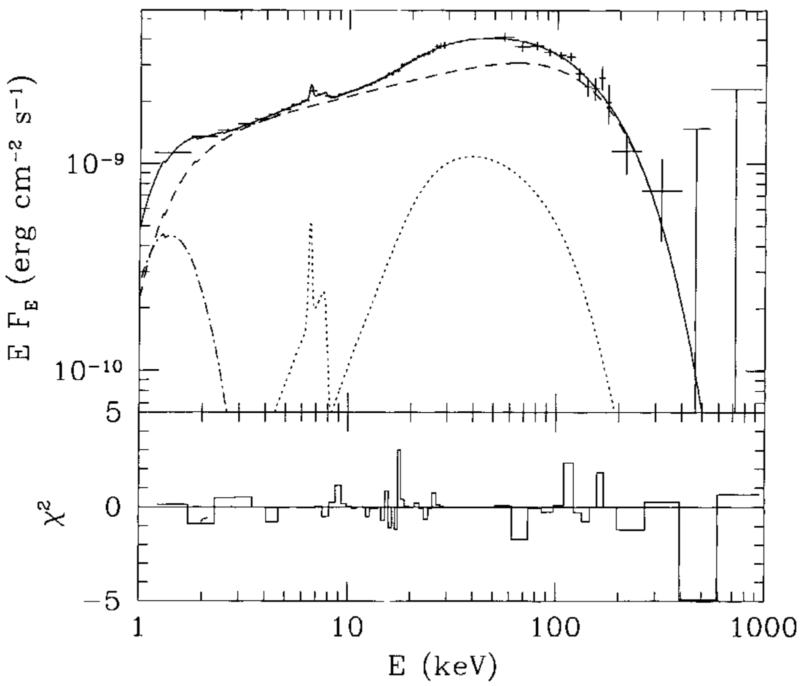

Figure 2.5: The X and γ-ray spectrum of GX 339-4 taken from Zdziarski et al. (1998) The data is fitted by a model consisting of black body radiation (dot-dashed line) providing seeds for thermal Comptonization in a hot plasma (dashed line). The hard radiation of the hot plasma is Compton-reflected from some cold medium also shown by the dotted line.

2.3.4 X-ray light curve

Outburst

Although spectral features of BH XRBs are almost the same for both LMXBs and HMXBs, the light curves are different. Many BH LMXBs show dramatic changes in their X-ray light curve called an outburst (Fig.2.6). This origin seems to be the hydrogen ionization instability (Osaki, 1996; Lasota, 2001). For low mass accretion rates, the temperature is low, and most hydrogen is neutral. In this case, the emission temperature of the accretion disk is also low, and photons are not absorbed in the accretion disk due to low opacity. When the temperature rises to 10^4 K, where the highest energy photons on the Wien tail of the thermal distribution from disk

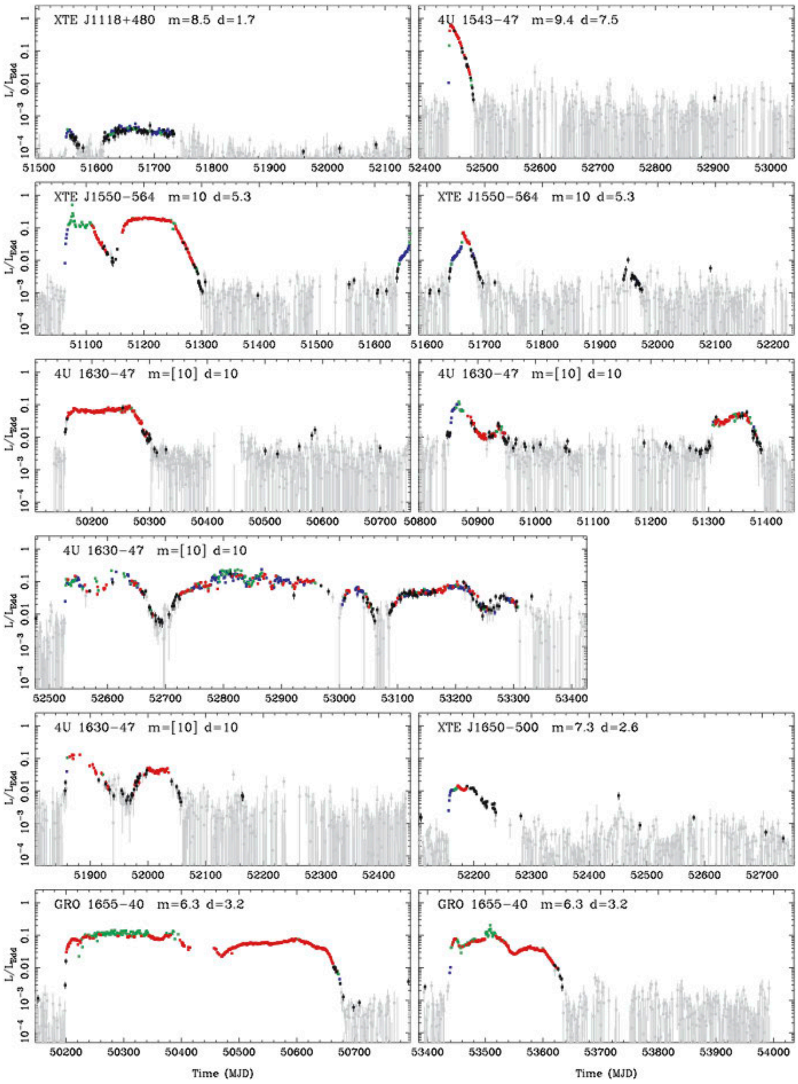

Figure 2.6: X-ray light curves of X-ray binaries taken from Done et al. (2007). These show the outburst. Color points show spectral hardness corresponding to the hard (blue), very high (green) and soft (red) state, while black points show unclear hardness because of large uncertainties to the assign state. Grey points show non-detections (3σ).

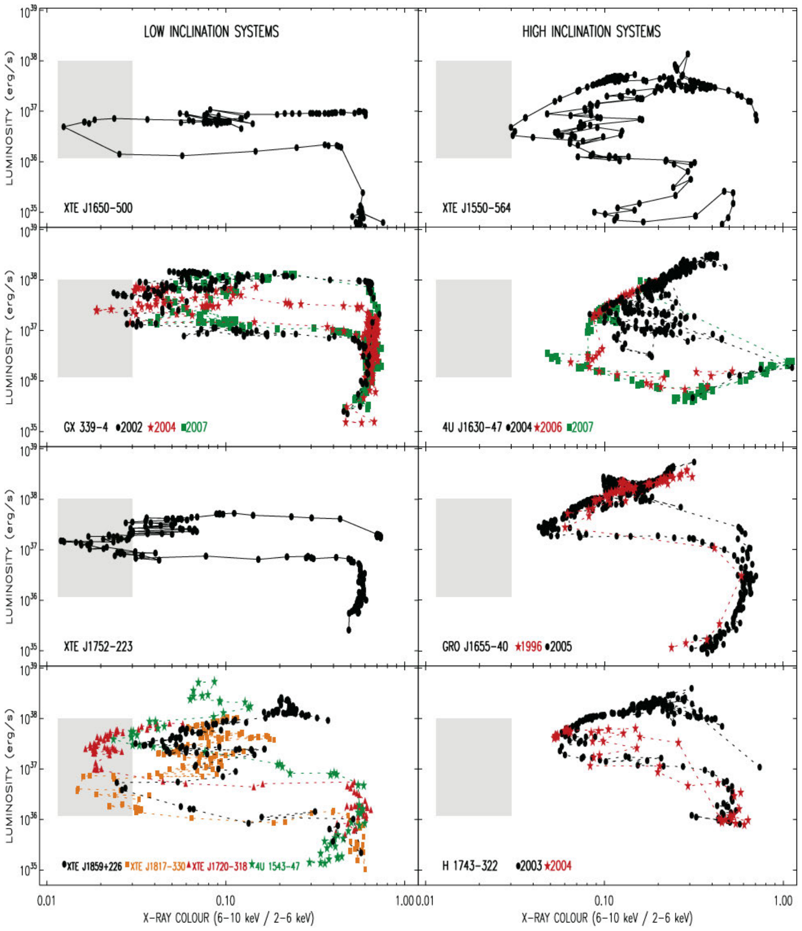

Figure 2.7: Hardness intensity diagram (HID) of X-ray binaries taken from Muñoz-Darias et al. (2013). The vertical axis shows X-ray luminosity and horizontal axis shows hardness ratio $6-10$keV to $2-6$keV obtained by *RXTE*. Left panels show low inclination systems, whereas right panels show high inclination systems. Grey marks the X-ray color-luminosity region reached solely by low inclination systems. This is explained by considering inclination-dependent relativistic effects on accretion disks.

emission start to ionize the hydrogen in the disk, this ionization effect absorb most photos, and the temperature of disk rises further. This series of events continues until most of the hydrogen is ionized. When the hydrogen is entirely ionized, high energy photons escape from disk, but the temperature and hence mass accretion rate is now much higher. Thus, the number of X-ray photons rises rapidly.

By summarizing the spectra transition and light curve, we can plot typical figures called hardness intensity (luminosity) diagram (HID or HLD) (Fig.2.7). These diagrams show the ratio of count rates of high energy X-rays to that of low energy X-rays in the horizontal axis and the total X-ray count rate (or luminosity) in the vertical axis. These figures are widely used to understand the evolution of spectra.

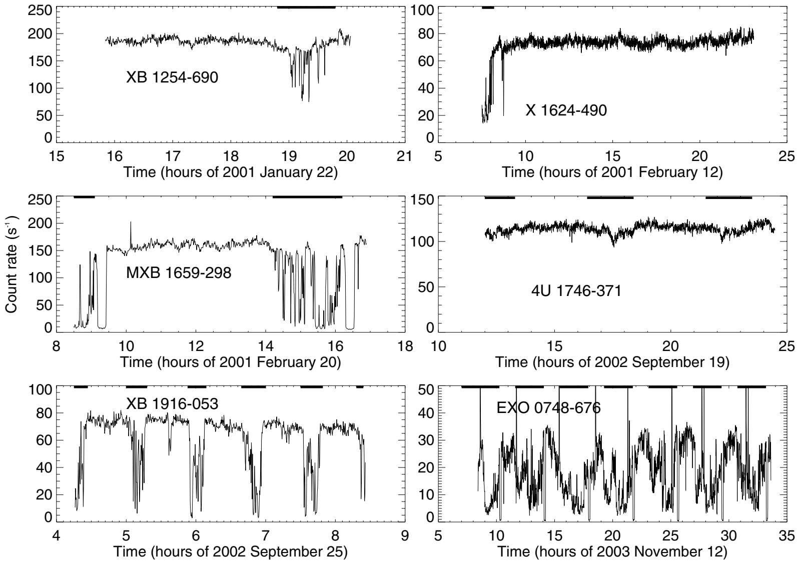

Figure 2.8: Light curves of some dippers taken from Diaz Trigo et al. (2005)

Dip and eclipse

LMXBs show some observational features depending on the inclination angle. One is the quasi-periodic dimming of the light curve called a dip (Fig.2.8). The origin of this dip is probably a bulge of material on the outer edge of the accretion disk, where the mass transfer stream from the companion hits the disk causing a thickening of the rim or bulge (Armitage & Livio, 1998). This vertical structure of the disk blocks the radiation from the central region and produces dipping events. Thus dippers show high inclination system ($i \sim 60° - 75°$). If central objects have a larger inclination angle than dippers ($i \sim 75° - 80°$), then these show also the eclipse by the companion in addition to the dip. In almost edge-on objects ($i \sim 80° - 90°$), most of the X-rays are blocked by the outer edge of accretion disk itself (Fig.2.9).

2.4 Neutron star LMXBs

NSs in LMXBs always have low magnetic fields. Although it is not clear why NSs with high magnetic fields have not been found, one explanation is due to dissipation of the high birth fields of $B > 10^{12}$G in the accretion torques during the long term evolution of the binary to Roche-lobe overflow (Bhattacharya & van den Heuvel, 1991). Because NSs in LMXBs have low magnetic fields ($B < 10^{8-9}$G), these magnetic fields do not affect the dynamics of the accretion flow. Thus, the accretion flow of NS in LMXBs has the same behavior as that of BHs, because these objects have similar gravitational potential energy. However, NSs have a solid surface while BHs do not. Thus the radiation from the boundary layer between the accretion flow, and

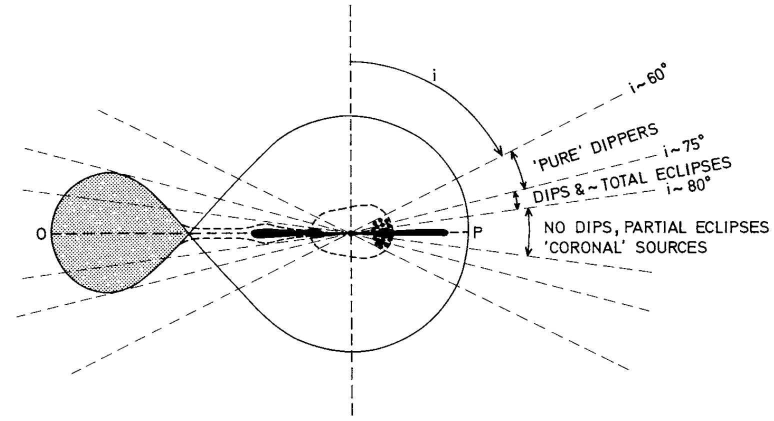

Figure 2.9: The classification of LMXBs by observational inclination angle taken from Frank et al. (1987) The solid line shows the Roche-lobe and left side is the companion.

solid surface is one of the most different points and its luminosity is comparable to the disk(Done & Gierliński, 2003).

NSs LMXBs are divided into two classes, Z and Atoll sources, based on their spectral features, luminosity, and timing properties (Hasinger & van der Klis, 1989). Z sources are typically brighter ($L/L_{\rm Edd} > 0.5$) while the atolls are seen over the same range of luminosities as BH LMXBs ($10^{-3} < L/L_{\rm Edd} < 1$).

2.4.1 Z source

The name of this class comes from the typical Z-track traced by their color-color diagram (CD). (Fig.2.10). These sources are Sco X-1, GX 17+1, GX 349+1, GX 340+0, GX 5-1, Cyg X-2, and GX 13+1. Z-shaped CD is consist of three branches called the horizontal branch (HB), normal branch (NB) and flaring branch (FB), top-left to bottom-right, and defines three distinct spectral states of the systems. Z sources are rapidly variable in X-rays and can trace the whole CD, transiting the different states, in hours to days. The overall spectra of sources are very soft and often described by the sum of a blackbody with $\sim$ 1keV from the accretion disk, and its Comptonized emission from thermal electrons of few keV in the boundary layer (Fig.2.11. In the HBs, similar to the soft state of BHBs, they show steep power-law components with $\Gamma > 2.0$ at energies above 30 keV (Di Salvo et al., 2000). This component is related to radio emission (Paizis et al., 2006) (maybe a jet), but it is unclear whether this origin is the same as BHBs. The origin of these branches is not yet clear, but radiation pressure from the high luminosity is believed to play an important role (Lin et al., 2009). Lin et al. (2009) suggested that the

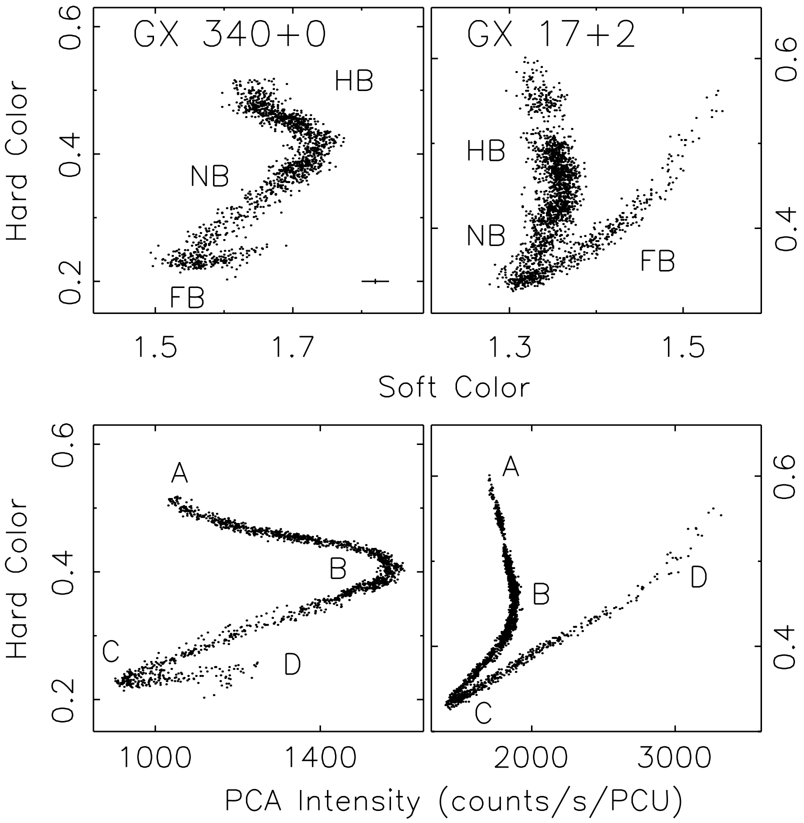

Figure 2.10: CDs and HIDs of Z sources from *RXTE*/PCA taken from (Lin et al., 2009). The soft color means the ratio of count rates in the (3.6–5.0)/(2.2–3.6) keV band and the hard color means that in (8.6–18.0)/(5.0–8.6) keV.

FB spectrum shows that the standard disk but, the mass accretion rate of HB and NB is above local Eddington mass accretion rate and, then disk change to super Eddington accretion flow called the slim disk (Abramowicz et al., 1988) which is supported strong radiation force.

2.4.2 Atoll source

Atoll sources show a similar spectral state as BH XRBs. They show two distinct (soft and hard) X-ray states. From the shape of the CD, these states are called the banana (soft) state and island (hard) state (Fig.2.12). The spectrum of the banana state can be described as blackbody radiation from accretion disk and its thermal Comptonized emission as Z sources (Gierliński & Done, 2002, in S4-8 in Fig.2.13) But in the spectra of island state, the temperature of Comptonized emission is much higher ($>$ 50 keV), and this optical depth is smaller than unity (in S1-3 Fig.2.13). This component comes from the same inner hot flow as hard state in BH XRBs plus boundary layer. Because the density of the boundary layer in the island state is low, due to the small mass accretion rate, this optical layer does not thermalize into

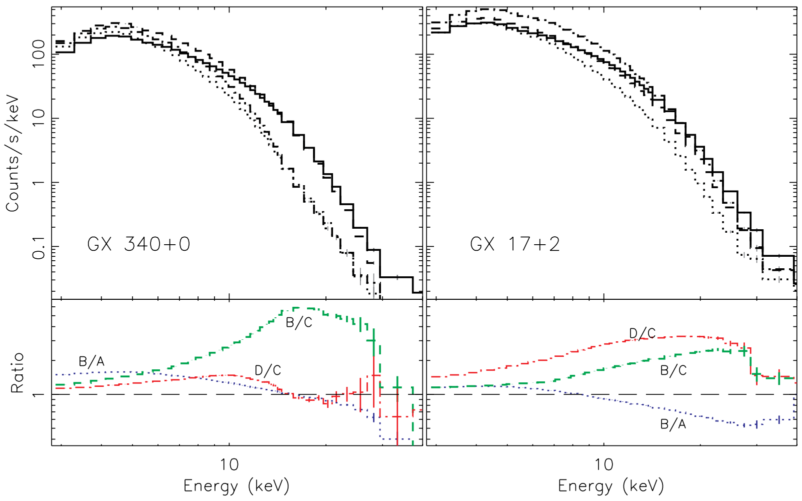

Figure 2.11: *RXTE*/PCA spectra of GX 340+0 and GX 17+2. The solid, dashed, dotted, and dot-dashed lines correspond to labels "A"-"D" in Fig.2.10, respectively. Bottom panels show the ratios. This figure taken from (Lin et al., 2009)

a blackbody but instead radiates the energy through Comptonization (Popham & Sunyaev, 2001).

2.5 Outflow from compact objects

Outflowing gas is ubiquitous in accreting systems. These outflows exist as a jet which is a highly collimated outflow observed in radio band via synchrotron radiation, and a disk wind which is observed as blueshifted absorption lines from ionized ions. Jets are seen in both HMXBs and LMXBs (Fender et al., 2004; Migliari & Fender, 2006). But the disk winds are only observed in LMXBs, both BHs and NSs because HMXBs have strong stellar winds and it is difficult to distinguish the disk winds and stellar winds.

2.5.1 Radio jets

Radio jets with Lorentz factor 1.3–3.5 (Saikia et al., 2019) are seen when the spectra are in the hard state. However, the radio flux collapses when the source makes a transition to the soft state, so there seems to be a direct causal relation between hot flows and radio jets. Meanwhile, in the soft state of BHBs, which have cold geometrically thin disks, jets are much weaker and are often not seen (Fig2.15). There are no clear explanations for this difference, but it is suggested that compared to thin disks, geometrically thick hot flows more easily advect the magnetic fields to black holes (Livio et al., 1999), or that these hot flows have so large kinetic energy

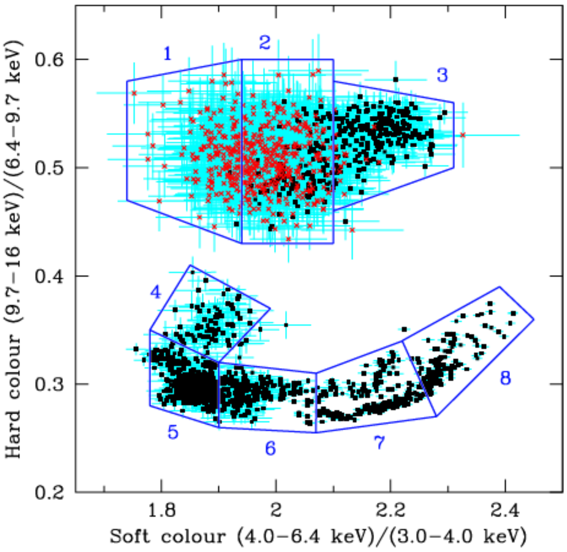

Figure 2.12: CD of atoll source 4U 1608-52 from *RXTE* taken from (Gierliński & Done, 2002). Top regions 1-3 are island (hard) state and bottom regions 4-8 shows banana (soft) state.

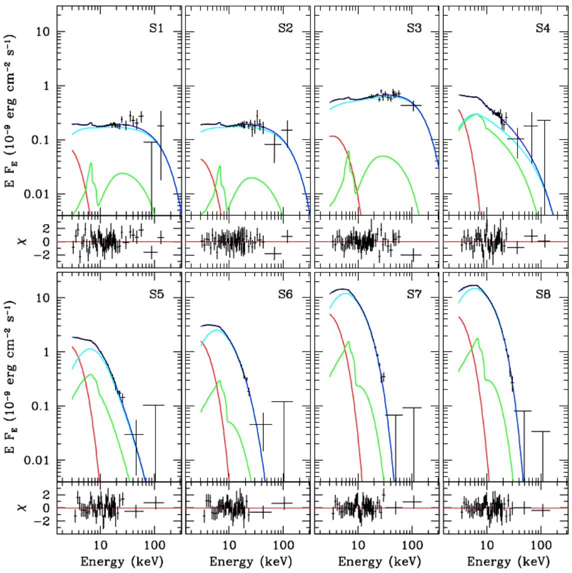

Figure 2.13: Spectra of 4U 1608-52 from *RXTE* taken by Gierliński & Done (2002). Labels correspond to the position in Fig.2.12. The mass accretion rate increases from S1 to S8. Each panel shows the unfolded data and models, as well as the residuals. Colors show disk blackbody (red), thermal Comptonization (cyan), and its reflection (green).

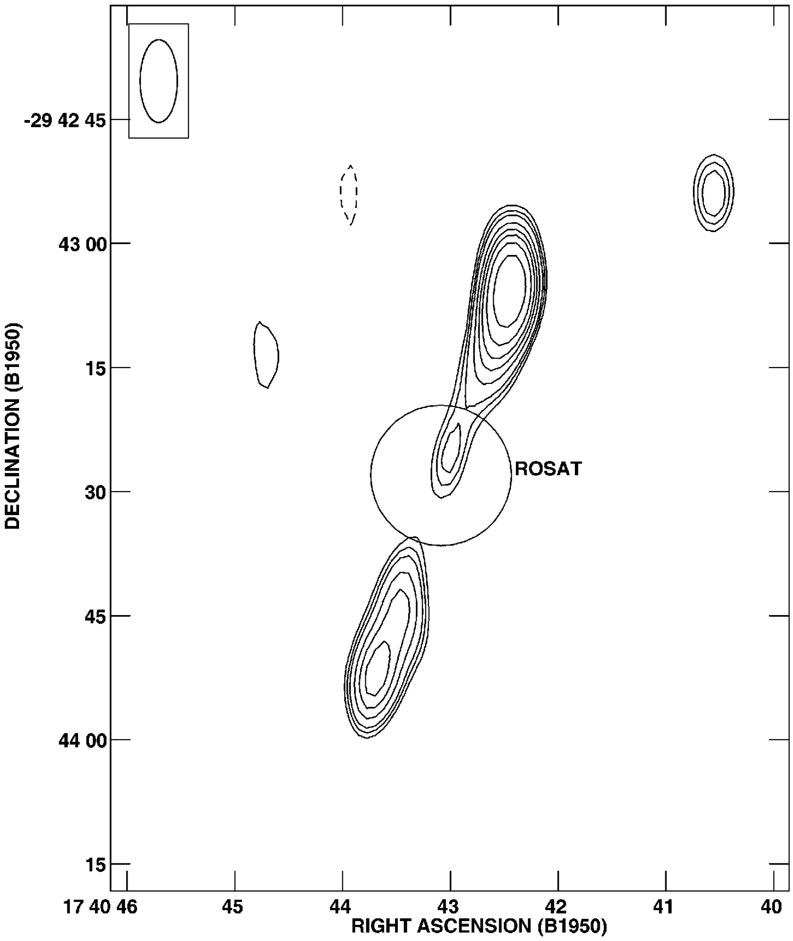

Figure 2.14: Direct image of jets from BH XRB in the hard state of 1E 1740.7-2942, taken from Mirabel & Rodríguez (1999). At a distance of 8 kpc the length of the jet structure would be ~ 5 pc.

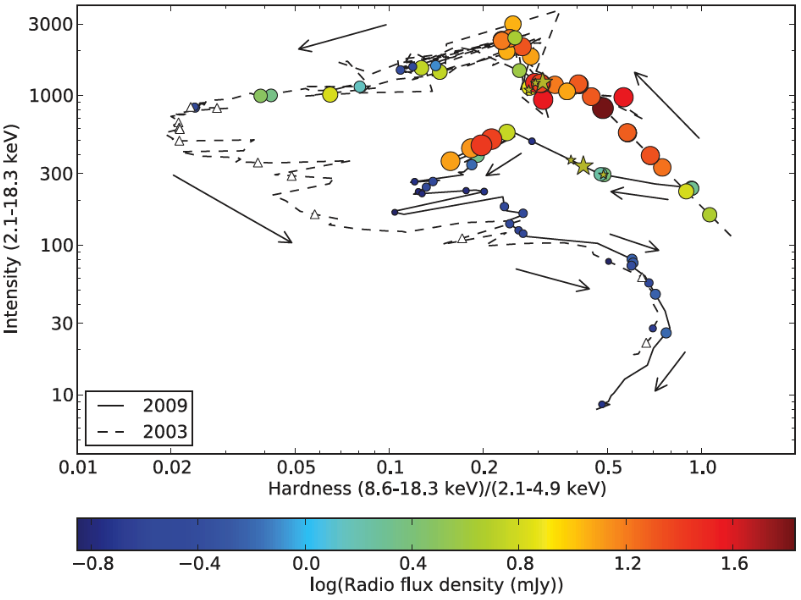

Figure 2.15: HID of H 1743-322 taken from Miller-Jones et al. (2012) Circles indicate radio detections and open triangles indicate non-detections. Radio emission from the jet is observed in the hard state.

to produce wind and jet easily(Blandford & Begelman, 1999).

Radio emission from jets is also seen in very high states of BH XRBs and in HBs of Z sources. In these state, strong steep hard tails are observed in addition to soft disk emission (Paizis et al., 2006). Thus these power-law components should be related with jets, but the details of this are not yet understood.

2.5.2 Accretion disk winds

Accretion disk winds are often observed as a characteristic spectral feature called a P-Cygni profile that consists of a red wing of the emission line and a blue shifted absorption line (Fig.2.16). Thanks to recent observations by high resolution grating spectrometers such as the High Energy Transmission Grating Spectrometer (HETGS) onboard *Chandra* and the Reflection Grating Spectrometer (RGS) onboard *XMM-Newton*, these line structures have been observed in more detail. LMXBs, both NSs and BHs show these features from lines of highly ionized ions which are mostly He- or H-like iron with a typical velocity less than 1000 km/s (Miller et al., 2015). These lines are preferentially seen in dipping source (high inclination systems) (Díaz Trigo & Boirin, 2016, Tab. 2.1). Because the mass transfer of LMXBs is driven by Roche-Lobe overflow, the origin of these lines is not caused by the stellar winds from companion stars. Instead, the source of the outflowing gas must be the accretion disk (Fig.2.18). These winds are seen only when spectra are soft and fairly

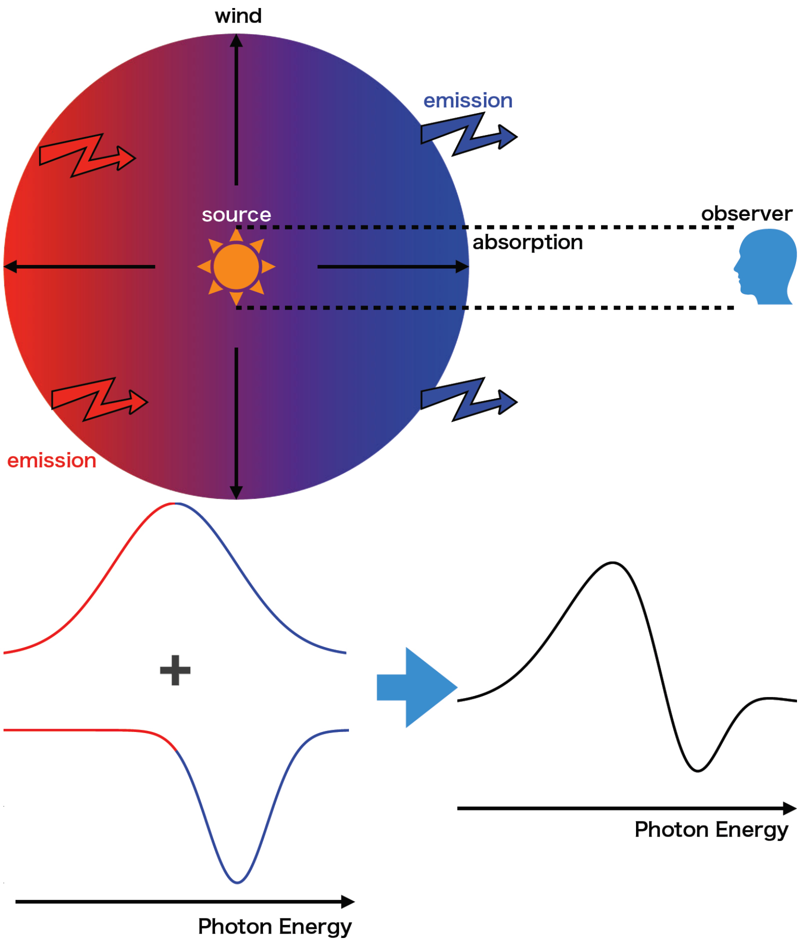
wind
emission
source
observer
absorption
emission
+
Photon Energy
Photon Energy

Figure 2.16: The schematic view of P-Cygni profile

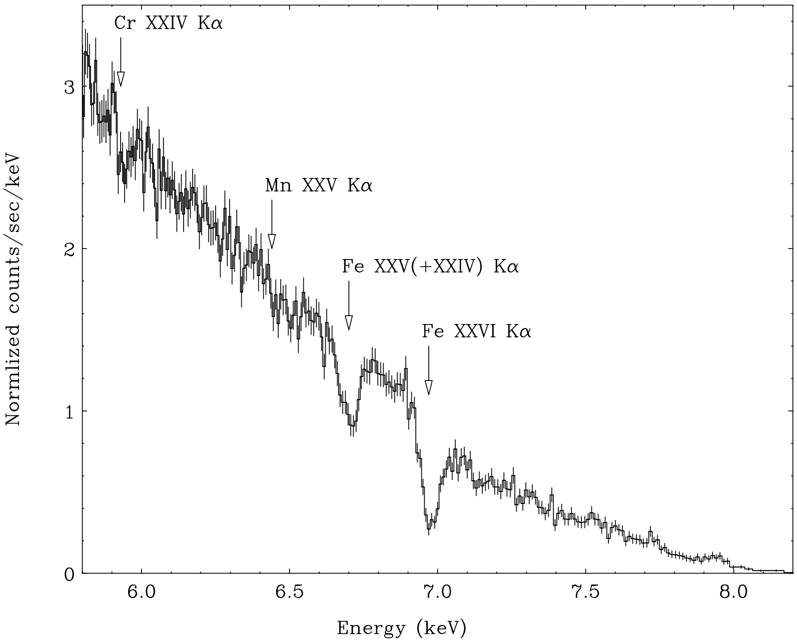

Figure 2.17: Bule shifted absorption lines in LMXB GX 13+1 taken from Ueda et al. (2004)

luminous, in the disk dominated soft states, rather than in Compton dominated hard states (Ponti et al., 2012; Ponti et al., 2014, Fig.2.21).

The strongest wind is observed from GRO 1655-40, but it has some very different properties to 'normal' LMXB winds. Fig.2.19 shows spectra from 2 Chandra observations, taken less than two weeks apart. The black spectrum shows a 'normal' wind, with only very high ionization absorption lines from H and He-like iron. However, the red spectrum shows many more absorption lines from lower ionization states. These lines are unique to this observation. None of the other sources, any other observations of this source show these absorption lines.

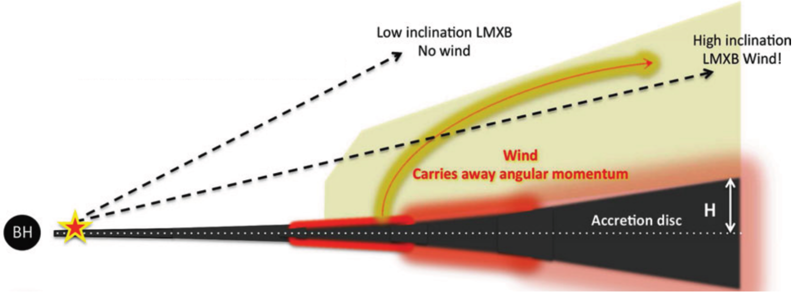
Low inclination LMXB
No wind
High inclination
LMXB Wind!
Wind
Carries away angular momentum
BH
Accretion disc
H

Figure 2.18: The schematic of disk winds taken from Ponti et al. (2012).

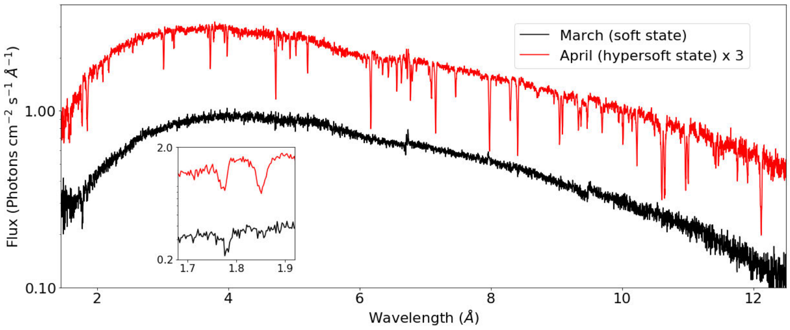

Figure 2.19: Spectra of GRO J1655–40 taken from Higginbottom et al. (2018). The two spectra are offset by a factor 3 for clarity. They are actually very similar in observed continuum luminosity and shape, with the red spectrum being only marginally softer than the black (Fig.2.20).

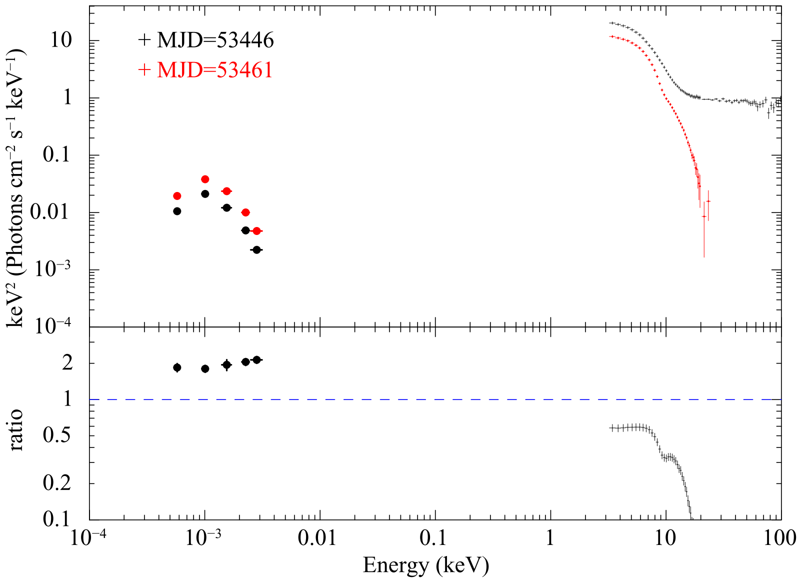

Figure 2.20: Multi-wavelength SEDs of GRO J1655–40 during the 2005 ourburst taken Shidatsu et al. (2016) (top). Colors show hypersoft state (red) in April, and normal soft state (black) in March. The bottom show ratio of the two SEDs. The former data (red) are divided by the latter (black).

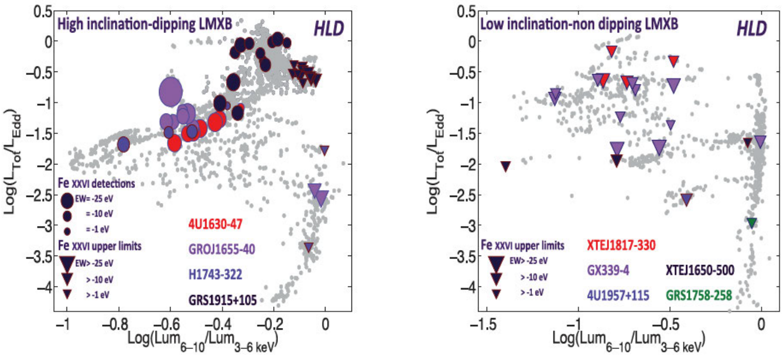

Figure 2.21: The relation between absorption lines and spectral state taken from Ponti et al. (2012). The left panel shows HID taken from *RXTE* over-plotting absorption equivalent widths by simultaneous *Chandra*/HEG in dipping sources. Absorption lines are only seen in soft state. The right panel shows the same as left but non-dippig source. They are not observed in non-dipping source.

Table 2.1: List of low-mass X-ray binaries for which a photoionized plasma local to the source has been detected in the absorption spectrum taken from Díaz Trigo & Boirin (2016). The first columns indicate the source name, the orbital period, the galactic column density towards the source after Kalberla et al. (2005), type of the compact object, whether it shows dips (D), and, if not, the source inclination (i). (See Liu et al. (2007) for the references on the period and inclination, unless otherwhise noted.) The last column indicates if the degree of ionization of the photoionised absorber(s) detected during persistent intervals (outside dips) is < 3 or ≥ 3 in $\log \xi$, whether the absorber seems to flow outwards (out), inwards (in) or to be bound as an atmosphere (atm), based on the velocity shifts of the absorption lines detected with *Chandra*/HETGS or *XMM-Newton*/RGS. "no grat." means that no contraints were published on the velocity shifts from these gratings.

Source	$P_{\rm orb}$	$N_{\rm H}^{\rm Gal}$	NS or BH	Dips or i(°)	$\log \xi$		Flow	References
		10^{21} cm^{-2}			< 3	≥ 3		
4U 1916–05	0.83 h	2.3	NS	D	x	x	atm	Boirin et al. (2004); Juett & Chakrabarty (2006)
1A 1744–361	1.62 h	3.1	NS	D		x	atm	Gavriil et al. (2012)
4U 1323–62	2.93 h	12	NS	D		x	no grat.	Boirin et al. (2005); Church et al. (2005)
EXO 0748–676	3.82 h	1.0	NS	D	x	x	atm	Díaz Trigo et al. (2006); van Peet et al. (2009)
XB 1254–690	3.93 h	2.0	NS	D		x	atm	Boirin & Parmar (2003); Díaz Trigo et al. (2006, 2009)
MXB 1658–298	7.11 h	1.9	NS	D	x	x	atm	Sidoli et al. (2001); Díaz Trigo et al. (2006)
XTEJ1650–500	7.63 h	4.2	BH	> 50	?[a]	?[b]	?[c]	Miller et al. (2002, 2004)
AXJ1745.6–2901	8.4 h	12	NS	D		x	no grat.	Hyodo et al. (2009); Ponti et al. (2015)
MAXI J1305–704	9.74 h[d]	1.9	BH	D	x		in	Shidatsu et al. (2013); Miller et al. (2014)
X-1624–490	20.89 h	20	NS	D		x	atm	Parmar et al. (2002); Díaz Trigo et al. (2006)
IGR J17480–2446	21.27 h[e]	6.5	NS	D		x	out	Miller et al. (2011)
GX 339–4	1.76 d	3.6	BH	> 45[f]	x		?[g]	Miller et al. (2004); Juett & Chakrabarty (2006)
GROJ1655–40	2.62 d	5.2	BH	D		x	out	Miller et al. (2006); Miller et al. (2008)
Cir X–1	16.6 d	16	NS	D	x	x	out	Brandt & Schulz (2000); Schulz et al. (2002)
GX 13+1	24.06 d	13	NS	D		x	out	Ueda et al. (2001); Ueda et al. (2004)
GRS 1915+105	33.5 d	13	BH	D		x	out	Kotani et al. (2000); Lee et al. (2002)
IGR J17091–3624	>4 d [h]	5.4	BH	> 53[j]		x	out	King et al. (2012)
4U 1630–47		17	BH	D		x	out	Kubota et al. (2007); Díaz Trigo et al. (2013, 2014)
H 1743–322		6.9	BH	D		x	out	Miller et al. (2006)

[a] Not estimated; absorption lines from Ne IX and of a Ne II (Miller et al., 2004). [b] Not estimated; absorption feature near 7 keV possibly due to Fe XXVI (Miller et al., 2002). [c] Detection of an unshifted line from Ne IX and of a Ne II line blueshifted by $\sim 510 \pm 60$ km/s possibly due to a local absorber (Miller et al., 2004). An interstellar origin was attributed to a similar Ne II line in GX 339-4. [d] Shidatsu et al. (2013) [e] Papitto et al. (2011) [f] Using the lower limit on the mass of the companion star estimated by Muñoz-Darias et al. (2008) and assuming that the black hole mass is less than 15 $M_{\odot}$ (Shidatsu et al., 2011). [g] Detection of several lines (Ne IX, OVII, etc) with blueshifts in the range 50–160 km/s and of lines from Ne II-III blueshifted by 510 ± 20 km/s (Miller et al., 2004). While the Ne IX line is produced mainly by a local absorber, the Ne II-III lines are consistent with being produced by the hot interstellar medium (Juett & Chakrabarty, 2006). [h] Wijnands et al. (2012) [i] Rao & Vadawale (2012)

2.5.3 Jet driving mechanisms

Many jet models have been proposed, but the current consensus is that jets are driven by a combination of magnetic fields and rotation. These models are generally divided into two types relating to the energy source, which is the rotational energy of the black holes and that of hot accretion flows. The former is electromagnetic extraction of black hole spin energy called the Blandford-Znajek (BZ) mechanism (Blandford & Znajek, 1977). The latter (accretion powered jets) is Blandford-Payne models(Blandford & Payne, 1982) driven by magneto centrifugal force or magnetic tower mechanism driven by the gradient force of magnetic or/and gas pressure Lynden-Bell (1996, 2003).This magnetic tower mechanism is seen in some MHD simulations (Shibata & Uchida, 1985, 1986; Kato et al., 2004; Ohsuga & Mineshige, 2011, Model C in Fig.2.22). Recent relativistic magneto-hydrodynamics simulations suggested that truly relativistic jets seen in AGNs are produced by the BZ mechanism and magnetic tower mechanism, whereas quasi-relativistic jet seen in X-ray binaries are driven by magnetic tower mechanism (McKinney & Gammie, 2004; Tchekhovskoy et al., 2011).

An alternative jet mechanism is proposed by Ohsuga et al. (2009); Ohsuga & Mineshige (2011, Model A in Fig.2.22), which is radiation accelerated magnetically collimated jet. When the mass accretion rate is larger than or close to the Eddington mass accretion rate, the disk changes to different regime called the slim disk (Abramowicz et al., 1988). Because of strong radiation, the scale height of this disk is larger than a standard disk. This intense radiation produce winds and jets near the compact object. The jet in the famous BH SS 433 is likely to be driven by this mechanism (Eggum et al., 1988). The origin of radio emission in the horizontal branch of Z source and very high soft state in BHs may also be due to this jet (Homan et al., 2016).

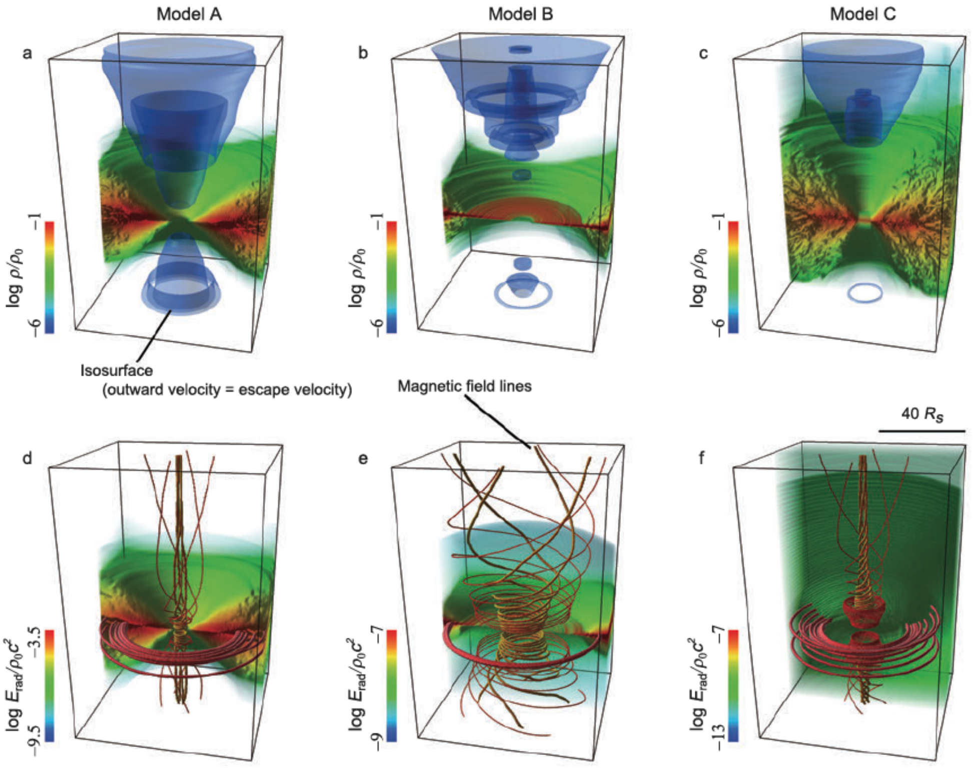
Model A
Model B
Model C
a
b
c
log ρ/ρ₀
−1
−6
Isosurface
(outward velocity = escape velocity)
Magnetic field lines
40 R_S
d
e
f
log $E_{rad}/\rho_0 c^2$
−3.5
−9.5
−7
−9
−7
−13

Figure 2.22: The results of Radiation Magneto Hydrodynamic (RMHD) simulations near the black hole for models slim disk (Super-Eddington accrtion), standard disk, and hot accretion flow (ADAF), from left to right, taken from Ohsuga & Mineshige (2011). Upper panels: Normalized density distributions (color) are overlaid with isosurfaces, at which the outward velocity equals to the escape velocity. The model of hot accretion flow is optically thin. Lower panels: The distributions of the normalized radiation energy density (color) is overlaid with the magnetic field lines.

2.5.4 Wind driving mechanisms

Accretion disk winds are produced by the gas pressure gradient force $-\nabla p$, where p is gas pressure ,by the radiation force $\boldsymbol{F}_{\rm rad}$, and by the Lorentz force given by the magnetic fields $\frac{1}{4\pi}(\nabla \times \boldsymbol{B}) \times \boldsymbol{B}$ ($\boldsymbol{B}$; magnetic fields). When the sum of these forces become larger than the gravity, winds are launched. This can be described by the equation of motion

$$\rho \frac{D\boldsymbol{v}}{Dt} + \rho \nabla \Phi = -\nabla p + \boldsymbol{F}_{\rm rad} + \frac{1}{4\pi}(\nabla \times \boldsymbol{B}) \times \boldsymbol{B} \tag{2.17}$$

where $\rho, \boldsymbol{v}, \Phi$ are the mass density, the velocity, and gravitational potential, respectively. D/Dt is the convective derivative or the Lagrangian derivative. The wind driving mechanisms are divided into a thermal driving, radiation driving, and magnetic driving depending on which force is dominant.

Thermal (Compton heated) winds

The thermal winds are produced by a gas pressure gradient force because of large temperature. In XRBs, bright X-ray radiation from the inner disk and corona heats the surface of the disk at outer radius to the Compton temperature of $T_{\rm IC} \sim 10^7 - 10^8$K, where Compton heating and cooling is balanced, and produce the atmosphere with this temperature. When the thermal energy is larger than gravitational potential, winds form. Begelman et al. (1983) constructed the first analytic model and Woods et al. (1996) first carried out the hydrodynamic simulations of thermal winds. The launching radius is about $0.2R_{\rm IC}$, where $R_{\rm IC} = \mu m_p G M_c/(kT_{\rm IC})$ called the Compton radius (Woods et al., 1996, see also Sec.3.2). This driving mechanism is proposed as a natural explanation for equatorial winds in soft state in LMXBs.

Radiative winds

When the radiation force of the disk is larger than gravity, winds form. If the source is near or above the Eddington luminosity, the radiation force on electrons drives winds (continuum driving). There are a number of objects that may drive super-Eddington (or close to Eddington) outflows, such as AGN with ultra-fast outflows (e.g. Reeves et al. 2008; Hagino et al. 2015), Narrow Line Seyfert Is (NLSI Done & Jin 2016; Hagino et al. 2016) and Ultra Luminous X-ray sources (ULX, Walton et al. 2013). Recent radiation hydrodynamic simulations show strong outflows produced from Super-Eddington accreting source (e.g. Ohsuga et al. 2005; Takeuchi et al. 2013, Fig.2.23) . However, there are few super-Eddington sources in XRBs, therefore this mechanism seems not to be primary driving mechanisms. Even if this mechanism is not primary, this could help wind driving because winds in XRBs are seen in soft state with luminosity above $L > 0.1L_{\rm Edd}$.

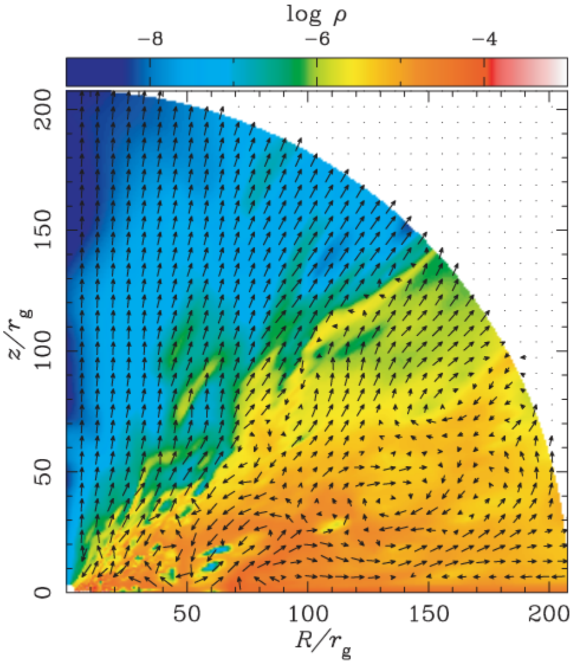

Figure 2.23: The simulated density distribution of super-Eddington accretion flow taken from Ohsuga et al. (2005). The arrows show velocity fields. The input mass accretion rate is $1000L_{\rm Edd}/c^2$ with $M_c = 10M_\odot$.

Radiation could forms winds if bound-bound transition of partially ionized ions in UV band is the dominant interaction between photons and materials even if luminosity is below Eddington limit. The cross-section of these interaction is larger than the Thomson cross-section by a factor 2000-4000 if the material is partially ionized (Castor et al., 1975). Therefore this mechanism is more efficient to accelerate than continuum driving. This mechanism is called line driving. Because the accretion disk of AGNs should emit strong UV, this UV could be the cause of UFOs.

Although numerical radiation hydrodynamic simulations shows strong UV-line driven winds (Proga et al., 2000; Nomura et al., 2016, Fig.2.24) in AGNs, it is still under discussion whether this mechanism is the origin of UFO or not. These simulations deal with the opacity, the radiation force from lines, and a net heating/cooling rate unrealistically. They use the cross-section of bound-free absorption σ_a as $\sigma_a = 100\sigma_T$ when $\xi < 10^4$ and $\sigma_a = \sigma_T$ when $\xi > 10^4$, where σ_T is the Thomson cross-section. The radiation force is calculated for stars which have very different spectra compared to AGNs. Due to the unrealistic treatment, more accurate ionization calculations using hydrodynamic simulations show large differences(Higginbottom et al., 2014). However, in XRBs, strong X-ray radiation ionize materials, so this mechanism seems not very significant (Proga & Kallman, 2002).

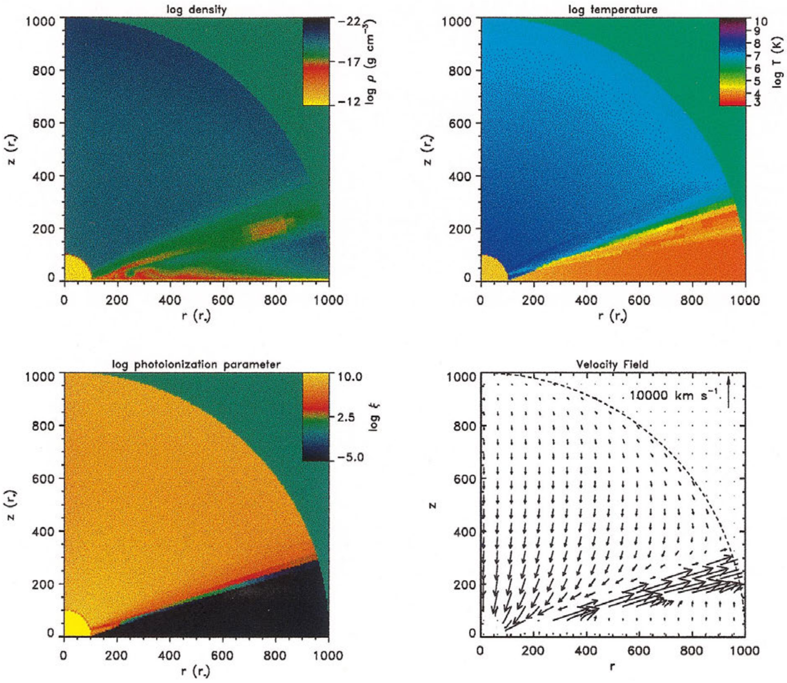

Figure 2.24: The result of radiation hydrodynamic simulaton taken from Proga et al. (2000). Panels show density distribution (top left), temperature (top right), ionization parameter ξ (bottom left), and velocity (bottom right). Materials accelerate at ionization region.

Magnetic winds

Winds are also launched by the Lorentz force. Although there is still uncertainty over the origin of magnetic fields in accretion disk and the physics of these magnetic process, the magnetic processes should play an important role in the accretion process especially in the angular transportation which is likely driven by MRI. Thus, magnetic driving could be a candidate of the wind driving mechanisms.

Another reason to study magnetic winds is rich absorption line spectrum seen from GRO J1655–40 in hypersoft state Fig. 2.19. This wind seems to be too hot, too dense, and too close to the BH to be driven by a radiation force or thermal pressure (Miller et al., 2006, 2008). This has low luminosity $L \sim 0.03 L_{\rm Edd}$ which is too low to drive the wind by radiation force alone, very high density $n_p = 10^{13-14}{\rm cm}^{-3}$ suggested by the line ratio of metastable levels for Fe XXII, and high ionization parameter $\xi = 10^{4.5-5.4}$ obtained by single zone absorption models. From these values, the radius of this wind was estimated to be $R_{\rm w} = \sqrt{L/(n_p \xi)} = 10^{9.0-9.4}{\rm cm}$ corresponding to $R_{\rm w} = 1000 - 2400 R_g$. The Compton radius of this spectra is

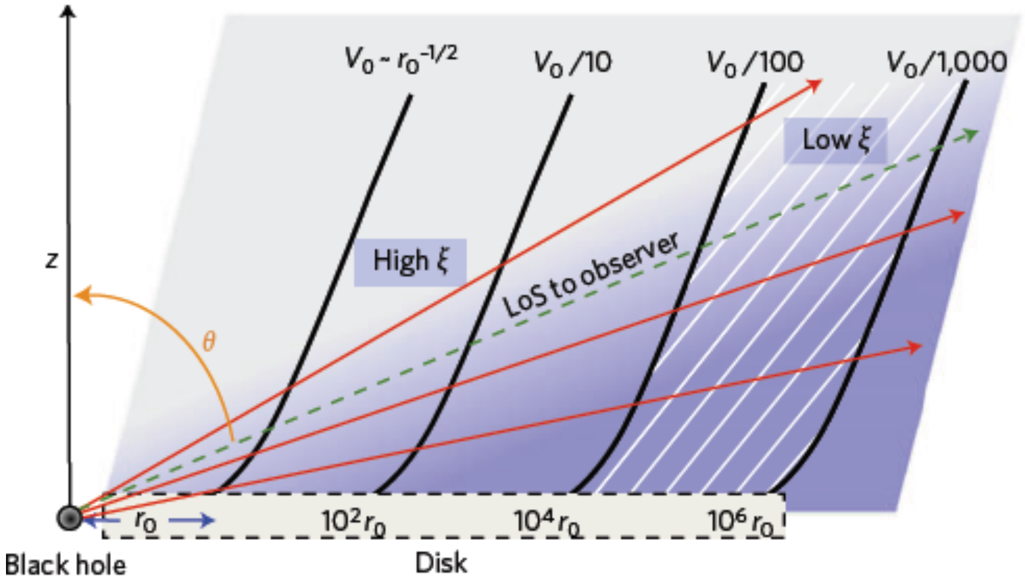

Figure 2.25: A schematic of the MHD wind taken from Fukumura et al. (2017). Poloidal two-dimensional wind streamlines (thick solid grey lines), the decreasing velocity ($V_0 \sim c$) and ionization parameter ξ with radius are illustrated. The hatched region represents the absorbing region with velocity 100–1000 km/s. The red arrows indicate possible lines of sight, with the green arrow believed to be the true line of sight based on published binary solutions.

$R_{\rm IC} = 5 \times 10^5 R_g$ and its launching radius is $\sim 0.2 R_{\rm IC} = 1.0 \times 10^5 R_g$. This means that the wind radius of this source is much smaller than the launching radius of the prediction from thermal winds. Therefore magnetic winds have been studied actively.

They are two main ways to drive winds by magnetic forces. One way is by magnetic tension and anther way is by magnetic pressure. The last term of Eq.2.17 is written as

$$\frac{1}{4\pi}(\nabla \times \boldsymbol{B}) \times \boldsymbol{B} = \frac{(\boldsymbol{B} \cdot \nabla)\boldsymbol{B}}{4\pi} - \nabla \left(\frac{B^2}{8\pi}\right) \tag{2.18}$$

The first term on the right hand side is considered as the magnetic tension associated with the field lines and the second terms as the isotropic magnetic pressure.

The most popular magnetic wind model is the one by Blandford & Payne (1982) driven by magnetic tension and centrifugal forces. This model requires large scale ordered magnetic fields with a strong poloidal component threading the disk. Recent analytic models of this mechanism show that they can explain the observed spectra both of AGNs and XRBs(Fukumura et al., 2014, 2017, Fig.2.25) assuming large scale self similar magnetic fields from the entire disk. Indeed this model well describes the unusual absorption lines seen in GRO J1655–40 (Fig.2.26). However, that model can not reproduce the abosption lines of metastable levels Fe XXII at 11.77 and 11.92

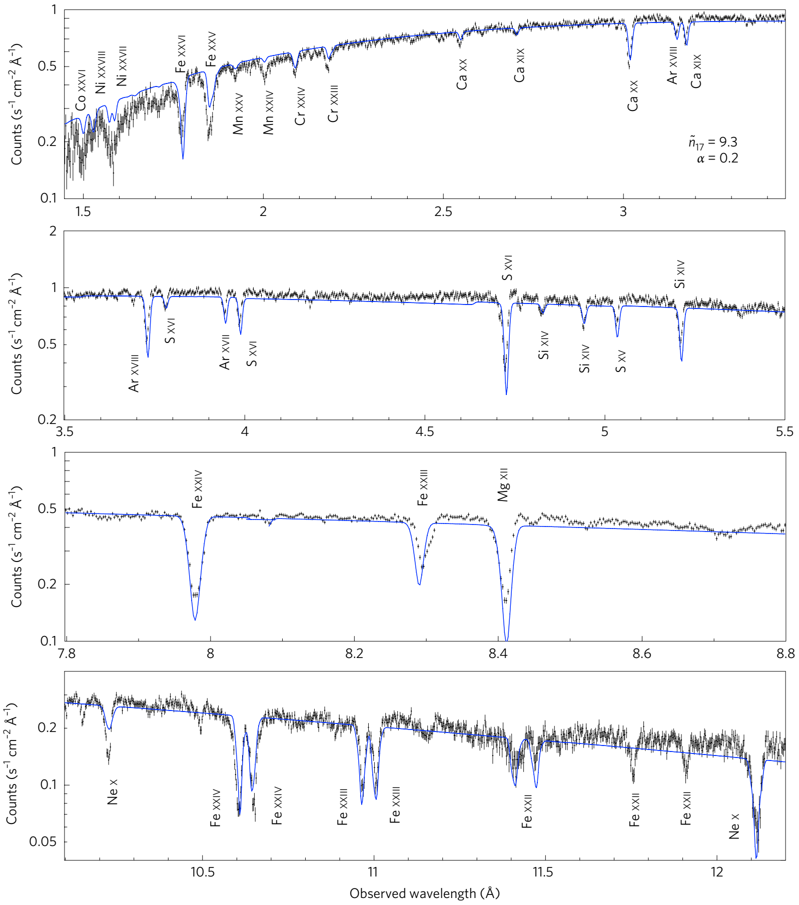

Figure 2.26: The *Chandra*/HETG spectrum of GRO J1655–40 overlaid on the global MHD wind model taken from Fukumura et al. (2017)

Å(bottom in Fig.2.26), which are used for density diagnosis and there is no guarantee such ordered magnetic fields can actually form around accretion disk. Also, it is suggested that the unusual wind in GRO J6155-40 is an optically thick continuum driven wind due to Super-Eddington accretion, and this radiation itself is attenuated by this thick wind (Neilsen et al., 2016; Uttley & Klein-Wolt, 2015; Shidatsu et al., 2016). The alternative model is driven by magnetic pressure (Proga, 2003). In this model, the toroidal component dominates over the poroidal component and forms a slow, dense outflow similar to thermal winds.

2.6 Radiative process in accretion disk winds

X-ray photons interact with the photoionized plasma and we observe these interaction in spectra. Thus, understanding these processes are important to the spectroscopic study of accretion disk winds. In this section, we briefly summarize these (see also e.g. Rybicki & Lightman 1979)

2.6.1 Photoinozed plasma

A gas irradiated by strong X-ray or UV photons from bright astrophysical objects such as AGNs, XRBs is ionized by photoinozation processes and forms a photoionized plasma. Accretion disk winds both AGNs and XRBs are generally considered as photoinoized plasma because of the strong X-ray/UV radiation from central objects.

Photoionized plasma is ionized and heated by photoionization and loses energy primarily through a cascade following radiative recombination. Both the equilibrium temperature and the charge state distribution of this photoionized plasma are determined by the shape and intensity of the X-ray spectra and also from the gas density. These are often characterized by ionization parameter.

$$\xi = \frac{L_X}{nR^2} \tag{2.19}$$

where L_X is the ionizing X-ray luminosity, n is the gas density and R is the distance to the X-ray source (Tarter et al., 1969)

The charge state distribution is determined by a balance between photoiozation and recombination. These processes depend on the temperature via level populations and Milne relation, and the temperature is determined by a balance heating/cooling rates. These are related to the radiative process which depends and the charge state distribution. To get equilibrium temperature and the charge state distribution, iterative treatment is required.

A computer program such as XSTAR (Kallman et al., 2004), CLOUDY (Ferland, 2003) and SPEX (Kaastra et al., 1996) can treat such iterative treatment and calculate the physical state of the photoionized plasma such as the equilibrium temperature and the charge state distribution. These codes also calculate the resultant spectrum through the photoionized plasma by solving the 1-dimensional radiation transfer. Fig.2.27 shows the charge state distribution of iron as a function of ξ.

2.6.2 Interactions between X-ray and photoionized plasma

Important interactions between X-ray and photoionized plasma are photoionization, photoexicitation, Compton process (Compton scattering, Inverse Compton scatter-

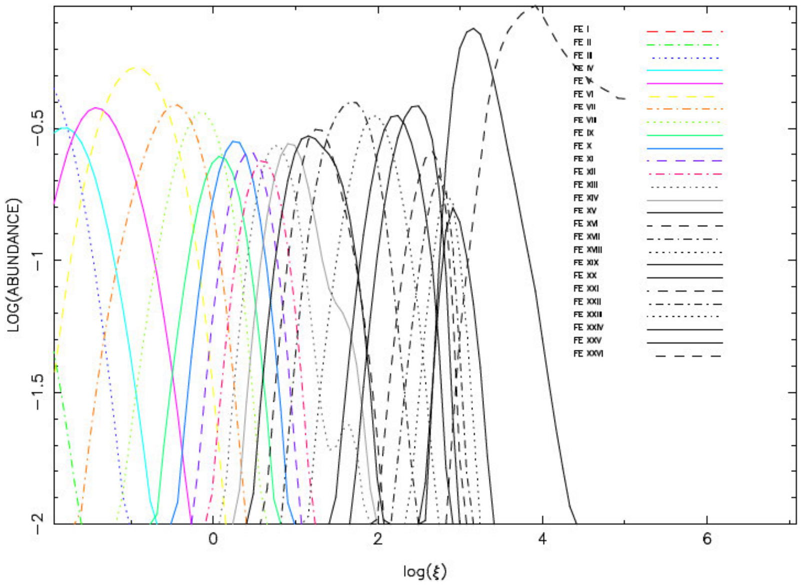

Figure 2.27: Ion fractions vs. ionization parameter ξ with an $F_E \propto E^{-1}$ ionizing continuum taken from Kallman et al. (2004)

ing). In this section, We briefly summarize these effects.

photoinoization and radiative recombination

Photoionization and readiative recombination follow the equation

$$X^{+r} + \gamma \longleftrightarrow X^{+r+1} + e^{-} \tag{2.20}$$

Photoionization is bound-free transition from an initial state composed of a photon γ and an ion X^{+r} to a final state composed of a free electron e^{-} and an ionized ion X^{+r+1}. The inverse process of photoionization is radiative recombination.

The photoinozation cross-section of Hydrogen-like ions for photon energy $E > Z^2 I_H (I_H \simeq 13.6 \text{ eV})$ is given by

$$\sigma_{pi}(E) = \sigma_0 \left(\frac{Z^2 I_H}{E} \right)^4 \frac{\exp(4 - 4\arctan(x)/x)}{1 - \exp(-2\pi/x)} \tag{2.21}$$

where $x = \sqrt{E/Z^2 I_H - 1}$. σ_0 is the cross-section when $E = Z^2 I_H$.

$$\sigma_0 \equiv \frac{2^9 \pi^2}{3\exp(4)} Z^{-2} \alpha a_0^2 \tag{2.22}$$

where α is fine-structure constant, a_0 is Bohr radius. When energy is small enough $E < 100 Z^2 I_H$, $\sigma_{pi} \approx \sigma_0 (Z^2 I_H / E)^3 \propto Z^4$. This suggest that the cross-section is highly depend on the atomic number. Thus this process occurs more easier in heavy elements such as iron.

The cross-section of radiative recombination can be related to the photoinization cross-section by applying a principle of detailed blance in thermodynamic equilibrium. This relationship is called the Milne relationship

$$\sigma_{rr}(v) = \frac{g_r}{g_{r+1}} \left(\frac{E}{m_e c v} \right) \sigma_{pi}(E) \tag{2.23}$$

where g_r is the statistical weight of the ion X^{+r}, whereas g_{r+1} is that of the ion X^{+r+1}. A photon energy of E and an electron velocity v are related by $E = m_e v^2/2 + I$ (I is the ionization potential).

When an ion has three or more electrons, the electrons in the inner shell get energy of photon. This effect appears as fluorescence or the Auger effect.

$$X_*^{+r} \longrightarrow \begin{cases} X^{+r} + \gamma & \text{(fluorescence)} \\ X^{+r+1} + e^- & \text{(Auger effect)} \end{cases} \tag{2.24}$$

In fluorescence process, the excited electron emits X-rays and goes back to the initial state. On the other hand, in the Auger effect, an electron drops into the vacancy, and the other electron(s) is ejected from the ion.

Photoexcitation

Photoexcitetion is a bound-bound transition from the low energy state l to high energy state u. In this interaction, an ion with energy E_l absorbs an photon with energy $E_u - E_l$ and is excited to the state with energy E_u.

$$X_l + \gamma \longrightarrow X_u \tag{2.25}$$

As a result, an absorption line with energy $E_u - E_l$ is observed. After photoexcitation, the excited ion goes back to the initial state by re-emitting energy as a photon or an electron. The former process is called radiative decay, and the latter is called autoinonization. The radiative decay shows emission lines with the same energy as the absorbed photon. These emission and absorption lines are important tools to probe the physical condition of the emitting/absorbing materials, providing the imformation of the dynamics, temperature, density and the abundances. Similar to the Auger effect, autoionization can occur only if the ion has multiple electrons.

The cross-section of photoexcitation from the low energy state l to the high energy state u is proportinal to its oscillator strength f_{lu}

$$\sigma_{lu}(\nu) = \frac{\pi e^2}{m_e c} f_{ul} \phi(\nu) \tag{2.26}$$

where $\phi(\nu)$ is the normalized line profile function with $\int \phi(\nu)d\nu = 1$. $\phi(\nu)$ is generally written as a combination of a Gaussian profile and a Lorentzian profile

$$\phi(\nu) = \frac{1}{\Delta\nu_D \pi^{1/2}} H(a, u) \tag{2.27}$$

where, $H(a, u)$ is the Voigt function

$$H(a, u) = \frac{a}{\pi} \int_{-\infty}^{\infty} \frac{\exp(-y^2)}{a^2 + (u - y)^2} dy \tag{2.28}$$

and, a, u,$\Delta\nu_D$ are

$$a = \frac{\Gamma}{4\pi\Delta\nu_D} \tag{2.29}$$

$$u = \frac{\nu - \nu_D}{\Delta\nu_D} \tag{2.30}$$

$$\Delta\nu_D = \nu_0 \sqrt{\frac{2kT}{m_{\rm ion} c^2}}, \tag{2.31}$$

where $m_{\rm ion}$ is the mass of an atom or an ion. $\Delta\nu_D$ shows the Doppler broadening due to the thermal motion of materials with temperature T. If the materials has additional turbulent motion with velocity v_t, then this effect appears as

$$\Delta\nu_D = \nu_0 \sqrt{\frac{2kT}{m_{\rm ion} c^2} + \frac{v_t^2}{c^2}}, \tag{2.32}$$

$$\Gamma = \sum_l A_{ul} \tag{2.33}$$

where A_{ul} is the transition probability per unit time from the upper state u to the lower state l for spontaneous emission, called the Einstein A-coefficient. Γ is influenced by natural broadening based on the uncertainty principle. The life time of the excited ion is small and its deviation is also small. Thus the uncertainty in the energy is large.

The energy level of an ion is characterized by the total orbital angular momentum L, the total spin angular momentum S and the total angular momentum J.

$$^{2S+1}\mathcal{L}_J \tag{2.34}$$

where $\mathcal{L} = S, P, D, F$ for $L = 0, 1, 2, 3$. Parity of the wave function of an electron is also important variable. The parity is even if $\prod_i (-1)^{l_i} = 1$, and odd if $\prod_i (-1)^{l_i} = -1$. where l_i is the orbital angular momentum of individual electron orbital.

The strongest transitions of H-like ions are called Lyman series;

- Ly$\alpha_{1,2}$: $2p\ ^2P_{3/2,1/2} \leftrightarrow 1s\ ^2S_{1/2}$

- Ly$\beta_{1,2}$: $3p\ ^2P_{3/2,1/2} \leftrightarrow 1s\ ^2S_{1/2}$
- Ly$\gamma_{1,2}$: $4p\ ^2P_{3/2,1/2} \leftrightarrow 1s\ ^2S_{1/2}$

These transitions are electronic dipole transitions and follows these selections;

1). parity must change

2). $\Delta L = 0, \pm 1$

3). $\Delta J = 0, \pm 1$ (except $J = 0 \leftrightarrow J = 0$)

4). $\Delta l = \pm 1$

5). $\Delta S = 0$

The transition which follow these selection is called the allowed transition.

Transitions of He-like ions are more complicated;

- $w : 1s2p\ ^1P_1 \leftrightarrow 1s^2\ ^1S_0$
- $x : 1s2p\ ^3P_2 \leftrightarrow 1s^2\ ^1S_0$
- $y : 1s2p\ ^3P_1 \leftrightarrow 1s^2\ ^1S_0$
- $z : 1s2p\ ^3S_1 \leftrightarrow 1s^2\ ^1S_0$

where w is the electronic dipole transition, and also called the resonance transition. x and y are called the intercombination transitions or semi-forbidden transitions, where selection rules in the above 1 to 4 are satisfied but $\Delta S = 0$. These transitions are much weaker than the allowed transitions. z is the magnetic dipole transition, where selection rules in the above 1, 4, 5 are not satisfied and called the forbidden transition. Each transition (resonance, intercombination and forbidden) often represented by symbols of r, i, f, respectively. Transitions of He-like ions between K-shell and L-shell ($n = 2 \leftrightarrow 1$) is called as Heα. Like Lyman series, $n = 3 \leftrightarrow 1$、 $n = 4 \leftrightarrow 1$ are called as Heβ, Heγ, respectively.

Compton scattering

Compton scattering is the scattering of a photon from an electron with energy exchange. If the electron is at rest, the scattered photon energy E_1 can be related to the incident photon energy E_0 and the scattering angle θ such that

$$E_1 = \frac{E_0}{1 + \frac{E_0}{m_e c^2}(1 - \cos\theta)} \tag{2.35}$$

If the incident energy is much smaller than the electron rest energy $E_0 \ll m_e c^2$,

$$E_1 \approx E_0 \left\{ 1 - \frac{E_0}{m_e c^2}(1 - \cos\theta) \right\} \tag{2.36}$$

The differential cross-section of Compton scattering by non-polarized photons is given by the Klein-Nishina formula

$$\frac{d\sigma_{comp}}{d\Omega} = \frac{r_0^2}{2} \frac{E_1^2}{E_0^2} \left(\frac{E_0}{E_1} + \frac{E_1}{E_0} - \sin^2\theta \right) \tag{2.37}$$

where $r_0^2 = e^2/m_e c^2$ is classical electron radius. The total cross-section is

$$\sigma_{comp} = \sigma_T \frac{3}{4} \left[\frac{1+x}{x^3} \left\{ \frac{2x(1+x)}{1+2x} - \ln(1+2x) \right\} + \frac{1}{2x} \ln(1+2x) - \frac{1+3x}{(1+2x)^2} \right] \tag{2.38}$$

where $x = E_0/m_e c^2$, and $\sigma_T = 8\pi r_0^2/3$ is the Thomson cross-section. If the incident energy is much smaller than the electron rest energy $x \ll 1$, this cross-section approaches σ_T.

If photon is scattered by a moving electron, the energy is transferred from the electron to the photon. This is the inverse process of Compton scattering called as Inverse Compton scattering. By applying the Lorentz transformation, the incident energy in the electron rest frame E_0' is written as

$$E_0' = E_0 \gamma (1 - \cos\theta) \tag{2.39}$$

where $\gamma = (1 - \beta^2)^{-1/2}$ is Lorentz factor, $\beta = v/c$ is the ratio of speed of electron to that of light, and θ is incident angle. The prime $'$ means the electron rest frame. When the incident photon energy is small enough ($E_0 \ll m_e c^2$), the cross section is σ_T. Thus, the scattered photon receives the same energy as the incident photon in the electron rest frame. The scattered photon energy can be written by applying Lorentz transformation to the observer's frame

$$E_1 = E_0' \gamma (1 - \beta \cos\phi) \tag{2.40}$$

where ϕ is the scattering angle. By averaging the incident and scattered angle, the scatterd photon energy in the observer's frame is written as $E_1 \approx \gamma^2 E_0$.

From Eq. 2.36, we can calculate the heating rate of electrons by Compton scattering. When we use the incident photon energy E, from Eq.2.36 the energy difference between before and after scattering ΔE is

$$\Delta E = E_1 - E \approx -E^2/(m_e c^2) \tag{2.41}$$

Thus the heating rate via Compton scattering is written as

$$
\begin{aligned}
\frac{dE_{up}}{dt} &= c\sigma_T \int \Delta E N(E) dE \\
&= c\sigma_T \frac{\int E^2 N(E) dE}{m_e c^2} \\
&= c\sigma_T \frac{\langle E\rangle}{m_e c^2} \int EN(E)dE
\end{aligned}
\tag{2.42}
$$

Where $N(E)$ is number density of photons $\langle E\rangle = \int E^2 N(E)dE / \int EN(E)dE$ is flux weighted mean energy of photons.

In the case of Inverse Compton scattering, using the Lorentz invariant $N(E)dE/E = N'(E')dE'/E'$ and $dE'/dt' = dE/dt$, the radiation power by Inverse Compton scattering dE_{IC}/dt is

$$
\begin{aligned}
\frac{dE_{IC}}{dt} &= \frac{dE'_{IC}}{dt'} \\
&= c\sigma_T \int E'_1 N'(E')dE' \\
&\approx c\sigma_T \int E' N'(E')dE' \ (\gamma^2 - 1 \gg E/m_e c^2) \\
&= c\sigma_T \int E'^2 \frac{N'(E')dE'}{E'} \\
&= c\sigma_T \int E'^2 \frac{N(E)dE}{E}
\end{aligned}
\tag{2.43}
$$

from Eq.2.39, $E' = E\gamma(1 - \beta\cos\theta)$ so,

$$
\frac{dE_{IC}}{dt} = c\sigma_T \gamma^2 (1 - \beta\cos\theta)^2 \int EN(E)dE \tag{2.44}
$$

The energy loss of the electrons dE_{down}/dt is the difference between the radiation power of Inverse Compton scattering and the incident photon energy.

$$
\frac{dE_{down}}{dt} = c\sigma_T \left\{\gamma^2(1 - \beta^2\cos\theta)^2 - 1\right\} \int EN(E)dE \tag{2.45}
$$

By averaging over the scattering angle,

$$
\frac{dE_{down}}{dt} = \frac{4}{3}\sigma_T c \gamma^2 \beta^2 \int EN(E)dE \tag{2.46}
$$

When this process is non-relativistic, $\gamma \approx 1$,$\langle\beta^2\rangle = 3kT/(m_e c^2)$ then

$$
\frac{dE_{down}}{dt} = c\sigma_T \frac{4kT}{m_e c^2} \int EN(E)dE \tag{2.47}
$$

The temperature at thermal equilibrium via Compton heating and cooling is written as

$$
T_{\rm IC} = \frac{\langle E\rangle}{4k} \tag{2.48}
$$

which called the Compton temperature.

Chapter 3

Formation of thermal winds

The theory of thermal winds first developed by Begelman et al. (1983) and numerical simulation was carried out by Woods et al. (1996). In this chapter, we develop a predictive model of the absorption features from thermal winds, based on Begelman et al. (1983); Woods et al. (1996). We couple this to a realistic model of the irradiating spectrum as a function of luminosity to predict the entire wind evolution during outbursts to investigate whether thermal winds can explain the absorption visibility at spectral state transition.

3.1 Thermal wind models

3.1.1 Thermal instability of photoionized plasma

The thermal equilibrium of optically thin photoionized plasma shows S-shaped curve (Fig. 3.1) at a giving gas temperature T and pressure ionization parameter $\Xi = p_{\rm rad}/p_{\rm gas}$ (Krolik et al., 1981). The solid line in the figure corresponds to the thermal equilibrium between radiative heating and cooling. At low temperatures, there is near balance between photoionization heating and cooling due to line excitation and recombination. At large temperatures, the equilibrium arises from a balance of Compton heating and cooling. The left side of this line shows cooling is larger than heating, whereas the right side shows heating is dominant. The thermal equilibrium curve with a positive slope ($dT/d\Xi > 0$) is thermally stable. If the temperature rises with fixed Ξ from S-curve, it moves into the cooling dominated region. Therefore the temperature goes down. On the other hand, the curve with a negative slope is thermally unstable for the opposite reason. The changing points of slope sign are instability points. This S-shaped curve depends on metal abundances and irradiation spectra.

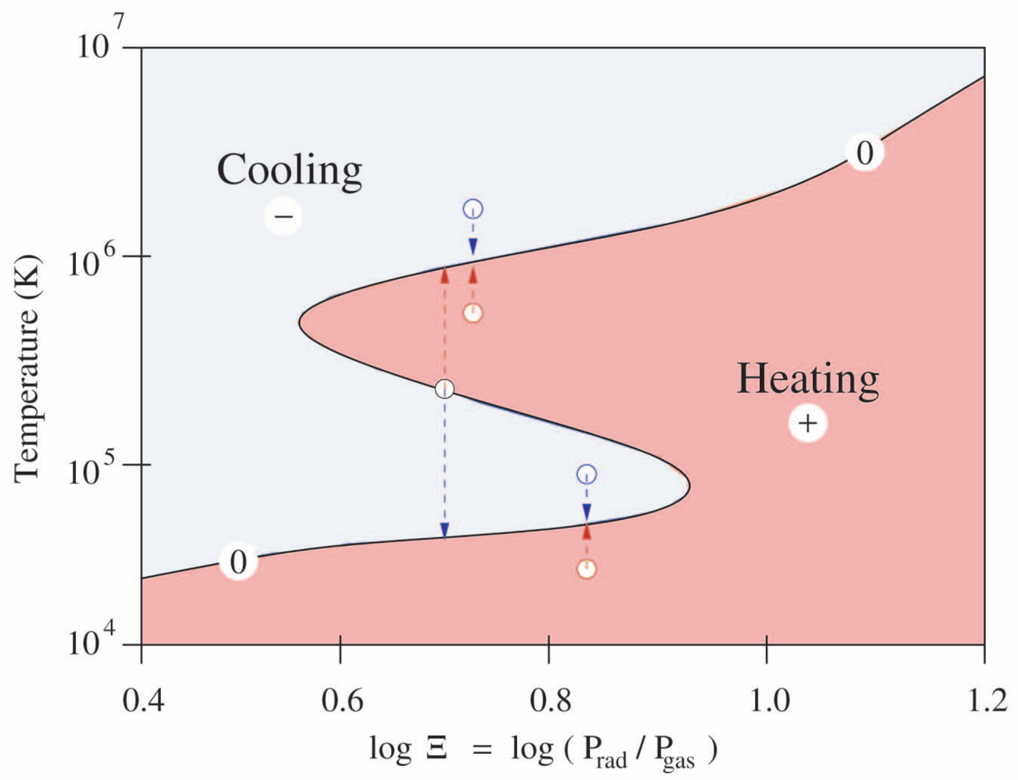

Figure 3.1: Schematic diagram of thermal equilibrium curve of photoionized plasma taken from Jimenez-Garate et al. (2002)

If we consider this thermal instability at the surface of an accretion disk, a top layer of the accretion disk make a completely ionized atmosphere which is supported by the Compton heating and cooling. When we consider going into the mid-plane of the disk, the ionization parameter is decreasing because of increasing the density. At some points instability happens, the state moves to lower branch and temperature decrease. That top layer which has Compton temperature can not escape due to gravity when these materials near the central object. These static material called Compton heated coronae (e.g. Begelman et al. 1983; Begelman & McKee 1983; Ostriker et al. 1991; Nayakshin et al. 2000; Jimenez-Garate et al. 2002). With increasing radius, the gravitational potential is smaller. When the gravitational potential is smaller than the thermal energy of this atmosphere, winds can form called Compton heated winds (Begelman et al., 1983; Begelman & McKee, 1983; Woods et al., 1996).

3.1.2 Features of thermal winds

The heated atmosphere forms winds at a larger radius. This atmosphere has Compton temperature, and its thermal energy is $kT_{\rm IC}$. Begelman et al. (1983) define the

Compton radius $R_{\rm IC}$where thermal energy of this atmosphere equal to the gravitational energy.

$$R_{\rm IC} = \frac{\mu m_p G M_c}{k T_{\rm IC}} \tag{3.1}$$

where $\mu = 0.61$ is the mean molecular weight. Roughly speaking, if the disk radius is larger than $R_{\rm IC}$, winds can form. More careful treatment considering the Bernoulli equation of adiabatic flow including the rotation of the disk, we can calculate the launching radius (Liffman, 2003). The total energy of this flow ϵ in cylindrical coordinate (R, ϕ, Z) is written as

$$\epsilon = \frac{1}{2} v_p^2 + \left(\frac{\gamma}{\gamma - 1}\right) \frac{p}{\rho} - \frac{G M_c}{\sqrt{R^2 + Z^2}} + \frac{l^2}{2R^2} \tag{3.2}$$

where $v_p^2 = v_R^2 + v_Z^2$, $p = \rho k T/(\mu m_p)$ and $l = R v_\phi$ are the poloidal velocity component, gas pressure, and angular momentum, respectively. Suppose that $v_p = 0$, $Z \ll R$ and $R = R_0$, i.e., the parcel of gas is at or near the surface of a thin disk. Then at this starting points of the flow.

$$\epsilon \sim \left(\frac{\gamma}{\gamma - 1}\right) \frac{p}{\rho} - \frac{G M_c}{2 R_0} \tag{3.3}$$

If $\epsilon > 0$, the system is unbound and winds can form. We can calculate the radius when $\epsilon = 0$.

$$R_0 = \frac{\gamma - 1}{2\gamma} \frac{G M_c \rho}{p} \tag{3.4}$$

If the temperature at starting points is $T_{\rm IC}$ and $\gamma = 5/3$, this radius gives $R_0 = 0.2 R_{\rm IC}$. This radius is consistent with the numerical hydrodynamics simulation (Woods et al., 1996).

If the heating rate is sufficient enough to Compton temperature, the mass-loss per unit area, $\dot{m}$ is then driven by the material in the atmosphere on the thermal sound speed (Begelman et al., 1983). For an isothermal flow, the pressure at the sonic point is a factor of 2 lower than at the base, so this gives

$$\dot{m} = \frac{p_0}{2 c_{IC}} \tag{3.5}$$

where $c_{\rm IC} = \sqrt{k T_{\rm IC}/(\mu m_p)}$ and

$$p_0 = p_{\rm rad}/\Xi_{\rm c,max} = \frac{L}{4\pi c R^2 \Xi_{\rm c,max}} \tag{3.6}$$

$\Xi_{\rm c,max}$ is the maximum pressure ionization parameter of the cold branch. The total mass-loss rate in the wind is written as

$$\dot{M}_{\rm w} = \int_{R_{\rm in}}^{R_{\rm disk}} \dot{m} \times 2 \times 2\pi R dR \tag{3.7}$$

$$= \frac{L}{2c \Xi_{\rm c,max} c_{\rm IC}} \ln(R_{\rm disk}/R_{\rm in}) \tag{3.8}$$

where factor 2 comes from the fact that the disk has two sides. From previous consideration, $R_{\rm in} = 0.2R_{\rm IC}$ and $R_{\rm disk}$ is the outer disk radius. This equation means that the total mass loss rate in the wind is directly proportional to the source luminosity.

However, the wind is only isothermal if it is heated sufficiently enough to $T_{\rm IC}$. This depends on the irradiating flux, which drops with increasing radius, so that wind is not heated so efficiently. The Compton heating rate on each electron can be written as

$$\Gamma_c = \frac{kT_{\rm IC}}{m_e c^2}\frac{\sigma_T L}{\pi R^2} \tag{3.9}$$

For large luminosities, the material is heated impulsively and reaches the Compton temperature at the isothermal sonic point, which is close to the disk. For lower luminosities, elections in the gas are heated steadily, reaching a characteristic energy

$$kT_{\rm ch} = \Gamma_e R/c_{\rm ch} \tag{3.10}$$

where R/c_{ch} is the time taken for the meterial to reach height $\sim R$. This equation determines the characteristic temperature $T_{\rm ch}$, and its corresponding sound speed $c_{\rm ch} = \sqrt{kT_{\rm ch}/(\mu m_p)}$ as

$$T_{\rm ch} = T_{\rm IC}\left(\frac{L}{L_{\rm crit}}\right)^{2/3}\zeta^{-2/3} \tag{3.11}$$

where $\zeta = R/R_{\rm IC}$ and $L_{\rm crit}$ is luminosity that is just able to heat the gas to $kT_{\rm IC}$ as it reaches height $\sim R$ so that it is able to escape, at distance $R = R_{\rm IC}$. Equivalently, this gives

$$c_{\rm ch} = c_{\rm IC}\left(\frac{L}{L_{\rm crit}}\right)^{1/3}\zeta^{-1/3} \tag{3.12}$$

and this critical luminosity $L_{\rm crit}$ is written as

$$L_{cr} \equiv \frac{1}{8}\left(\frac{m_e}{\mu m_p}\right)^{1/2}\left(\frac{m_e c^2}{kT_{\rm IC}}\right)^{1/2} L_{\rm Edd} \sim \ 0.03 T_{\rm IC,\,8}^{-1/2} L_{\rm Edd} \tag{3.13}$$

where $T_{\rm IC,8} = T_{\rm IC}/10^8$K. This luminosity is understood as the luminosity which is satisfied with $T = T_{\rm IC}$ at $R = R_{\rm IC}$. If the luminosity of central source is larger than $L_{\rm crit}$, winds form more effectively.

Woods et al. (1996) run hydrodynamics simulations of thermal winds in AGNs using photoionized plasma code CLOUDY (Ferland, 2003). They calculate a net heating/cooling rate as functions of pressure ionization parameter Ξ and temperature assuming AGN irradiation spectra (left, Fig.3.2) , and incorporate these to the energy conservation of hydrodynamic simulation. Middle and right in Fig. 3.2 are resultant thermal equilibrium curves using AGN spectra. Each Compton temperature is $T_{\rm IC} = 1.3\times10^7$K (Spectrum 1) and $T_{\rm IC} = 1.0\times10^8$K (Spectrum 2).

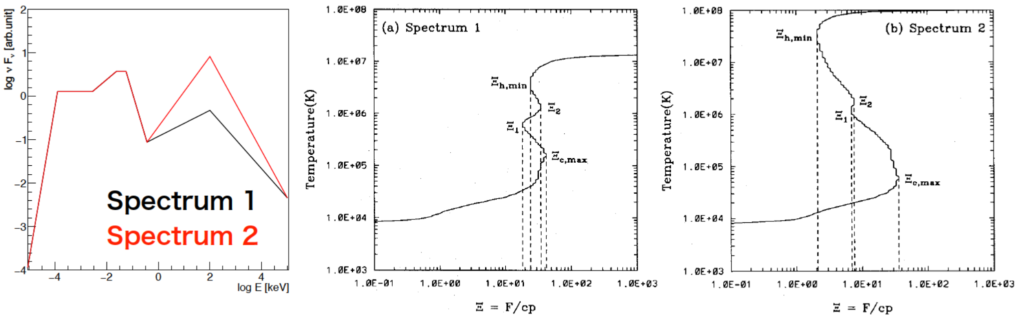

Figure 3.2: Input spectra and their thermal equilibrium curves taken from Woods et al. (1996).

Under conditions irradiated by these spectra, disk surface is heated up to Compton temperature when the Ξ reaches to maximum pressure ionization parameter of cold branch $\Xi_{\rm c,max}$ because of thermal instability.

They run hydrodynamic simulations many times under different central luminosity using two different spectra (Spectrum 1 and Spectrum 2) and calculate mass flux densities from each simulation. By fitting to these results of hydrodynamic simulations, They give the mass flux density [g cm^{-2} s^{-1}] from a disk surface

$$\dot{m} = \dot{m}_{ch} \left\{ \frac{1 + [(0.125L/L_{cr} + 0.00382)/\zeta]^2}{1 + [(L/L_{cr})^4(1 + 262\zeta^2)]^{-2}} \right\} \exp\{-[1 - (1 + 0.25\zeta^{-2})^{-1/2}]^2/2\zeta\} \tag{3.14}$$

where

$$\dot{m}_{ch} = p_0/c_{ch} = \frac{L}{4\pi R^2 c \Xi_{\rm c,max}} \sqrt{\frac{\mu m_p}{kT_{ch}}} \tag{3.15}$$

and $\Xi_{\rm c,max} \sim 40$ gives the maximum temperature of cold phase in Fig.3.2. The left panel in Fig. 3.3 shows luminosity dependence of this equations whose $T_{\rm IC,\,8} = 0.13$ The critical luminosity of $T_{\rm IC,8} = 0.13$ is $L_{\rm crit} = 0.08 L_{\rm Edd}$. The peak of this mass flux density is about 0.2 $R_{\rm IC}$. This value is consistent with the analytic estimation of Eq.3.4.

The right panel in Fig.3.3 shows the corresponding cumulative mass-loss in the wind, $\dot{M}$ as a function of $R/R_{\rm IC}$. This shows that the total mass-loss rate in the wind rises quickly at $R \sim 0.2\ R_{\rm IC}$, and then increases more slowly with increasing R. This can be understood from the previous plot of specific mass-loss rate, as this declines as R^{-2} in the wind. Hence, the increasing area at larger distances means that the total mass-loss rate from the disk increases with increasing size scale of the disk, as $\dot{M} \propto \ln(R_{\rm disk}/R_{\rm IC})$. This is same dependence of analytic estimation of mass-loss rate in Eq.3.8.

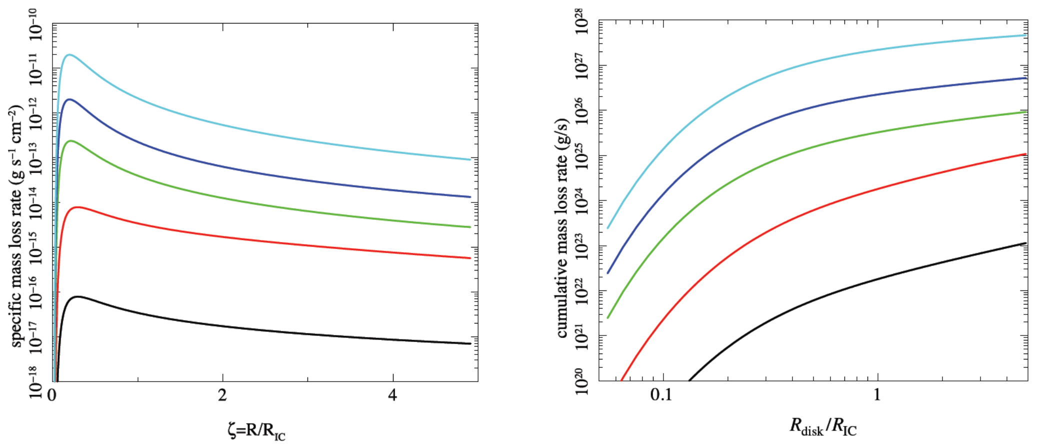

Figure 3.3: Left: The mass flux density from a $10^8 M_\odot$ BH per unit area of disk at a scaled radius $\zeta = R/R_{\rm IC}$ for $\log L/L_{\rm Edd}$ =−3 (black) −2 (red), −1 (green), 0 (blue) and 1 (cyan), as in Woods et al. (1996). These correspond to $L/L_{\rm crit} = 0.0125$–125 for the assumed constant $T_{\rm IC,\,8} = 0.13$. Right: The corresponding cumulative mass-loss rate from the disk at $R_{\rm disk} < 5\ R_{\rm IC}$.

3.2 Highly simplified model for observable

We make quantitative observables (i.e. column density and ionization state) using Eq.3.14. Although Eq.3.14 is calculated for AGNs, the total mass loss rate $\dot{M}_{\rm w} = \int_{R_{\rm min}}^{R_{\rm disk}} \dot{m} 2\pi R dR \times 2$ (Fig.3.4) is proportional to mass (Fig.3.4). Thus we use that equation for LMXBs.

Using these total mass loss rate, we try to reproduce column densities obtain hydrodynamic simulations of $L/L_{\rm Edd} = 0.3$, 0.08 and 0.01 with $T_{\rm IC,8} = 0.13$. We calculate density distribution assuming spherical flow, but the inclination dependence is $n \propto (1 - \cos\theta)$.

$$n_p = \frac{\dot{M}_{\rm w}(1-\cos\theta)}{4\pi R^2 v_{\rm out} m_i} \tag{3.16}$$

where $m_i = 2\mu m_p$ is the mean ion mass per electron and the integration region of mass loss rate is $R_{\rm min} = 0.01 R_{\rm IC}$ and $R_{\rm disk} = 5\ R_{\rm IC}$ $(L/L_{\rm Edd} = 0.3,\ 0.08)$, $12\ R_{\rm IC}$ $(L/L_{\rm Edd} = 0.01)$. This outer radius is same simulation box size as Woods et al. (1996). $v_{\rm out}$ is mass-loss weighted average isothermal sound speed of $\min(T_{\rm ch}, T_{\rm IC})$. This give $v_{\rm out} = 140, 350$ and 420 km/s for $L/L_{\rm Edd} = 0.01$, 0.08, and 0.3, respectively.

The ionization parameter is written as

$$\xi = \frac{L}{n_p R^2} = \frac{4\pi m_i v_{\rm out} L}{\dot{M}(1-\cos\theta)} \tag{3.17}$$

The ionization state is lower close to the orbital plane $\cos\theta = 0$,where the density of the wind is high.

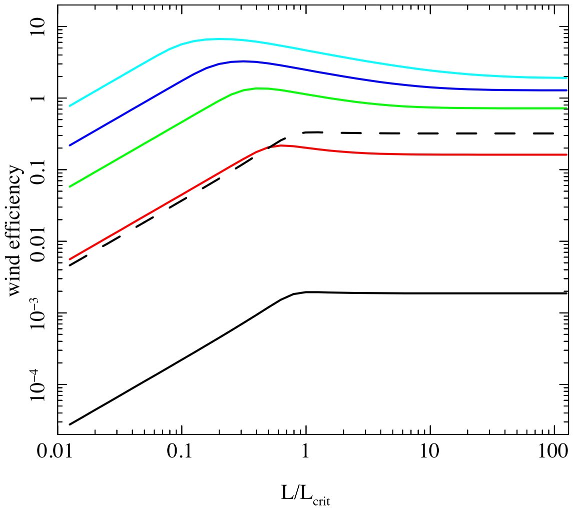

Figure 3.4: The effect of disk size on the efficiency of wind production per unit mass accretion rate taken from Done, Tomaru, & Takahashi (2018). The vertical axis shows $\dot{M}_{\mathrm{w}}/\dot{M}_{\mathrm{a}}$ ($\dot{M}_{\mathrm{a}} = L/(0.1c^2)$). The horizontal axis shows the luminosity normalized by the critical luminosity $L_{\mathrm{crit}} = 0.08L_{\mathrm{Edd}}$ with $T_{\mathrm{IC}} = 1.3 \times 10^7$K. The disk size $R_{\mathrm{disk}}/R_{\mathrm{IC}} = 0.1$ (black), 0.3 (red), 1 (green), 3 (blue) and 10 (cyan). All disk show that disk is increasingly efficient at producing a wind with increasing mass accretion rate for $L/L_{\mathrm{crit}} \to 1$ but the efficiency stabilized to a constant for $L/L_{\mathrm{crit}} \gg 1$.

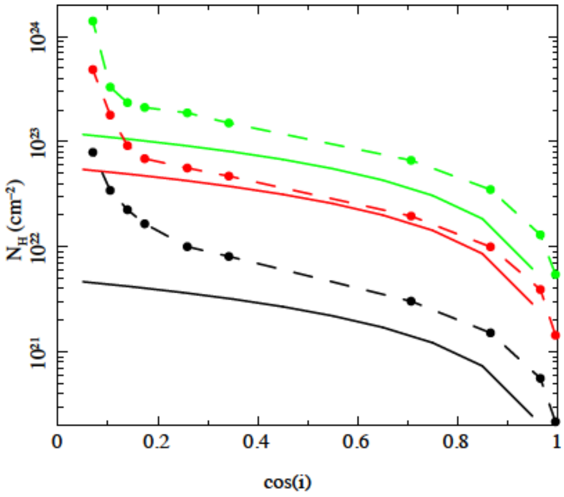

Figure 3.5: Column densities of Woods et al. (1996) (doted line) and Done, Tomaru, & Takahashi (2018) (solid line). Colors show $L/L_{\mathrm{Edd}} = 0.3$ (green), 0.08 (red) and 0.01 (black), respectively.

By integrating density, we can get hydrogen column density as

$$N_H = \frac{\dot{M}(1-\cos\theta)}{4\pi R_{\rm in} v_{\rm out} m_i} \tag{3.18}$$

where $R_{\rm in}$ is the wind launching radius (Begelman et al., 1983).

$$R_{\rm in}/R_{\rm IC} = \begin{cases} 0.2 & (L > L_{\rm crit}) \\ 0.2/(L/L_{\rm crit}) & (L < L_{\rm crit}) \end{cases} \tag{3.19}$$

As a result, we succeed in reproducing column densities (Fig.3.5) within factor 2. This is a remarkable match given the simplistic assumptions.

3.3 Evolution of the wind with $L/L_{\rm Edd}$

Most BH LMXBs are transient, showing outbursts in which the mass accretion rate onto the central object changes dramatically due to the Hydrogen ionization disk instability (see, e.g. the review by Lasota, 2001). There is an abrupt transition in the spectral state on the fast rise from a hard spectrum which can be roughly described by a power-law with photon index $\sim 1.6-2.0$, to a much softer spectrum which is dominated by a multi-color disk component. This hard to soft transition is not at a well defined luminosity, most probably because the mass accretion rate is changing too rapidly for the disk to be in steady-state (Smith et al., 2002; Gladstone et al., 2007). Instead, the slow decline is more stable, with the spectrum changing back from a disk to power-law spectrum at $L \sim 0.02L_{\rm Edd}$ (Maccarone, 2003). During the disk dominated, most luminous phase, the characteristic disk temperature is $kT_{\rm max} \propto (L/L_{\rm Edd})^{1/4}$. The outer disk sees this at a high inclination, so the Doppler blueshift increases the temperature seen by the disk. We model a $10M_\odot$ black hole with spin $a_* = 0.5$ using the KERRBB code in XSPEC which has full general relativistic emissivity and ray tracing. Assuming a mass accretion rate of 3.5×10^{17} g s^{-1} ($L/L_{\rm Edd} \sim 0.02$), with a color temperature correction of $f_{\rm col} = 1.7$, the outer disk sees a spectrum similar to a multicolor disk blackbody with maximum temperature of 0.6 keV, which corresponds to $kT_{\rm IC} = 0.31$ keV which is 0.036×10^8 K. Hence this predicts that in the disk dominated spectra,

$$T_{\rm IC,8} = 0.036[L/(0.02L_{\rm Edd})]^{1/4} \tag{3.20}$$

The transition to the hard state is complex, with the disk temperature decreasing rapidly, as expected if the thin disk starts to recede from the innermost stable circular orbit (e.g. Gierliński et al., 2008). Here we assume that the spectrum abruptly changes to a power law of photon index $\Gamma = 2$ at $L = 0.02L_{\rm Edd}$,

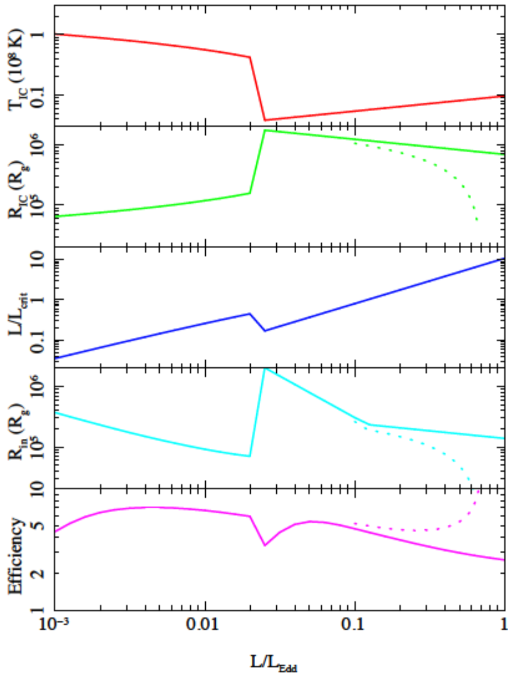

Figure 3.6: The upper panel shows the assumed change in $T_{\rm IC}$ with $L/L_{\rm Edd}$ (red). The power-law spectral index softens with increasing luminosity in the hard state, so the inverse Compton temperature drops. The abrupt drop at $L/L_{\rm Edd} = 0.02$ marks the transition to the disk dominated state, where the Compton temperature increases with luminosity. The second panel shows the effect of this on $R_{\rm IC}$ (green). A higher Compton temperature means that the wind can escape from smaller radii. The third panel shows how $L/L_{\rm crit}$ changes (blue). An increase in Compton temperature means that the radiation heats the gas faster, so it can drive the temperature up to $T_{\rm IC}$ at $R_{\rm IC}$ at a lower luminosity. The assumed $L/L_{\rm Edd} - T_{\rm IC}$ behavior means that the luminosity is only above the critical luminosity for $L > 0.1L_{\rm Edd}$. Thus the wind is lauched from $R_{\rm in} = 0.2R_{\rm IC}$ only for $L > 0.1L_{\rm Edd}$. Below this, the wind instead is launched from $R_{\rm in} = 0.2R_{\rm IC}/(L/L_{\rm crit})$, so the wind launch radius (cyan) decreases with increasing $L/L_{\rm Edd}$ in the hard state, as the increase in $L/L_{\rm crit}$ more than offsets the increase in $R_{\rm IC}$. The lower panel (magenta) shows the wind efficiency (mass outflow rate in terms of the mass accretion rate). This is fairly constant at $\sim 5\times$ the mass accretion rate required to produce the luminosity, except for more complex behavior around the transition. The dotted lines on all panels show the effect of including a simple radiation pressure term to reduce the effective gravity. The wind can be launched from progressively smaller radii, and the mass loss rates increase.

flattening to $\Gamma = 1.6$ at $L/L_{\rm Edd} = 2 \times 10^{-3}$. Interpolating logarithmically $\Gamma = 1.6 + 0.4 \times \log_{10}[L/(0.002L_{\rm Edd})]$. The Compton temperature for a hard power-law depends on the high energy cutoff, but this dependence saturates above 100 keV due to the rollover in the Klein-Nishima cross-section compared to the constant cross-section assumed in Thomson scattering. Hence we fix the upper limit of the flux integral at 100 keV, and assume a lower limit of 0.1 keV. This gives an inverse Compton temperature of 3.6 keV (0.42×10^8 K), increasing to 7.6 keV (0.88×10^8 K) for the hardest spectra/lowest luminosities considered here, so that

$$T_{\rm IC,8} = 0.88 - 0.46 \times \log_{10}[L/0.002L_{\rm Edd}] \tag{3.21}$$

We use this correlated change in $kT_{\rm IC}$ with $L/L_{\rm Edd}$ to explore the predicted wind behavior over the range $10^{-3}L_{\rm Edd} < L < L_{\rm Edd}$, with the total mass loss rate in the wind $\dot{M}$ calculated from the fitting formulae of Eq.3.15 and the column/ionization state observables approximated as in Section 2 above. We assume a generic black hole of mass $M = 10M_\odot$ and set the disk outer radius to 3.7×10^{12} cm ($2.5 \times 10^6 R_g$, which corresponds to $5R_{\rm IC}$ for $T_{\rm IC,8} = 0.13$ as used in most of the simulations in Woods et al. 1996). We note that most BH LMXBs have much smaller disks, but the most dramatic winds are indeed seen in systems which are known to be in long period orbits (GRS 1915+105, GRO J1655–40), or where the orbital periods are unknown but consistent with being long (H1743–322, 4U1630–522) (Díaz Trigo & Boirin, 2016, Tab.2.1)

The upper panel of Fig. 3.6 shows the Compton temperature as a function of $L/L_{\rm Edd}$, illustrating the dramatic change in behavior at the hard/soft spectral transition at $L \sim 0.02L_{\rm Edd}$. This transition has a similarly dramatic impact on the radius at which Compton temperature allows the material to escape, $R_{\rm IC}$, shown as the solid line in the second panel of Fig. 3.6. However, the effective launch radius, $R_{\rm in}$, depends on luminosity relative to the critical luminosity, which is required to launch the wind efficiently, which itself depends on $T_{\rm IC}$. The third panel in Fig. 3.6 shows $L/L_{\rm crit}$. This only reaches unity for $L > 0.1L_{\rm Edd}$, so only above this luminosity is $R_{\rm in} = 0.2R_{\rm IC}$ (fourth panel, Fig. 3.6). Below this, $R_{\rm in} = 0.2R_{\rm IC}/(L/L_{\rm crit})$ so it decreases with increasing luminosity in the hard state, as well as showing more complex behavior at the transition due to the jump in Compton temperature. The final panel shows the wind efficiency, i.e., the ratio of mass loss rate in the wind with the mass accretion rate required to produce the assumed luminosity. This is fairly constant as the outer disk is always in one of the active wind regions, and high at $\sim 5\times$ the input mass accretion rate. This is a little larger than in the simulations in Woods et al. (1996) and Fig. 3.4 as we are assuming a black hole with spin 0.5

rather than spin 0, so the same luminosity is produced with a lower mass accretion rate.

3.4 Radiation pressure correction

Neither Begelman et al. (1983) nor Woods et al. (1996) includes radiation pressure on electrons in their hydrodynamic simulations. But this must become important as $L \to L_{\rm Edd}$. By definition, static material above the disk will be driven out as a wind at $L > L_{\rm Edd}$, as the radiation pressure reduces the effective gravity to $GM/R^2(1 - L/L_{\rm Edd})$. However, the wind material is not static as it has the Keplerian rotation velocity from where it was launched as well as thermal motion driven by the pressure gradients. This will mean that it becomes unbound at all radii at luminosities somewhat below $L_{\rm Edd}$. A lower limit to this completely unbound luminosity is $L_{\rm Edd}/2$, which could be reached if all the Keplerian azimuthal rotational velocity ($v_\phi = v_{\rm esc}/\sqrt{2}$) were converted to radially outward velocity (Ueda et al., 2004). Conserving angular momentum as well as energy pushes this up to $L_{\rm Edd}/\sqrt{2}$. This estimation is very close to the results of a full calculation in Proga & Kallman (2004). In the case where the disk luminosity at the wind launch radius is negligible, they show (equations 20-22) that the effective gravity goes to zero at $H \sim R$ for $L \sim L_{\rm Edd}/(1 + \pi/8) \approx L_{\rm Edd}/\sqrt{2}$. This equation gives a simple correction to the Compton radius of

$$\overline{R}_{\rm IC} \approx R_{\rm IC}\Big(1 - \frac{L}{0.71 L_{\rm Edd}}\Big) \tag{3.22}$$

We first assume that this correction to the inverse Compton radius, $\overline{R}_{\rm IC}$, is the only change in wind properties, and rerun the black hole binary simulation. The new results are shown as the dotted lines in Fig. 3.6. The lower effective gravity as the luminosity increases towards Eddington means that $R_{\rm IC}$ and hence $R_{\rm in}$ both decrease dramatically, formally going to zero at $0.71 L_{\rm Edd}$ (dashed green and cyan lines in the second and fourth panels). The wind can then be launched from everywhere on the disk, so the mass loss rates also increase. We note that this is likely to be an underestimate of the increase in mass loss rate as we still assume that the wind velocity is given by the sound speed, but it should be higher due to the contribution of radiation pressure to the acceleration.

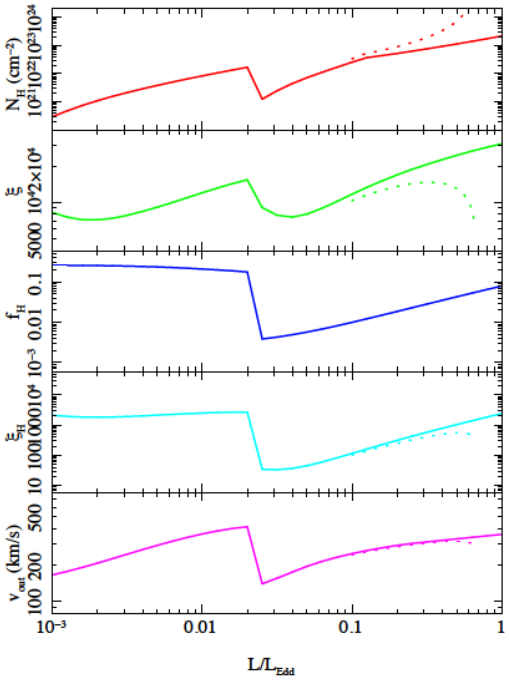

Figure 3.7: The upper panel (red) shows the column density at $\cos\theta = 0.25$ i.e. an inclination angle of $\sim 75°$. This is roughly proportional to the mass accretion rate, but with a dip at the spectral transition due to the lower Compton temperature of the dimmest soft states. The second panel (green) shows the ionization state calculated from the total bolometric flux, $\xi = L_{\rm bol}/nR^2$. This is fairly constant, as the increase in luminosity is mostly balanced by an increase in density of the wind. The third panel shows the fraction of bolometric flux which is emitted in the 8.8-30 keV high energy band pass (blue). These are the photons which are most effective in photoionizing He- and H-like iron, and this shows a dramatic dip around the spectral transition, even including a power-law to higher energies which carries 5% of the total disk luminosity. The fourth panel shows the high energy ionization parameter, $\xi_H = f_H L_{\rm bol}/nR^2$ (cyan). This is almost completely constant in the hard state, but dips dramatically in the soft state due to the much softer spectra, and only recovers to the same value as seen in the hard state at the highest luminosities. The bottom panel shows the outflow velocity. This mirrors the behavior of the launch radius of the wind shown in Fig.3.6d. The dashed lines show the effect of including a simple radiation pressure correction. The wind becomes optically thick.

3.5 Predicted absorption features

3.5.1 Behavior at the transition

We calculate the observable features of the simple model for the BH XRB spectral evolution as a function of $L/L_{\rm Edd}$ introduced in the previous sections. Fig.3.7 shows the observables of N_H (upper panel, red) and ξ (middle panel, green), extracted for an inclination of 75° ($\cos\theta = 0.25$). The solid lines show the standard thermal wind model results. The column density is roughly proportional to mass accretion rate, but with a drop at the spectral transition due to the large change in spectral shape by changing the Compton radius and critical luminosity. There should be an abrupt increase in the column by around a factor 10 as the source declines and makes the transition to the hard state. This prediction is exactly opposite to the claimed behavior of the wind shutting off in the hard state.

However, the visibility of the wind is also controlled by its ionization state. The ionization parameter calculated from the full luminosity, $\xi = L/(nR^2)$, is almost constant, changing only by a factor 5 as the luminosity varies by a factor of a thousand. This is because the ionization is roughly proportional to the ratio of luminosity and wind mass loss rate, so these cancel in the regime where the wind efficiency is approximately constant. However, the photoionization of iron depends on the high energy 8.8-30 keV flux, which changes dramatically at the transition. This high energy flux would be minimal for the lowest luminosity soft states as these have low temperature disks with very few photons emitted above 8.8 keV. However, such pure disk spectra are rare. Most soft states have a small, soft power-law tail giving some higher energy flux. Hence we also include an additional power-law in the soft state, with index fixed at $\Gamma = 2.2$, which carries 5% of the total power. This power has little impact on the Compton temperature, but will determine the photoionization of iron ions. The third panel in Fig.3.7 (blue) shows the fraction of the bolometric flux, which is emitted in the high energy 8.8-30 keV bandpass, f_H, while the fourth panel (cyan) shows the corresponding high energy photoionization parameter, $\xi_H = f_H L/(nR^2) = f_H \xi$. This fraction drops by a factor of more than 50 at the transition, so the photoionization of the wind changes dramatically.

However, the baseline ion population of iron is set by collisional ionization rather than photoionization - the wind is heated to a temperature $T_{\rm ch}$, so the ion populations cannot drop below those which characterize material at this temperature. We will explore this in detail in a subsequent paper, but here we note that neither the Compton temperature nor the high energy photoionization parameter is high enough to strip iron in the wind in the hard state completely. Thus while there is a significant change in ion populations in the wind across the transition, it is not likely that this is the origin of the lack of iron absorption features in the wind in the hard state (Neilsen & Lee, 2009; Miller et al., 2012).

3.5.2 Comparison to observations across the transition

We analyze the constraints from the data across the transition in more detail. The observations of Neilsen & Lee (2009) are of GRS 1915+105, a source that is close to its Eddington limit, even in its hardest spectral states, which is a hard intermediate state rather than a true hard state (Done et al., 2004). Hence this requires more detailed modeling, which will be the subject of a later paper (Shidatsu & Done, 2019). However, the observations of H1743–322 of Miller et al. (2012) are in standard hard and soft states which are directly comparable to those simulated in the previous section. Hence we can use our models to directly compare to the observed thermal wind features across the spectral transition.

We extract the simultaneous *RXTE/Chandra* data for these observations to constrain the continuum shape and luminosity as well as the wind features. The standard pipeline *RXTE* continuum spectra are shown in Fig.3.8 (ObsIDs P95368-01-01-00 and P80135-02-01-11 for the hard and soft states, respectively), with the inset showing the *TGCat* coadded HEG ± 1 *Chandra* high resolution spectra (ObsIDs 3803 and 11048, respectively) around the iron line bandpass. There is a significant change in bolometric luminosity, as well as the state change and the change in wind absorption features. The wind should have a higher column in this particular soft state than the comparison hard state simply because the source has higher bolometric luminosity (see Fig.3.6 and 3.7).

Integrating the model to get an unabsorbed bolometric flux gives 9.7×10^{-9} ergs s^{-1} cm^{-2} for the hard state using the NTHCOMP model with an assumed electron temperature of 100 keV, while the DISKBB model for the soft state gives 4.3×10^{-8} ergs s^{-1} cm^{-2}. However, the intrinsic luminosity of the soft state is probably higher due to projection effects as the disk is seen at high inclination as evidenced by the fact it has a disk wind (Ponti et al., 2012) and a strong low frequency QPO (Ingram et al., 2016) as well as a high temperature disk (Muñoz-Darias et al., 2013).

The system parameters are not well known, but Dunn et al (2010) show the hardness-intensity diagram for the outbursts look similar to those of other BHB for a canonical 10 $M_\odot$ mass and 5 kpc distance. These parameters then give $L/L_{\mathrm{Edd}} = 0.02$ (hard) and 0.1 (soft) without any projected area correction, or $L/L_{\mathrm{Edd}} \sim 0.4$ with a cosine dependence assuming $\theta \sim 75^\circ$ (Steiner et al., 2012). This fits rather well with the observed spectrum, as the DISKBB temperature is 1.2 keV, i.e. $2\times$

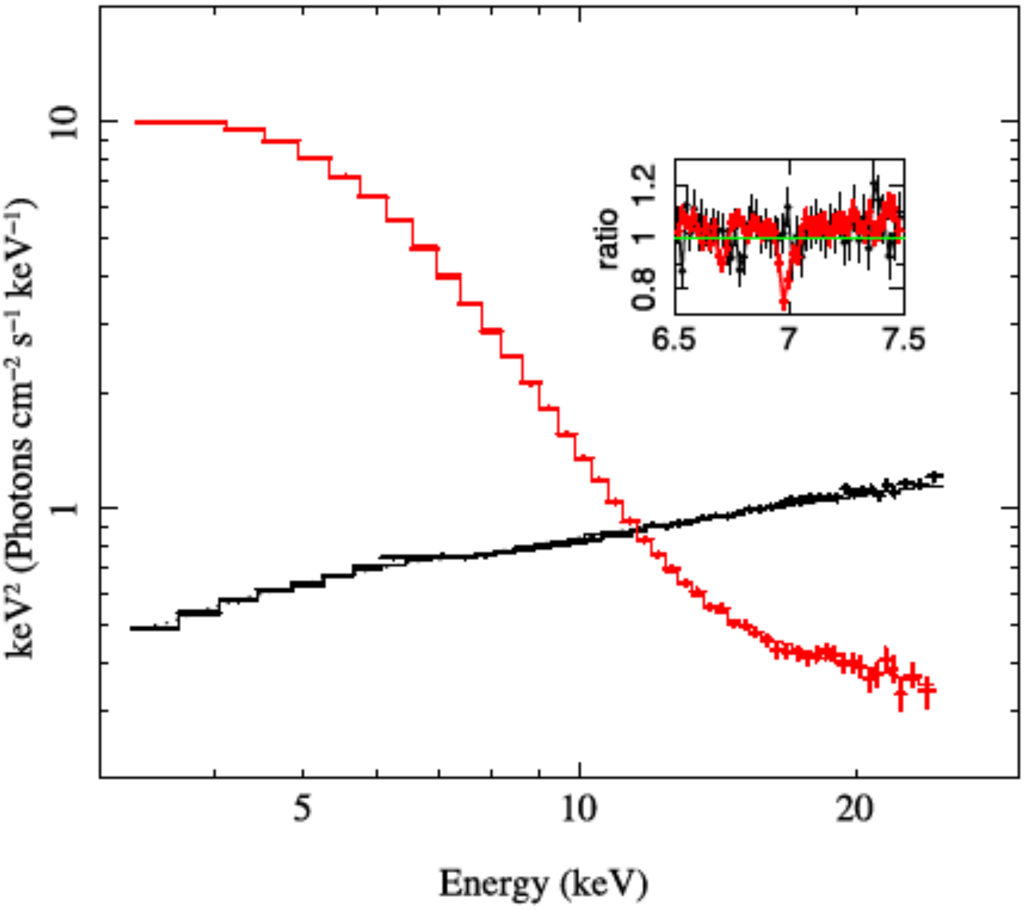

Figure 3.8: The hard (black) and soft (red) spectra from *RXTE* data on H 1743-−322, with the inset showing the simultaneous Chandra data, with a clear difference in wind absorption features taken from Done et al. (2018). The high energy 8.8– 30 keV photoionizing flux is quite similar between the two data sets, but the overall luminosity is quite different. If the wind stayed constant, responding only to the high energy photoionizing flux, then the difference in wind properties would require a change in the wind structure, potentially linked to the appearance of the jet. However, thermal winds respond to the overall flux, as well as to the high energy part, and this predicts that the column should be smaller by a factor of ˜5 in the low/hard state, consistent with the observations.

higher than that assumed at the transition at $L/L_{\rm Edd} = 0.02$, so the luminosity should be $2^4 = 16\times$ higher, at $L/L_{\rm Edd} \sim 0.3$. The tail in the soft state carries roughly 5% of the total bolometric power, so these two spectra are very comparable to those assumed in the simulations shown in Figs.3.6, 3.7.

The thermal wind model then predicts that there should be a wind column of $\sim 8 \times 10^{22}$ cm^{-2} in the soft state, a factor 5 larger than the expected column of 1.6×10^{22} cm^{-2} in the hard state even though the high energy luminosities are similar in the hard and soft states. Thermal winds respond to changes in total luminosity and spectral shape and are not just dependent on the high energy photoionizing flux. The models predict that the high energy photoionization parameter is lower by a factor 5 in the soft state, as there is a stronger wind, but with similar high energy flux. However, this photoionization is not sufficient to fully strip the wind in the hard state, so the clear prediction of the thermal wind model is that the absorption features should be $\sim 5\times$ bigger in the soft state at $L/L_{\rm Edd} = 0.3 - 0.4$ compared to the brightest hard state at $L/L_{\rm Edd} = 0.02$, despite them having similar high energy fluxes. This is easily compatible with the Miller et al. (2012) results.

3.5.3 High luminosities and the wind in GRO J1655-40

The dotted lines in Fig.3.7 show the effect of the simple radiation pressure correction (see Sec.3.4). The column increases dramatically as $L \rightarrow 0.7L_{\rm Edd}$, becoming optically thick to electron scattering, with a corresponding drop in ionization state. The dotted lines on Fig.3.6 show that this much stronger wind is launched from progressively smaller radii.

Our assumed disk dominated spectra at high luminosity are too simple to describe those seen from GRS 1915+105, so here we concentrate only on the comparison to GRO J1655–40, which had a very soft spectrum at the time when it produced the most extreme wind seen from this or any other black hole binary. This anomalous wind has a large column, $\log N_h \sim 23.8$ and (compared to other binary winds) low ionization state, $\log \xi = 4$ (Miller et al., 2006, 2008; Kallman et al., 2009). This ionization state is comparable to those predicted here for the simple radiation pressure correction at $L \rightarrow 0.7L_{\rm Edd}$, but the observed column is not optically thick, and the observed luminosity is only $\sim 0.05L_{\rm Edd}$ (Miller et al., 2006, 2008; Kallman et al., 2009).

Nonetheless, it seems possible that this could still be at least partly (there are multiple velocity components: Kallman et al. 2009; Miller et al. 2015, 2016) due to a thermal-radiative wind. The pure source luminosity will be underestimated if the wind becomes optically thick, and this optically thick material could be hidden by being completely ionized, with the observed absorption lines arising from a thin outer skin of partially ionized material. In this picture, an optically thick wind is launched by thermal-radiative driving from the inner disk and expands outwards. Electron scattering in the completely ionized, optically thick material reduces the observed X-ray flux along the line of sight, with the observed absorption lines arising in an outer, optically thin, photosphere of the wind. The detection of the metastable Fe XXII shows that this photosphere must have $n \sim 10^{15}$ cm^{-3} (Miller et al., 2006), and it is illuminated by the same (suppressed) continuum, which we see as it is along the line of sight. Hence the observed $\log \xi = 4$ implies a position for this photosphere at $R \sim 8 \times 10^{8}$ cm ($\equiv 800 R_g$), as in the magnetic wind models. The difference in this thermal-radiative picture is that the wind is actually launched from even closer to the black hole, and we see only the outer shell of the expanding optically thick material.

This may seem an unnecessarily complex picture given the success of the magnetic wind models in fitting the data quantitatively (e.g., Fukumura et al. 2017). However, while the magnetic models can quantitatively fit the observed optically thin wind with the observed low luminosity, they do not explain why this wind is only seen in this one observation of GRO J1655-40. There are other similarly low luminosity *Chandra* datasets from this source which show much higher ionization winds, consistent with a thermal driving (Neilsen & Homan, 2012), and similarly low luminosity *Chandra data* from other sources which show only the expected thermal wind signatures of H- and He-like iron (e.g., Ponti et al. 2012). The magnetic wind model also does not explain the other unusual features of GRO J1655-40 in this dataset, namely the unusual lack of variability seen in the corona of this state (Uttley & Klein-Wolt, 2015), or its unusually steep spectrum (Neilsen & Homan, 2012), or give a geometry where the absorption lines only partially cover the source (Kallman et al., 2009). By contrast, all these other features can be explained fairly naturally in an optically thick wind model. Downscattering in the wind steepens the spectrum, suppresses variability, and makes an extended source geometry for partial covering, and it is rare for LMXBs to reach (or exceed) Eddington, which explains why this wind has such different properties.

Nevertheless, a thermal-radiative wind from a source with $L \to L_{\rm Edd}$ remains a speculative explanation for this observation of GRO J1655–40. To test whether this scenario can work quantitatively requires a hydrodynamic code to calculate the two-dimensional wind structure, including radiative continuum driving (e.g., Proga & Kallman 2004) with full Monte-Carlo radiation transport to handle the scattered flux (e.g., Higginbottom et al. 2014). However, the limitations of the magnetic wind models in explaining why the wind in this observation of GRO J1655–40 is so different from other observations of this and other LMXBs motivate consideration of the possibility.

3.6 Summary

We use the analytic models for thermal winds of Begelman et al. 1983; Woods et al. 1996, combined with a very simplified geometric/kinematic model for the structure of the wind to predict the column density, ionization and velocity along any line of sight at any luminosity for any spectrum. We combine this with a simplified model of the spectral evolution with luminosity in BH LMXBs, including the significant change in Compton temperature at the hard-soft spectral transition, as well as the smaller but systematic change in Compton temperature with luminosity within each state.

We show that the column density of the wind seen at any luminosity generally increases with increasing mass accretion rate except for a dip just after the transition to the soft state, where the much lower Compton temperature suppresses the wind. This column predicts that there is more wind material just after the source makes a transition to the hard state, in direct contrast to claims that the wind is suppressed in the hard state and seen only in the soft state. While photoionization also plays a role in the visibility of the wind, we show that this is probably not enough to suppress a wind just after the transition to the hard state if it was visible in the soft state just beforehand.

We critically examine the data on which the claims of wind suppression are based. GRS 1915+105 (Neilsen & Lee, 2009) is close to Eddington and has complex spectra, so the simplified models used here are probably not applicable. Instead, H1743–322 (Miller et al., 2012) shows canonical hard and soft states, with *Chandra* data clearly showing that the wind in the soft state is absent in hard data with similar high energy luminosity. However, these two spectra are very different in total luminosity, and this difference is enhanced by the cosine dependence of the disk flux in the soft state, while the hard state emission is more isotropic. We estimate that these two spectra differ by an order of magnitude in intrinsic luminosity, so the much stronger wind in the soft state is entirely in line with the thermal wind predictions.

This removes any need for suppression of the wind at the transition via magnetic fields switching from powering the wind in the soft state, to powering the jet in the hard state (Neilsen & Lee, 2009) Indeed, such a switch would be very surprising, as the jet is almost certainly launched from the inner disk, while the low outflow velocities seen in the wind shows that it is most likely launched from the outer disk.

Radiation pressure should become important as the source approaches the Eddington limit, increasing the mass loss rate as material above the disk is unbound at progressively smaller radii. We include a simple correction for this which predicts stronger winds launched from smaller radii as $L \rightarrow L_{Edd}$. This may be able to explain the anomalous wind seen in GRO J1655-40 (Miller et al., 2006) if the wind becomes optically thick, suppressing the observed luminosity (Shidatsu et al., 2016). However, a quantitative comparison requires hydrodynamic simulations in the Eddington regime, which are beyond the scope of this paper. Alternatively, (Fukumura et al., 2017) have shown quantitatively that magnetic driving can be consistent with the broad properties of this anomalous wind. However, their model does not explain why similar winds are not seen in this or other BH LMXBs at similar luminosities, nor does it address the likelihood of the required magnetic field configuration.

We conclude that there is at present no strong requirement for magnetic winds in the majority of BH LMXBs, and it is possible that they are not required in the super-massive black holes either (e.g., Hagino et al. 2015, 2016). Known wind launching mechanisms (thermal, UV line driven, and Eddington continuum) should be explored in detail before ruling them out in favor of magnetic winds.

Chapter 4

Framework for constructing comprehensive models

In the previous Chapter, we indicate that thermal winds could explain the visibility of absorption lines at the spectral state transition. Also, at high luminosity radiation force from a central object is essential. To determine whether thermal winds are the origin of absorption lines in LMXBs, we need to solve the dynamics of the wind and the resultant spectrum seen through the wind to compare with the observed spectra. Such a highly physical model calculated theoretical calculation is important when we will analyze high resolution spectroscopic data at 5 eV resolution which will be realized by the next generation X-ray observatory *XRISM* (planted launch in 2022). For this reason, we have developed a new radiation hydrodynamic (RHD) simulation code and Monte-Carlo radiation transfer (MCRT) simulation code. In this chapter, we describe the details of this simulation code.

4.1 Definition of framework

The dynamics of thermal-radiative winds depend on X-ray irradiation from a central region and these winds launched at outer radii. Thus using irradiation spectra which influence the radiative heating/cooling and radiative acceleration (radiation force) obtained from observed data is important when we run RHD simulations. Recently, these simulations which do not include the radiation force are being implemented.(Dyda et al., 2017; Higginbottom et al., 2017). However, the simulation by Dyda et al. (2017) is only one dimensional and Higginbottom et al. (2017) did not use the observed spectra for verification. To better simulate thermal-radiative winds using realistic irradiation and radiation force, we have developed a RHD simulation code whose input is the irradiation spectral shape, and its luminosity obtained from observation. We compute line profiles by MCRT simulations using the density/velocity distribution obtained from this RHD simulation (Fig.4.1). Ideally,

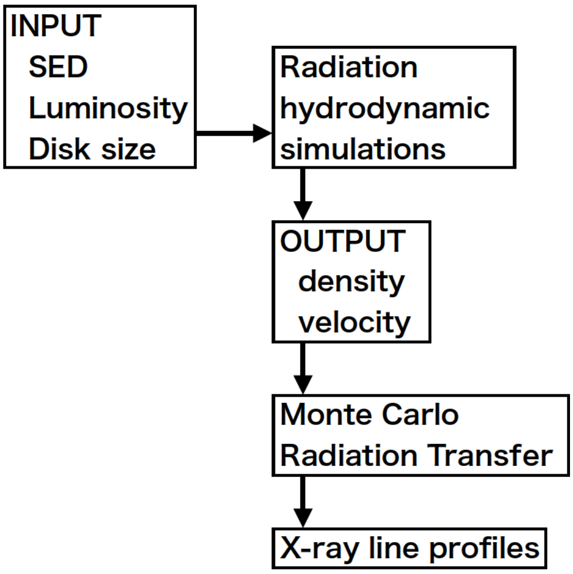
INPUT
SED
Luminosity
Disk size
Radiation hydrodynamic simulations
OUTPUT
density
velocity
Monte Carlo Radiation Transfer
X-ray line profiles

Figure 4.1: The outline of our numerical simulations

the RHD simulation, the MCRT simulation and ionization calculation should be performed at the same time in a self-consistently manner because they are strongly coupled. However, such a self-consistent simulation costs a huge amount of computational time (maybe unrealistic). Because disk winds usually are not optically thick, we calculate the effect of radiation on to the outflowing photoionized gas in the one dimensional radiation transfer case.

4.2 Radiation hydrodynamics code

4.2.1 Basic equations

The RHD code provides a calculation of the time evolution of the density, velocity, and temperature based on a two-dimensional spherical polar coordinate assuming axisymmetry rotation axis of the accretion disk. Our RHD simulation code was developed by Takahashi & Ohsuga (2013), and more recently by Nomura et al. (2016). The code is similar to the code used in earlier work of Proga et al. (2000); Proga & Kallman (2004). The basic equations in spherical polar coordinates (R, ϕ, θ) are the equation of continuity,

$$\frac{\partial \rho}{\partial t} + \nabla \cdot (\rho \boldsymbol{v}) = 0 \tag{4.1}$$

equation of motions,

$$\frac{\partial(\rho v_R)}{\partial t} + \nabla\cdot(\rho v_R \boldsymbol{v}) = -\frac{\partial p}{\partial R} + \rho(\frac{v_\theta^2}{R} + \frac{v_\phi^2}{R} + g_R + f_{\rm rad}(\xi,T)) \tag{4.2}$$

$$\frac{\partial(\rho v_\theta)}{\partial t} + \nabla\cdot(\rho v_\theta \boldsymbol{v}) = -\frac{1}{R}\frac{\partial p}{\partial \theta} + \rho(-\frac{v_R v_\theta}{R} + \frac{v_\phi^2}{R}\cot\theta) \tag{4.3}$$

$$\frac{\partial(\rho v_\phi)}{\partial t} + \nabla\cdot(\rho v_\phi \boldsymbol{v}) = -\rho(\frac{v_\phi v_R}{R} + \frac{v_\phi v_\theta}{R}\cot\theta) \tag{4.4}$$

and conservation of energy,

$$\frac{\partial}{\partial t}\left[\rho(\frac{1}{2}v^2 + e)\right] + \nabla\cdot\left[\rho\boldsymbol{v}(\frac{1}{2}v^2 + e + \frac{p}{\rho})\right] = \rho\boldsymbol{v}\cdot\boldsymbol{g} + \rho\mathcal{L}(\xi,T) \tag{4.5}$$

where ρ is the mass density, $\boldsymbol{v} = (v_R, v_\theta, v_\phi)$ is the velocity, p is the gas pressure, e is the internal energy per unit mass, and $\boldsymbol{g} = (g_R, 0)$ is the gravitational acceleration of the black hole. We assume an adiabatic equation of state $p/\rho = (\gamma-1)e$ with $\gamma = 5/3$.

A net heating/cooling term $\rho\mathcal{L}(\xi,T)$ and radiation force term $f_{\rm rad}(\xi,T)$ in Eq.4.2 are features of these equations. The former is defined by

$$\rho\mathcal{L} = \left(\frac{\rho}{\mu m_p}\right)^2 [\Gamma(\xi,T) - \Lambda(\xi,T)] \tag{4.6}$$

where mass density and number density are related by$\rho = n\mu m_p$. and the latter is

$$f_{\rm rad} = \frac{k_{\rm es}M(\xi,T)}{c}F_x[cms^{-2}] \tag{4.7}$$

where $\kappa_{\rm es} = 0.34$ cm^2 g^{-1} is the mass-scattering coefficient for free electrons.

The heating, Γ, and cooling, Λ, rates per unit volume are calculated by CLOUDY (Ferland, 2003) (left in Fig.4.2). CLOUDY is a multi-purpose code designed to handle photoionized plasma. Included in the net heating/cooling is the Compton process, bound-bound, bound-free, free-bound, free-free of all the ionization stages for elements. These heating/cooling rates depend on the shape of the illuminating spectrum, which is discussed more detail in the next Chapter, as well as on the temperature T and ionization parameter

$$\xi(R,\theta) = \frac{L_x}{nR^2} = \frac{4\pi\mu m_p F_{\rm x}}{\rho} \tag{4.8}$$

where F_x is the X-ray flux and L_x is the X-ray luminosity at each grid point. These are defined from the intrinsic luminosity, $L_{\rm x0}$, which is modified for absorption/scattering along the line of sight so that $L_x = L_{\rm x0}e^{-\tau(R,\theta)}$. We assume that the corona and inner disk are both effectively a central point source, so that

$$\tau(R,\theta) = \sum M(\xi,T)\kappa_{\rm es}\rho(R,\theta)\delta R + \tau_0(\theta) \tag{4.9}$$

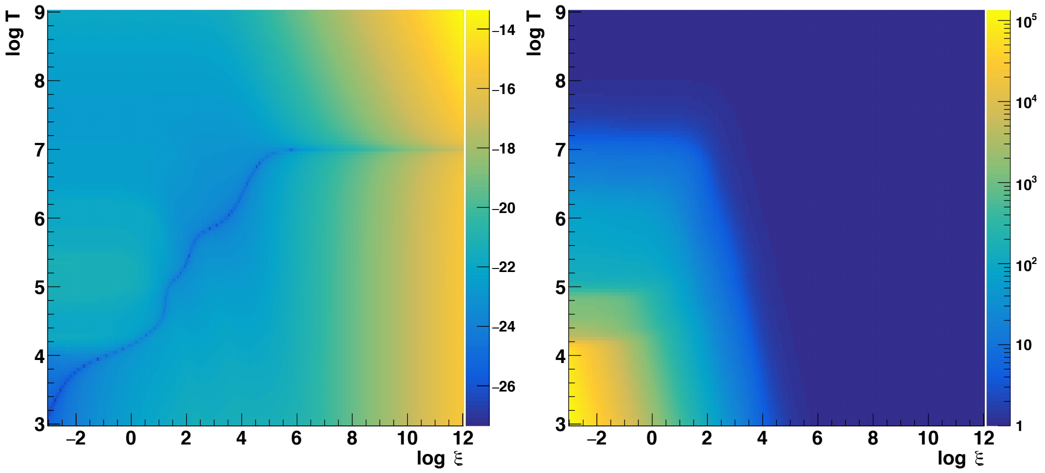

Figure 4.2: The net heating/cooling rate (log $|\Gamma - \Lambda|$) (left), and Force multiplier $M(\xi, T)$ (right) with the irradiation spectrum of BH XRB H1743-322 in soft state. The spectrum itself is taken from Shidatsu & Done (2019).

τ_0 is the optical depth of inner corona described in Sec.6.4. $M(\xi, T)$ in radiation force term is the force multiplier defined by Tarter & McKee (1973). This is the ratio of total opacity (electron scattering, photoelectric absorption and line process) to that of electron scattering calculated by CLOUDY (right in Fig.4.2). We use these atomic processes like scattering.

The hydrodynamic terms for an ideal fluid are solved using an approximate Riemann solver, the HLL method (Harten, 1983). We treat the radiation force as an explicit external force term using the force multiplier supplied via biliner interpolation from pre-calculated CLOUDY table. The numerical procedures are i) calculation of Eq.4.1–4.4 and Eq.4.5 except for the net heating/cooling term, ii) implicit update of temperature using net heating/cooling rate (see next section).

The time step is determined using the Courant-Friendrichs-Levi condition. At each grid, we calculate

$$\delta t = 0.3 \frac{\min(\delta R, R\delta\theta)}{\sqrt{(v_R + c_s)^2 + (v_\theta + c_s)^2}} \tag{4.10}$$

where $\delta R, \delta\theta$ are the grid sizes, while c_s is the isothermal sound speed. The minimum value of δt in all grids is used as the time step.

4.2.2 Integration method of energy equation

We have implemented a new integration source code to calculate Eq.4.5. This code implicitly updates the temperature by including a net heating/cooling term via

$$T^{n+1} = T^n + \delta t \frac{(\gamma - 1)\mu m_p}{k} \mathcal{L}(\xi, T^{n+1}) \tag{4.11}$$

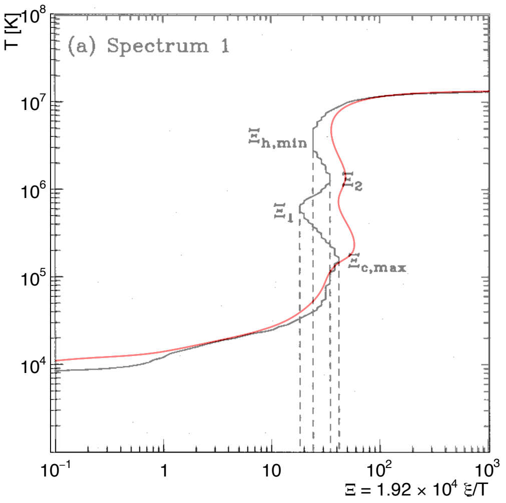

Figure 4.3: thermal equilibrium curve obtained by CLOUDY C17.01 (red) and that of Woods et al. (1996) (black) which use old version CLOUDY

where $\mathcal{L}(\xi, T)$ is taken from a 2 dimensional table file (left 4.2) from CLOUDY via a bilinear interpolation. The 2 dimensional table file is functions of ξ and T. Eq.4.11 is the backward Euler method where the heating rate during the n th time step is calculated by the temperature at the (n+1) th time step. The alternative forward Euler method to calculate the heating rate during the n th time step by the temperature n th time step. While the backward Euler method can treat the time evolution of temperature smoothly when the temperature is close to equilibrium, numerical root finder is required to solve Eq.4.11. For this root finding, we use the Brent's method (Press et al., 1992), which is a combination of the bisection method, the secant method and inverse quadratic interpolation. This method has been widely used in the root finding algorithm. We set an accuracy of root finding $|T_{\rm k+1}/T_{\rm k}| < 10^{-6}$, where k is the iteration number of root finding.

4.3 Numerical test; comparison with previous work

We test our code against the previous work (Woods et al., 1996) by setting $M_c = 1.0 \times 10^8 M_{\odot}$. We calculate a net heating/cooling rate using the current version of CLOUDY C17.01 and using the same irradiation considered by Woods et al. (1996) (Spectrum 1 in Fig.3.2).

4.3.1 The test of energy equation

We calculate the thermal equilibrium curve (red Fig.4.3). Our thermal equilibrium curve shows some differences, but the Compton temperature and the difference of overall structure is not so large. This is basically an update of the atomic data. We calculate the net heating/cooling to generate a table file $\Gamma(\xi, T) - \Lambda(\xi, T)$. The calculation grid of CLOUDY is 161×101 logarithmically spaced grid (ξ, T) in a domain $1.0 \times 10^4 \leq T \leq 1.0 \times 10^9$ and $1.0 \times 10^0 \leq \xi \leq 1.0 \times 10^8$. In this calculation, CLOUDY does not return thermal equilibrium temperature, instead it returns the heating and cooling rate at a given (ξ, T).

We solve thermal equilibrium ($\Gamma(\xi, T) - \Lambda(\xi, T) = 0$) and obtain same equilibrium temperature as Fig.4.3 at given ξ using obtained a net heating/cooling rate (left in 4.4). This is test of our Brent's root finding algorithm. Right panel in Fig.4.4 shows the comparison between the equilibrium temperatures obtained using our root finding algorithm (red) and that of CLOUDY (black). Our implemented code can solve the thermal equilibrium accurately.

We also test Eq.4.11 to obtain T^1 at $\rho_0 = 10^{-12}, 10^{-13}\mathrm{g\ cm^{-3}}$, $\xi_0 = 10^6$,and $T^0 = 10^6\mathrm{K}$ by changing δt. Eq.4.11 shows that when $\delta t \to \infty$, T^1 should reach T_{eq}, where $T_{eq} = T_{\rm IC} = 1.3 \times 10^7\mathrm{K}$ is the thermal equilibrium temperature at $\xi_0 = 10^6$. The equilibrium time scale $t_{\rm eq}$ is written as

$$t_{\rm eq} = \frac{\mu m_p k (T_{\rm eq} - T^0)}{(\gamma - 1)\rho_0(\Gamma(\xi_0, T^0) - \Lambda(\xi_0, T^0))} \tag{4.12}$$

This equation shows that time scale should be proportional to $1/\rho_0$ At a heating/cooling rate of $\Gamma(\xi_0, T^0) - \Lambda(\xi_0, T^0) = 1.1 \times 10^{-21}\mathrm{erg\ s^{-1}\ cm^3}$, these time scales should be $\sim 20\mathrm{s}$ ($\rho_0 = 10^{-13}\mathrm{g\ cm^{-3}}$), and $\sim 2\mathrm{s}$ ($\rho_0 = 10^{-12}\mathrm{g\ cm^{-3}}$), Fig.4.5 shows the results of the time evolution of the energy equation. This figure shows that our calculation is consistent with the estimated time scales. Thus, we conclude that we succeed in implementing the time evolution of the energy equation.

4.3.2 Hydrodynamic simulation of thermal winds

In order to reproduce the result of Woods et al. (1996) we run a HD simulation. We neglect the radiation force and attenuation. We set the radial grid and polar angle grid as $R_{i+1} = 1.01 R_i$ from $0.1 R_{\rm IC}$ to $5\ R_{\rm IC}$ and $\theta_{j+1} = 0.98\theta_j$ from $0°$ to $90°$. The total grid points are 144×144. The boundary conditions for the radial direction are both outflow boundary which means materials can go outside of the boundary but can not enter computational domain. The boundary condition of the polar angle $\theta = 0°$ is axisymmetric (ρ, p and v_R are symmetric , while v_θ and v_ϕ are axntisymmetric). At the boundary $\theta = 90°$, we apply a reflection boundary (ρ, p, v_R, and v_ϕ are symmetric but v_θ is antisymmetric), while the radial velocity is fixed to be null and the rotational velocity is fixed to be the Keplerian velocity, and also the density is fixed to be satisfied with constant ionization parameter, which is

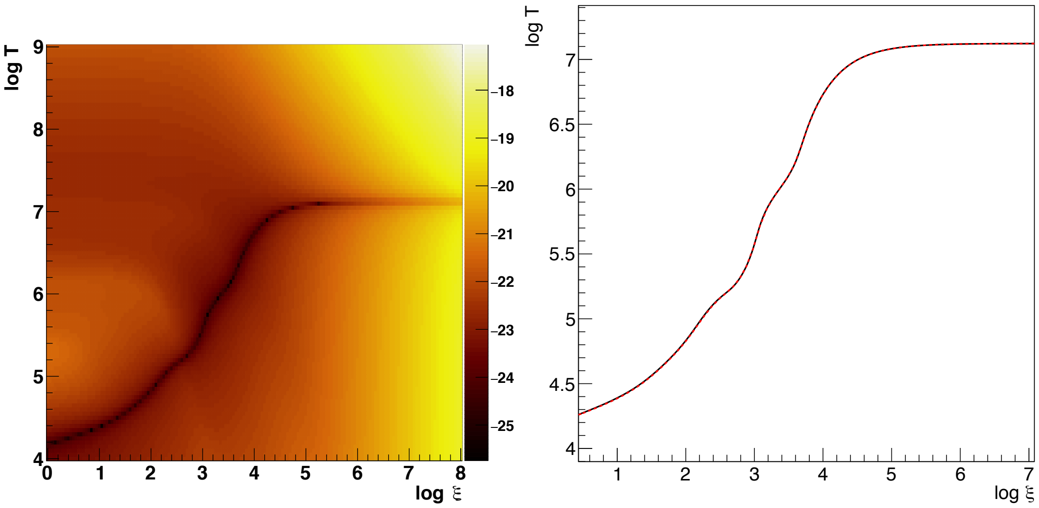

Figure 4.4: The net heating/cooling rate $\log_{10}|\Gamma(\xi, T) - \Lambda(\xi, T)|$ (left). The numerical test for thermal equilibrium temperature (right). The black line show thermal equilibrium temperature from CLOUDY calculation. The red dashed line shows our thermal equilibrium using our root finder.

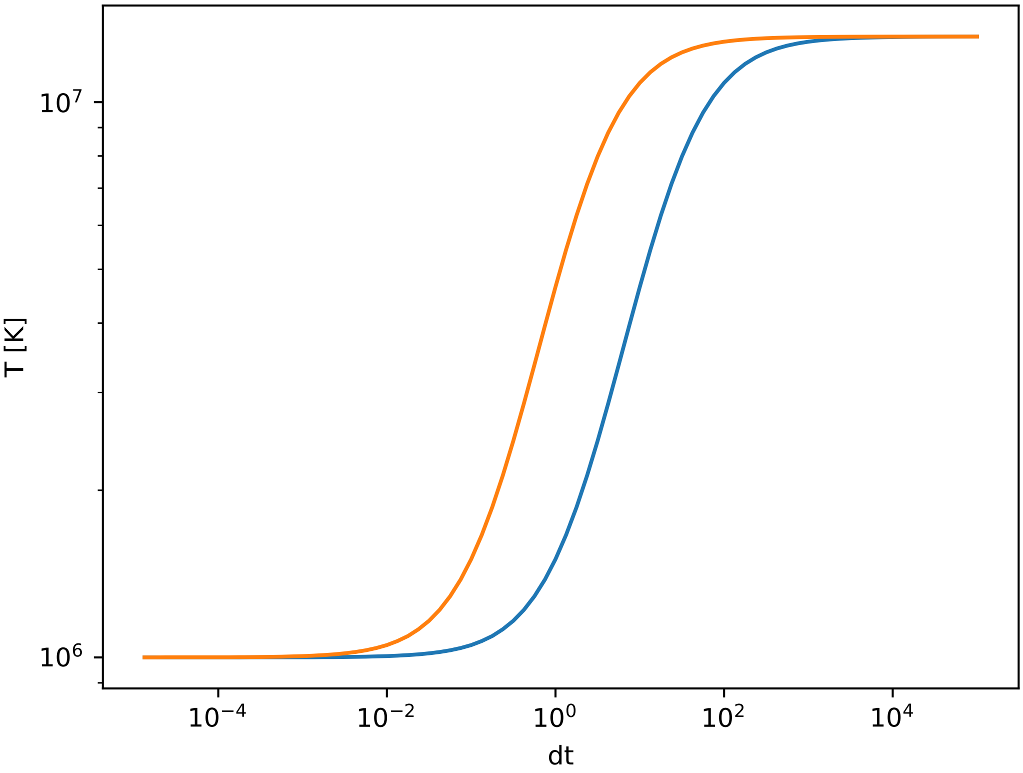

Figure 4.5: The time evolution of energy equation with $\xi_0 = 10^6, T^0 = 10^6$K. Colors show $\rho_0 = 10^{-13}$g cm^{-3} (blue) and 10^{-12}g cm^{-3} (orange).

$\rho = \mu m_p L/(\xi_{\rm c,max} R^2)$, where $\xi_{\rm c,max} = 6.0 \times 10^2$ which corresponds $(\Xi_{\rm c,max}, T_{\rm c,max}) = (60, 2 \times 10^5{\rm K})$. The initial condition is hydrostatic equilibrium with temperature $T = 2.0 \times 10^5$K. We run the simulation for 30 sounds crossing time ($30 \times R_{\rm IC}/c_{\rm IC} = 5.4{\times}10^{12}$s). The resultant density and temperature are shown in Fig.4.6. Most of the temperature is Compton temperature 1.3×10^7K. Thus, the heating/cooling term which we implement works well. We also compare our integral column density with that of Woods et al. (1996). Although our simulation has different hydrodynamics scheme and coordinates, the simulations are in good agreement.

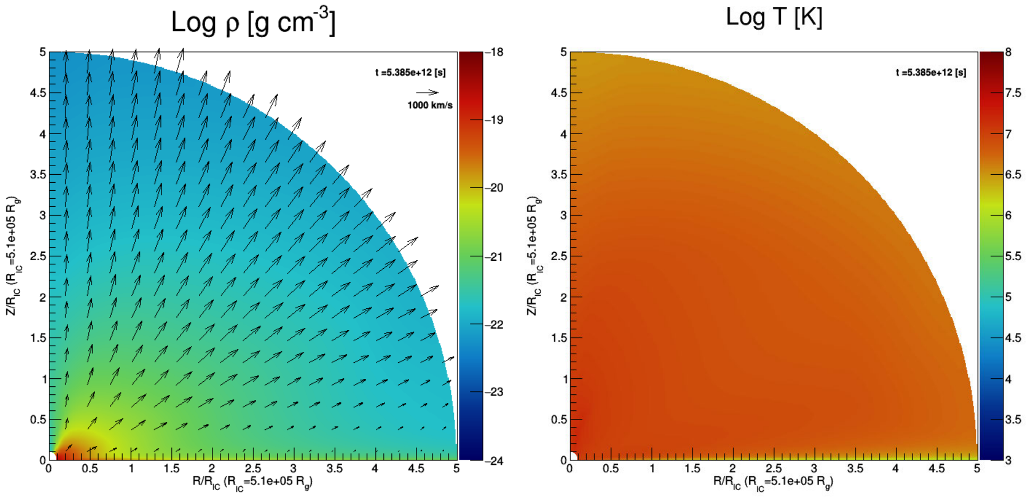

Figure 4.6: Distributions of density (left) and temperature (right). The temperature is heated up to the Compton temperature.

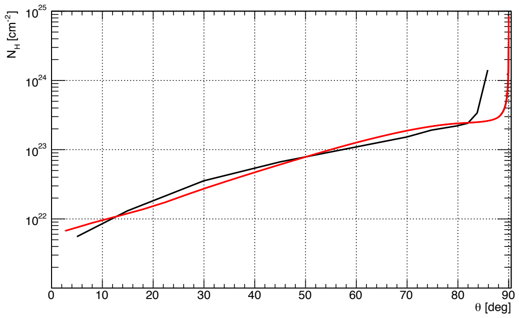

Figure 4.7: The comparison with the column density Woods et al. (1996). Colors show the column density of our simulation (red) and that of Woods et al. (1996) (black). The large column at a high inclination angle means the disk surface.

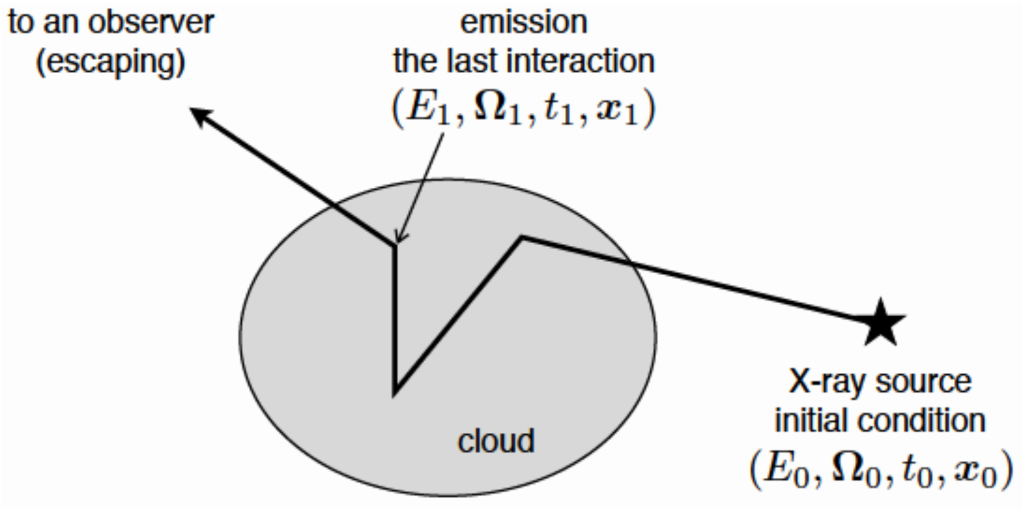

Figure 4.8: Schematic diagram of Monte Carlo simulation taken from Odaka et al. (2011).

4.4 Radiation transfer based on the Monte-Carlo method

We use our Monte Carlo simulation code called MONACO (Odaka et al., 2011) to calculate the detail line profile from the wind. MONACO is a general-purpose framework for the synthesis of X-ray radiation from astrophysical object by calculating radiation transfer based on the Monte Carlo method. This code has been applied to UFOs (Hagino et al., 2015, 2016), molecular tori (Tanimoto et al., 2019) in AGNs, disk winds in X-ray binary (Tomaru et al., 2018), and continuum radiation from accretion column in a neutron star (Odaka et al., 2014). MONACO uses the Geant4 toolkit library (Agostinelli et al., 2003) for photon tracking in an arbitrary three-dimensional geometry, but has its own modules for handling photon interactions Watanabe et al. (2006); Odaka et al. (2011) so that it can treat interactions such as photoionization or photo-excitation, and photons generated via recombination and atomic de-excitation. Scattering by free electrons is also taken into account. The code also handles the Doppler shift of the absorption cross section from the velocity structure of the material. This cross section is calculated for the photon energy in the co-moving frame and Lorentz tansformed back into the rest frame. The Doppler broadening of the temperature and turbulent motion is also considered.

In the Monte Carlo simulation, a photon is tracked by calculating its propagation and interaction with material. These calculations are performed in two steps as shown in Fig.4.8. First, a photon starts from a certain initial point, the next interaction position is determined by considering a mean free path .

$$l = \frac{1}{\sum n_i \sigma_i} \tag{4.13}$$

where n_i and σ_i are a number density of a target material and a cross section of an interaction labeled by i. The length to the next position of interaction x is determined by sampling the exponential distribution $P(x) = 1/l \exp(-x/l)$ using the mean free path as

$$x = -l \ln(1 - X) \tag{4.14}$$

where X is a random number sampled uniformly from 0 to 1. A interaction which occurs at the determined position is selected by a probability distribution proportional to $n_i \sigma_i$. Second, when a photon interacts with a material, it is absorbed or scattered. If it is absorbed, one or more photons can be reemitted through a certain process such as radiative decay. If it is scattered, the energy and direction are changed following a differential cross section. These two steps are applied repeatedly until the photon is absorbed or escapes from the system. The atomic data for all the transitions considered are tabulated in Tab.4.1, and the overall abundances are $A_{\mathrm{Fe}} = 3.3 \times 10^{-5}$ (iron) and $A_{\mathrm{Ni}} = 1.9 \times 10^{-6}$ (nickel) from Lodders et al. (2009).

Although MONACO can treat the detail radiation transfer, it does not calculate the temperature and ion fractions of photoionized gas. To obtain these quantities, we simply calculate the ionization structure by solving the 1 dimensional radiation transfer by using XSTAR or CLOUDY. We use the distribution of temperatures and ion fractions from XSTAR or CLOUDY as the input parameters in addition to the distribution of density and velocity of MONACO.

Table 4.1: Detailed parameters for each line included in these MONACO simulations. Note that we list only lines which have larger oscillator strength than 10^{-3}. These are listed from the lowest energy.

Line ID	Energy [keV]	Oscillator strength
Fe XXV Heα y	6.668	6.57×10^{-2}
Fe XXV Heα w	6.700	7.26×10^{-1}
Fe XXVI Lyα_2	6.952	1.36×10^{-1}
Fe XXVI Lyα_1	6.973	2.73×10^{-1}
Ni XXVII Heα y	7.765	8.50×10^{-2}
Ni XXVII Heα w	7.805	7.06×10^{-1}
Fe XXV Heβ w	7.881	1.39×10^{-1}
Ni XXVIII Lyα_2	8.073	1.36×10^{-1}
Ni XXVIII Lyα_1	8.102	2.72×10^{-1}
Fe XXVI Lyβ_2	8.246	2.55×10^{-2}
Fe XXVI Lyβ_1	8.253	5.23×10^{-2}
Fe XXV Heγ w	8.295	5.10×10^{-2}

Chapter 5

Spectral modeling of thermal winds by Monte Carlo method

We explore the thermal wind predictions in more detail, using a 3–dimensional Monte-Carlo radiation transfer (MCRT) simulation to predict the detail shape of absorption (and emission) line profile. Before we run RHD simulations, we use simple density and velocity structure of thermal winds. We test this on the persistent wind seen in the bright neutron star binary GX 13+1, with luminosity $L/L_{\rm Edd} \sim 0.5$.

5.1 Radial streamlines

5.1.1 Geometry and Parameters

We first consider the radial streamline wind model of Done, Tomaru, & Takahashi (2018, Sec.3.2). This calculates the analytic mass-loss rate per unit area, $\dot{m}(R)$ where R denotes distance along the disk plane. Integrating over the whole disk gives the total mass-loss rate in the wind, $\dot{M}$. This is assumed to flow along radial (centered at the origin) streamlines from a launch radius which is $0.2R_{\rm IC}$ for high $L/L_{\rm Edd}$, with constant velocity set at the mass-loss weighted average escape velocity. The mass-loss rate along each radial streamline is weighted with angle such that $\dot{M}(\theta) \propto \dot{M}(1-\cos\theta)$, and then mass conservation gives $n(r,\theta) \propto (1-\cos\theta)/r^2$. Done et al. (2018, Sec.3.2) show that these assumptions lead to a total column density through the structure which matches to within a factor 2 of that in the hydrodynamic simulations of Woods et al. (1996) (see also Sec.5.2).

We put this structure into MONACO for $L = 0.3L_{\rm Edd}$ with $T_{\rm IC} = 1.3 \times 10^7$ K and $R_{\rm out} = 5R_{\rm IC}$ (mass loss rate $\dot{M}_{\rm w} = 2.0 \times 10^{19}{\rm g\ s^{-1}}$ for a $10M_\odot$ black hole which means the ratio of mass-loss rate to mass accretion rate $\dot{M}_{\rm w}/\dot{M}_a = 3.9$,

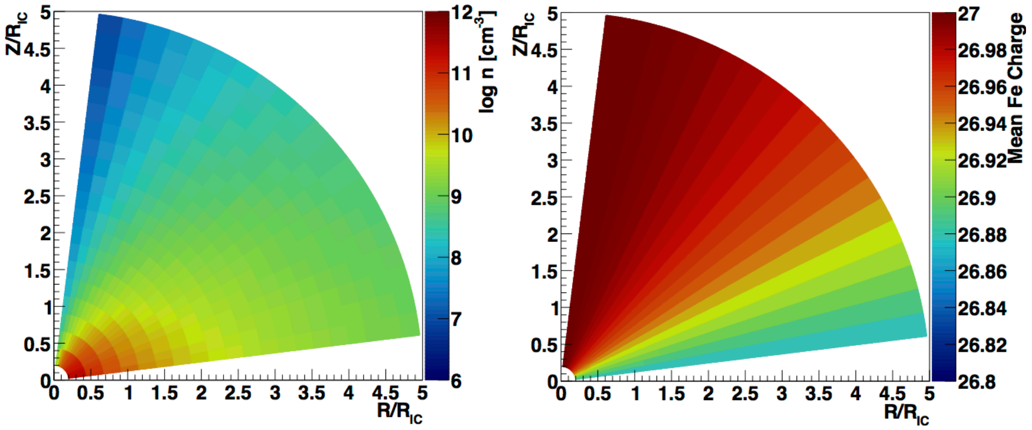

Figure 5.1: Distribution of density (left) and mean Fe ionization state (right) for the radial streamline model

where the $\dot{M}_a = L/(0.1c^2)$, launch radius of $0.2R_{\rm IC} \approx 10^5 R_g$ and weighted average $v_{\rm out} = 420{\rm km/s}$). We include turbulence, assuming $v_{\rm turb} = v_{\rm out}$, and calculate the rotation velocity along each stream line assuming angular momentum conservation (see Appendix A.1.1).

We make a grid which follows the symmetry of the assumed structure, i.e. centered on the origin, with 20 linearly spaced spherical shells from $0.2 - 5R_{\rm IC}$, and 20 angles, linearly spaced in θ from $7 - 83^\circ$ (see below). This density structure is shown in the left panel of Fig. 5.1, while the right panel shows the mean Fe ion state obtained from the XSTAR calculation. This is constant along each streamline because the ionization parameter $\xi = L/(nr^2)$, and the constant velocity radial streamlines mean that density decreases as $1/r^2$. Fe is almost completely ionized over the whole grid, with a small fraction of hydrogen-like iron remaining only for high inclination streamlines.

5.1.2 Result of radiation transfer

Fig. 5.2 shows the resulting spectra at three different inclination angles. These show that the emission lines are always similarly weak, and that the electron scattered continuum flux makes only a $\sim 0.5\%$ contribution to the total flux, but that the absorption lines strongly increase at higher inclination angles. We calculate the equivalent width (EW) of each emission and absorption line by fitting the continuum outside the emission and absorption regions with an arbitrary function ($F(E) = aE^{bE+c}$ Odaka et al. 2016). The EW of each emission and absorption line is then measured by numerical integration of the difference between the model and the simulation data. The left panel of Fig. 5.3 shows the EW of the He-like (red) and H-like Lyα_2 (green) and Lyα_1 (blue) absorption lines. The corresponding emission

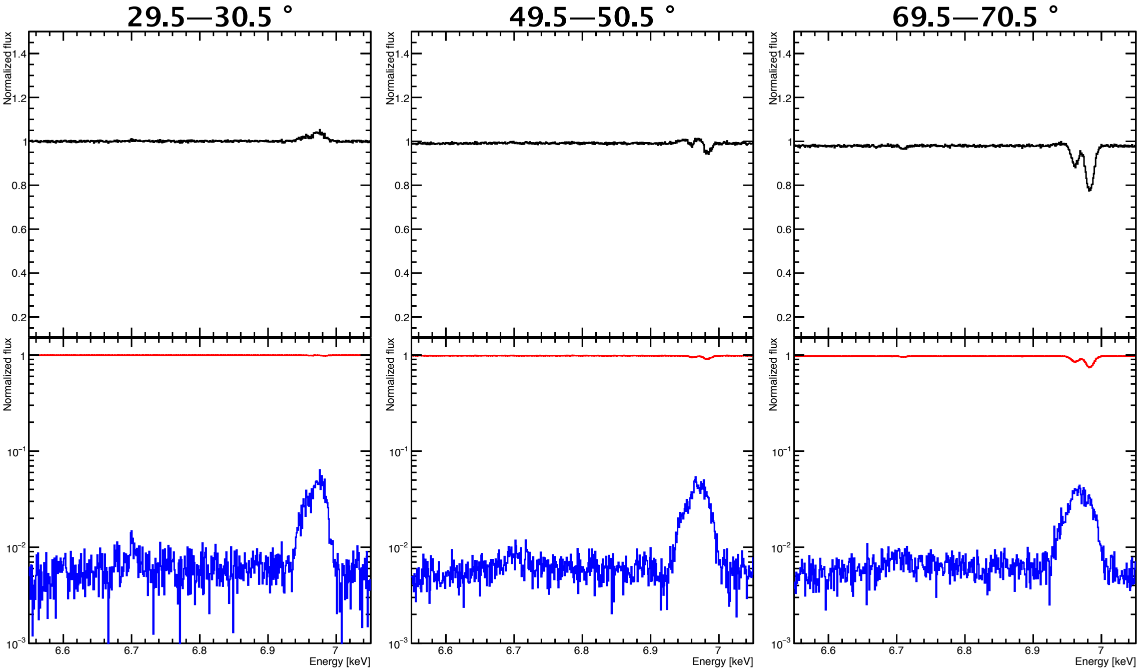

Figure 5.2: Spectra computed for the radial streamline model with 1 eV resolution for different lines of sight. Each panel shows the spectrum in a different inclination angle bin (the angular bin sizes are indicated the top of each panel). The total spectrum is shown in black (top), the spectrum direct photons in red and scattered/reprocessed spectrum is blue (bottom). Note that the vertical axis is plotted linearly in the top panels but logarithmically in the bottom panels. Lines are Fe XXV (6.668 keV for Heα y and 6.700 keV for Heα w) and Fe XXVI (6.952 keV for Lyα_2 and 6.973 keV for Lyα_1). The equatorial density structure of the wind means that the absorption is much stronger at high inclination angles. The emission is more isotropic, so it can clearly be seen at low inclination angles, but is absorbed by the wind at high inclinations.

lines always have EW lower than 0.1 eV so are not seen on this plot. The strong increase of the absorption line EW with inclination clearly shows that the wind is equatorial (by construction from the $1 - \cos\theta$ density dependence and constant velocity assumptions). At inclinations above 70°, the Doppler wings of the Kα_1 and Kα_2 absorption lines merge together due to the turbulent velocities, so Fig. 5.3 shows only a single EW for this blend.

Fig. 5.3 (right) shows the outflow velocity, as measured from the energy of the deepest absorption lines (with error set by the resolution of the simulation to ± 0.5 eV). These velocities are constant within 25 % as a function of inclination, again by construction due to the assumption of constant radial velocity along radial streamlines.

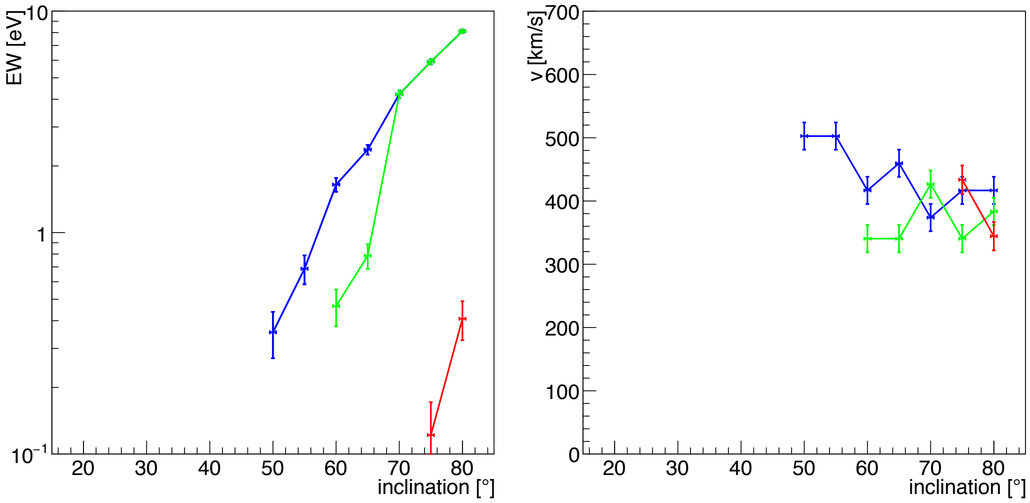

Figure 5.3: Left panel: EW of the absorption lines as a function of inclination angle, Fe XXV (Heα w, red) and Fe XXVI (Lyα_2, green and Lyα_1, blue). The EW of all absorption lines increases strongly at higher inclination, showing the assumed equatorial disk wind geometry. The Doppler wings (with width set by turbulent velocity) of the two H-like absorption lines start to merge for inclinations above 70° so above this we show the total EW of the two lines. Right panel: the blue shifted absorption line velocity for each ion species. This clearly shows the assumed constant velocity structure of the radial streamline.

5.2 Diverging wind

In previous section, we considered a wind model with constant velocity along radial streamlines. However, the expected thermal wind geometry is instead much more like an accelerating, diverging biconical wind Waters & Proga (2012). Full streamline structures which give the density and velocity of the wind at all points can only be found by hydrodynamic calculations (but see Clarke & Alexander 2016 for some analytic approximations). Since modern calculations only exist for the singular case of GRO J1655-40, we follow Done et al. (2018) and use the Woods et al. (1996) simulation results. Woods et al. (1996) do not give full density/velocity structures, but do give total column density through the wind at three different luminosities. We use these to match to our assumed streamline and velocity structure, which is the standard biconical diverging disk wind used in a variety of systems including cataclysmic variables (Knigge et al., 1995; Long & Knigge, 2002) and Active Galaxies (Sim et al., 2010; Hagino et al., 2015).

5.2.1 Geometry and Parameters

The geometry can be defined by 3 parameters (Fig. 5.4).

1. $R_{\rm in} = 0.1R_{\rm IC}$, the distance from the source to the inner edge of the wind
2. $R_{\rm out}$, the distance from the source to outer edge of the wind
3. $\alpha_{\rm min}$, the angle from z axis to the inner edge of the wind

The disk wind is fan-shaped, with a focal point offset down from the center by a distance $d = 0.1R_{\rm IC}/\tan\alpha_{\rm min}$ so that the wind fills the angles from $\alpha_{\rm max} - \alpha_{\rm min}$ down to the disk surface. We use R to denote distance along the disk surface, and r, θ denote radial distance and polar angle from the origin, as before. $\alpha_{\rm min}$ (or equivalently d) is a free parameter, which sets the wind geometry.

Streamlines are assumed to be along lines of constant angle α (where $\alpha_{\rm min} < \alpha < \alpha_{\rm max}$) from the focal point. Distance along a streamline which starts on the disk at radius R is $l(R)$ (see Appendix. A.1.1). Velocity along the streamline is assumed to be of the form $v(r,\theta) = f_v c_{ch}(r)\sqrt{\frac{l(r,\theta)}{R(r)}}$, i.e. this wind accelerates with distance along the streamline, with a terminal velocity which is related via a free parameter f_v to the characteristic sound speed c_{ch}, given by the balance between heating and cooling in the time it takes the wind to reach a height $H \sim R$ (Done et al., 2018). The density structure is solved by the mass conservation continuity equation along streamlines (see Appendix.A.1.2). We calculate the wind properties out to a distance which is twice that of the focal point of the wind to $R_{\rm out}$.

We set the free parameter values, f_v and $\alpha_{\rm min}$, and calculate the total column along each line of sight, $N_H(\theta)$, to the central source for parameters matching to the three Woods et al. (1996) simulations. These are $L/L_{\rm Edd} = 0.3, 0.08$ with $R_{\rm out} = 5R_{\rm IC}$ and $L/L_{\rm Edd} = 0.01$ with $R_{\rm out} = 12R_{\rm IC}$. We adjust f_v and $\alpha_{\rm min}$ to minimise the difference between our model and Woods et al. (1996). We find $\alpha_{\rm min} = 7^\circ$ and $f_v = 0.25$ matches within a factor 2 of the results from Woods et al. (1996). Fig. 5.5 shows results with these parameters (filled circles), compared to the radial wind model of Sec. 5.1 (open circles) as well as the Woods et al. (1996) results (solid line). These more physically realistic geometry and velocity give a similarly good match to the simulations as the Done et al. (2018) radial wind.

The resulting density structure from this different geometry and velocity is shown in the left panel of Fig. 5.6 for $L/L_{\rm Edd} = 0.3$. Comparing this with the radial wind shows that the density is higher closer to the disk, and lower further away due to the material accelerating away from the disk rather than being at constant velocity. We run XSTAR as before, and the right panel of Fig. 5.6 shows that this

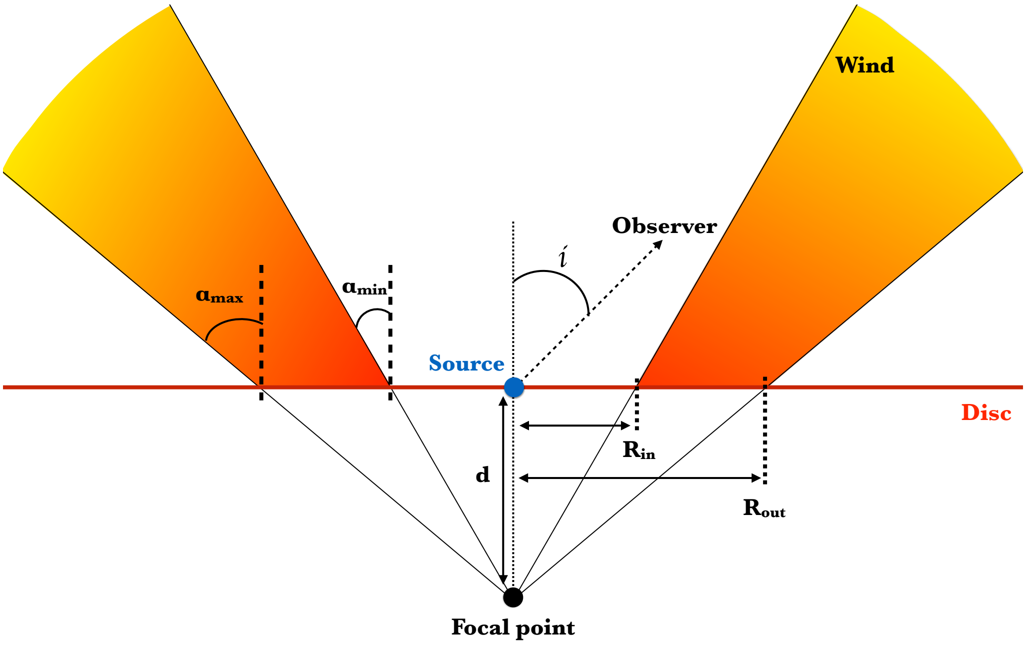
Wind
Observer
i
$\alpha_{\max}$
$\alpha_{\min}$
Source
Disc
R_{in}
d
R_{out}
Focal point

Figure 5.4: The geometry of the diverging biconical wind model.

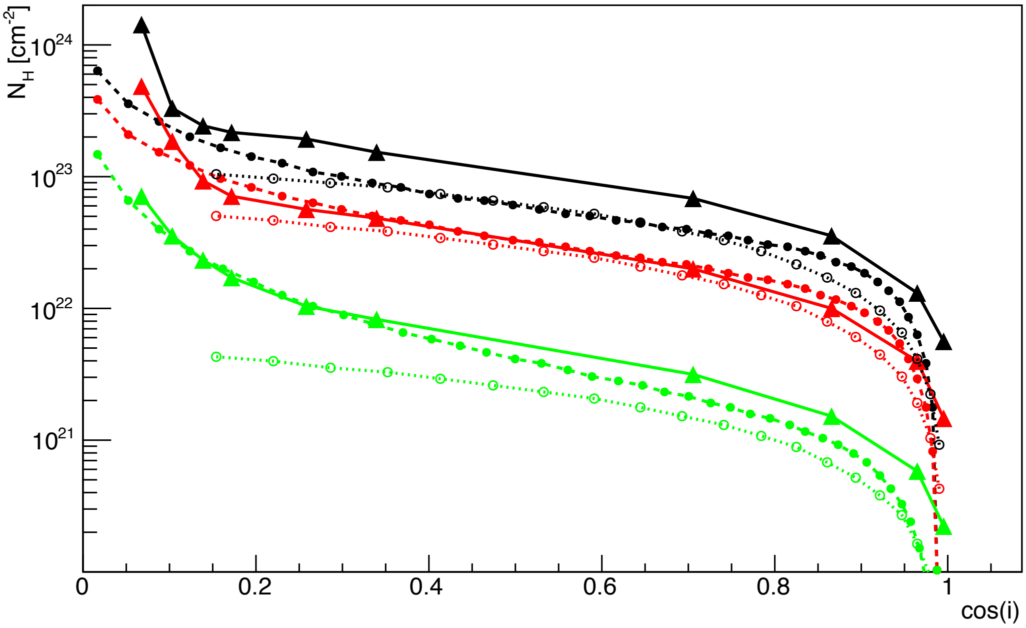

Figure 5.5: The solid lines show column density as a function of the cosine of the inclination angle through the wind resulting from the hydrodynamic simulations of Woods et al. (1996) for $L/L_{\mathrm{Edd}} = 0.01$(green), 0.08 (red), 0.3 (black). The filled circles show that resulting from the diverging biconical wind (Section 4) while the open circles show the radial streamline model of Done et al. (2018)(Section 3).

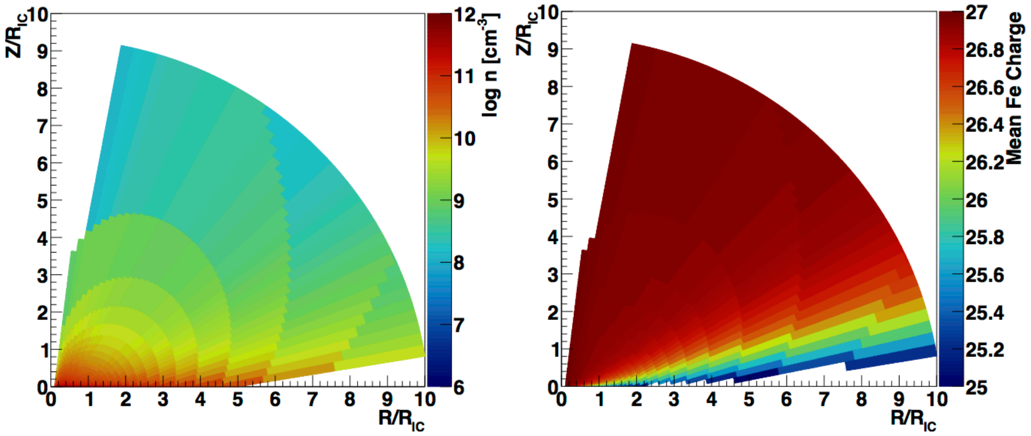

Figure 5.6: Distribution of density (left) and Fe ionization state (right) for the diverging wind geometry. The accelerating flow gives higher density material close to the disk compared to the constant velocity outflow model in Fig. 5.1, giving lower mean ionization state.

leads to a lower mean ionization state of Fe than before, and this is no longer constant along the radial sightline due to the different wind geometry.

5.2.2 Result of radiation transfer

We calculate the emission and absorption lines resulting from the different wind structure (Fig. 5.7). The diverging bipolar wind has higher density material closer to the source compared to the radial wind geometry, so it subtends a larger solid angle to scattering. This means that there is more emission line contribution, as well as a higher fraction of electron scattered continuum (around 2%, see the lower panel of Fig. 5.7). The left panel of Fig. 5.8 shows the emission line EW (dotted lines) for each ion species (red: Fe xxv w, green: Fe xxvi Lyα_2, blue: Lyα_1). These can now be of order 1 eV for face on inclinations, decreasing at higher inclination as they are significantly suppressed by line absorption.

The corresponding absorption line EWs are shown as the solid lines (compare to Fig. 5.3). The lower mean ionization state leads to more He-like Fe, so there is more of this ion seen in absorption than in the radial streamline model. These absorption lines increase as a function of inclination angle as before, but now the Lyα_1 and Lyα_2 do not merge together at the highest inclination angles due to the different velocity structure (see right panel of Fig. 5.8). The lines are formed preferentially in the higher density material close to the disk. The assumed acceleration law means that the typical velocities here are lower than in the constant velocity model, as the material has only just begun to accelerate. Thus the turbulence is also lower, so the Doppler width of the absorption lines is smaller. This also means that the

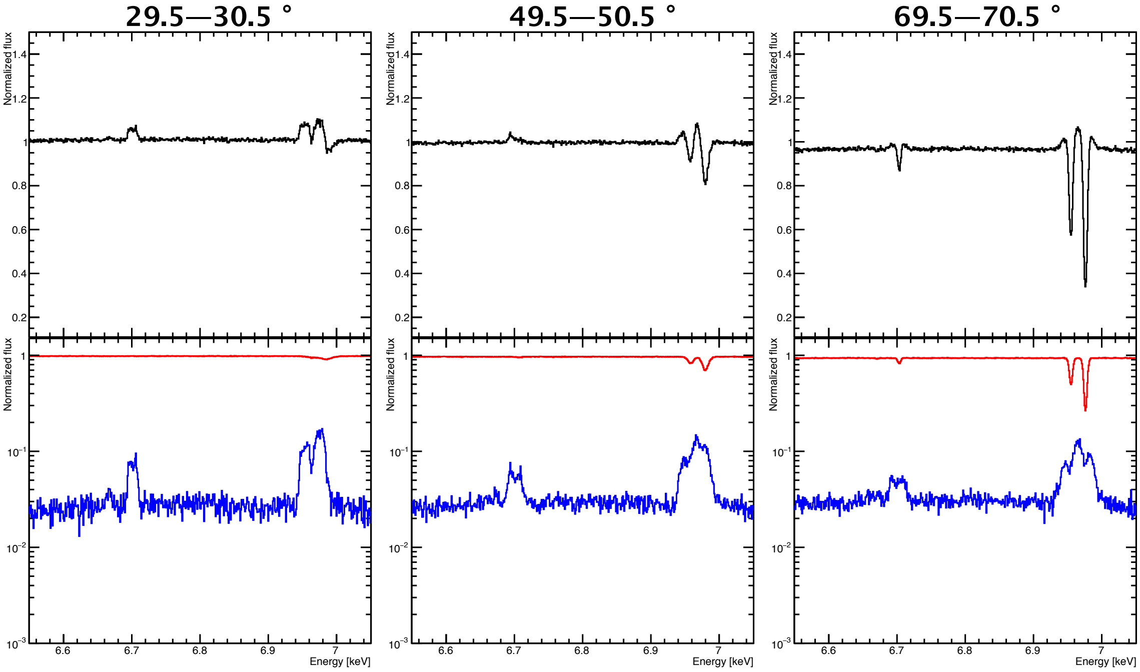

Figure 5.7: As in Fig 5.2, but for the diverging biconical wind geometry.

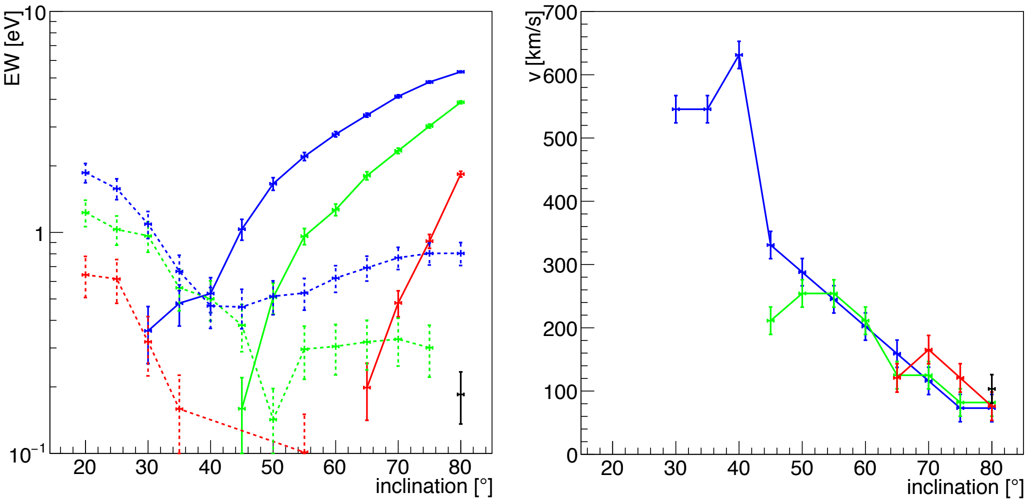

Figure 5.8: As in Fig. 5.3, but for the diverging wind model. The lower The lower ionization state means that there is also a contribution from the intercombination line of Fe xxv Heα y (black) at the highest inclinations.

absorption line saturates to a constant EW at lower column density, so the EW of the absorption lines does not increase so strongly as before at the highest inclination angles.

5.3 Comparison with GX13+1

We now use the more physically motivated diverging biconical wind geometry to compare with observational data. An ideal source would be one which is not too different from the parameters simulated in the previous sections, as here we know the total column from Woods et al. (1996) and know that our assumed velocity/density matches to this. Of the sources listed in Díaz Trigo & Boirin (2016), the neutron star LMXB GX13+1 is the source which has most similar $L/L_{\rm Edd}$ and $T_{\rm IC}$ to that assumed here, and it also has the advantage that it is a persistent source, with relatively constant luminosity and spectral shape, and it shows similarly strong absorption lines in multiple datasets.

5.3.1 Observational data

GX13+1 was observed by the *Chandra*/HETGS 5 times in two weeks in 2010 (Table. 2.1). The first order data are shown in D'Aì et al. (2014) and reveal multiple absorption features from highly ionized elements (see also Ueda et al. 2004 for similar features in an earlier observation). Higher order grating spectra give higher resolution, as demonstrated for the black hole binaries by (Miller et al., 2015). Here we show for the first time the third order HETGS data for GX13+1 by stacking the TE mode data (OBSID:11814-11817). We extract first- and third-order HEG spectra from these observations, using CIAO version 4.9 and corresponding calibration files. We reprocess the event files with "chandra_repro", and make response files using "mktgres" to make the redistribution and ancillary response files. We run "tgsplit" to get the HEG ±3 spectra, and run "combine_grating_spectra" to combine HEG plus and minus orders for each observation to derive a single 1st order spectrum (black), and a single 3rd order spectrum (red) as shown in Fig. 5.9. The 1st order spectra can resolve the components of the He-like Fe triplet, with a clear dip to the low energy side at the resonance line energy of 6.7 keV, but the H-like Lyα_1 and α_2 are blended together. The higher resolution of the 3rd order spectra is able to clearly separate the He-like intercombination and resonance lines, and even the H-like Lyα_1 and α_2 (Miller et al., 2015).

Table 5.1: List of the *Chandra*/HETGS observations

OBSID	MODE	Data	Exposure (ks)
11815	TE	24/07/2010	28
11816	TE	30/07/2010	28
11814	TE	01/08/2010	28
11817	TE	03/08/2010	28
11818	CC	05/08/2010	23

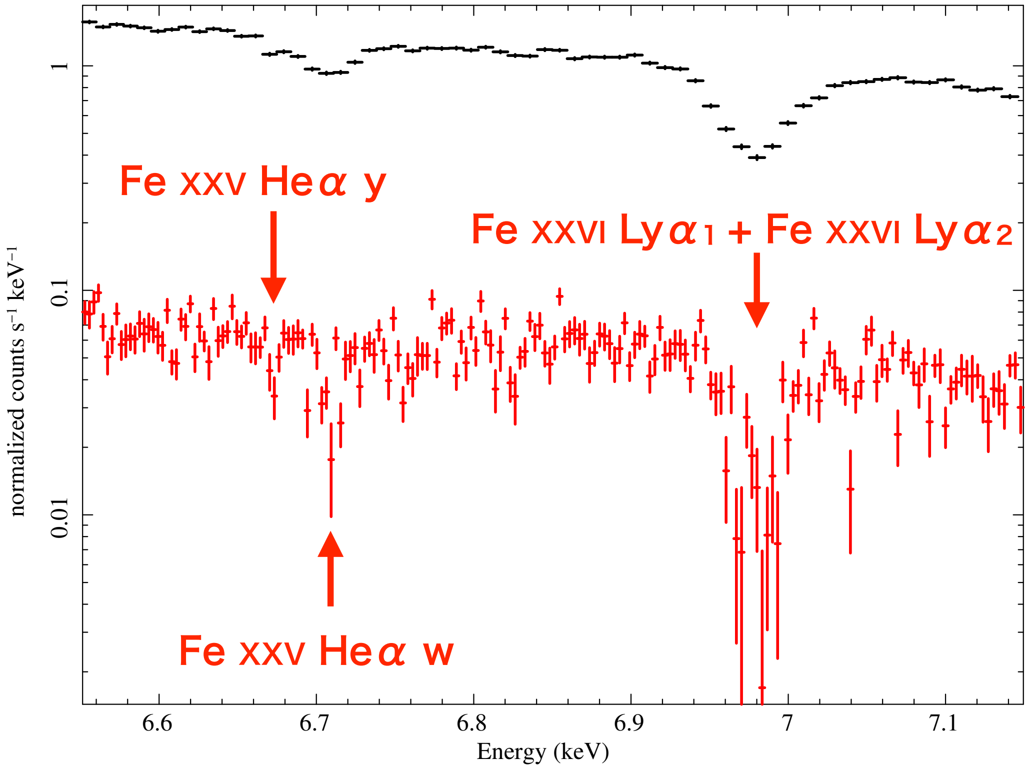

Figure 5.9: HEG spectra of GX 13+1 from 1st order (black) and 3rd order (red) by stacking 4 dataset (OBSID:11814-11817).

5.3.2 Model of GX 13+1

We fit the contemporaneous RXTE spectrum (ObsID 95338-01-01-05) with a model consisting of a disk, Comptonised boundary layer and its reflection. The resulting inverse Compton temperature of the continuum (disk plus Comptonisation) is $T_{\rm IC} \sim 1.2 \times 10^7$ K, almost identical to the simulation (see also D'Aì et al. 2014). The luminosity is $L = 0.5L_{\rm Edd}$ (Díaz Trigo et al., 2014; D'Aì et al., 2014), similar to the maximum simulation value of $L = 0.3L_{\rm Edd}$ in Woods et al. (1996). The simulation also requires $R_{\rm out}$, which can be calculated from the orbital period and mass of binary stars. GX 13+1 has 24 day orbital period, and the neutron star and companion have masses of $1.4M_\odot$ and $5M_\odot$ respectively (Bandyopadhyay et al., 1999; Corbet et al., 2010). This gives a binary separation $a = 4.6 \times 10^{12}$cm, for a Roche-lobe radius $R_R/a = 0.27$. The disk size is then $R_{\rm out} = 10R_{\rm IC}$ assuming that $R_{\rm out} = 0.8R_R$ (Shahbaz et al., 1998), double the value assumed in the simulations. Done et al. (2018) shows that this increase in disk size makes the predicted column slightly larger, but the effect is fairly small (Fig. 3: Done et al. 2018). Fig. 5.10 (blue line) shows the predicted column density through the wind as a function of inclination angle. This is very similar to the column predicted for the fiducial simulations (Fig. 5.5)

However, Done et al. (2018) show that radiation pressure should make a rapidly increasing contribution to the wind as $L/L_{\rm Edd}$ increases from $0.3-0.7$. The GX13+1 luminosity is midway between these two, so radiation pressure should significantly lower the effective gravity, meaning that the wind can be launched from smaller radii. We follow Done et al. (2018) and estimate a radiation pressure correction to the launch radius of $\bar{R}_{\rm IC} = (1.0 - 0.5L_{\rm Edd}/0.71L_{\rm Edd})R_{\rm IC} = 0.30R_{\rm IC}$, hence $R_{\rm out} = 33\bar{R}_{\rm IC}$, dramatically larger than assumed in the fiducial simulations. This correction predicts a density which is 11 times larger and column along any sightline which is 3.3 times larger assuming (as in Done et al. 2018) that the velocity structure is unchanged (red line, Fig. 5.10). This increase in $R_{\rm out}$ in terms of $R_{\rm IC}$ means that more wind is produced (as in Done et al. 2018), so the wind efficiency increases to 4.0 (from 2.3).

The column density goes close to 10^{24} cm^{-2} at high inclinations, so electron scattering becomes important. This effect reduces the illuminating ionising flux by $e^{-\tau_T}$ from the central source along the line of sight to each wind element, and also increases the contribution of diffuse and scattered emission from the wind to the ionising continuum. We include scattering, reducing the XSTAR illumination by $e^{-\tau_T}$ along each line of sight, but do not include the diffuse emission as the timescale to integrate over the entire wind at each point is prohibitive.

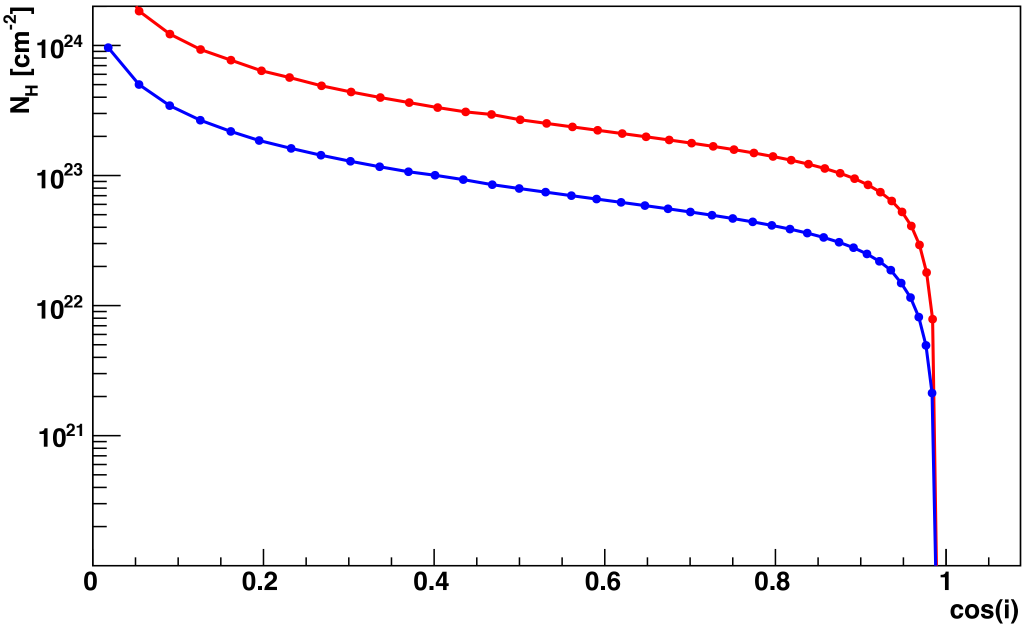

Figure 5.10: The column density as a function of the cosine of the inclination angle for the diverging biconical wind calculated for the system parameters of GX13+1. The blue line shows the predictions for a purely thermal wind, while the red includes a very simple treatment of radiation pressure. The source has $L/L_{\rm Edd} \sim 0.5$, so the thermal wind can be launched from closer in due to the lower effective gravity. This effect has a large impact on the predicted column, so the details of how this radiation pressure correction affects the velocity and density structure will be important in determining the line profiles.

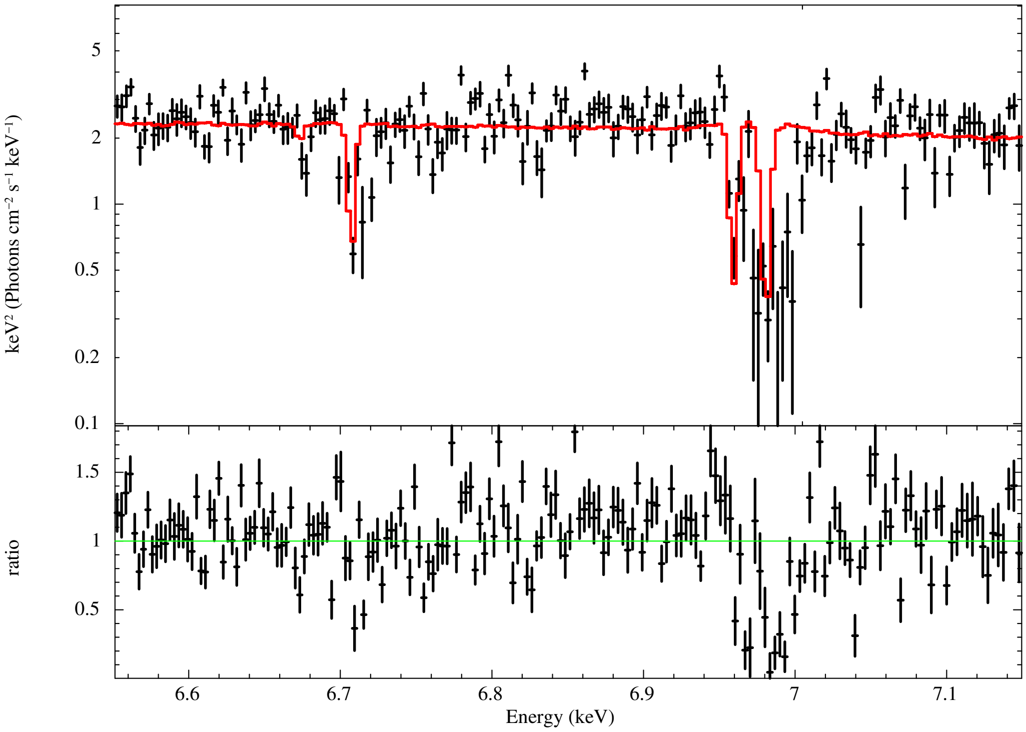

Figure 5.11: The model (red) and HEG 3rd order spectrum (black). The best fit inclination angle is $i = 80°$. This gives roughly the correct column of Fe xxv and xxvi at low velocity, but fails to match the observed higher velocity blue wing to the absorption features.

We run MONACO on this wind structure to predict the detailed absorption line profiles for comparison to the 3rd order HEG data. Fig. 5.11 shows the result assuming an inclination angle of 80° (Díaz Trigo et al., 2012) which gives the best fit to the data. This gives a fairly good match to the overall absorption, except for the highest velocity material seen in the data. Lower inclination angles give higher blueshift, but lower absorption line equivalent width, while higher inclination gives larger absorption line but lower blueshift (see Fig. 5.12). Thus it is not possible to completely reproduce the observed lines in GX13+1 with our simple radiation pressure corrected thermal wind model. This is not surprising, as radiation pressure will almost certainly change the velocity law by radiative acceleration as well as changing the launch radius. Full radiation hydrodynamic simulations are required to predict the resulting velocity and density structure. Nonetheless, our result demonstrates for the first time that hybrid thermal-radiative wind models can give a good overall match to the column and ionization state of the wind in GX13+1, and that current data can already give constraints on the velocity and density structure of this material.

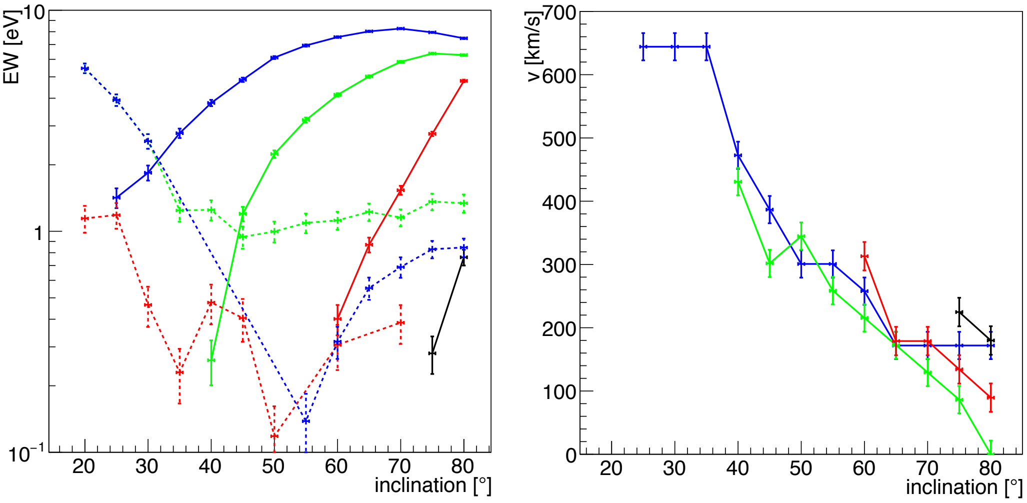

Figure 5.12: As in Fig. 5.8, but with the system parameters of GX 13+1 and the simplest radiation pressure correction to make a hybrid thermal/radiative wind.

Chapter 6

Hydrodynamic model of H 1743–322

In chapter 3, we predict that thermal winds could explain absorption appearance in soft state and its disappearance in hard state. In chapter 5, we show that radiation force is important and RHD simulation is required to construct more realistic model to compare with observed spectrum. In this chapter we run RHD simulations to confirm the effect of radiation force and whether we can get same ion columns and velocities as observation.

6.1 BH LMXB H 1743-322

The low mass X-ray binary H 1743-322 is the best target to test our model because this object shows clear relation between type of accretion flow and appearance of absorption liens Miller et al. (2012, Fig.6.1), and its spectral shape is typical disk dominate soft state and Comptonized hard state. This object also show a relativistic jet by both X-ray and radio (Corbel et al., 2005). There are currently four BHBs which show wind features in their soft states, namely GRO J1655-40, GRS 1915+105, H 1743-322 and 4U 1630-472 (see e.g. the compilation of Ponti et al. 2012). The anomalous features of the wind in one observation of GRO J1655-40 are discussed above (though see Higginbottom et al. 2018) for a thermal wind simulation of a more normal soft state. GRS 1915+105 has a mean luminosity around Eddington, so radiation force will be extremely important. It also typically shows complex spectra rather than standard soft or hard states, and has a truly enormous disk so needs a very large simulation domain. The system parameters for 4U 1630-472 are not well known and it has a very large galactic column which makes determining the soft state disk luminosity difficult. This leaves H 1743-322 as the best object to model in detail to reveal the physical origin of the relation between accretion flow and winds.

This object shows many outbursts which have been observed by *RXTE* and *Swift*. The high resolution spectroscopy by *Chandra*/HETGS was carried out several times. *Chandra*/HETGS observations during a standard disk dominated state in 2003 show blueshifted absorption lines from Fe XXV and Fe XXVI (ObsID:3803, see Miller et al. 2006), with only upper limits on these absorption lines in the hard state in 2010 (ObsID:11048, see Miller et al. 2012). We reanalyze the data soft state, and fit with Gausssan absorption line (GABS in XSPEC) and get columns and velocity. We find these values are within $\pm 1\sigma$ errors of those of previously reported i.e. the column and velocity of Fe XXV, $N_{\rm XXV} = 8.2^{+1.2}_{-1.1} \times 10^{16}$ cm^{-2} and $V_{\rm XXV} = 370 \pm 120$ cm^{-2}, while those of Fe XXVI are $N_{\rm XXVI} = 4.0 \pm 0.3 \times 10^{17}$ cm^{-2} and $V_{\rm XXVI} = 630^{+80}_{-120}$ km/s. We use upper limits of absorption equivalent width reported by Miller et al. (2012) converting to column densities $N_{\rm XXVI} < 3.6 \times 10^{16}$ cm^{-2} and $N_{\rm XXV} < 2.5 \times 10^{16}$ cm^{-2} in hard state.

Although we do not know the system parameters correctly, there are some estimations. The inclination and distance of this object is estimated from the trajectory of jets as $75 \pm 3°$ and 8.5 ± 0.8kpc (Steiner et al., 2012). We do not know the mass of compact object but we assume $M = 7M_\odot$ same as Shidatsu & Done (2019). We also use previously reported luminosities by Shidatsu & Done (2019) as $L = 0.3\ L_{\rm Edd}$ (soft state) and $L = 0.06\ L_{\rm Edd}$ (hard state). We note that these are different to those assumed in Sec.3.5.2 (soft; $L/L_{\rm Edd} = 0.1$, hard; $L/L_{\rm Edd} = 0.02$) (Done et al., 2018).

The remaining key parameter which determines the strength of a thermal wind is the disk size, $R_{\rm disk}$ because mass-loss rate is depends on disk size. This is quite poorly known. Done et al. (2018) assume $R_{\rm disk} = 5R_{\rm IC}$ to connect to the hydrodynamic simulations of Woods et al. (1996) but Shidatsu & Done (2019) note that the outburst frequency puts the source on the edge of the disk instability, similarly to GX339-4. We use the MAXI lightcurve to measure the mean X-ray luminosity over a 10-year time span. The mean MAXI 2-20 keV count rate is about 10 times lower than the count rate seen during the low/hard state ($L/L_{\rm Edd} = 0.06$) used by Shidatsu & Done (2019), which is at $L/L_{\rm Edd} = 0.06$ for the assumed black hole mass and distance. This converts to a mean mass transfer rate of $\sim 6 \times 10^{16}$ g s^{-1}, where the disk instability condition predicts an orbital period of ~ 7 hours (Coriat et al., 2012). Assuming the companion star has a similar mass ratio as in GX339-4 then this implies a Roche lobe size of 1.7×10^{11} cm, and hence a disk radius of 1.2×10^{11} cm (70% Roche lobe size), which is 0.2 $R_{\rm IC}$. This is the point at which

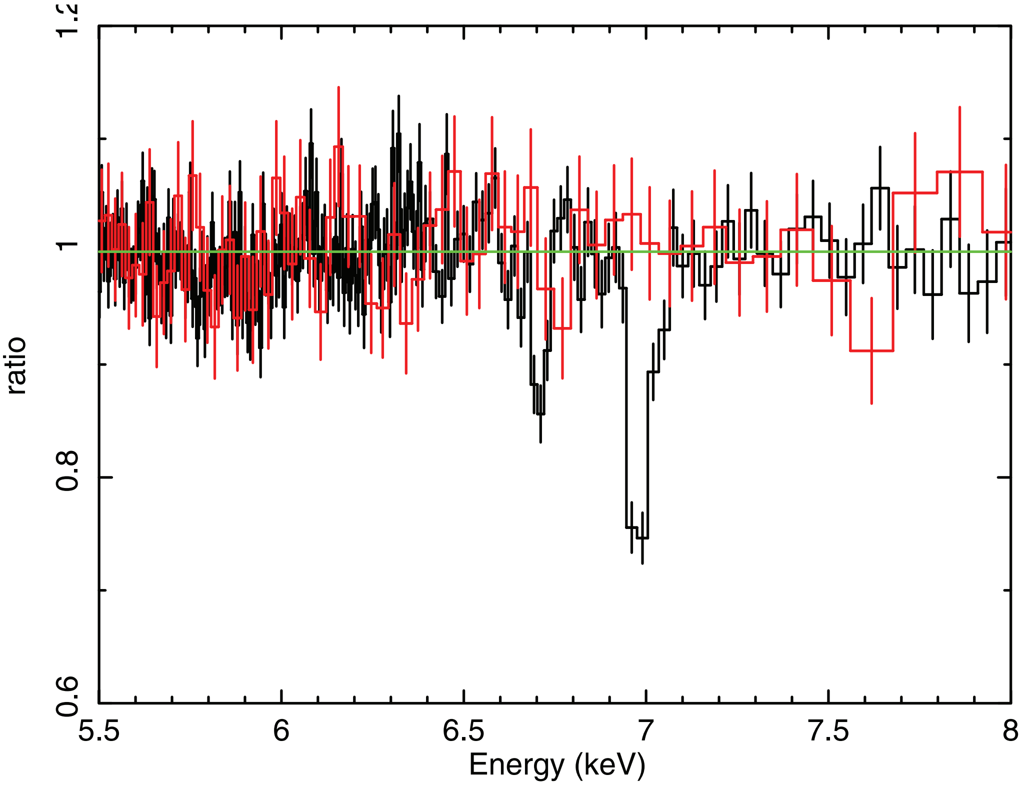

Figure 6.1: Line spectra from soft state (black) and hard state (red) *Chandra*/HETGS observations of H 1743-322 taken from Miller et al. (2012).

thermal winds are launched, so the wind will depend quite sensitively on size scale here. Given the uncertainties, we start first by calculating the wind produced by a disk with $R_{\rm disk} = R_{\rm IC}$, and then explore the effect of changing parameters.

6.2 Simulation setup

We define computational domain from $R_{\rm in} = 0.01R_{\rm out} \le R \le R_{\rm out}$, $0 \le \theta \le \pi/2$. We solve over $N_R = 120$ grid points in R and $N_\theta = 240$ grid points in θ. The radial grid is set with geometric spacing as

$$R_i = R_{\rm in}(R_{\rm out}/R_{\rm in})^{i/N_R},\ (0 \le i \le N_R) \tag{6.1}$$

In polar angular grid, We adopt an irradiated disk shape, where $H_{\rm d}/R \propto R^{2/7}$ (Cunningham 1976, as recast by Kimura & Done 2019) where

$$\begin{aligned} H_{\rm d}/R = 1.5\times10^{-3}\left(\frac{L}{L_{\rm Edd}}\right)^{1/7}\left(\frac{M_c}{M_\odot}\right)^{-1/7}\left(\frac{R_{\rm out}}{R_{\rm g}}\right)^{2/7}\left(\frac{R}{R_{\rm out}}\right)^{2/7} \\ = f_d\left(\frac{R}{R_{\rm out}}\right)^{2/7} \end{aligned} \tag{6.2}$$

In the simulation grid, we set angle of disk from mid-plane $\alpha_d(R) = \arctan\{H_d(R)/R - H_d(R_{\rm in})/R_{\rm in}\}$ in order to set $\alpha_d = 0$ $(\theta = \pi/2)$ at inner radius of computational domain $R_{\rm in}$. We set the polar angular grid in two sections, one to follow the scale height of the disk to resolve the irradiated launch region Eq.6.2 and one to sample the wind behavior of the rest of the domain with constant solid angle. We define these using the angle from the mid-plain $\alpha_j = \pi/2 - \theta_{{\rm N}_\theta - {\rm j}}, (0 \leq j \leq N_\theta)$

$$\alpha_j = \begin{cases} \arctan\left[f_d\left\{(R_{\rm j}/R_{\rm disk})^{2/7} - (R_{\rm in}/R_{\rm disk})^{2/7}\right\}\right], & (0 \leq j \leq N_R) \\ \arcsin\left\{\frac{1.0 - \sin(\alpha_{\rm N_R})}{N_\theta - N_R}(j - N_R) + \sin(\alpha_{\rm N_R})\right\}, & (N_R < j \leq N_\theta) \end{cases} \tag{6.3}$$

where $\theta_0 = 0, \theta_{{\rm N}_\theta} = \pi/2$. The disk surface is the top of Eq.6.3.

We apply the axially symmetric boundary at the rotational axis of the accretion disk, $\theta = 0$ so that ρ, p and v_r are symmetric, while v_θ and v_ϕ are antisymmetric). We apply a reflecting boundary at $\theta = \pi/2$ so that ρ, p, v_r and v_ϕ are symmetric, but v_θ is antisymmetric. Outflow boundary conditions are employed at the inner and outer radial boundaries, so that matter can freely leave but not enter the computational domain. In the disk zone and disk surface, we set $v_R = 0, v_\phi = v_k = \sqrt{GM_c/R}\sin\theta$ at each time step. We initially set temperature $T(R,\theta) = 1.1 \times 10^7 (R/6R_{\rm g})^{-3/4}$K, density $\rho_0(R,\theta) = 1.0 \times 10^{-33}$g cm^{-3} (except in the disk region), $v_R(R,\theta) = 0$, $v_\phi(R,\theta) = \sqrt{GM/R}\sin\theta$, and $v_\theta(R,\theta) = 0$.

6.3 Ionization state calculations

We focus first on the soft state of LMXB H 1743-322, where the absorption lines are detected, and show the SED from quasi-simultaneous RXTE PCA data (ObsIDs P95368-01-01-00) in Fig. 6.2a. taken from Shidatsu & Done (2019). We use this to calculate the heating and cooling rates and force multiplier from CLOUDY, assuming that the illuminated gas is optically thin. The calculation grid is an 301 × 121 logarithmically spaced grid (ξ, T) in a domain $1.0 \times 10^3 \leq T \leq 1.0 \times 10^9$ and $1.0 \times 10^{`3} \leq \xi \leq 1.0 \times 10^{12}$. Fig.6.2b shows the heating and cooling rates for material at a given temperature and pressure ionization parameter Ξ. This thermal equilibrium curve has a very complex shape, with four stable branches separated by regions of instability and/or rapid change (Fig.6.2b, with zoom in Fig.6.2c). This is very different to the single S shaped thermal equilibrium curve using in (Begelman et al., 1983), where there is a minimum pressure ionization parameter associated with the material on the hot branch, $\Xi_{\rm h,min}$ at the temperature $\sim \frac{1}{2}T_{\rm IC}$ which marks the bottom of the heated atmosphere, while the maximum pressure ionization parameter associated with material on the cold branch $\Xi_{\rm c,min}$, marks the

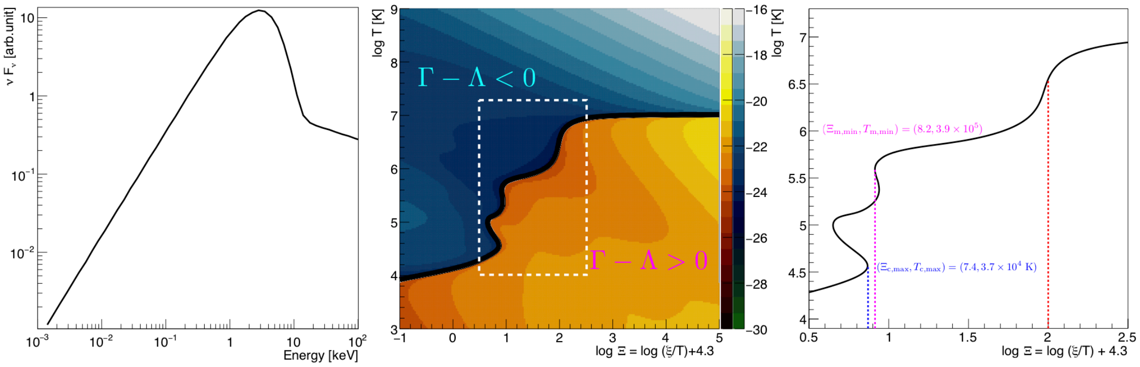

Figure 6.2: a) The energy flux of H 1743-322 which consists of a disk-blackbody plus Comptonized power-law (DISKBB+DISKBB*SIMPLE in XSPEC). b) The heating and cooling function ($\Gamma - \Lambda$). The black curve shows the thermal equilibrium ($\Gamma - \Lambda = 0$), the right colour bar shows the absolute logarithm value of heating minus cooling function ($\log|\Gamma - \Lambda|$). The Compton temperature of this spectrum is $T_{\rm IC} = 1.0 \times 10^7$ K. c)The zooming figure of b) surrounding by white dashed line. The vertical lines show the instability points. Red vertical lines is $\Xi_{\rm h,min} = 100$.

top of the disk. Instead, for this more complex shape, we take the minimum pressure ionization parameter of the long middle branch (associated with partially ionized Oxygen and Iron L shell) to mark the bottom of the heated atmosphere i.e. we set $\Xi_{\rm H,min} = \Xi_{\rm m,min} = 8.2$, where $T \ll T_{\rm IC}$.

Fig.6.3a shows this equilibrium curve in the standard ionization parameter representation. The $\Xi_{\rm m,min}$ point corresponds to material with $\xi = 170$, where the soft X-ray opacity is already substantial. The maximum pressure ionization parameter on the cold branch, $\Xi_{\rm c,max} \sim 7.4$ has standard $\xi \sim 14$ (see Fig.6.3a), so it is underneath layers with $14 \leq \xi \leq 170$. This material has very substantial opacity so it seems very unlikely that it can be irradiated directly by the source SED. Hence we assume the disk surface also has $\Xi_{\rm m,min}$ i.e. we set $\Xi_{\rm C,max} = \Xi_{\rm m,min}$. These are almost identical in Ξ (see Fig.6.2c), but quite different in ξ due to their very different temperatures. We use thermal equilibrium to set density at the disk surface to $\xi = 170$. At each time step, the density of disk surface is update via $n = L_x/(170R^2)$ and check that temperature is hotter than that of the viscous heated disk across the entire grid.

For comparison with observation, we calculate the ion density of Fe XXVI and Fe XXV from simulations via $n_{\rm XXVI} = n\ A_{\rm Fe} f_{\rm XXVI}(\xi, T)$ and $n_{\rm XXV} = n\ A_{\rm Fe} f_{\rm XXV}(\xi, T)$. We use these to define the ion column density along any line of sight, and to calculate the column density weighted mean velocity for each ion.

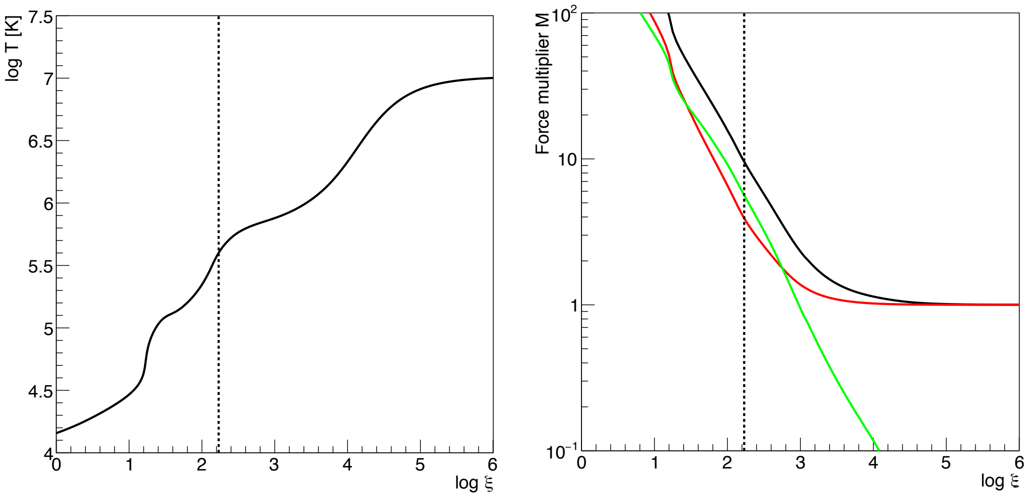

Figure 6.3: a)Thermal equilibrium curve of $\log \xi$vs$\log T$. b): Force multiplier of continuum process(bound-free plus scattering, red), line (green) and total (black) at the thermal equilibrium state. The vertical dashed line shows $\xi_{\rm H,min} = 1.7 \times 10^2$ which is the ionization parameter of disk surface.

6.4 Inner corona

The original thermal wind paper of Begelman et al. (1983) gives an overview of the structure of the Compton heated upper layers of the disk for optically thin material. In this limit, the heated material above the inner disk forms a static atmosphere with scale height $H_c/R \sim (v_{\rm IC}/v_g) = (T_{\rm IC}/T_g)^{1/2}$ where v_g (T_g) is the escape velocity (virial temperature). This gives $H_c \sim [2R^3/R_{\rm IC}]^{1/2}$. However, Begelman & McKee (1983) show that it is easy for this heated atmosphere to go optically thick in the radial direction along the disk plane, so it forms an inner attenuation zone, reaching

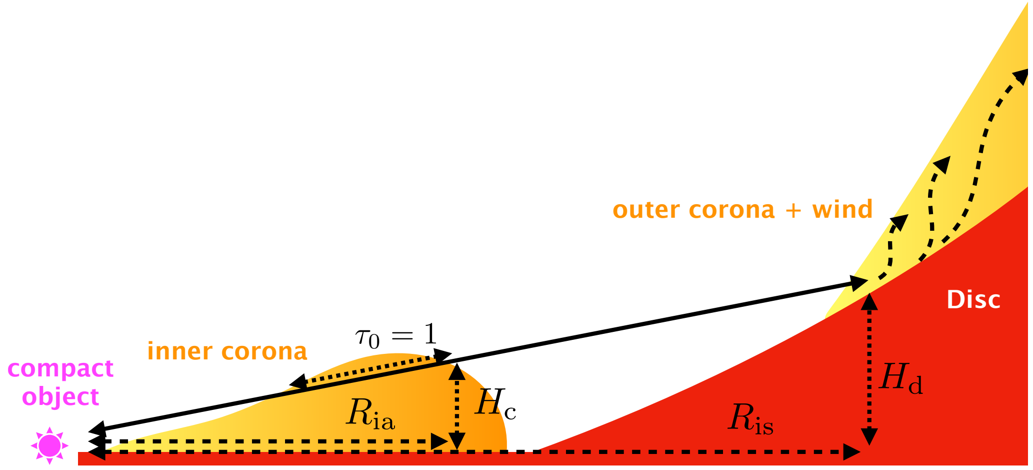

Figure 6.4: schematic view of geometry of our hydrodynamic simulation

$\tau_0 = 1$ at $R_{\rm ia}$ given by

$$\frac{R_{\rm ia}}{R_{\rm IC}} = 0.021 \Big[\frac{T_{\rm IC,8}(L/L_{\rm Edd})}{\Xi_{\rm H,min}}\Big]^{1/2} \tag{6.4}$$

For our soft state simulation this gives $R_{\rm ia} \sim 0.0004 R_{\rm IC} \sim 200 R_g$. This radius is on scales which are more than an order of magnitude smaller than the starting point of our radial grid, so this structure cannot be resolved by our simulation. However, it strongly affects the wind properties in the simulation range as it casts a shadow over the disk surface out to large radii (see Fig.6.4). The outer disk is only directly irradiated again when the disk scale height increases by a large enough factor that it rises above the shadow zone. For an irradiated disk with scale height given by equation 4, then the shadow cast by the inner attenuation zone ends at $R_{\rm is}$, where the disk is directly illuminated again. The geometry gives $H_d/R_{\rm is} = H_c/R_{\rm ia}$ so that

$$R_{\rm is} = 3.0 \times 10^7 \; T_{\rm IC,8}^{7/8} \; \left(\frac{M_c}{M_\odot}\right)^{1/2} \left(\frac{L}{L_{\rm Edd}}\right)^{3/8} \Xi_{\rm h,min}^{-7/8} R_{\rm g} \tag{6.5}$$

This gives $R_{\rm is} = 0.18 R_{\rm IC}$ for $L/L_{\rm Edd} = 0.3$ for our assumed system parameters with the soft state SED. We incorporate the sub-grid physics of this inner attenuating corona by changing the illumination pattern onto the disk in the outer regions which are covered by the hydrodynamic grid. We define a critical angle from the mid-plane $\alpha_c H_c/R_{\rm ia}$ and assume that the optical depth from the centre to any point on the disk surface has $\tau_0 = \exp[1-(\alpha/\alpha_c)^2]$ and use this to attenuate the X-ray luminosity by $e^{-\tau_0}$ before it enters the grid. When we implement this effect, we treat as

$$\alpha_c = \arctan[fd(R_{\rm is}/R_{\rm disk})^{2/7} - (R_{\rm in}/R_{\rm disk})^{2/7}] \tag{6.6}$$

6.5 Results for fiducial soft state spectral energy distribution

Table 6.1: The summary of simulations and inner corona parameters

SED[a]	$L/L_{\rm Edd}$	$F_{\rm rad}$	$T_{\rm IC}$ [10^8K]	$R_{\rm IC}/R_{\rm out}$	$H_{\rm out}/R_{\rm out}$	$\Xi_{\rm h,min}$	$R_{\rm ia}$ [$R_{\rm g}$]	$H_{\rm c}$ [$R_{\rm g}$]	$R_{\rm is}/R_{\rm out}$	$R_{\rm disk}/R_{\rm out}$	$\dot{M}_{\rm w}$ [10^{18} g s^{-1}]	$\dot{M}_{\rm w}/\dot{M}_{\rm a}^{b}$
S	0.3	Y	0.10	1	0.044	100	240	6.4	0.18	1.0	21	6.0
S	0.3	N	0.10	1	0.044	100	240	6.4	0.18	1.0	8.7	2.5
S	0.3	Y	0.10	1	0.044	100	240	6.4	0.18	0.18	1.2	0.34
S	0.5	Y	0.10	1	0.047	100	310	9.5	0.22	1.0	28	4.8
S	0.5	N	0.10	1	0.047	100	310	9.5	0.22	1.0	14	2.4
S	0.1	Y	0.10	1	0.038	100	140	2.8	0.12	1.0	1.8	1.5
S	0.3	Y	0.10	1	0.044	–	640	28	1.0	1.0	5.6	1.6
S	0.5	Y	0.10	1	0.047	–	730	34	1.0	1.0	7.9	1.3
H	0.06	N	0.70	0.14	0.035	3.3	220	22	11	1.0	0.43	0.61

[a] S:soft state, H:hard state

[b] $\dot{M}_a = L/(0.1c^2)$

We run a series of simulations as described below, with parameters and resulting mass-loss rates given in Tab.6.1. All simulations run for 9 sound crossing time ($c_{\rm IC}/R_{IC} = \sqrt{kT_{\rm IC}/(\mu m_p)}/R_{\rm IC}$). This corresponds to 1.7×10^5 s. The resultant column densities are plotted in Fig.6.5.

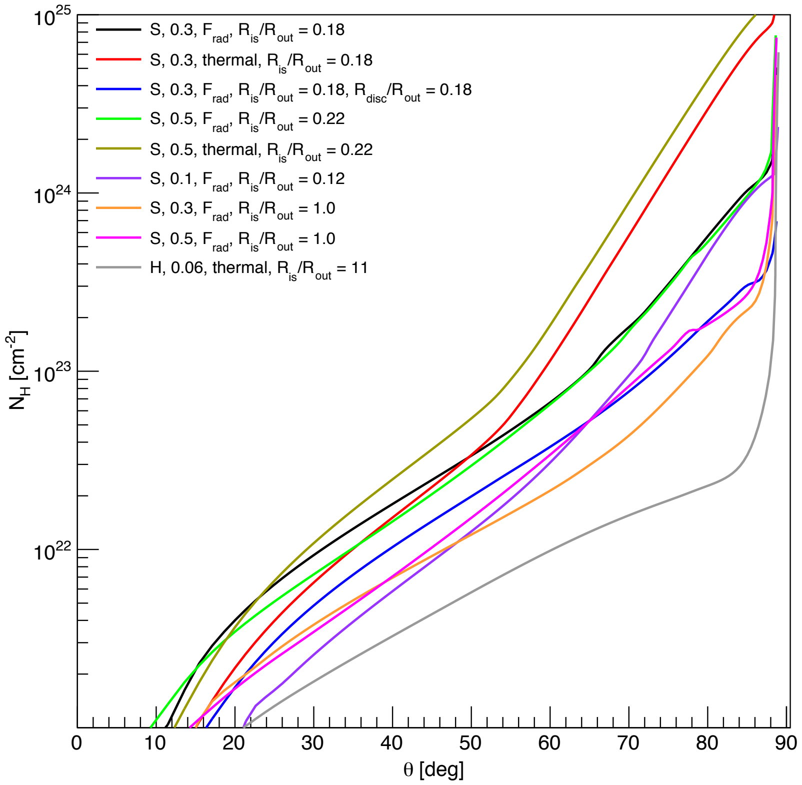

Figure 6.5: Hydrogen column density of all simulations in Tab.6.1.

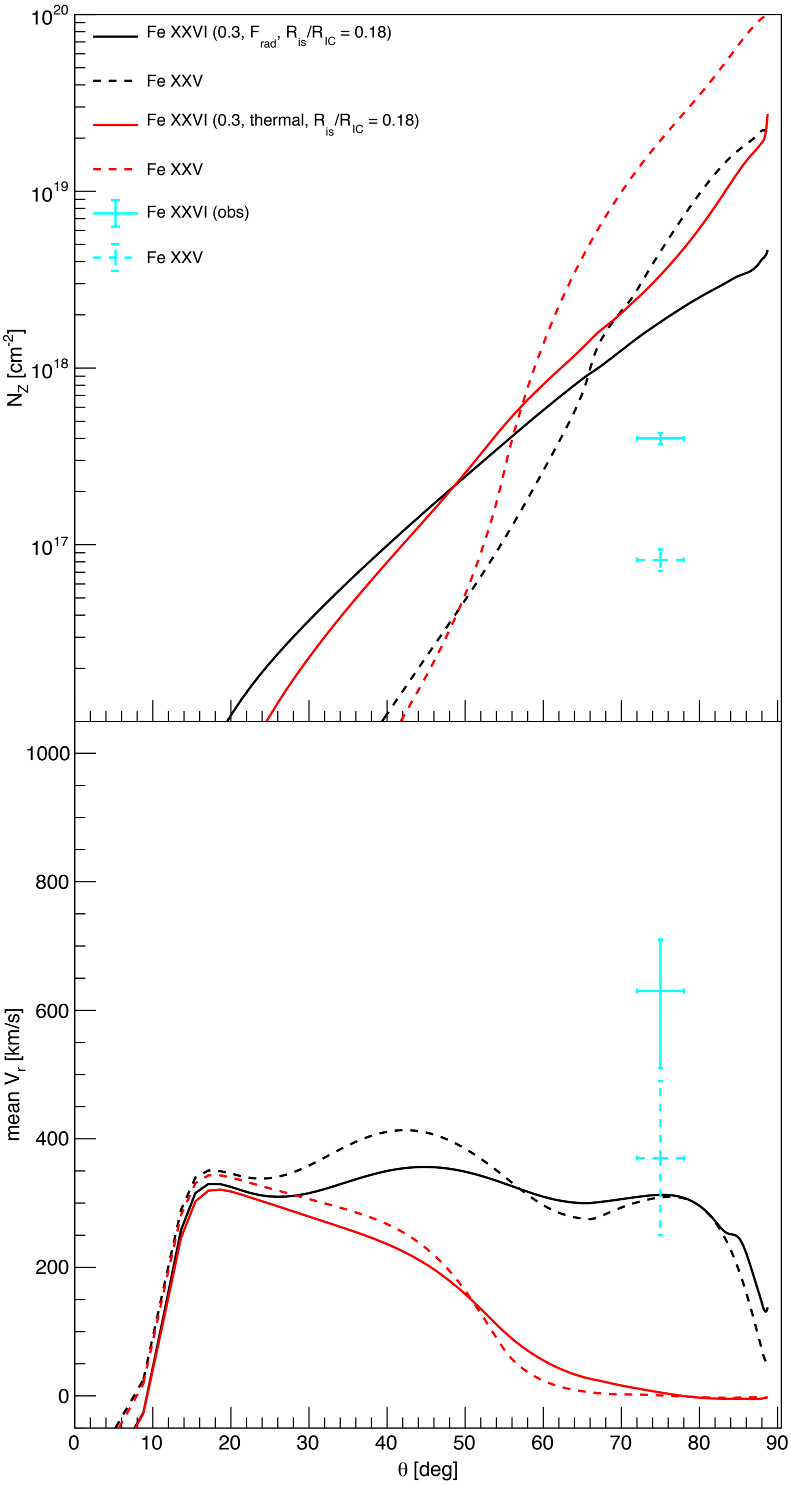

Figure 6.6: Top : the inclination dependence of column densities of Fe xxvi (solid line) and Fe xxv (dashed line). Bottom: the inclination dependence of column weighted mean velocities of Fe xxvi (solid line) and Fe xxv (dashed line). The colours show the thermal-radiative wind of $L/L_{\rm Edd} = 0.3$, $R_{\rm IS}/R_{\rm IC} = 0.18$(black) and the thermal wind (red).

6.5.1 Fiducial simulations: effect of radiation force

We first run a fiducial simulation, for the soft state SED in Fig.6.2, assuming $L/L_{\mathrm{Edd}} = 0.3$. We include all radiation force terms (electron scattering, bound-free and line), attenuation of these effects and fiducial inner corona defined by Eq.4.9. The derived density and temperature structure are shown in the Appendix (top left in Fig.6.7) and the total mass-loss rate through the outer boundary is 21×10^{18} g s^{-1} (see Table 1). The black lines in Fig.6.6 show the column density (upper panel) and velocity (lower panel) as a function of inclination angle for this simulation, with Fe xxvi as the solid line and Fe xxv as dashed.

We compare this to the results from a simulation where we turn off all the radiation force terms and their attenuation except inner corona ($M = 0$ in Eq.4.9), so that the wind only is thermally driven (top middle in Fig. 6.7 and red lines in Fig. 6.6). This simulation has much lower total mass-loss rate, of 8.7×10^{18} g s^{-1}, so it is clear that radiation force is important, and that this wind is better described as thermal-radiative rather than simply thermal. The thermal wind has a very low velocity at high inclination angles, close to the equatorial plane of the disk, so it has very large column density in these directions. Neither of these matches well to the observations at the inferred high inclination angle of H 1743-322 (shown by the cyan points).

Including the full radiation force terms gives a dramatic increase in velocity at large inclination angles. This is because this material close to the disk is mainly on the middle branch of the thermal equilibrium curve. At an ionization parameter close to $\xi \sim 170$, the corresponding temperature is substantially less than the Compton temperature, so the material forms a mainly static atmosphere rather than an outflowing corona (Higginbottom & Proga, 2015; Higginbottom et al., 2018). The presence of the middle branch of the S curve for this soft continuum spectrum gives the difference between these calculations and the earlier exploration of Proga & Kallman (2002), where they showed that the radiative force was negligible for a much harder continuum.

Instead, when radiation force is included, this warm, partially ionized material has enough opacity for bound-free and bound-bound opacity to accelerate it out so it can escape as a wind. This increases in velocity more than offsets the increased amount of material which escapes, so the column density decreases.

We investigate which term of the radiation force is most important at any ξ. Fig.6.3b shows force multiplier of the continuum process (red), lines process (green) and their sum (black) at thermal equilibrium state. Radiation force on free elections may have some impact on the simulations, but at our luminosity of only $0.3L_{\mathrm{Edd}}$, this alone is not enough to unbind much material. We run an additional simulation including only this term, and find a total mass-loss rate of 8×10^{18} g s^{-1}, so same within 10%. than the purely thermal wind. Fig.6.3b shows that the radiation force on lines and photo-electric opacities have similar magnitudes, and that adding all the terms together gives a force multiplier of around $M = 9.6$ at $\xi = 170$, thus the ratio of total radiation force to gravity is $M \times L/L_{\mathrm{Edd}} = 0.3 \times 9.6 > 1$. Neglecting line opacity but including electron scattering and bound-free gives a force multiplier of 3.6, so this is just enough to get to unbind the material when it is launched, but not enough to continue accelerating it once it becomes more ionized. We rerun a simulation including only electron scattering and bound-free opacities and find a mass-loss rate of 9.8×10^{18} g s^{-1}. Thus it is the combination of all opacity sources which is important at high but subcritical L/L_{Edd} values, and a single correction factor for L/L_{Edd} (as in Sec.3.2) is too simplistic to describe the behavior revealed.

6.5.2 Changing the disk size

Thermal winds depend most sensitively on the shape of the spectrum, the luminosity, and the size of the disk. The spectral shape is defined by observations, but the overall luminosity and disk size depend on the assumed system parameters which are poorly known. The analytic models give a dependence on $N_H \propto \log R_{\mathrm{disk}}/R_{\mathrm{in}}$ where $R_{\mathrm{in}} = 0.2R_{\mathrm{IC}}$ is the launch radius of the wind. However, the reduction in column required from the data is not simple to produce in the analytic approximation of (Done et al., 2018) as Fe XXVI should decrease by factor 5 but that of Fe XXV should decrease by 2 orders magnitude at 75°. However, we note that our disk size is already only $R_{\mathrm{disk}} = R_{\mathrm{IC}}$, and the analytic approximations probably become unreliable as we approach the wind launch radius.

Instead, we reduce the disk size to $R_{\mathrm{disk}} = 0.18R_{\mathrm{out}}$, which is the same radius as inner shadow radius as well as the wind launch radius, then we re-run the simulation including full radiation force. We run the simulation over the same grid as before, but set a very low density at mid-plain ($\theta = 90°$) when the radius is larger than the disk radius. The blue line in Fig. 6.9 shows the results of this simulation. We can reproduce the ion columns seen in the data, and in particular we now have a higher column of Fe XXVI than Fe XXV, indicating a higher ionization state for the wind. The wind is launched, but only just. The mass-loss rate is 20 times smaller than that of fiducial simulation, so the density of the wind is quite low. It is still slightly overshadowed, so the disk is not fully illuminated by the central source, but the drop in overall mass accretion rate reduces the density sufficiently for the ionization parameter to be higher than before. This means that the contribution of line and

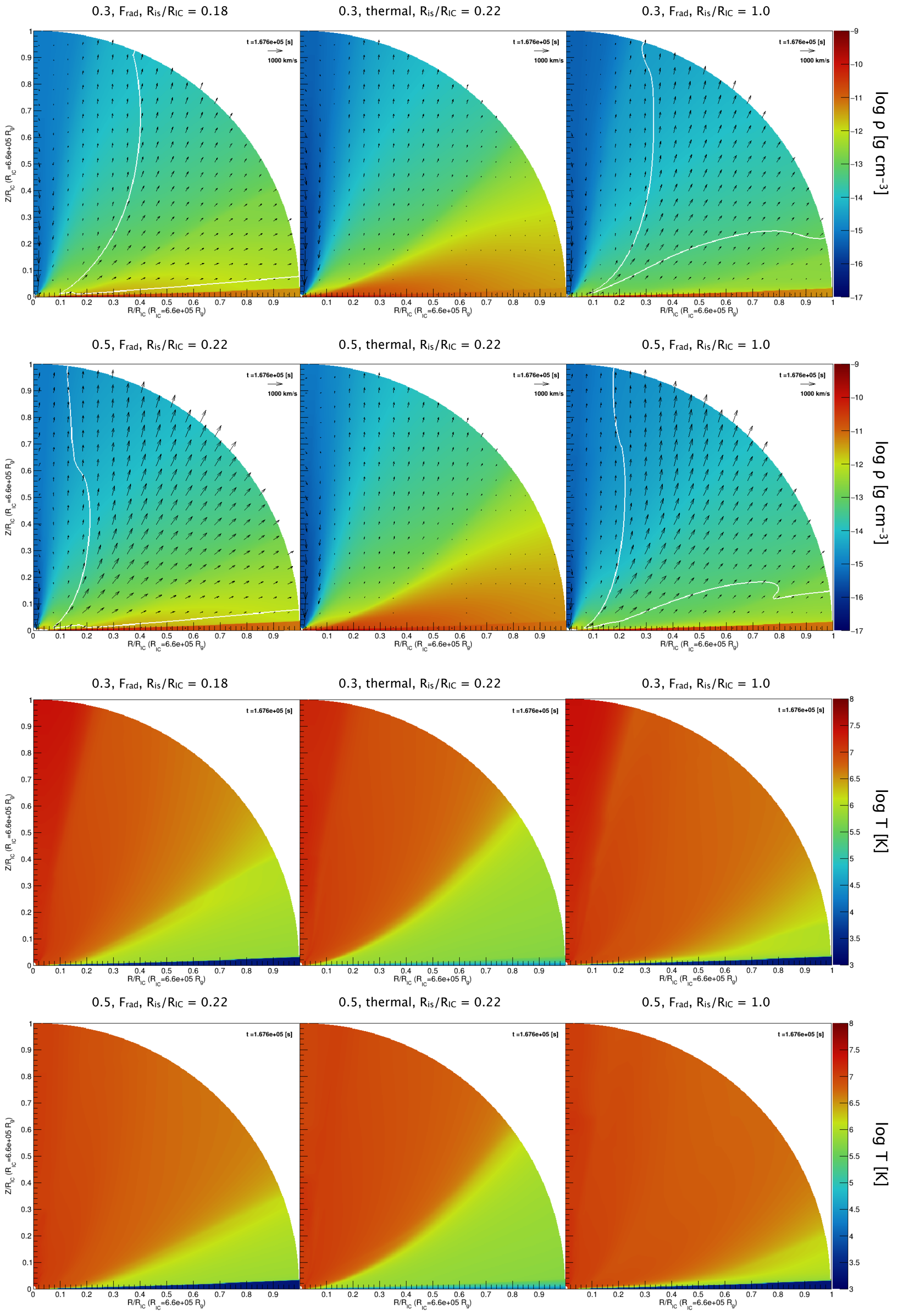

Figure 6.7: Distributions of density (top) and temperature (bottom), the solid white lines show Mach 1 surface of radial velocity and black arrows show velocity.

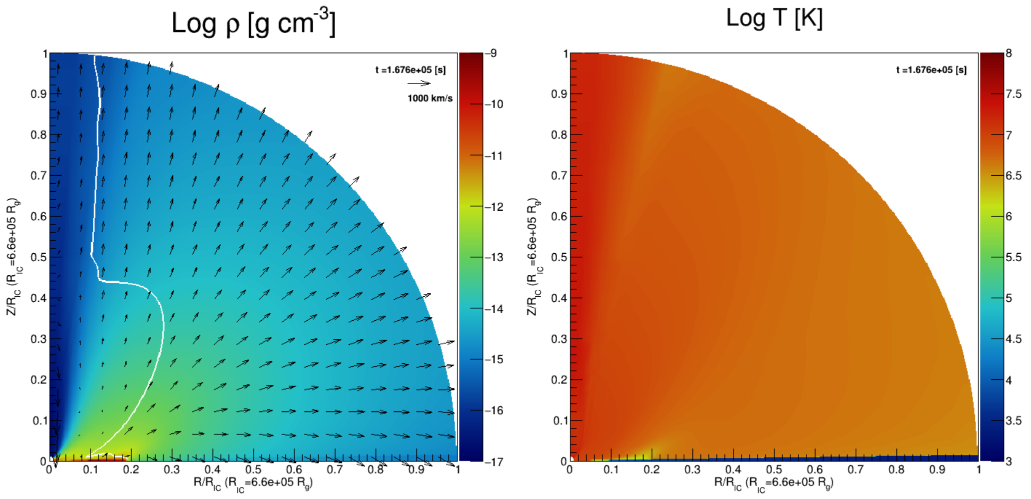

Figure 6.8: The distribution of density (left) and temperature (right) of small disk simulation.

photo-electric absorption to the driving is almost negligible. This wind is driven by the combination of radiation force on electrons and gas pressure gradient force, and its velocity matches well to that measured in the data.

We explore the effect of some of the other parameters input into the fiducial simulation below in order to illustrate their impact on the predicted wind, but this is our best match overall to the observed data.

6.5.3 Changing luminosity:$L/L_{\mathrm{Edd}} = 0.5$ and 0.1

We now consider the effect of changing luminosity. We run an additional set of simulations with $L/L_{\mathrm{Edd}} = 0.5$ for the same SED. This changes the radius of inner attenuation zone and the outer disk scale height, so that the shadow extends to $R_{\mathrm{is}} = 0.22 R_{\mathrm{out}}$. Fig. 6.10 shows the resultant column density (upper) and velocity (lower) for this simulation including all radiation forces (green) compared to a purely thermal wind at the same luminosity (yellow). The purely thermal results are very similar to those at $L/L_{\mathrm{Edd}} = 0.3$, with very low velocity at high inclination angles, and consequently large column density. This material is again mainly on the middle branch of the ionization instability, so it does not have high enough temperature to escape. However, including radiation force on this material makes even more difference at these higher luminosities, so the column is lower and the velocity higher than for $L/L_{\mathrm{Edd}} = 0.3$, bringing the models closer to the observed data points (cyan).

We also run a simulation including all radiation force terms with the same SED but $L/L_{\mathrm{Edd}} = 0.1$. Fig.6.11 shows the column and velocity from this (violet) compared to $L/L_{\mathrm{Edd}} = 0.3$ (black) and 0.5 (green) including all radiation force terms.

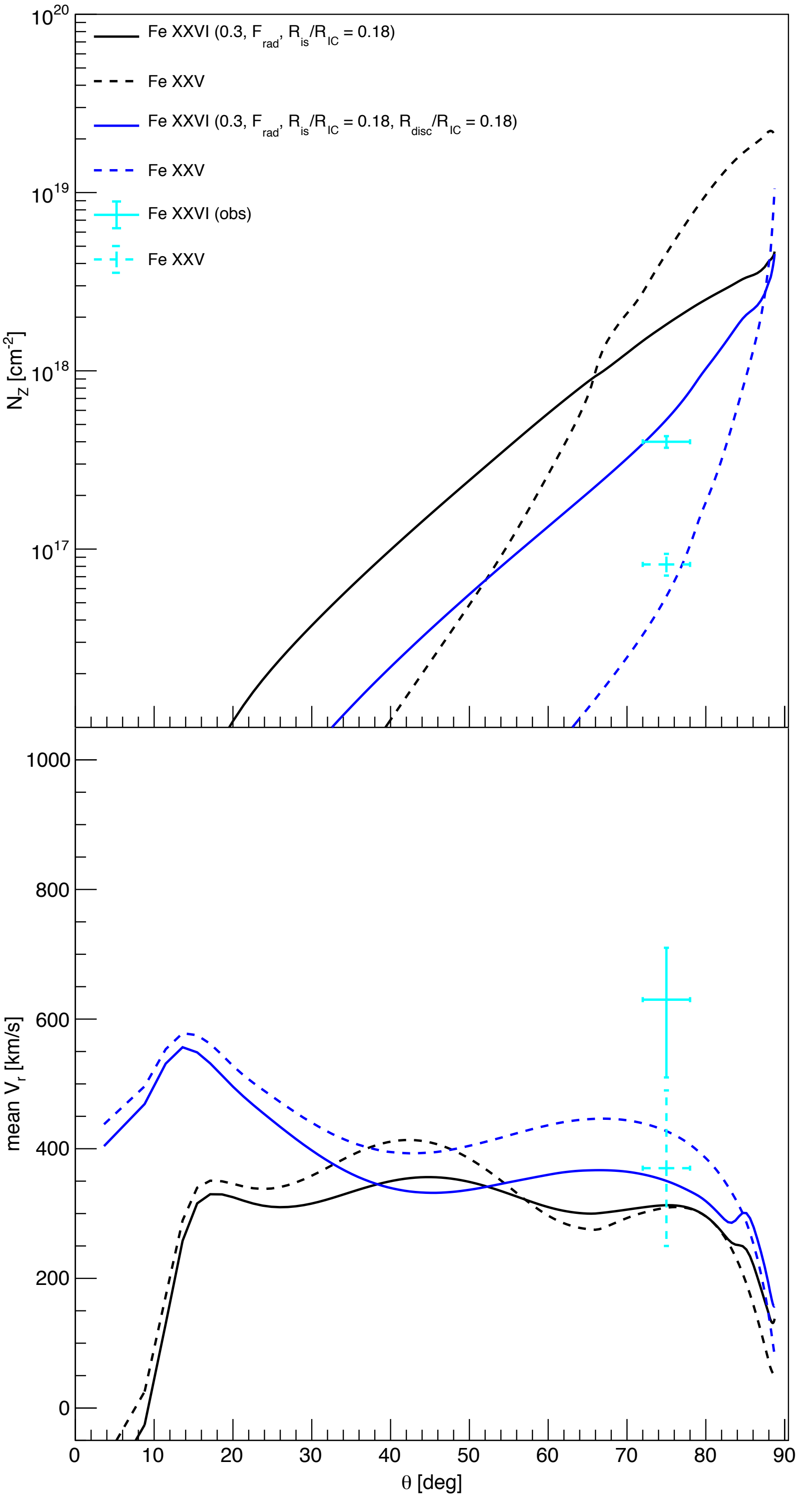

Figure 6.9: As in Fig. 6.6 but $R_{\rm disk}/R_{\rm IC} = 1.0$ (black) and 0.18 (blue).

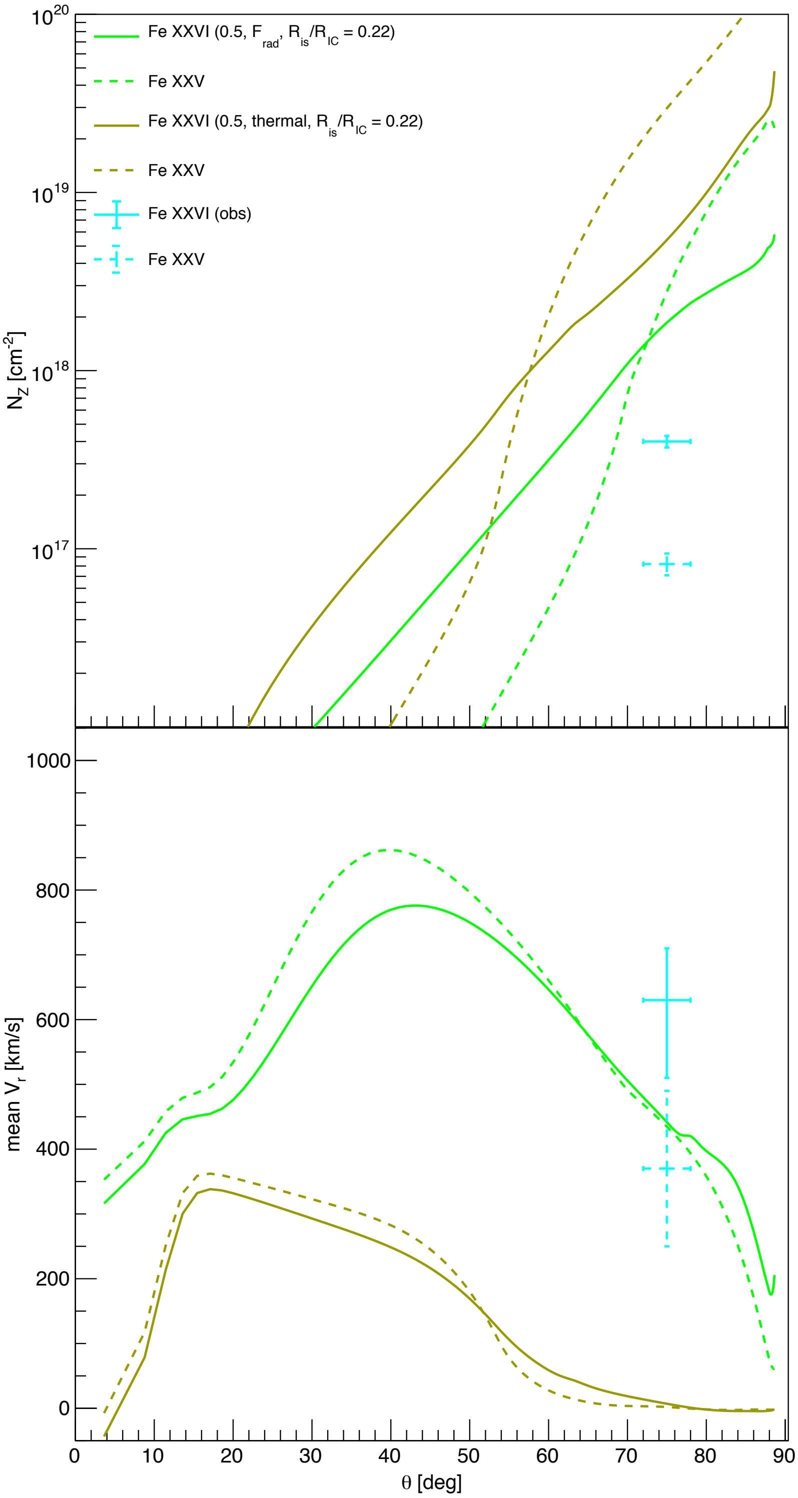

Figure 6.10: As Fig.6.6 but for $L = 0.5L_{\mathrm{Ldd}}$.

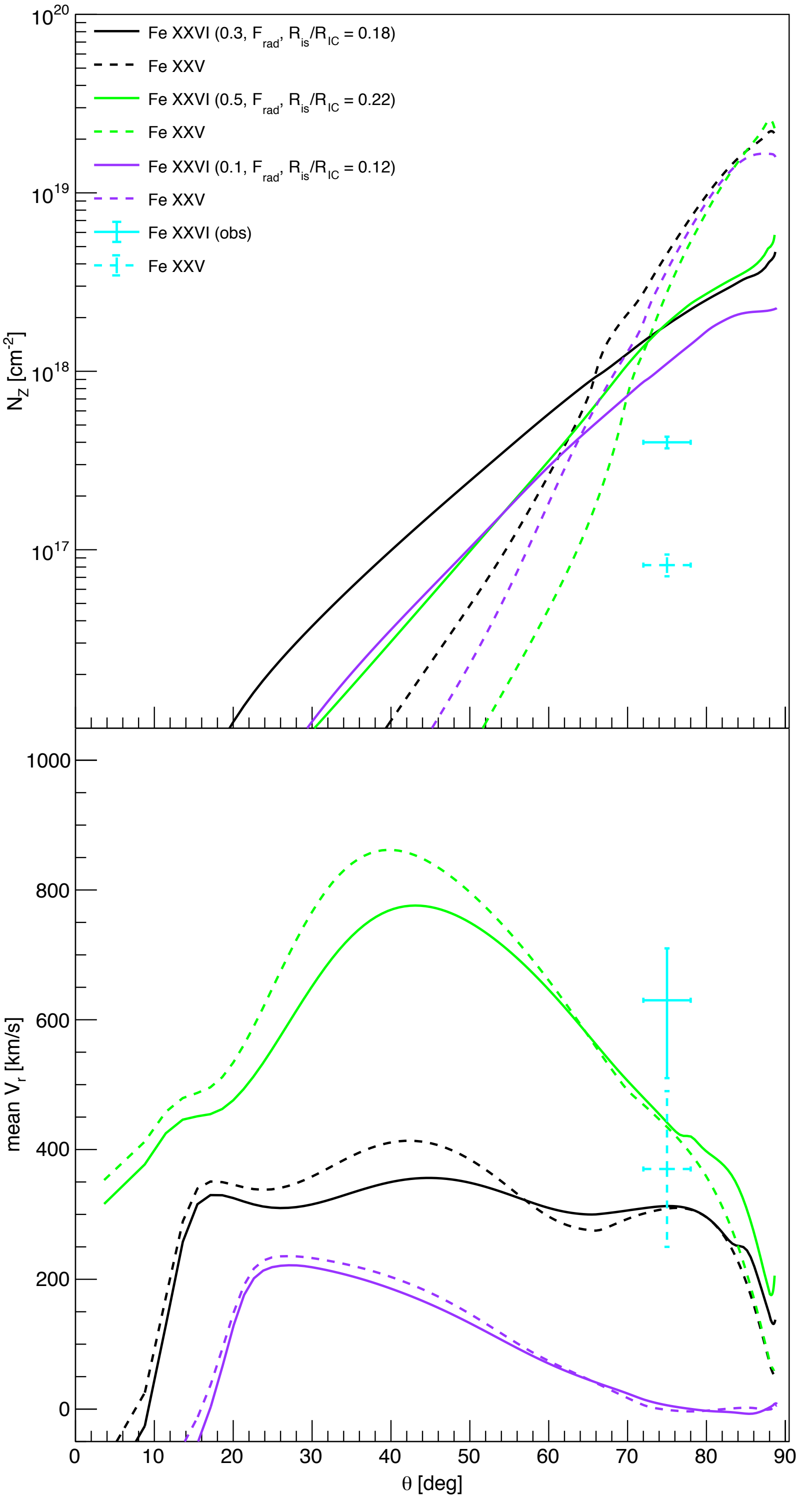

Figure 6.11: As in Fig.6.6 but for $L/L_{\rm Edd} = 0.1$ (violet), 0.3 (black), 0.5 (green)

The column densities in each ion are remarkably similar, but the velocity increases dramatically at high inclination angles, and the total mass-loss rate increases from 1.8 to 21 to 28 $\times 10^{18}$ g s^{-1}.

Fig.6.11 clearly shows that thermal-radiative winds are fast enough to match the observations for $L/L_{\rm Edd} \gtrsim 0.3$, but that these luminosities give columns which are a factor of 3–10 larger than observed. There are multiple ways we can reduce the wind efficiency. As we already indicated in Sec.6.5.2, the first is by reducing the size or height of the outer disk (the system parameters are quite uncertain, and the disk scale height needs not exactly follow the irradiated disk shape (see e.g. Kimura & Done 2019)), the second is by changing the irradiation pattern as a function of angle. Section 3.3 assumed a very simple exponential attenuation with angle produced by the inner corona. Density structure in the inner corona could give slightly stronger attenuation of both the disk and X-ray source at large inclination angles, or the different radiation pattern of the flat disk and more isotropic X-ray source could give different spectral illumination of the disk surface compared to that observed.

6.5.4 Changing the extent of the shadow from the inner attenuation zone

We quantify the ideas above by simply reduce the illumination of the outer disk by changing the shadow size to $R_{\rm is}/R_{\rm IC} = 1.0$ on each of the simulations for $L/L_{\rm Edd} = 0.3$ and 0.5, including full radiation force.

The lines in black and orange in Fig. 6.12 show the effect of this for $L/L_{\rm Edd} = 0.3$, while the lines in green and magenta show this for $L/L_{\rm Edd} = 0.5$. The extended shadow means that the illuminating flux is lower for the given simulation, which means that the wind mass-loss rate is lower (Done et al., 2018). However, the velocity remains mainly unchanged, as once the wind rises up it sees the same radiation force as before. Hence this makes the column lower, whilst maintaining the fast velocity, giving a better match to the data (cyan).

A changing radiation pattern from the flat disk and more isotropic X-ray source would have a similar effect in reducing the illumination of the disk surface, but keeping the full radiation force on the wind once it rises up, though this is more complex to model as the Compton temperature would also change as a function of height.

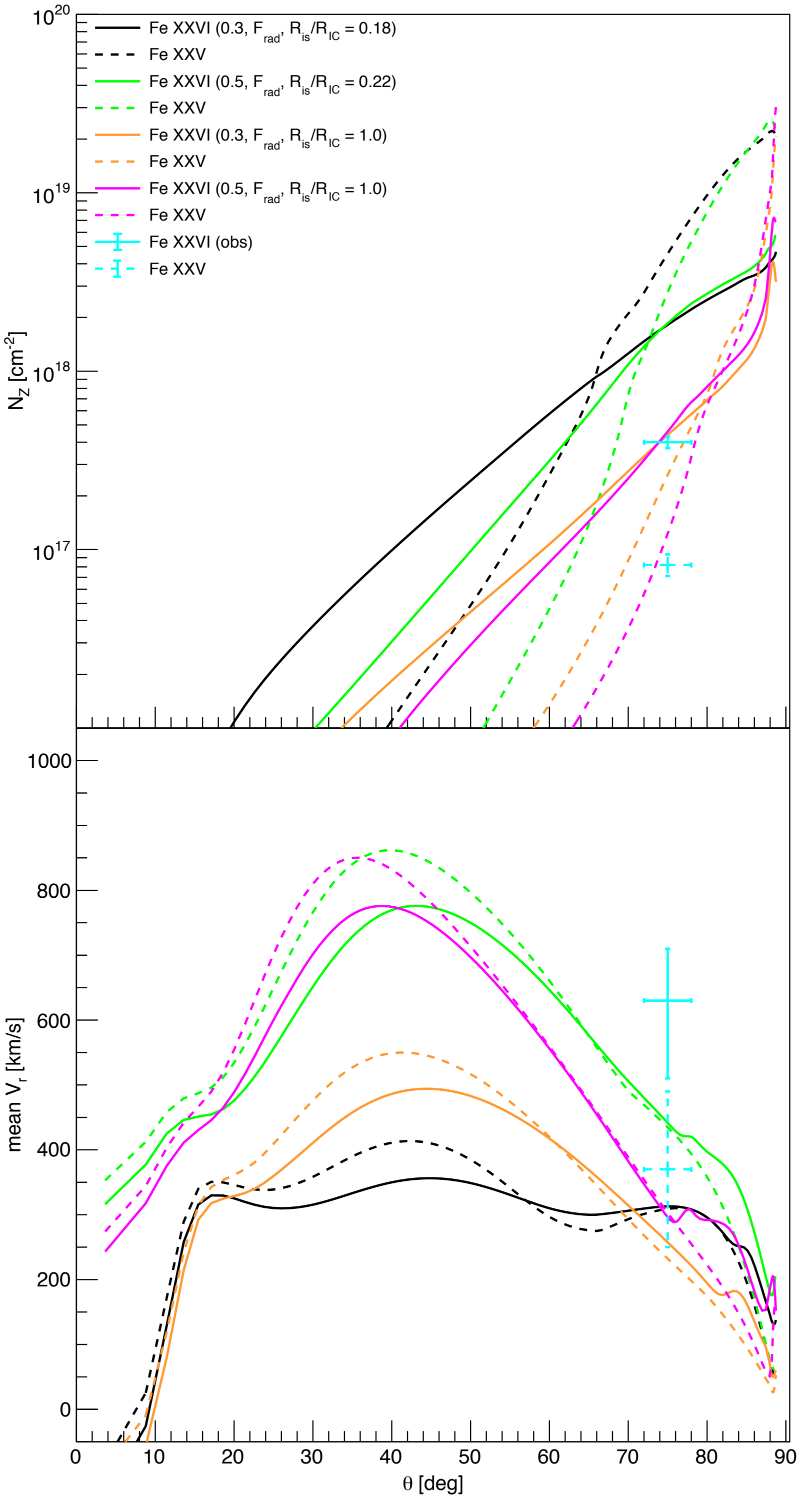

Figure 6.12: As in Fig.6.6 but for $L/L_{\rm Edd} = 0.3,\ R_{\rm IS}/R_{\rm IC} = 0.18$ (black), $L/L_{\rm Edd} = 0.5,\ R_{\rm IS}/R_{\rm IC} = 0.22$ (green), $L/L_{\rm Edd} = 0.3,\ R_{\rm IS}/R_{\rm IC} = 1.0$ (orange), and $L/L_{\rm Edd} = 0.5,\ R_{\rm IS}/R_{\rm IC} = 1.0$ (magenta).

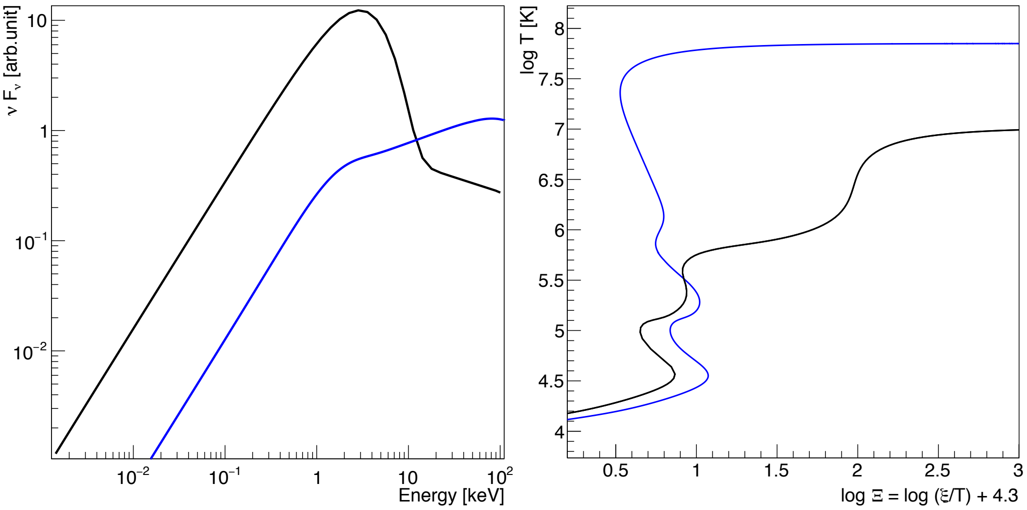

Figure 6.13: a) Spectra of soft state(black) and hard state (blue). b) The thermal equilibrium curves. colours correspond to input spectra of a) .

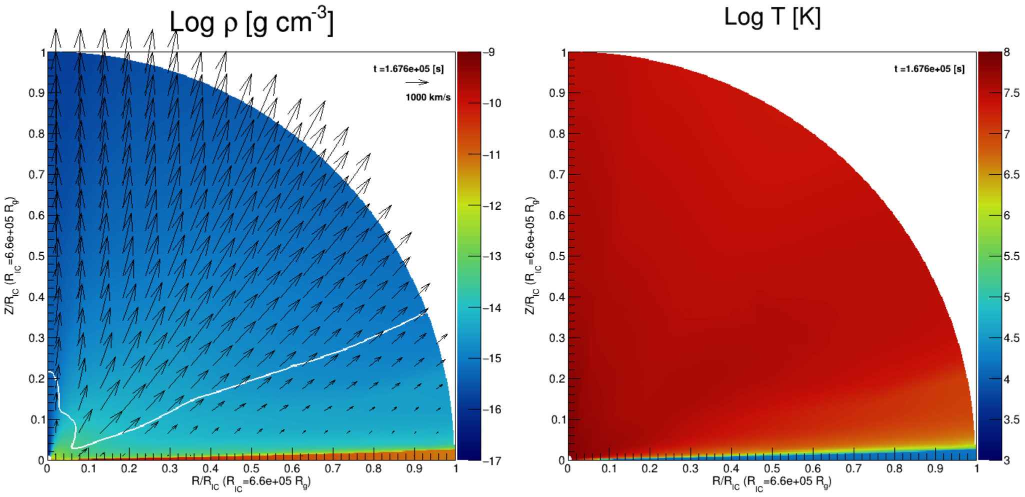

Figure 6.14: The distribution of density (left) and temperature (right) of hard state

6.6 Result for the hard state spectral energy distribution

We now consider the predicted wind properties in the hard spectral state. The blue line in Fig. 6.13a shows the observed SED after the switch to the hard state. This has a much higher Compton temperature than the soft state (black), and the thermal equilibrium curve is now closer to the classic S curve of Begelman et al. (1983). The luminosity is fairly low, but the high Compton temperature means that the thermal wind can be launched from closer to the black hole than in the soft state, so it can be more highly ionized (see Sec.3.2). However, the key new aspect in this work is the realisation that the inner attenuation zone also responds to the changing SED.

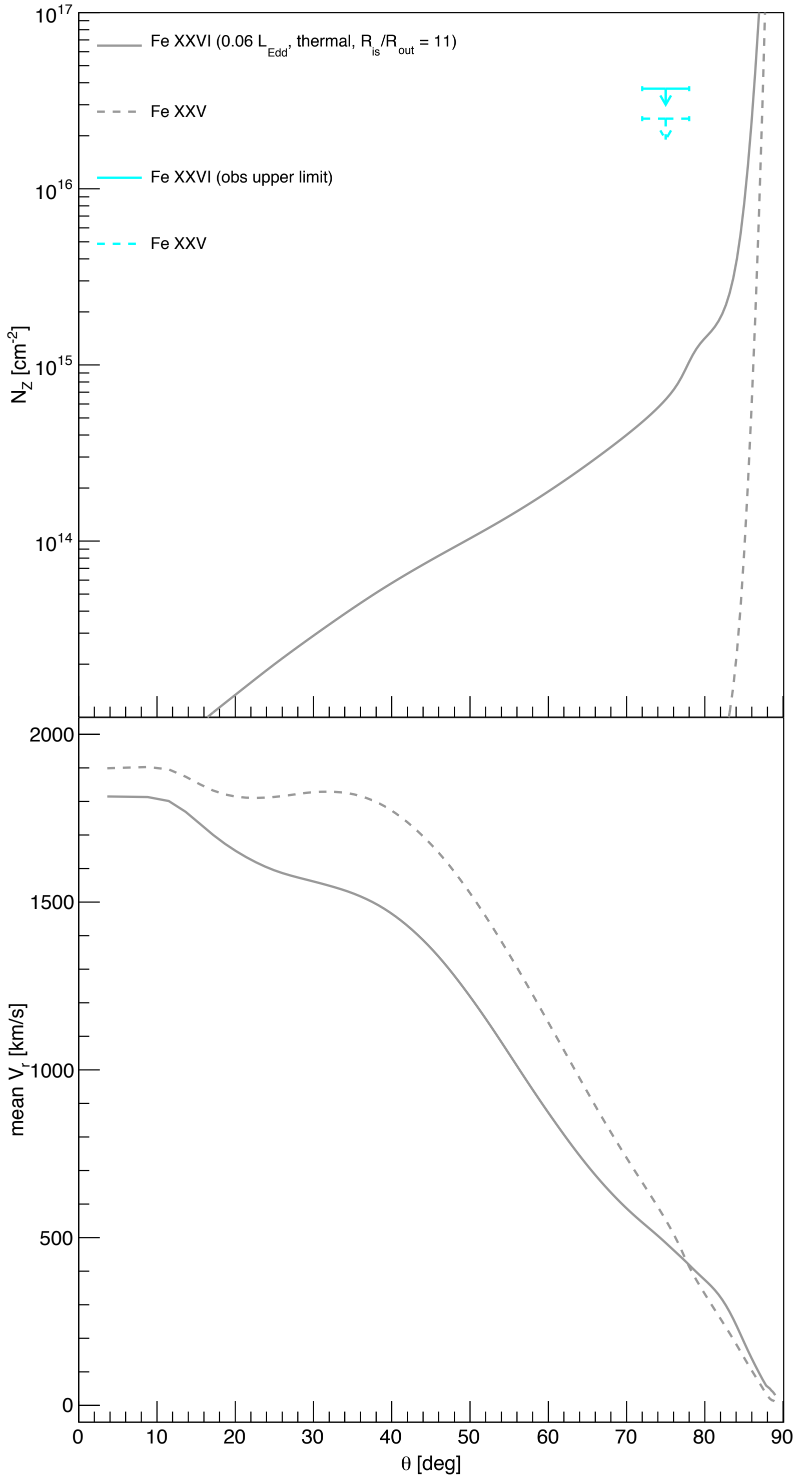

Figure 6.15: The angular dependence of column densities Fe xxvi (black solid line), Fe xxv (black dashed line) and those of column weighted velocities (bottom) of hard state. Cyan shows the observational upper limit calculated from Miller et al. (2012)

The higher Compton temperature means that this has higher scale height, so it now casts a deep shadow over the entire outer disk, with $R_{\rm is} = 11R_{\rm out}$. This completely suppresses the thermal wind unless the hard X-ray source has scale height which is larger than the inner attenuation zone $H_{\rm c} \sim 20R_{\rm g}$. The response of the wind to the changing SED is not then simply due to the wind being launched from closer in, and being more highly ionized, as suggested by Sec. 3.2. Instead, here there is no thermal wind since the outer disk is not irradiated. The inner attenuation zone responds to the changing SED, increasing in scale height and hence increasing the shadow cast over the disk.

We run a final simulation for this hard state to confirm that the wind is suppressed sufficiently to match with the observational data. We use the hard state spectrum to calculate a new set of heating and cooling rates. These define the disk surface at $\Xi_{\rm c,max} = 12$, $T_{\rm c,max} = 3.5 \times 10^4$K, which gives the $\xi_{\rm c,max} = 22$ from thermal equilibrium curve (blue line in Fig.6.13b). Thus, we set the density at the disk surface as $n = L_x/(22R^2)$ at each time step and the grid size is the same as that of soft state. We include the illumination attenuation from the inner corona but do not include line force as this is entirely negligible for highly ionized, very optically thin material.

Fig. 6.15 shows that the predicted iron columns are more than a factor of 10 lower than the observational upper limits (the density and temperature structure are Fig. 6.14), so our thermal wind simulation can indeed explain the disappearance of the wind in the hard state. This is because of over ionization by the hard X-ray and large size of inner corona. In the hard state, when the thermal instability once occurs, the temperature rapidly heats up to the Compton temperature $T_{\rm IC} = 7.0 \times 10^7$K (Fig. 6.14). This rapid rise gives strong gas pressure gradient force, so the velocity is larger than that of soft state (Fig.6.15b). The large velocity leads the low density if we consider mass continuity, and also the large inner corona suppresses the wind density.

However, there is still a wind, and the mass-loss rate is over half of the mass accretion rate. We can understand this result by using the analytic estimates in Sec.3.2. These show that the critical luminosity, where the Compton heating is sufficient to produce a wind from $R_{\rm IC}$, is $L_{\rm crit} \sim 0.04$. This is below the observed luminosity of $L_{\rm bol} = 0.06\ L_{\rm Edd}$, but the attenuation by the inner corona means that the flux illuminating the inner edge of the hydrodynamic grid is a factor 10 lower. Thus $L/L_{\rm crit} \sim 0.1$, but the disk is large compared to $R_{\rm IC}$ ($R_{\rm out}/R_{\rm IC} = 7.0$), so the wind is still quite effective (see cyan line in Fig.3.4). Thermal winds have a large impact on the mass available for the outburst for systems with a large disk, explored in more detail in Dubus et al (2019, in prep).

6.7 Discussion

We have shown results from the first RHD simulations of a thermal-radiative wind. Including the radiation force gives important differences to the structure of the thermal wind for $L > 0.1L_{\rm Edd}$ (Sec.6.5.1 ,6.5.3). We include electron scattering, bound-free absorption and line opacity as these all give corrections which are of similar order, and all of them together act to produce a force multiplier which is large enough for these sub-Eddington flows to become super-Eddington. Thermal winds alone are too slow to match to the observed winds (see also Higginbottom et al. 2018), but these thermal-radiative winds can produce both the column density and velocity of the material seen in the soft state of H1743-322.

We identify the key role played by the inner static corona, on size scales of a few hundred $R_{\rm g}$ (Sec.6.5.4,). This material is part of the Compton heated atmosphere of the disk, but is on size scales much less than $R_{\rm IC}$ so it is bound, and has $H \ll R$. Nonetheless, it is important in determining the illumination of the outer disk where the wind arises. It is very easy for this corona to become optically thick in the equatorial plane, so that it shadows much of the outer disk from the inner disk emission. This material is below our grid scale, so we incorporate it analytically following BM83. The scale height of the inner corona casts a shadow which prevents direct illumination of the outer disk until it rises out of this shaded zone because of the intrinsically concave (saucer-like) shape of the disk. The small scale height of the inner attenuating corona in the soft state means that the outer disk is directly illuminated in the soft state. Conversely, the much larger scale height of the inner corona in the hard state completely shadows the entire disk, so the wind is suppressed. This contrasts with the explanation in Done et al. (2018) where the thermal wind is still present in the hard state, but is less visible due to its higher ionization which is a consequence of its smaller launch radius (Sec.6.6). Reality may be a mixture of the two, as the structure of the hard X-ray source itself is changing during the transition. The inner disk evaporates into an X-ray hot flow whose scale height probably increases as the source dims. Evidence for this is that the electron temperature increases as shown by Motta et al. (2010), which can be modelled by an expanding hot flow region (Gardner & Done, 2014; Kara et al., 2019; Marcel et al., 2018b). The disk only starts further out, so the inner shadow corona starts further out, and the larger scale height of the X-rays means that some fraction can directly illuminate the outer disk as they extend above the shadow corona. A change in illumination pattern should have observable consequences on the optical continuum as well as on the X-ray wind properties. In bright BHB the optical continuum is generally due to reprocessing of X-rays in the outer disk, showing that the outer disk is illuminated (van Paradijs, 1996). This reprocessed optical emission can be seen directly in broadband spectra in the soft state (Hynes et al., 2002; Kimura & Done, 2019), and especially in fast variability, where the optical emission is variable on timescales of $\sim 1-20$ s, lagged behind but correlated with the X-rays (O'Brien et al., 2002). The hard state is more complex, but close to the spectral transition there are still clear signatures that part of the optical emission is produced by reprocessing in the outer disk (Hynes et al. 2009; Veledina et al. 2017 for Swift J1753, though this reprocessing signal disappears as the source dims:Veledina et al. 2017). Simultaneous fast optical and X-ray variability data can directly measure the changing irradiation pattern on the disk and test these models of an inner attenuation zone.

The inner corona can also have an impact on the soft state spectrum. The shadow affects the corona structure when it becomes optically thick along the disk direction, but this is also associated with a vertical optical depth which is ~ 0.05. Thus 5% of the inner disk flux is scattered rather than being directly produced in the disk photosphere, and so at this level, it is clear that the disk emission should differ from even the best pure disk photosphere calculation such as those of Davis et al. (2005); Davis & Hubeny (2006). This high ionization state layer on top of the disk will also change the reflected coronal flux from the disk, with around 5% of the corona flux being scattered from this much higher ionization state layer than from the disk itself.

Chapter 7

Iron line prediction from thermal-radiative winds in H 1743-322

In previous chapter, we show the best current simulations of the absorption and emission features predicted from thermal-radiative winds produced from X-ray illumination of the outer accretion disk in binary systems. In this chapter, we use the density and velocity structure derived from a RHD simulation as input to a MCRT.

7.1 Monte-Carlo radiation transfer

We show the simulation in Sec. 6.5 which is most consistent with the overall wind properties seen in the *Chandra*/HETGS. We use the density and velocity results of this RHD simulation (Fig. 7.1) as input to the MCRT code MONACO (Odaka et al., 2011). We rebin these via bi-linear interpolation to reduce the simulation grid from $(N_r, N_\theta) = (120, 240)$ to $(60, 120)$ and only include the region of $\theta = 30 - 88^\circ$ i.e. removing the low density polar region and the high density disk region. We explicitly include azimuth, so the total grids we use are 60 (radial) and 51 (polar) and 32 (azimuth).

MONACO also requires the distribution of ion populations and temperature in addition to density and velocity. We obtain these more accurately than is possible in the more approximate approach of the RHD by solving the one dimensional radiation transfer along line of sight using CLOUDY. We chain CLOUDY radially through the density structure and use the output spectrum of inner grid as the input spectrum to the next grid. The initial source spectrum is the same as that used to make the RHD simulation i.e. is the spectrum of H1743-322 in its soft state at the time of

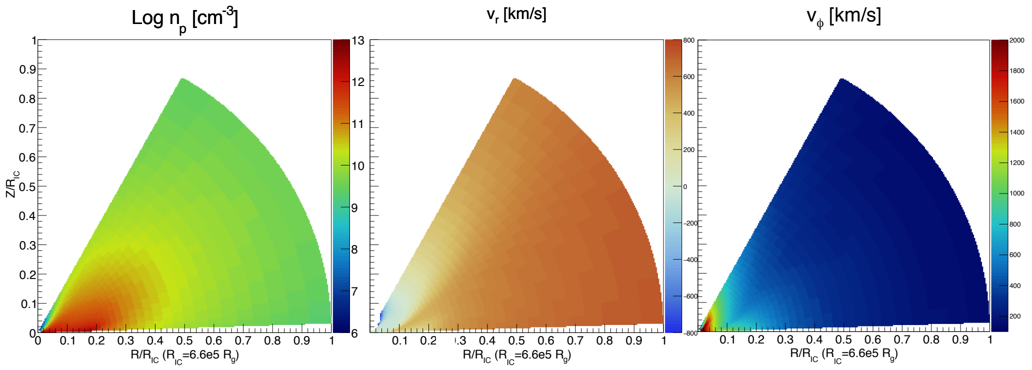

Figure 7.1: Distribution of the density (left), outflow velocity (middle), and rotation velocity (right). The dark blue region of outflow velocity map means negative velocity.

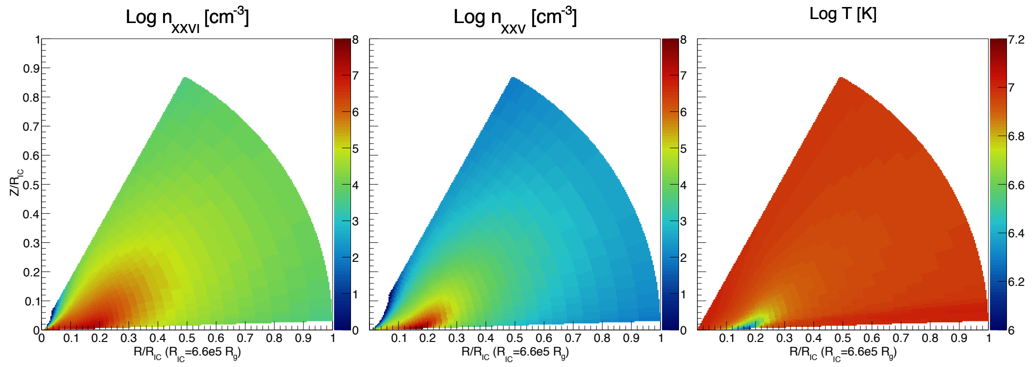

Figure 7.2: Distributions of ion density Fe xxvi (left), Fe xxv (middle) and temperature (right) calculated by CLOUDY

the *Chandra* grating observation of Miller et al. (2006).

Fig. 7.2 shows the resulting distribution of the density of Fe xxvi, Fe xxv (left, middle) and temperature (right). The density of both H and He-like Fe is highest near to the mid-plane because this is where the wind density is highest (see Fig.7.1. H-like iron is produced interior to He-like iron as it is formed at a higher ionization parameter. The temperature in most of the wind region is the Compton temperature ($T_{\rm IC} = 0.1 \times 10^8$K), except for the highest density region near to the disk surface.

We generate photons isotropically from the center over the energy range 6.5 − 8.5 keV with 1 eV resolution (2000 bins). The total number of input photons is 1.4×10^8. MONACO tracks all the interactions of these photons from their creation to eventual escape.

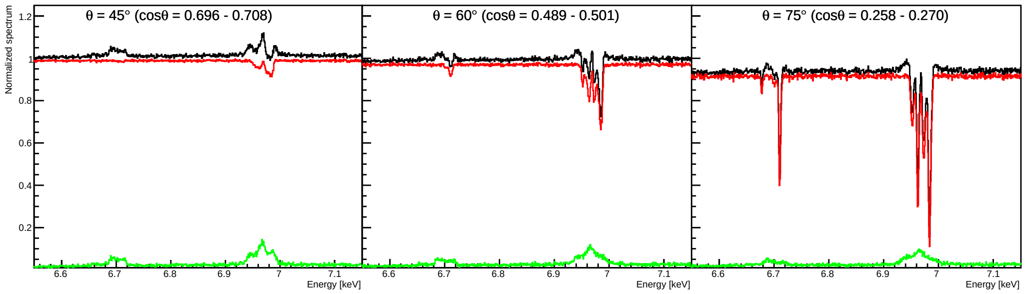

Figure 7.3: The results using the density/velocity structure from the hydrodynamic simulations (i.e. no additional turbulent velocity). Each panel shows the calculated spectra (black) seen at inclination of $45°, 60°$ and $75°$, normalised by the incident spectrum. The transmitted (red) and scattered (green) components are also shown.

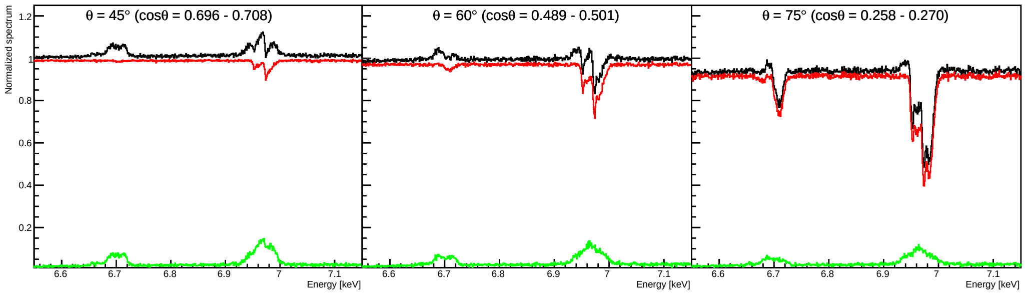

Figure 7.4: As in Fig.7.3 but including additional saturated turbulent velocity ($v_{\rm turb} = v_R$)

7.2 Iron line Emission and Absorption line Profiles

We first simulate the spectrum exactly as predicted by the radiative hydrodynamic model. While this is the best calculation of the wind structure to date, there are still some 3D effects which it does not include, such as warping of the disk from radiation pressure and tidal forces (Schandl & Meyer, 1994; Ogilvie & Dubus, 2001), and the impact of the accretion stream onto the disk and wind (Smak, 1970; Armitage & Livio, 1998). These processes could result in additional velocity components, which could develop into a fully turbulent flow, characterised by $v_{\rm turb} = v_R$, so we show a second simulation including isotropic turbulence at this level. The only impact of this turbulence is to give additional Doppler broadening to the emission and absorption lines.

Fig. 7.3 (without turbulence) and 7.4 (with turbulence) show the resulting spectra at three difference inclination angles. In both models, the absorption lines increase strongly with inclination angle as the line of sight intercepts more of the

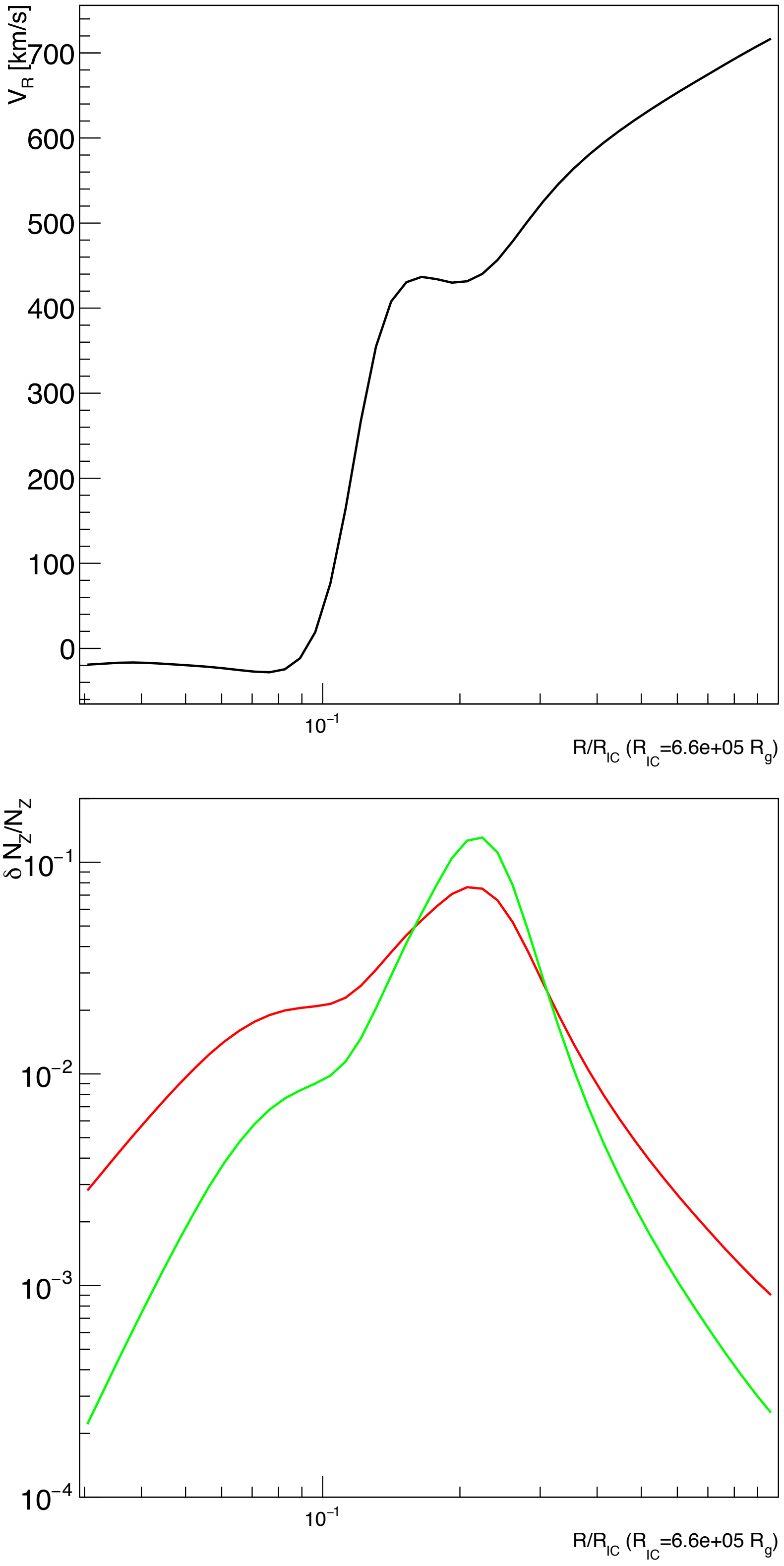

Figure 7.5: The radial profile of velocity (top) and ratios of local ion column density to that of total at $i = 75°$ (bottom). Colours show Fe xxvi (red) and Fe xxv (green), respectively,

higher density material close to the disk plane, whereas the scattered component (sum of continuum plus the emission lines) is almost constant with inclination angle. Hence the emission lines are more prominent at low inclination angles as they are not filled in by the absorption.

The model without turbulence shows that there are separate velocity components to the absorption lines at high inclinations. Fig. 7.5 shows the velocity structure along a line of sight at 75°, together with the ion columns in He- and H-like iron. The velocity plot clearly shows that there is static/inflowing material at small radii, at high ionization state. There is then a rapid acceleration zone from $R = 0.1 - 0.2\ R_{\rm IC}$ as the thermal-radiative wind starts to be launched. The wind is most efficiently launched at radii $\geq 0.2\ R_{\rm IC}$ so the wind mass-loss rate rises towards larger radii, but its velocity also rises so the ion columns remain mostly constant in this region. The columns start to rise again as the velocity accelerates past 200 km/s and towards a plateau at 400 km/s, and the increase in density means a decrease in ionization state, increasing the contribution from Fe xxv. Edge effects then come into play as the outer disk radius is reached at $R_{\rm out} = 0.2\ R_{\rm IC}$ for this simulation. The wind runs out of new material, so there is no back pressure from the wind outside of this point. The streamlines splay outwards, giving a fast drop in density, and hence a fast decrease in ion columns and increase in ionization state (Fig.7.5b). Thus the major part of both He- and H-like iron absorption arises from $\sim 0.2\ R_{\rm IC}$, where the material has a fairly constant velocity of around 400 km/s, with an additional column of predominantly H-like Fe in the acceleration zone. This explains the two sets of narrow Fe xxvi doublet lines seen in Fig. 7.3c.

Our assumption for the fully turbulent solution is that $v_{\rm turb} = v_R$, so the turbulent velocity follows the radial outflow velocity structure. This smears out some of the obvious velocity substructure, but the acceleration zone has lower turbulent broadening so is still distinct in the simulation.

We show the equivalent width (EW) of the H- and He-like absorption lines at each angle in Fig. 7.6. We measure these following Tomaru et al. (2018) by fitting the total spectrum (black lines in Fig. 7.4) by an arbitrary function aE^2+bE+c (a, b and c are free parameters), excluding the line regions, then numerically integrate the difference between this continuum and the simulation data. EWs for the model including turbulence are larger at the highest inclination angles as the lines in the initial simulation are saturated. The maximum Fe xxvi EW is around ~ 30 eV (with turbulence) compared to ~ 20 eV (without). There is also emission from the wind, but the EW of these features is very small.

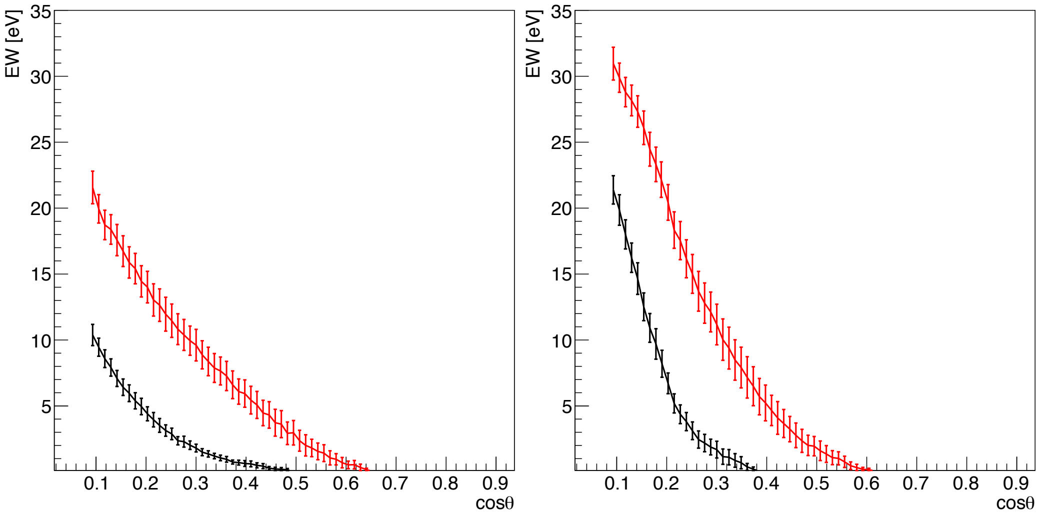

Figure 7.6: The angular dependence of equivalent width Fe xxvi (Lyα_1: 6.953 keV + Lyα_2: 6.973 keV, red) and Fe xxv (Heα y: 6.668 keV + Heα w: 6.700 keV, black) with $v_{\rm turb} = 0$ (left) and $v_{\rm turb} = v_R$ (left). Error bars are calculated from Poisson noise.

7.3 Fitting to current and future high resolution data

7.3.1 *Chandra*/HETGS

We now take the MONACO results both without and with turbulence and fit them to the *Chandra*/HETGS first order data of the soft state in H1743-322 (OBSID:3803). We use HEG first order data because the HEG has twice the spectral resolution as the MEG. Free parameters in these fits are inclination angle and normalization (We implement these models into XSPEC as tabulated additive model). Both models can fit the observational data equally well (Fig. 7.7) for inclination angles of 78° (with turbulence) or 81° (without). This could indicate a marginal preference for turbulence as the expected angle from the binary parameters is 75 ± 3° (Steiner et al., 2012), but the difference is small and the difference in χ^2 is more to do with the line equivalent width (which could be changed easily by changing the disk size and/or source luminosity: Paper I) than with the intrinsic width.

To really resolve the line profiles such as the velocity separation of static corona and the outflowing wind and understand whether or not turbulence is present requires higher resolution than possible in *Chandra* grating data. Hence we now consider whether the X-ray micro calorimeters on-board future X-ray satellites such as *XRISM* can better distinguish the intrinsic velocity structure.

7.3.2 Simulated *XRISM*/Resolve observations

We simulate a *XRISM*/Resolve observation from the simulation models which give the best fit to the *Chandra*/HETGS data. The Resolve calorimeter gives 5 eV energy resolution at 6 keV in its best modes (High plus Medium resolution events, hereafter H+M). However, this energy resolution is produced by modelling the pulse height shape to determine the total energy of the event. This is done by template matching to the fast rise, exponential decay shape, and the energy in the event can be accurately reconstructed if no other event arrives in the 30 millisecond period covered by the template. Where events overlap, the energy cannot be reconstructed so accurately (Low resolution events). With higher sampling rate it might be possible to determine the pulse shape more accurately for these piled-up events, but the on-board computer power is limited and can only handle template matching for a maximum 50 c/s. Above this limit, Low resolution events give a degraded resolution of around 30 eV at iron (comparable to *Chandra*/HETGS first order data).

The *XRISM*/Resolve detector is split into four quadrants, with counts from each quadrant handled separately, so the maximum count rate is 200 c/s, which corresponds to around 100 mCrab source for an on-axis point source. Sources with higher predicted count rates will need mitigation strategies for the observations to reduce the count rates to these levels, using a combination of filters and/or offsets. These effects can be seen in the Hitomi/SXS observation of the Crab. This was performed with the gate valve closed, which cuts out all flux below 2 keV and reduces the higher energy count rate by a factor 2 compared to a standard observation. These SXS data did indeed show a $\sim$ 50 c/s/quadrant limit (Hitomi collaboration 2017)

We simulated the soft spectrum of H1743-322 from a continuum model determined from the quasi-simultaneous RXTE data corresponding to the *Chandra*/HETGS data (OBSID:3803). This has 2-10 keV of 1.7×10^{-8} ergs cm $^{-2}$ s $^{-1}$, or around 1 Crab, and predicted 0.3-2 keV flux of 2.3×10^{-9} ergs cm^{-2} s^{-1} using an assumed column density of 1.6×10^{22} cm^{-2} (Shidatsu & Done, 2019). This results in 1000 c/s, clearly outside of the scope of the electronics, so we consider mitigation strategies.

The Beryllium filter is designed especially to reduce the low energy flux so as to leave as many counts as possible in the higher energy bandpass. However, interstellar absorption in our Galaxy produces a similar effect. It makes only a 20% reduction in the count rate of H1743-322, though all the counts lost are soft. The effect is similar to a neutral column density of 2.5×10^{22} cm^{-2}, so this will not have much effect for more absorbed bright Galactic sources. The ratio of flux in the iron line band (6.5-7.5 keV) to the full band (0.3-10 keV) is $\sim$ 1/40 without the Be filter, and $\sim$ 1/33 with the Be filter. A combination of the Be filter and an offset pointing,

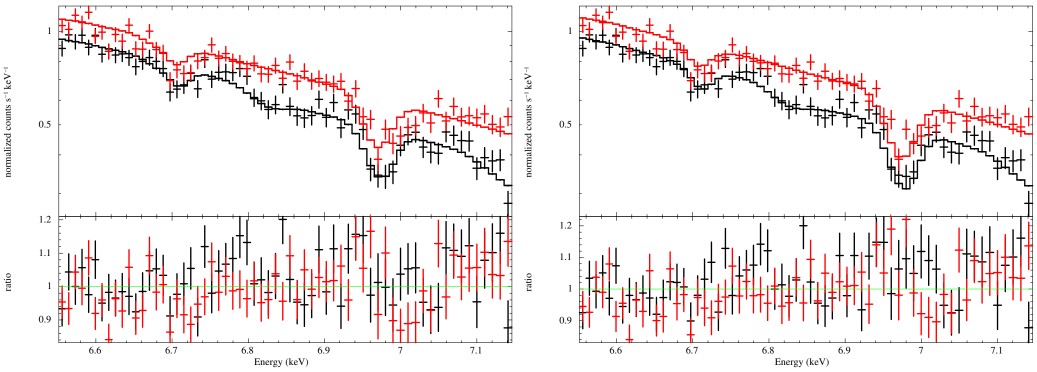

Figure 7.7: *Chandra*/HETGS data with best fit model of $v_{\rm turb} = 0$ (left) and $v_{\rm turb} = v_R$ (right). Best fit inclination angle is 81° and 78° respectively. The data is taken from HEG +1 (Black) and -1 (red).

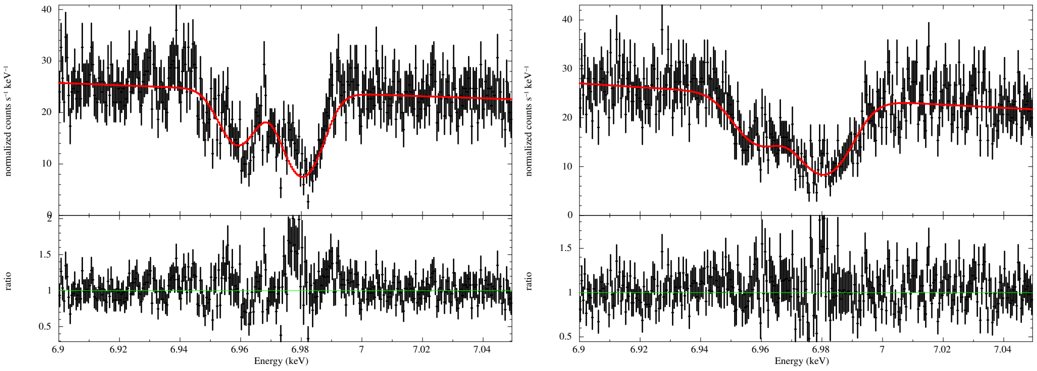

Figure 7.8: Simulated spectrum of a 30ks *XRISM* observation (live time fraction of 0.1) for the model with no additional turbulence (left), and $v_{\rm turb} = v_R$ (right) around the Fe XXVI Kα doublet line energy. The absorption is modelled using a single KABS component (red). The lower panel shows the residuals as a ratio between the data and model at each energy. Clearly Resolve can determine the velocity structure in the lines even at these low velocities.

so that the image is centred on one quadrant rather than illuminating all quadrants equally, may completely saturate one quadrant, but allow events from the other 3 quadrants to be close to the maximum, giving H+M events. The total H+M high resolution events could then be up to 150 c/s, though 100 c/s is a more reasonable expectation factoring in potential losses from cross-talk.

Alternatively, there is a neutral density filter which reduces flux at all energies by a factor 4. This would reduce our predicted count-rate to ~ 250 c/s not far from the electronics limit of ~ 200 c/s.

Hence we expect a maximum count rate of 100-200 c/s for the H+M resolution data from our initial spectrum which has 1000 c/s. We conservatively assume a factor 10 loss, so we simulate a 3 ks *XRISM*/Resolve exposure as corresponding to

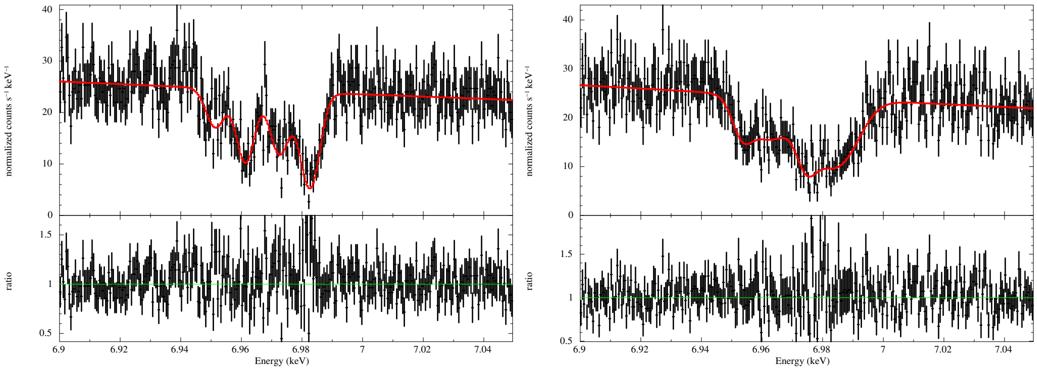

Figure 7.9: As Fig. 7.8 but fitted by double KABS model

Table 7.1: Single KABS fits to the simulated XRISM Resolve data

	$v_{\rm turb} = 0$	$v_{\rm turb} = v_R$
$N_{\rm XXVI}$ (10^{18} cm^{-2})	0.55 ± 0.04	0.67 ± 0.05
kT (keV)	30^{+6}_{-5}	59^{11}_{-10}
$z \times 10^{-3}$	-1.04 ± 0.08	-1.1 ± 0.1
χ^2/ν	350/294	326/294

a 30 ks observation. Fig. 7.8 shows the resulting energy spectrum and its statistical uncertainties around the Fe XXVI iron line band for the model without turbulence and then one with turbulence. We fit both spectra with a single KABS component (Ueda et al. 2004, including corrections from Kubota et al. 2007). This model includes the full Voigt line profile for both components of the doublet (Kα_1 and Kα_2, with ratio fixed to that expected from atomic physics). The free parameters are the column density of the ion, the isotropic turbulent velocity, in terms of the equivalent temperature, kT keV, and any red or blue shift indicating bulk inflow/outflow. The lower panel shows the residuals to this fit, with parameters detailed in Table 7.1.

There are clear residuals in the pure hydrodynamic simulations results. We

Table 7.2: Double KABS fits to the simulated XRISM Resolve data

	$v_{\rm turb} = 0$	$v_{\rm turb} = v_R$
$N_{1,\rm XXVI}$ (10^{18} cm^{-2})	$0.46^{+0.14}_{-0.06}$	$0.49^{+0.11}_{0.18}$
kT_1 (keV)	$3.4^{+2.3}_{-1.8}$	43 ± 22
$z_1 \times 10^{-3}$	-1.35 ± 0.05	$-1.5^{+0.3}_{-0.4}$
$N_{2,\rm\ XXVI}$ (10^{18} cm^{-2})	0.18 ± 0.03	$0.17^{0.17}_{-0.09}$
kT_2 (keV)	$4.4^{+5.7}_{-3.1}$	$5.4 \pm^{+11}_{-5.0}$
$z_2 \times 10^{-3}$	$0.08^{+0.09}_{-0.11}$	$-0.2^{+0.1}_{-0.2}$
χ^2/ν	261/291	308/291

include a second KABS component and the fit is very significantly improved, with $\Delta\chi^2 = 90$ for 3 additional free parameters. There is a smaller but still significant improvement for the turbulent wind, with $\Delta\chi^2 = 20$, with all parameters of the two components shown in Table 7.2. This shows that *XRISM* can resolve the infall/outflow velocity structure expected even in the fairly weak thermal-radiative wind modelled here, and even in the presence of fully developed turbulence.

7.4 Discussion: distinguishing between thermal-radiative and magnetic winds

The *XRISM* simulations shown here can clearly resolve the line produced in this thermal-radiative simulation into two velocity substructures, one which is static (or slightly infalling) from the X-ray heated disk atmosphere at small radii where the material does not have enough thermal energy to escape, and the outflowing wind at larger radii. This can be seen even in the presence of saturated turbulence. Conversely, current models of magnetically driven winds (e.g.Fukumura et al. 2010; Chakravorty et al. 2016) which assume self-similar magnetic fields from the entire disk launch winds at all radii, with velocity decreasing going outwards. These models do not predict that there can be static material anywhere, least of all at radii smaller than where the outflow is produced. However, this static material in the thermal-radiative winds can only be seen if there is substantial column in Fe XXVI and XXV at the launch radius. A much higher luminosity could result in material close to the launch radius being completely ionized, so that Fe XXVI and XXV are predominantly produced at larger radii so would not show this characteristic signature. Alternatively, a much larger disk but with the same irradiating spectrum and luminosity would produce more wind, so the contribution of the static material might be lost in the heavier absorption from the outflow. H1743-322 in this soft state ($L \sim 0.3L_{\rm Edd}$ and $T_{\rm IC,8} \sim 0.10$) has the ideal parameters to show this transition from static corona to wind predicted in the thermal-radiative models

However, we note that testing this characteristic velocity pattern is already possible using the neutron star binary systems. The sample accumulated by Díaz Trigo & Boirin (2016) shows that winds are only seen in systems with large disks, whereas systems with small disks have only static absorption features. Thus it is already clear that the absorbing material forms a structure where there is static material at smaller radii, with the wind produced only at larger radii. This is clearly consistent with expected behaviour of thermal-radiative winds as stressed by Díaz Trigo & Boirin (2016). However, here we stress the converse, that this is *inconsistent* with self-similar magnetic wind models, since they are outflowing everywhere, and with larger velocity at smaller radii. These models predict that systems with smaller disks which show absorption features should have faster winds. This is not observed, ruling out a origin of self-similar magnetic winds for these features.

There could still be magnetic winds which are important dynamically, but are too highly ionized to give absorption features. Large scale magnetic fields torque the disk, so can be the source of angular momentum transport even if the resulting Blandford-Payne wind (Blandford & Payne, 1982) is not the source of the observed absorption features. However, there are also problems with this approach as a self-similar magnetic wind is (by definition) launched at all radii, so it will disrupt the static disk atmosphere at small radii predicted by the thermal wind models, and seen in the small disk systems. This atmosphere (and wind in the larger system) acts as a calorimeter, showing how much energy and momentum is transported by an otherwise invisible magnetic wind. While the thermal-radiative wind region has dense material preferentially in equatorial directions, the X-ray heated disk atmosphere lies directly above the disk so is sensitive to energy/momentum flux from a magnetic wind launched in any direction. The extent to which *XRISM*/Resolve observations show consistency with the thermal-radiative disk atmosphere/wind predictions also strongly constrains the existence of self-similar magnetic wind from the disk.

One of magnetic winds not constrained by these considerations is one which arises only in the hot inner flow region. This is characteristic of the truncated disk models for the low/hard state in black hole binaries (equivalently the island state in neutron stars). This region is radially separated from the disk, so a Blandford-Payne wind anchored into this inner hot flow would not impact and/or disrupt the X-ray heated atmosphere/wind over the disk. However, a more common name for such a wind is the jet, and the best current models which use large scale magnetic fields to transport angular momentum in the hot flow region are focused on powering the compact radio jets seen in this state (Marcel et al., 2018a,b).

Chapter 8

The comprehensive model for GX 13+1

In Chapter 6, we clearly show that thermal-radiative winds can naturally explain absorption visibility at state transition and also wind observable such ion columns and velocities by running RHD simulations. Chapter 7 show that simulated line profile using density and velocity distribution also well describe observed spectra. In this chapter, we use these method as an united model to neutron star binary GX 13+1 which has largest disk in terms of units R_g we check the parameter dependence of our simulations. Using our model, we confirm that the wind driving mechanism are common between BHs and NSs.

8.1 The NS LMXB GX 13+1: system parameters

GX 13+1 is a bright persistent NS LMXB in the Galactic bulge. This object orbits an evolved late-type K5 III star with a mass of 5 $M_\odot$ and its distance is estimated as 7 ± 1kpc (Bandyopadhyay et al., 1999). The infrared and X-ray light curves show that a binary orbital period is 24.5 days (Corbet et al., 2010; Iaria et al., 2013). There are X-ray dips (D'Aì et al., 2014) so this object has a moderately high inclination angle (Díaz Trigo et al., 2012, $60^\circ - 80^\circ$, but more likely towards the lower end of this range as the dips are occasional events rather than seen regularly in each orbit). The disk outer radius of this object is $R_{\rm disk} = 1.0 \times 10^{12}$cm $= 5.0 \times 10^6 R_g$ (Chap.5).

The first moderate resolution spectra from *ASCA* Ueda et al. (2001) showed highly ionized iron K absorption lines, the first seen in a NS rather than BH binary system. This absorption is most clearly seen in high resolution spectroscopy with *Chandra*/HETG, where Kα lines from H-like, Fe, Mn, Cr, Ca, Ar, S, Si, and Mg are detected as well as He-like Fe. The blueshift of these lines show that the material is outflowing with $v_{\rm out} \sim 400$ km/s (Ueda et al., 2004; Madej et al., 2014; Allen et al., 2018).

8.2 Observational data

Table 8.1: Fits to the absorption lines of OBSID: 11818 using KABS. Errors are calculated by 90% confidence level.

ions	N_z [10^{18} cm^{-2}]	kT [keV]	$z \times 10^{-3}$
Fe XXVI	$3.6^{+46}_{-2.4}$	< 49	$-0.9^{+0.4}_{-0.5}$
Fe XXV	$0.5^{+1.2}_{-0.2}$	7^{+14}_{-6}	$-1.1^{+0.2}_{-0.6}$
Ca XX	$0.06^{+2.0}_{-0.02}$	$3.8^{+11}_{-3.7}$	$-1.8^{+0.16}_{-0.7}$
S XVI	0.07 ± 0.03	$0.7^{+0.2}_{-0.4}$	$-1.27^{+0.06}_{-0.04}$
Si XIV	0.05 ± 0.01	$1.1^{+0.5}_{-0.3}$	$-1.2^{+0.07}_{-0.1}$
Mg XII	$0.014^{+0.8}_{-0.013}$	< 4.7	$-1.0^{+0.14}_{-0.28}$

There are 8 separate *Chandra*/HETG observations, each showing highly ionized absorption lines (Ueda et al., 2004; Allen et al., 2018). We focus on the sequential observations in 2010 (Tab.5.1). These all have similar continuum shape (all data is in HB or NB branch (Homan et al., 2016)) and the EWs of the absorption lines are consistent within statistical errors for all these spectra (Allen et al., 2018). We use the first order spectra from the Continuous Clocking (CC) mode observation (ObsID 11818) to determine the absorption line ion column densities, as this mode is less affected by pileup. We extract the third order spectra from the remaining 4 observations and co-add them in order to increase the signal-to-noise (Tomaru et al., 2018, Chap.5).

The absorption line equivalent width increases with increasing column density in the ion, but saturates when the core of the line goes black. The line depth cannot increase below zero intensity, so increasing the ion absorption column beyond this point only makes the line slightly wider - its equivalent width remains approximately constant. This makes it difficult to unambiguously determine the ion column from the absorption line equivalent width unless the line profile is fully resolved. We use the KABS absorption line model (Ueda et al., 2004), which calculates the full Voigt profile rather a Gaussian function, giving an estimate for the ion column which includes the effect of saturation. This is why the uncertainties on the ion columns are large, even when the uncertainty on line equivalent width is small (Ueda et al., 2004; Allen et al., 2018).

The Doppler width of the line is set by the *r.m.s.* sum of the microscopic sound speed $\sqrt{2kT_{\rm ion}/m_{\rm ion}}$ and the macroscopic velocity dispersion from turbulence or velocity shear in the wind, $v_{\rm turb}$ (Eq.2.32). Table 8.1 shows the ion columns determined from the main absorption lines along with their Doppler width (expressed as ion temperature, assuming that all of the velocity width is from this) and outflow velocity (expressed as a blueshift). The ion temperature in the wind is at most $T_{\rm IC} \sim 0.13$ keV (see below), so only Si XXIV and S XVI line width are anywhere near this limit. All the rest have upper limits on the width which are much larger, where bulk motion rather than temperature dominates. These give a baseline set of ion columns to compare with the results of the RHD simulations.

8.3 Radiation hydrodynamic simulation

8.3.1 Fiducial model: $L/L_{\rm Edd} = 0.5$

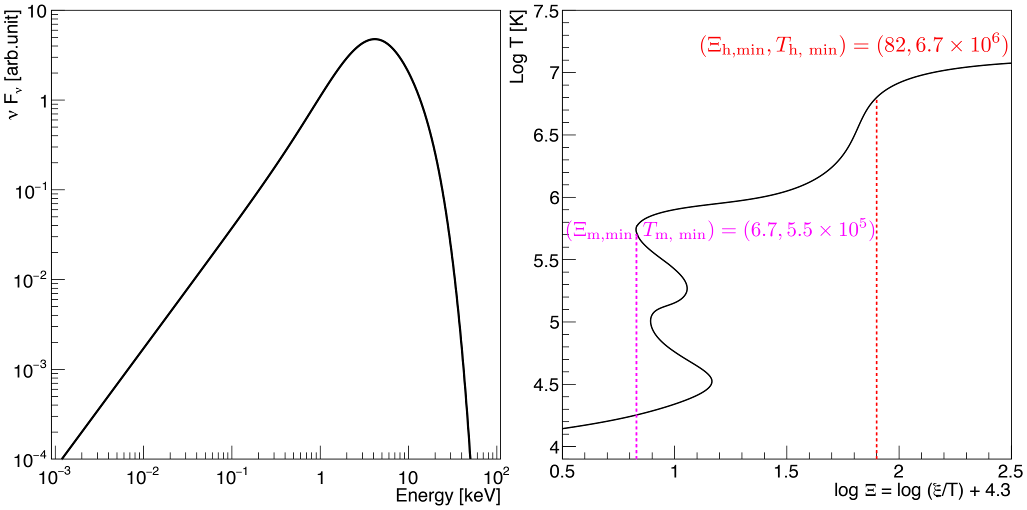

Figure 8.1: The SED of GX 13+1 (left) and its thermal equilibrium curve (right)

Table 8.2: The summary of simulations and inner corona parameters for GX 13+1

$L/L_{\rm Edd}$	$R_{\rm disk}$ $[R_{\rm IC}]$	$R_{\rm ia}$ $[R_g]$	$H_c[R_g]$	$R_{\rm is}$ $[R_{\rm IC}]$	$\dot{M}_{\rm w}$ $[10^{18}$ g/s$]$	$\dot{M}_{\rm w}/\dot{M}_a$
0.5	10.0	300	10	0.20	9.5	8.1
0.7	10.0	350	13	0.22	13	7.7
0.5	1.0	300	10	0.20	4.0	3.4

The code requires the X-ray spectral energy distribution (SED) in order to set the net heating/cooling rates and radiation force for the hydrodynamic code. We extract this from *RXTE* data (ObsID: 95338-01-01-07) which is simultaneous

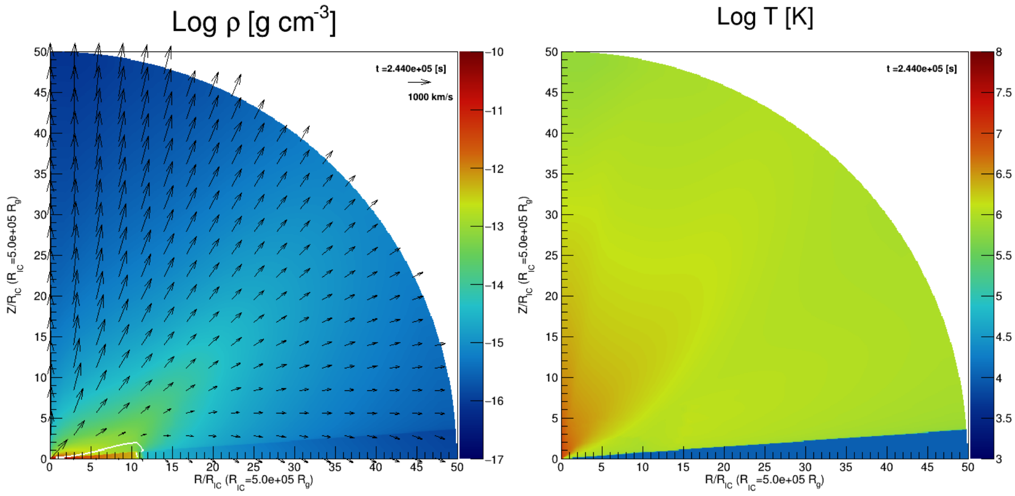

Figure 8.2: The distribution of density (left) and temperature (right)

with the CC observation of *Chandra*/HETGS (OBSID:11818). We show the derived SED in the left panel of Fig.8.1 (DISKBB+NTHCOMP in XSPEC). The Compton temperature of this SED is $T_{\rm IC} = 1.3 \times 10^7$K and the corresponding Compton radius is $R_{\rm IC} = 5.0 \times 10^5 R_g$. The outer radius is $R_{\rm disk} = 10R_{\rm IC}$, and its luminosity is $L \sim 0.5L_{\rm Edd}$. We use these values for our fiducial simulation.

While thermal winds are launched from the outer disk, (Tomaru et al., 2019a, Chap.6) also highlight the importance of irradiation of the inner disk. Begelman & McKee (1983) show that this results in a static X-ray heated atmosphere at small radii which easily goes optically thick to electron scattering along the equatorial plane. This forms a shadow on the disk, shielding it from direct irradiation, until the convex intrinsic shape of the disk lifts its surface above this shadow. For the fiducial parameters, the radius at which the disk re-emerges from the inner region shadow is $R_{\rm is} = 0.2R_{\rm IC}$. Thus we choose a radial grid for our radiation hydrodynamic calculation from $R_{\rm in} = 0.05\ R_{\rm IC}$ and $R_{\rm out} = 50\ R_{\rm IC}$ so as to resolve the entire region of the outer disk which is directly illuminated, and to capture the wind behavior as it expands out beyond the outer edge of the disk at $10R_{\rm IC}$.

We calculate the thermal equilibrium curve from the SED using CLOUDY (right panel of Fig.8.1). This is very similar to that derived for the soft state SED in the black hole binary H1743-322 in that it has a complex shape rather than the simple S curve characteristic of harder spectra (see e.g. Fig. 6.13 and Fig. 3.2). Similarly to H1743-322 (Tomaru et al., 2019b, Chap.7), we take the disk photosphere/wind boundary to be the minimum value of the pressure ionization parameter on the middle branch, $\Xi_{\rm m,min} = 6.7$, which has $T_{\rm m,\ min} = 5.5 \times 10^5$ K. This corresponds to a standard ionization parameter of $\xi_{\rm m,min} = 190$. This already has fairly large opacity,

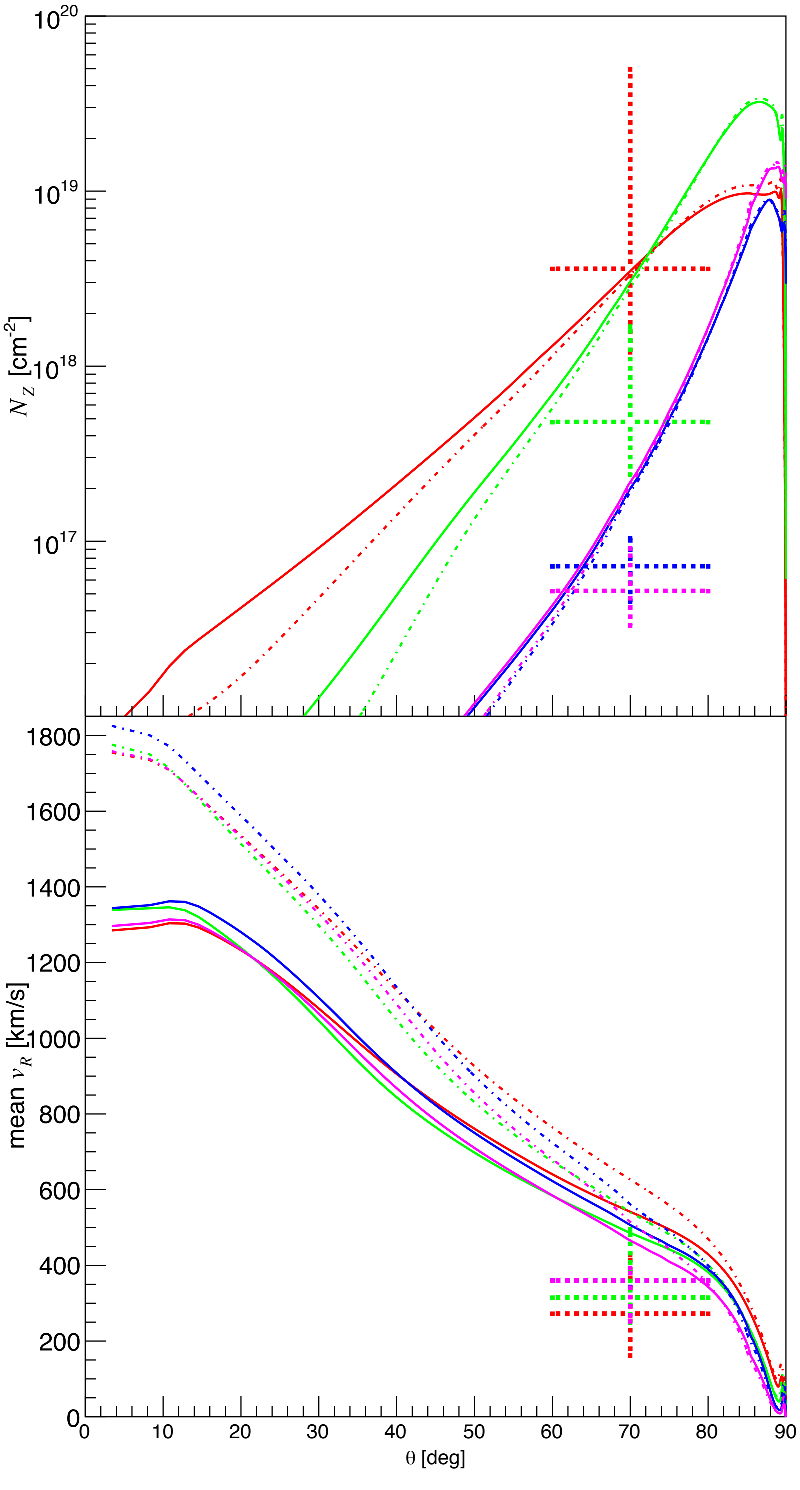

Figure 8.3: The angular dependence of ion columns (top) and ion column weighted mean velocities (bottom). Color show Fe XXVI (red), Fe XXV (green), S XVI (blue), and Si XIV (magenta). Solid lines show simulation of $L/L_{\rm Edd} = 0.5$ whereas Dashdotted lines show that of $L/L_{\rm Edd} = 0.7$. Dashed crosses show the observational values.

so effectively shields material on the lower branches from irradiation.

We run the RHD code of (Tomaru et al., 2019a, Chap.6) on a radial grid from with this net heating/cooling curve and corresponding force multiplier so that the radiation force includes both bound-free and line opacity as well as electron scattering. We end the simulation after 10 sound crossing times to ensure that this has converged, and show an overview of the wind properties in Table 8.2.

The efficiency of the wind, $\eta = \dot{M}_{\rm w}/\dot{M}_{\rm a} \sim 8$. This is about 4 times larger than in the analytic estimates of Done et al. 2018 (cyan line in their Fig. 3.4 has the same disk size and Compton temperature as here and tends to $\eta \to 2$ at high luminosities). This is due to their assumption that the base of the wind/photosphere of the disk was at $\Xi_{\rm c,max} = 40$. The wind mass-loss rate is estimated by the sonic points of flow via Eq.3.5 which is inversely proportional to the pressure ionization parameter at this point. Hence using $\Xi_{\rm m,min} = 6.7$ rather than $\Xi_{\rm c,max} = 40$ increases the mass-loss rate by this factor. Thus the analytic estimates are a fairly good description of the simulation results when the correct heating/cooling is included.

The density and temperature structure resulting from the simulation is shown in Fig. 8.2. The density plot clearly shows how the streamlines splay outwards for $R \gg R_{disk}$, and this increased adiabatic cooling pulls the gas temperature down below the Compton temperature at large radii.

We integrate along different lines of sight to get ion column densities as a function of inclination angle. We do this for Si XIV (magenta) and S XVI (blue) as well as H- and He-like iron (red and green), and compare these with the observed columns inferred from the fitting above (Fig.8.3). The predicted ion columns are well matched to the data, without any free fitting parameters, showing that the thermal wind simulation gives a very good overall match to the observed properties of the wind in GX13+1.

8.3.2 Changing luminosity: $L/L_{\rm Edd} = 0.7$

The wind material is very highly ionized, so while the ion columns derived above are quite small, the total column is quite large, of order 10^{24} cm^{-2} at high inclination (Fig. 8.4). Electron scattering reduces the observed luminosity along these lines of sight, so the intrinsic luminosity is underestimated. Hence we run a new simulation, increasing the luminosity to 0.7 $L_{\rm Edd}$ and compare the ion column densities and their velocities (dashed-dot lines) to the previous fiducial simulation (solid lines) and the data (dashed points) in Fig.8.3. Surprisingly, there is little change in the predicted column densities, and only a slight increase in predicted velocity. This is very different to the very simple radiation pressure correction of Done et al. (2018,

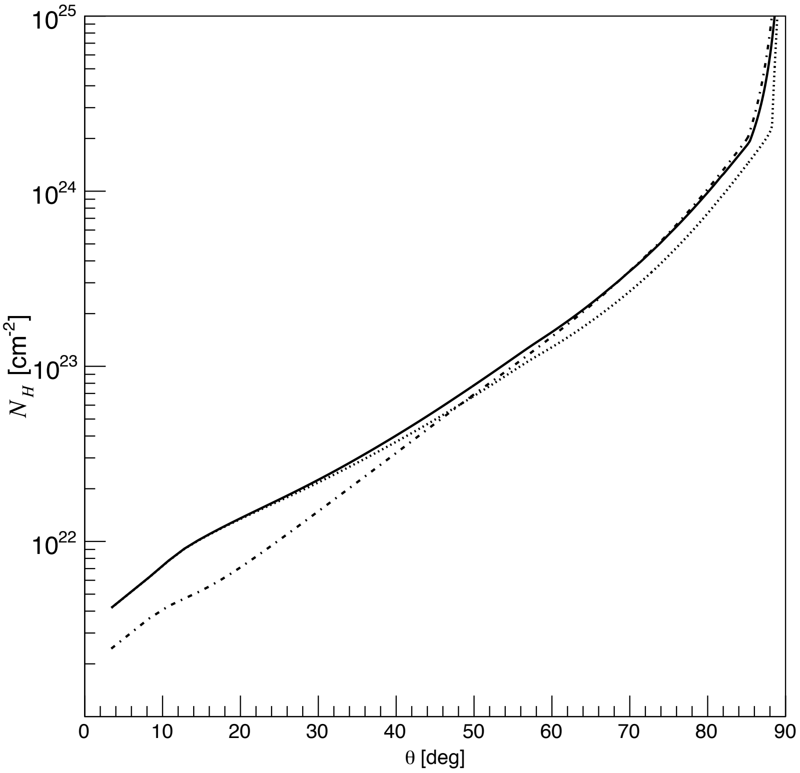

Figure 8.4: The angular dependence of hydrogen column density with $(L/L_{\mathrm{Edd}}, R_{\mathrm{disk}}/R_{\mathrm{IC}}) = (0.5, 10.0)$ (solid line), $(0.7, 10.0)$ (dashed-dot line), and $(0.5, 1.0)$ (dotted line).

Sec.3.4) which predicts a much larger column as $L \to 0.71\ L_{\rm Edd}$ due to radiation pressure reducing the effective gravity, allowing the wind to be launched from closer in.

The difference is due to the effect of the X-ray heated atmosphere over the inner disk. This was not included in Done et al. (2018, Chap.3), but here it effectively limits the launch radius of the wind to the radius at which the disk curvature allows it to emerge from the shadow, $R_{\rm is} \sim 0.2 R_{\rm IC}$. This is around the classic thermal wind launch radius, so increasing the luminosity does not decrease the radii at which the wind can form. In fact, the increased luminosity predicts a slightly increasing scale height of the inner X-ray heated disk atmosphere, so gives a slightly larger shadowed region. We strongly caution that the calculation of this inner attenuation zone is sub-grid physics which is not included in our RHD simulations. It is instead based on analytic approximations which do not include the effects of radiation pressure Begelman & McKee 1983; Tomaru et al. 2019a, Sec.6.4. Nonetheless, we physically expect the shadow to still be present, and for its extent not change too dramatically between $L = 0.5 \to 0.7\ L_{\rm Edd}$, so the inner edge of the wind is fixed at $\sim 0.2\ R_{\rm IC}$ rather than decreasing to encompass most of the inner disk. In this case the overall mass-loss rate increases more or less linearly with the increase in luminosity so that the wind efficiency remains constant, with $\dot{M}_w \propto \dot{M}_a$ (Tab. 8.2). Thus the total mass loss increases with the luminosity, but the radiation force increases the wind velocity, so the total ion columns remain rather similar as mass continuity sets the wind density $\propto \dot{M}_{\rm w}/v_R$.

This result suggests that ion columns are not as sensitive to changing luminosity in the high $L/L_{\rm Edd}$ regime as predicted in (Done et al., 2018, Sec.3.4). Instead, the shadow cast by the inner attenuating zone is very important in determining the extent of the wind.

8.3.3 Changing disk size: $R/R_{\rm IC} = 1.0$

For the comparison of the wind efficiency from the analytic estimate, we run another simulation with a small disk of $R/R_{\rm IC} = 1.0$ (Tab.8.2). The wind efficiency of this simulation is 3.4, which is also about 4 times higher than the analytic prediction in the previous chapter (green in Fig.3.4). The disk size dependence of mass-loss rate is consistent with the analytic estimate in high luminosity regime Eq.3.8, which is $\dot{M}_{\rm w} \propto \ln(R_{\rm disk}/R_{\rm in})$. The inner edge of this wind is $R_{\rm in} = R_{\rm is} = 0.2 R_{\rm IC}$. Thus the ratio of mass-loss rate of $R_{\rm disk}/R_{\rm IC} = 10.0$ to that of $R_{\rm disk}/R_{\rm IC} = 1.0$ should be $\ln(10.0/0.2)/\ln(1.0/0.2) = 2.4$, and this is precisely the same value as that of simulated mass-loss rate $8.1/3.4 = 2.4$.

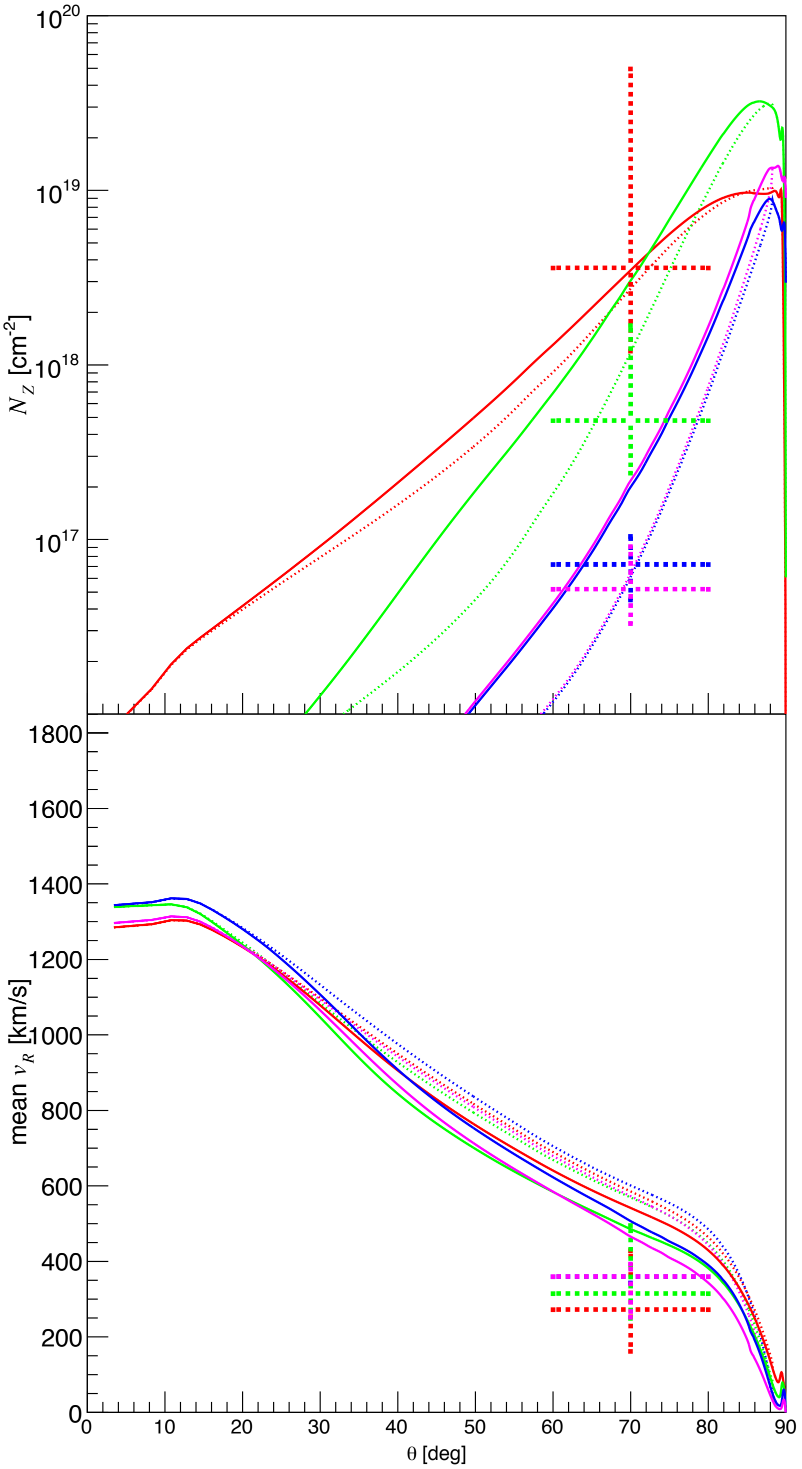

Figure 8.5: As in Fig.8.3 but the $R_{\rm disk}/R_{\rm IC}$ =10.0 (solid lines) and 1.0 (dotted lines).

On the other hand, the disk size dependence of hydrogen column densities is different with our simplified model Eq.3.18 which is also proportional to $\ln(R_{\rm disk}/R_{\rm in})$. The hydrogen column density of this simulation is shown in Fig.8.4 (dotted lines). The difference of columns between $R/R_{\rm IC} = 10.0$ and 1.0 is small. The column of $R/R_{\rm IC} = 1.0$ is about 20% smaller than that of $R/R_{\rm IC} = 10.0$ at $\theta = 70^\circ$. This result shows that our simplified model assuming the spherical flow geometry in Chap 3.2 is too simple to describe the hydrogen column of hydrodynamic simulation.

We also measure of ion columns and velocities (Fig.8.5). At $\theta = 70^\circ$, the column of Fe XXVI of $R/R_{\rm IC} = 1.0$ is about 20% smaller than that of $R/R_{\rm IC} = 10.0$, whereas the that of Fe XXV is about 60% smaller. Because the ionization parameter ξ is proportional to the ratio of ion populations $N_{\rm Fe\ XXVI}/N_{\rm Fe\ XXV}$, the ionization parameter of $R_{\rm disk}/R_{\rm IC} = 1.0$ is about twice as large as that of $R_{\rm disk}/R_{\rm IC} = 10.0$. This result shows that low ionized materials come from disk outer part. These ion columns are also consistent with those of observation.

8.4 Monte Carlo radiation transfer

8.4.1 Calculation setup

We calculate the detailed radiation transfer through the hydrodynamic simulations as in previous Chapter. We reduce the θ grid to $30 - 80^\circ$ in order to speed up the calculation, as we now also include an azimthal grid so that the radiation transport is fully 3D. The total grids we use are 60 (radial) and 51 (polar) and 32 (azimuth). The input density and velocity are shown in Fig.8.6.

MONACO requires the distribution of ion populations and temperature in addition to density and velocity. In order to obtain the distribution of ion populations and temperature in addition to density and velocity, we solve the one dimensional radiation transfer along line of sight using CLOUDY as in previous Chapter. We chain CLOUDY radially through the density structure and use the output spectrum of inner grid as the input spectrum to the next grid. This gives the resulting ion columns of Fe XXV and XXVI for input into MONACO, along with the self consistent temperature (bottom panels of Fig.8.6). The radial distribution of these ions is shown for a representative line of sight at 65° in the upper panel of Fig. 8.7, while the lower panel shows the total column weighted mean radial (solid) and azimuthal (dashed) velocity (lower panel). The peak radius at which the higher ionization Fe XXVI ($\sim R_{\rm IC}$) is produced is smaller than that of Fe XXV ($\sim 10R_{\rm IC}$). The corresponding radial velocity is ~ 600 km/s (Fe XXVI) and ~ 400 km/s (Fe XXV), while

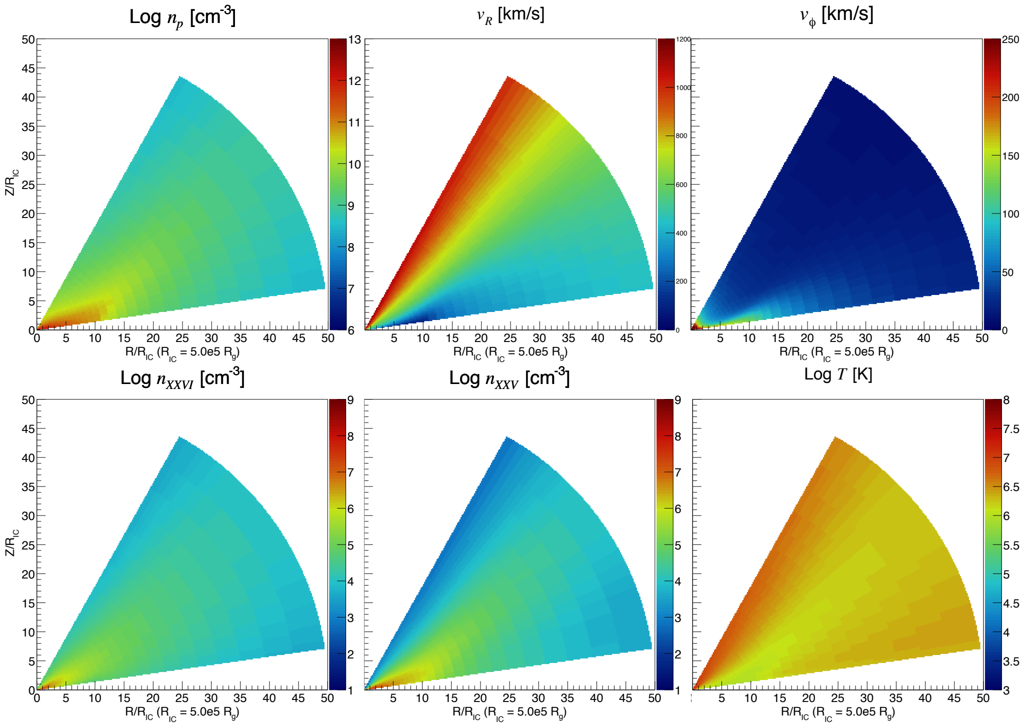

Figure 8.6: Top: The distribution of density (left), radial velocity (middle), and rotation velocity (right) extracted radiation hydrodynamic simulation Bottom: The CLOUDY output as the input MONACO.

the rotational velocity is lower, at ∼ 200km/s (Fe XXVI) and ∼ 50km/s (Fe XXV).

8.4.2 The effect of additional turbulent velocity

The ion columns are large so the line profiles are strongly dependent on the turbulent velocity (see also Tomaru et al., 2019b, Sec.7.2). Fully developed turbulence has $v_{\rm turb} \sim v_{\rm flow}$. However, there are two potential flow velocities in our simulation as we now have a fully 3D structure. One is the radial velocity, v_R, and the other is the azimuthal velocity v_ϕ (lower lanel of Fig. 8.7). Our 2D RHD simulation can capture some aspects of $R - \theta$ turbulence, so the lack of vortices in our results may signal that this is not present (see also Woods et al. 1996). However, there is also an azimuthal shear layer between the disk photosphere and the wind which is not included in our 2D simulation, and which could give rise to turbulence via the Kelvin-Helmholtz instability.

We explore the effect of turbulence by running MONACO with $v_{\rm turb} = v_\phi$ in addition to $v_{\rm turb} = 0$ and $v_{\rm turb} = v_R$. Detailed fits to the Chandra/HETGS line profiles already show that the widths are less than ∼ 200 km/s Allen et al. (2018), so $v_R \sim 400 - 600$ km/s is likely too large, but we include it here in order to show this explicitly.

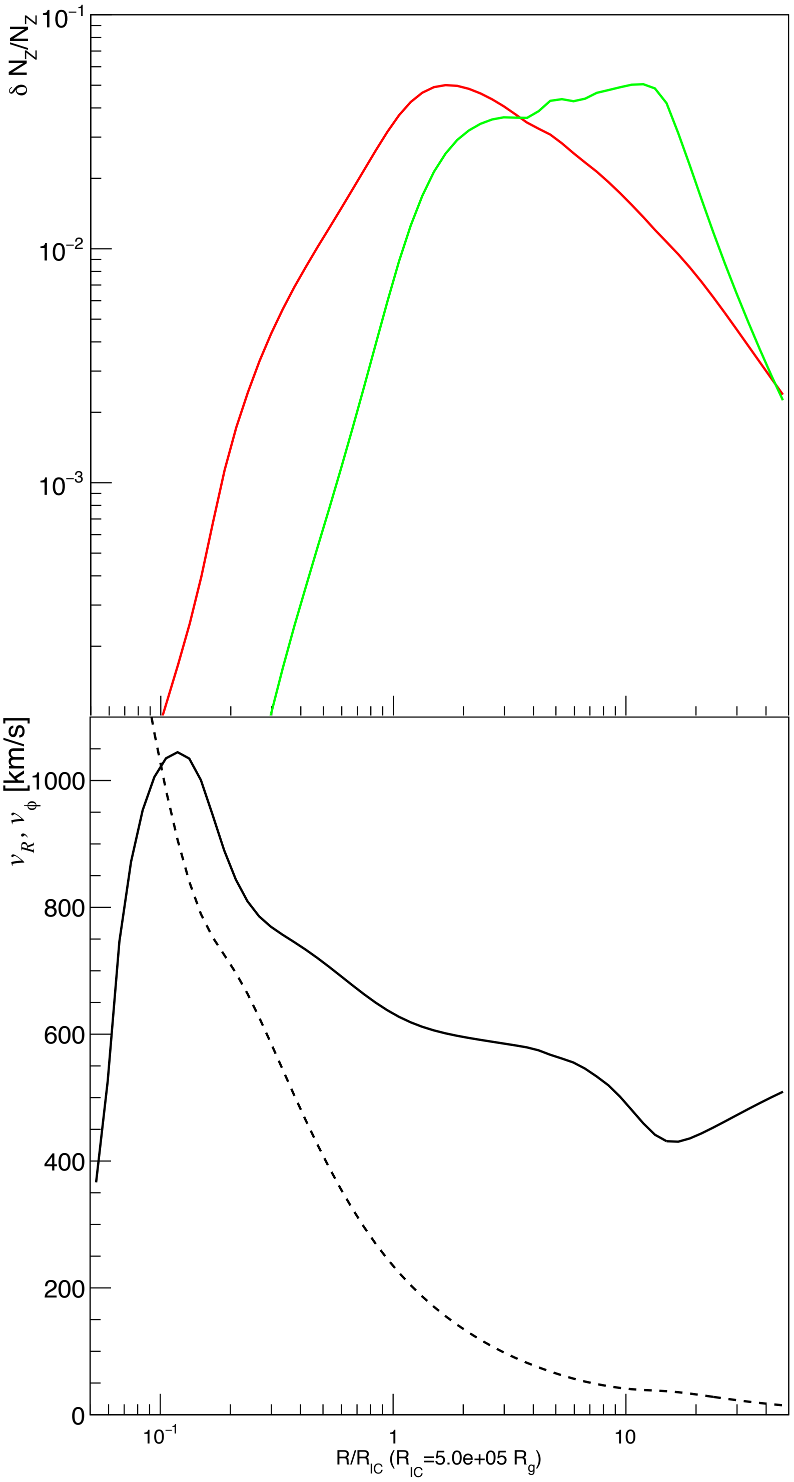

Figure 8.7: Radial profile of ion column densities (top) and velocities (bottom) at 65°. Color show Fe XXVI (red) and Fe XXV (green). The solid line shows radial velocity and the dashed line shows rotation velocity.

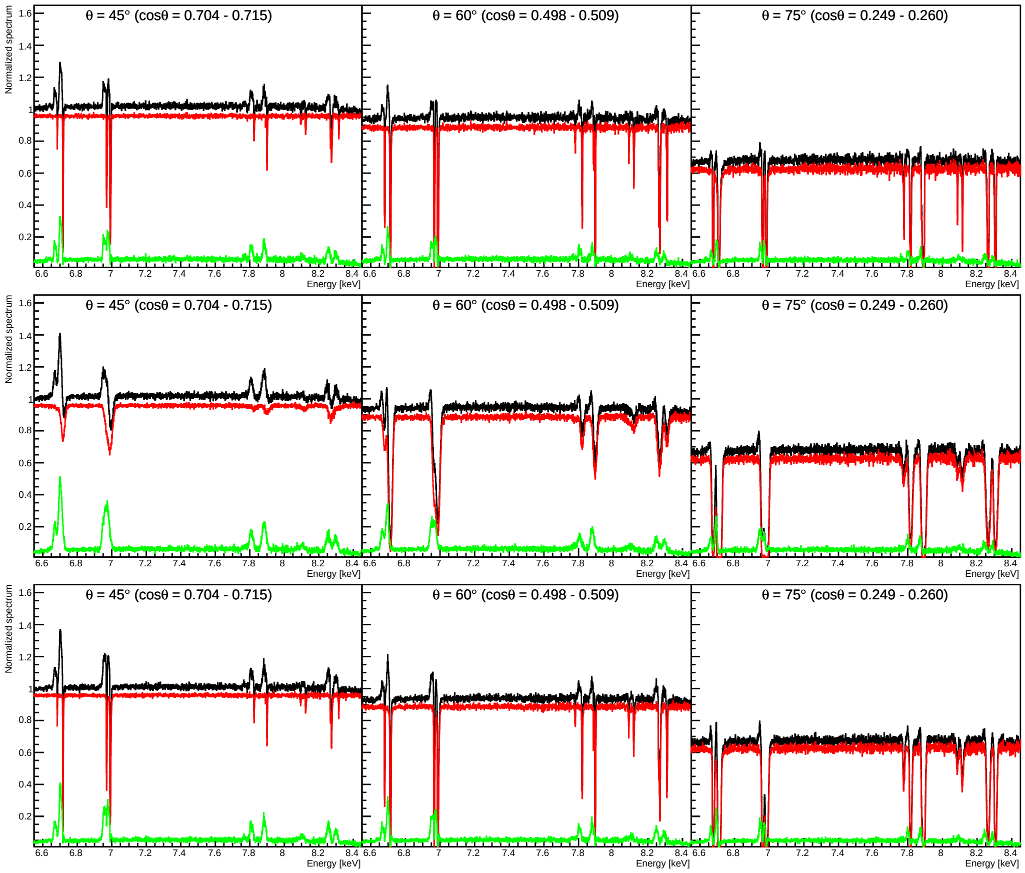

Figure 8.8: The angluar dependence of line profiles for $v_{\rm turb} = 0$ (top), v_R (middle), and v_ϕ (bottom).

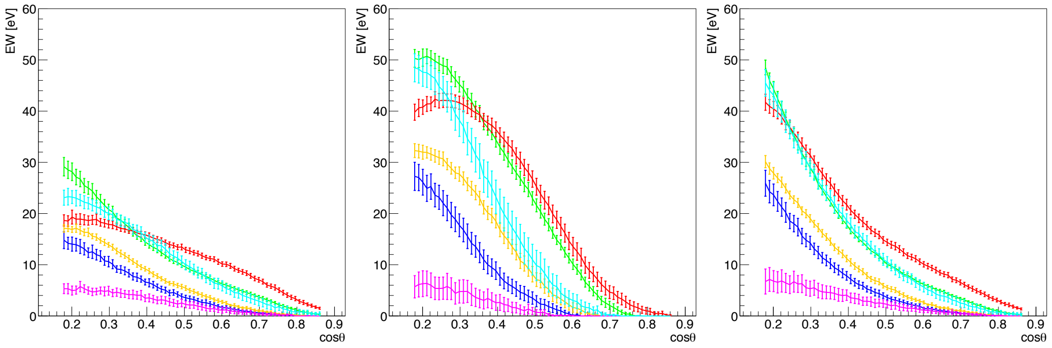

Figure 8.9: The inclination dependence of EWs for $v_{\rm turb} = 0$ (left), v_R (middle) and v_ϕ (right) Colors show Fe xxv Heα $y + w$ (green), Fe xxvi Ly$\alpha_1 + \alpha_2$ (red), Ni xxvii Heα $y + w$ (blue), Fe xxv Heβ w (orange), Ni xxviii Ly$\alpha_1 + \alpha_2$ (magenta), and Fe xxvi Ly$\beta_1 + \beta_2$ + Fe xxv Heγ w (cyan).

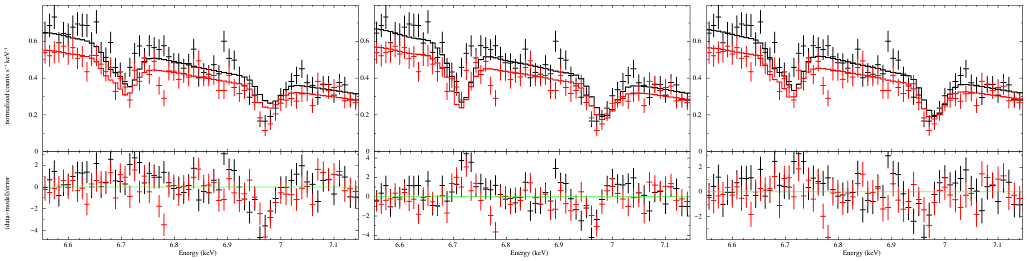

Figure 8.10: The comparison with our line profile and observed spectrum taken from HEG 1st order (OBSID: 11818). Models are $v_{\rm turb} = 0$(left), v_R (middle), and v_ϕ (right). Inclination angles are $\cos\theta = 0.29, 0.47, 0.33$

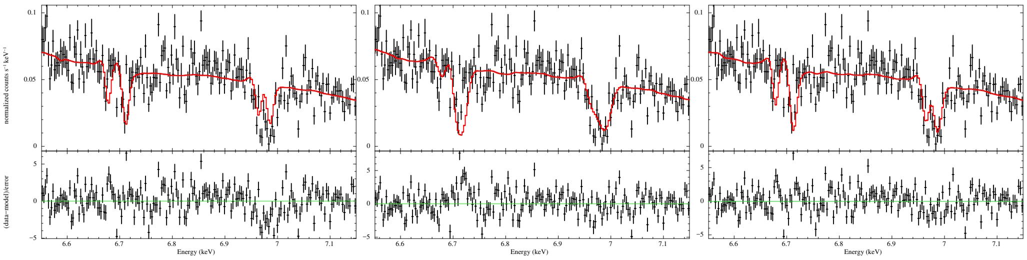

Figure 8.11: The comparison with our line profile and observed spectrum taken from *Chandra*/HEG 3rd order. Models are $v_{\rm turb} = 0$ (left), v_R (right), and v_ϕ (right) Inclination angles are $\cos\theta = 0.35, 0.47, 0.37$

We plot the resulting line profiles at three different angles in Fig. 8.8 The behavior of these profiles show a similar trend to that in H1743-322 (Tomaru et al., 2019b, Sec.7.2), i.e. the absorption lines are stronger at higher inclination angle and at higher turbulent velocity, while the scattered flux (green line which is ~ 0.05 of the intrinsic continuum level) is constant with inclination and turbulence.

Unlike H1743-322, the Fe XXV and XXVI Kα absorption lines often go to zero intensity in the transmitted spectrum (red line) i.e. are saturated due to the higher column density in GX 13+1 because of its larger disk. The Fe Kα lines remain saturated even for the highest turbulent velocities at high inclination angles. Hence we now also include the higher energy band, predicting the Fe Kβ and Ni Kα lines (see Table 4.1). These higher energy lines are always less saturated than the corresponding Fe Kα ion transitions (as the Fe Kβ transitions have lower oscillator strength, while Ni has much lower abundance than Fe) so give a better constraints on the ion column density.

Fig. 8.8 shows that without turbulence even the Helium-like Ni Kα w (resonance) line goes optically thick at high inclinations. The only unsaturated lines are the Kα y (intercombination) line of Ni XXVII at 7.765 keV, along with the H-like Ni XXVIII Kα resonance lines at 8.073 and 8.102 keV. However, the impact of scattering

Table 8.3: Fitting results

OBSID	χ^2/ν ($v_{\rm turb}=0$)	χ^2/ν ($v_{\rm turb}=v_R$)	χ^2/ν ($v_{\rm turb}=v_\phi$)
11815	429/124	192/124	168/124
11816	345/124	250/124	223/124
11814	174/124	180/124	128/124
11817	262/124	259/124	158/124
11818	215/124	225/124	171/124

and emission in the wind can also be easily seen in Fig.8.11, preventing the lines in the total (observed) spectrum (black line) from going completely to zero at their core, even though they are mostly highly saturated.

We quantify the predicted absorption line EWs of all the lines in this energy bandpass as in (Tomaru et al., 2018, 2019b, Chap.5,7), by fitting the line-free regions with a quadratic to estimate the continuum level. The results are shown in Fig.8.11. The Ni XXVIII (H-like) Kα lines (magenta) are the only lines with identical EW in all simulations. All the others are saturated to a greater or lesser extent, so increase in EW with increasing turbulence.

Unfortunately, due to its small effective area, spectra taken from *Chandra*/HETGS are not sensitive to the higher energy band. However, observations using *XMM-Newton*/EPIC pn have reported EWs of these lines (Díaz Trigo et al., 2014) of ~ 20 eV around 8.2 keV coming from Fe XXVI Ly$\beta_{1,2}$+ Fe XXV Heγ w, and ~ 15 eV around 7.9 keV coming from Ni XXVII Heα $w+y$ + Fe XXV Heβ w. These EWs have large uncertainty but are consistent with our estimates here only for the simulation without additional turbulence. Future observations with the calorimeters on *XRISM* and *Athena* will show this region of the spectrum with much higher accuracy, and tightly constrain the level of saturation.

8.4.3 Fitting to *Chandra*/HETG first and third order spectra

We now directly fit these models to the first order *Chandra* (ObsID:11818 CC mode). Fig. 8.6 shows that all the different assumptions on the turbulence leave some residuals, but the fit quality is better for models with $v_{\rm turb}=v_\phi$. This is also seen in fits to the TE mode spectra (Tab.5.1) though these are more affected by pileup (see Allen et al. 2018). These all show consistently that the models with $v_{\rm turb}=v_\phi$ have the lowest χ^2, then those with $v_{\rm turb}=0$, and finally $v_{\rm turb}=v_R$, as expected from the line velocity widths in Allen et al. (2018).

We can now look in more detail at the line profiles using 3rd order HEG data from the 4 co-added TE spectra, as this has 3 times higher resolution than 1st order Miller et al. (2016). Fig. 8.11 shows the data and our models. This clearly shows that the model with $v_{\rm turb} = v_R$ overestimates the observed line widths, but more unexpectedly reveals that the model with $v_{\rm turb} = 0$ is a good description of the observed line widths. There is enough change in radial velocity through the wind to produce the observed line profiles without additional turbulence (see 8.7). The main issue with the zero turbulence fit is that it underestimates the *depth* of the Fe XXVI Kα doublet. This is initially surprising as the ion columns in the model match to those determined by the KABS fits (see Fig.8.3). The total number of photon at each bin is determined by the integration of the number of photons per energy in that bin. When the turbulent velocity is small, the zero level regions exist very small energy range. As a result, the number of photons of absorption line is larger than the observation. This result suggest that about ~ 200 km/s turbulent velocity is required for lines of Fe XXVI using same ionization state. Although the origin of this turbulent is unknown from our model, our result suggests the azumuthal velocity is one of candidates.

Alternatively, we can also understand this underestimate depth as small ionization state. Indeed, the column density of Fe XXV obtained by RHD simulation is slightly above the observed value (green in Fig.8.3). Our RHD simulation and ionization calculation using CLOUDY did not include scattered flux, but this is important at the large column densities seen here at high inclination angle. These scattered flux ionized outer part of winds, reduce the ion column of Fe XXV which exist outer part of disk (Fig.8.7), and increase that of Fe XXVI.

Chapter 9

Summary and Discussion

9.1 Summary

9.1.1 Radiation transfer through a phenomenological biconical wind model for GX13+1

We construct a MCRT code to calculate detailed spectra from any given density and velocity distribution of highly ionized material. We use this to explore the absorption and emission lines of H and He-like Fe for the mass loss rates predicted from thermal wind models. We first use the radial streamline, constant velocity model of Done et al. (2018) which is able to reproduce the column derived from the hydrodynamic calculations of Woods et al. (1996), but then extend this to a more realistic disk-wind geometry with gas accelerating along diverging streamlines, again reproducing the column from Woods et al. (1996). The different assumed velocity and density structures for the thermal wind mass loss rates give different predictions for the overall ionization state of the material, the resulting EW of emission and absorption lines, and their velocity shift. These show the potential of observations to test the detailed structure of the wind.

We apply the biconical disk wind model to some of the best data on winds from an LMXB. The neutron star GX 13+1 shows strong and persistent absorption features in Chandra first order HETG spectra(Ueda et al., 2004; D'Aì et al., 2014), but here we show for the first time the higher resolution third order data. We find that while the source is fairly well matched to the parameters of the brightest fiducial simulation in terms of $T_{\rm IC}$, the higher luminosity ($L/L_{\rm Edd} = 0.5$ compared to 0.3 for the simulation) makes a significant impact on the predicted wind properties as it puts the source firmly into the regime where radiation pressure driving should become important.

We use the simple radiation pressure correction suggested by Done et al. (2018) and calculate the line profiles from a hybrid thermal-radiative wind. The additional radiation pressure driving means that the wind can be launched from much closer to the central source, and has higher mass loss rate. This is the first detailed test of the absorption line profiles predicted by physical wind models on any source other than the singular wind seen in GRO J1655-40 (Luketic et al., 2010). Our simulations quantitatively match many of the observed features except for the highest velocity material. This is not surprising, given the simplistic assumptions about the effect of radiation pressure.

9.1.2 Radiation transfer through a radiation hydrodynamic wind model for H1743-322

We show that thermal-radiative winds can match the observed wind properties in H1743-322. This includes both the column density and velocity of the wind seen in the soft state. We confirm the results of Higginbottom et al. (2018) and suggestion from Chap.5 that thermal winds alone are too slow, but we show that radiation pressure (on both electrons and ions) has a significant effect, producing a force multiplier which transforms these sub-Eddington luminosities to being effectively super-Eddington. Our model also shows the disappearance of the wind in the hard state due to complete shadowing of the outer disk by the inner static corona. There is no requirement for a magnetic wind to explain the behavior of the absorption features observed in this source.

We tailored this simulation to explain the column density, ionization state and velocity of the absorption features seen in *Chandra*/HETGS data from the black hole binary system H1743-322 in its soft, disk dominated state. We calculate the detailed absorption and emission line profiles predicted by this model by using the density/velocity structure as input to a MCRT code. The results fit well to the HETGS data, showing that these physical wind models can indeed be the origin of the absorption features seen, rather than requiring a magnetically driven wind.

This is the best current calculation of these winds and their observable absorption/emission features, but it does not incorporate all the potential physics of the outer disk. This could include warps and the impact of the accretion stream, both of which could induce turbulence, so we also calculate the line profile predicted for saturated turbulence in the thermal-radiative wind. Current HETGS data can neither distinguish models with and without additional turbulence nor identify the velocity separation between the static corona and the outflowing wind, but we show that future observations with *XRISM*/Resolve (due for launch Jan 2022) will be able to distinguish the detailed velocity structure in the absorption lines at this level, giving an unprecedented view of the wind launch and acceleration processes.

While it is already clear that thermal-radiative winds are consistent with current observations of H1743-322, using the entire sample of absorption features detected from accreting black holes and neutron stars gives more information. These show that static absorbers are seen in systems with small disks, whereas winds are only seen in larger systems. This is not only consistent with thermal-radiative winds, but crucially, is inconsistent with self-similar magnetic winds as these instead predict faster outflows at smaller radii. Thus, these magnetic winds are strongly disfavored as the origin of the absorption features seen in the black hole and neutron star binary systems.

The result also strongly constrains magnetic winds which are too highly ionized to produce any observable features. Such winds still carry kinetic energy and momentum (and angular momentum) and so give additional energy input into the thermal/radiative wind. The good match of the predicted and observed velocity structure in the thermal-radiative wind shows that such input is small. Thus any magnetic wind must be predominantly vertical and only from the inner disk, so it does not intersect the thermal-radiative wind. Such a magnetic field geoemtry is normally associated with the jet rather than with a wind. Additionally, this vertical field needs to be confined to inner radii. The transition between the hot inner flow and thin disk gives a natural place for a magnetic field transition, suggesting an accretion geometry such as that in Fig.9.1 as proposed by Marcel et al. (2018a,b).

These result suggest the accretion geometry like Fig.9.1. In the soft state, the accretion disk is formed around the compact object. The small scale magnetic fields in the disk support the disk formation via the MRI. There are no large scale ordered magnetic fields. There is strong blackbody radiation from the disk, and a weak tail to high energies formed by inverse Compton scattering. This radiation illuminates the disk surface and produces the hot atmosphere. That atmosphere is launched as the wind. In the hard state, the inner disk evaporates into a hot flow, and this larger scale height flow forms an anchor for large scale magnetic fields. These fields produce a radio jet. The thermal winds may exist at larger radii, but are too ionized to observe.

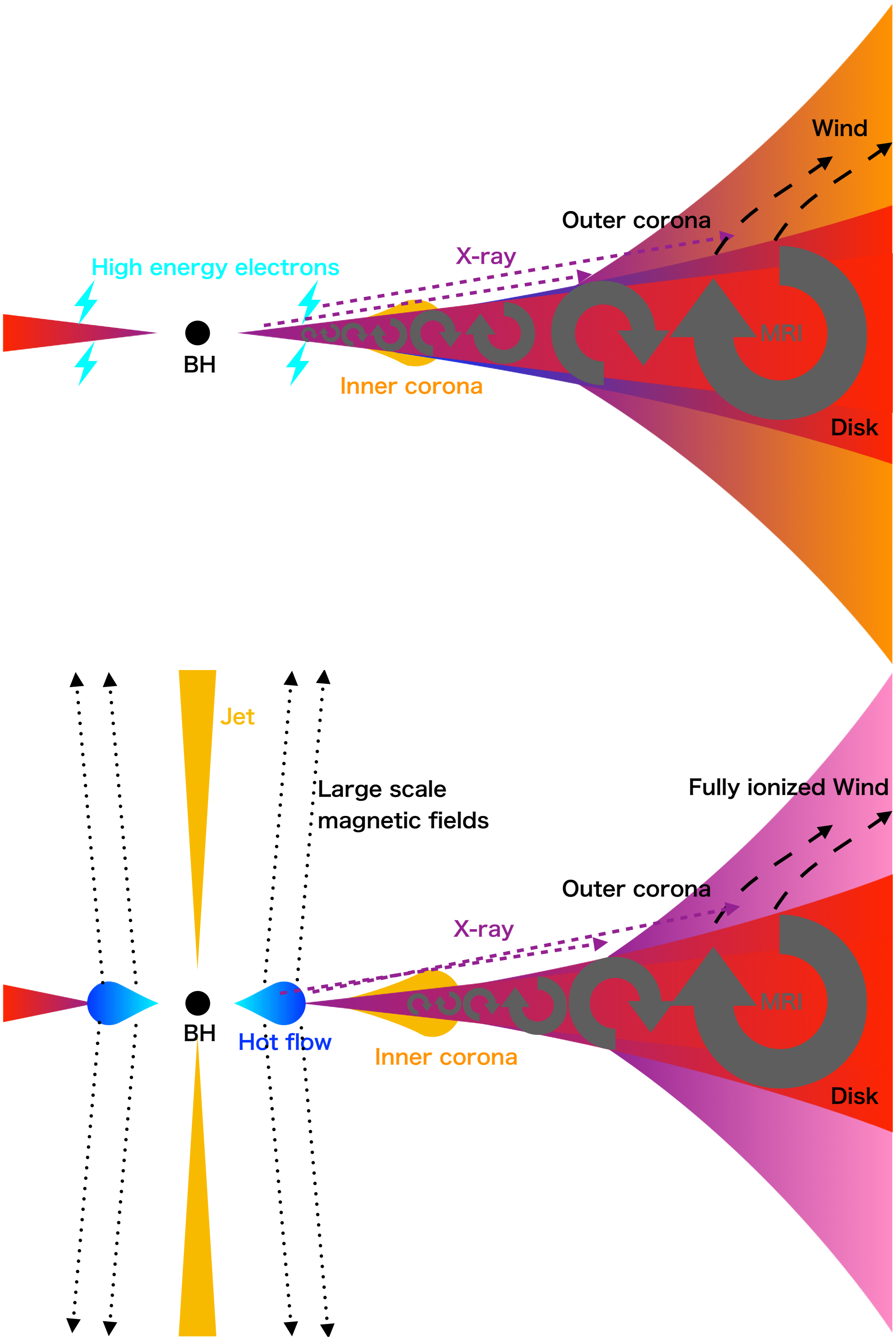
Wind
Outer corona
X-ray
High energy electrons
BH
MRI
Inner corona
Disk
Jet
Large scale
magnetic fields
Fully ionized Wind
Outer corona
X-ray
BH
Hot flow
MRI
Inner corona
Disk

Figure 9.1: The schematic diagram of inflow-outflow geometry in soft (top) and hard state (bottom) suggested by our work.

9.1.3 Radiation transfer through a radiation hydrodynamic wind model for GX 13+1

We show state of the art simulations of the neutron star binary system GX 13+1. This has the largest disk (in gravitational units) of any known system, and is highly luminous at $\sim 0.5L_{\mathrm{Edd}}$. Our RHD code which includes radiation pressure on electrons and ions (bound free and lines) as well as X-ray heating predicts an extremely strong thermal-radiative wind, and the detailed line profiles computed from fully 3D MCRT through this wind include a substantial contribution from emission and scattering in the wind, as well as absorption. These absorption lines are strongly saturated at high inclination. The Fe XXVI and XXV Kα absorption lines go to zero intensity but only over a very narrow range in energy which is not resolved even by the Chandra 3rd order grating data so the observed lines do not appear black. The extreme nature of the column is revealed instead by comparison with the equivalent width of the less saturated Fe Kβ and Ni Kα absorption lines.

The level of saturation of the absorption lines depends sensitively on the velocity structure. Our RHD simulation has the self consistent velocity shear from acceleration along the line of sight, but we also include the possibility of additional isotropic turbulence at a level comparable to the radial velocity of $\sim$ 500 km/s or the azimuthal velocity of $\sim$ 100 km/s. Turbulence at the level of the radial velocity is already ruled out by the *Chandra*/HETGS 3rd order spectra, which clearly show that the observed absorption line profiles are narrower than this value. The line profiles instead appear more consistent with no additional turbulence, with an upper limit from the line profile around the level of the typical azimuthal velocity.

However, while the Fe Kα XXVI and XXV line widths are well fit at very low levels of turbulence, the line depth of the Fe XXVI Kα is clearly underestimated for zero turbulence. It is slightly better fit by including turbulence at the level of the azimuthal velocity, but the line depth is still underestimated, and the line width starts to show some tension. This indicate that our RHD simulations have slightly lower ionization than observation. The column density of Fe XXV obtained in the simulation is slightly above the observed value (green in Fig.8.3) so we could increase the Fe XXVI ion while still matching the Fe XXV column by slightly increasing the ionization state of the wind, shifting some of the Fe XXV to XXVI. Our models do not include the effect of the scattered flux on the ion populations in the RHD simulation and ionization calculation so we could have underestimated the ionization state. Especially, the wind base has large column density and the lower ionization in the outer part of disk (green in Fig.8.7) Thus this scattered flux may give additional ionization of the outer parts of the winds, reducing the ion column of Fe XXV, and increasing that of Fe XXVI.

Alternatively, the mismatch in ion columns could be due to our simplified model of the shadow from the inner heated disc atmosphere. Our analytic models for this do not include the effect of radiation pressure, yet this should be important at the high Eddington fraction of GX 13+1. Additionally, the disk structure itself may start to puff up, changing the shapes and size of the shadow on the outer disk.

Despite these tensions, overall the predicted thermal-radiative wind captures most of the observed behaviour of the source. The line widths strongly limit the velocity shear in the wind region to much less than the observed outflow velocity.

9.2 Discussion

We show that absorption lines BH LMXB H 1743-322, and NS LMXB GX 13+1 are consistent with thermal-radiative winds from RHD simulations via MCRT simulations. We show that the self similar magnetic wind models (Chakravorty et al., 2013; Fukumura et al., 2017) are inconsistent with the low velocities observed in small disk systems, We similarly show that the large disk systems are consistent with undisturbed thermal-radiative winds, again ruling out a strong contribution from magnetic winds. The only system where there is potential evidence for magnetic winds in the unusual wind seen in a single observation of the large disk black hole system GRO J1655-40. This observation was the driver for the self similar magnetic wind models, and they can match the overall properties of the absorption lines (though we note that the model does not match the density diagnostic lines, and is fundamentally inconsistent as the total completely ionized wind column is very optically thick). Nonetheless, the unusual properties of this one wind means that it is not representative of most of the winds seen in these systems. We will extend our model to superEddington luminosities in future work, to see if the thermal-radiative wind can become optically thick so that the observed luminosity is strongly underestimated.

The lack of magnetic winds in the galactic binaries also gives us insight into winds in AGNs. We observe winds are ultrafast outflows (high velocity, high ionization) and warm absorbers (low velocity, lower ionization). If there are likewise no magnetic winds in AGN then these winds should also be thermal or radiatively powered. The main difference between AGNs and LMXBs are disk temperature and resultant radiation energy coming from the difference of mass. Disk temperatures of AGNs are $\sim 10^4 - 10^5$ K (UV band), while those of LMXBs are $\sim 10^7$ K (X-ray band). This difference influences the atomic physics of the gas such as bound-bound and bound-free transitions Because there are a lot of transition lines in UV band, radiation force from AGN disk is much larger. On the other hand, magnetic fields in disk should be same both AGNs and LMXBs, especially MRI in the disk which is essential for the formation of disk. We will apply our method of RHD and MCRT to AGN winds in the future.

Chapter 10

Conclusion

We develop a new simulation framework of thermal-radiative winds to determine the driving mechanism of accretion disk winds by comparing with the observed spectra. Our framework consists of full radiation hydrodynamic simulation, with post processing in a Monte Carlo radiation transfer code to predict detailed profiles of the absorption/emission lines.

Our RHD code includes physical processes than previous codes, as it uses the observed spectrum to calculate the radiative heating/cooling curves, and also includes radiation forces (electron scattering, bound-free and bound-bound) Our MCRT code use the density/velocity distribution from RHD simulations so we self consistently calculate the radiation transfer and reprocessing of the X-ray photons.

By applying this framework to BH LMXB H 1743-322, we show that thermal-radiative winds can explain observables such as ion columns, velocity, and observed spectra itself in soft state and the absorption disappearance in the hard state. We also indicate the inconsistency of current magnetic winds models assuming self-similar large scale magnetic fields.

We also apply these framework to bright NS LMXB GX 13+1. Our RHD simulation shows that mass loss rate is consistent with analytic model (Done et al., 2018). This simulation match the observed ion columns and velocities using the spectral shape, the luminosity, and the disk size, without any additional parameter. Current data cannot completely determine the turbulent velocity, though they do limit it to be much less than the radial outflow speed. Our model still needs some development in terms of the shadow cast by the inner (subgrid) heated atmosphere, and including the scattered emission in the ionization balance. Nontheless, we conclude We conclude that the origin of absorption lines in both BH and NS LMXBs are thermal-radiative winds. We can now robustly predict the properties of these winds to match to current and future observations.

Acknowledgements

I would like to thank my supervisor Prof. T. Takahashi for patiently giving me advice throughout my PhD. I also would like to thank Prof. C. Done for her kind explanation and helping me to get the point of the matter. She also strongly supported me throughout this work, which started from her idea. I also strongly appreciate Dr. H. Odaka . His simulation code MONACO is essential for this thesis. I also thank Prof. K. Ohsuga for his useful advice to run radiation hydrodynamic simulations and to analyze those results. I also thank Dr. M. Nomura. Her original radiation hydrodynamic simulation code also essential for this theses. To all of the above people; thank you for being part of a collaboration that does some great science, but also knew when to discuss a disastrous code bug with a knowing smile and ironic joke. I would also like to thank Dr. S. Watanabe, Dr. G. Sato, Dr. S. Takeda, Dr. K. Hagino, Dr. T. Sato, Dr. Y. Ichinohe, Dr. U. Uchida, Dr. M. Mizumoto, Dr. M. Katsuragawa and countless others for useful correspondence or stimulating scientific conversations. Finally I thank my family who has always supported me throughout my studies. With their help, I evolve into what I am today. This thesis is supported by JSPS KAKENHI Grant Number JP 19J13373

Bibliography

Abramowicz, M. a., Czerny, B., Lasota, J. P., & Szuszkiewicz, E. 1988, ApJ, 332, 646

Agostinelli, S., et al. 2003, Nucl. Inst. Meth. Phys. Res. A, 506, 250

Allen, J. L., Schulz, N. S., Homan, J., Neilsen, J., Nowak, M. A., & Chakrabarty, D. 2018, ApJ, 861, 26

Armitage, P. J., & Livio, M. 1998, ApJ, 493, 898

Bachiller, R. 1996, Annual Review of Astronomy and Astrophysics, 34, 111

Balbus, S. A., & Hawley, J. F. 1998, Reviews of Modern Physics, 70, 1

Bandyopadhyay, R. M., Shahbaz, T., Charles, P. A., & Naylor, T. 1999, MNRAS, 306, 417

Begelman, M. C., & McKee, C. F. 1983, ApJ, 271, 89

Begelman, M. C., McKee, C. F., & Shields, G. A. 1983, ApJ, 271, 70

Bhattacharya, D., & van den Heuvel, E. P. J. 1991, Phys. Rep., 203, 1

Bjerkeli, P., van der Wiel, M. H. D., Harsono, D., Ramsey, J. P., & Jørgensen, J. K. 2016, Nature, 540, 406

Blandford, R. D., & Begelman, M. C. 1999, MNRAS, 303, L1

Blandford, R. D., & Payne, D. G. 1982, MNRAS, 199, 883

Blandford, R. D., & Znajek, R. L. 1977, MNRAS, 179, 433

Boirin, L., Méndez, M., Trigo, M. D., Parmar, a. N., & Kaastra, J. S. 2005, Sciences-New York, 208, 195

Boirin, L., & Parmar, A. N. 2003, A&A, 407, 1079

Boirin, L., Parmar, A. N., Barret, D., Paltani, S., & Grindlay, J. E. 2004, A&A, 418, 1061

Brandt, W., & Schulz, N. 2000, ApJ, 544, L123

Burrows, C. J., et al. 1996, ApJ, 473, 437

Carrasco-González, C., Rodríguez, L. F., Anglada, G., Martí, J., Torrelles, J. M., & Osorio, M. 2010, Science, 330, 1209

Castor, J. I., Abbott, D. C., & Klein, R. I. 1975, ApJ, 195, 157

Chakravorty, S., Lee, J. C., & Neilsen, J. 2013, MNRAS, 436, 560

Chakravorty, S., et al. 2016, A&A, 589, A119

Church, M. J., Reed, D., Dotani, T., Balucińska-Church, M., & Smale, A. P. 2005, MNRAS, 359, 1336

Clarke, C. J., & Alexander, R. D. 2016, eprint arXiv:1605.04089, 3051, 3044

Corbel, S., Kaaret, P., Fender, R. P., Tzioumis, A. K., Tomsick, J. A., & Orosz, J. A. 2005, ApJ, 632, 504

Corbet, R. H. D., Pearlman, A. B., Buxton, M., & Levine, A. M. 2010, ApJ, 719, 979

Coriat, M., Fender, R. P., & Dubus, G. 2012, MNRAS, 424, 1991

Cunningham, C. 1976, ApJ, 208, 534

D'Aì, A., Iaria, R., Di Salvo, T., Riggio, A., Burderi, L., & Robba, N. R. 2014, A&A, 13

Davis, S. W., Blaes, O. M., Hubeny, I., & Turner, N. J. 2005, ApJ, 621, 372

Davis, S. W., & Hubeny, I. 2006, The Astrophysical Journal Supplement Series, 164, 530

Di Salvo, T., et al. 2000, ApJ, 544, L119

Díaz Trigo, M., & Boirin, L. 2016, Astronomische Nachrichten, 337, 368

Díaz Trigo, M., Migliari, S., & Guainazzi, M. 2014, A&A, 76, 1

Díaz Trigo, M., Miller-jones James, C. A., Migliari, S., Broderick, J. W., & Tzioumis, T. 2013, Nature, 504, 260

Diaz Trigo, M., Parmar, a. N., Boirin, L., Mendez, M., & Kaastra, J. S. 2005, A&A, 445, 19

Díaz Trigo, M., Parmar, A. N., Boirin, L., Méndez, M., & Kaastra, J. S. 2006, A&A, 445, 179

Díaz Trigo, M., Parmar, A. N., Boirin, L., Motch, C., Talavera, A., & Balman, S. 2009, A&A, 493, 145

Díaz Trigo, M., Sidoli, L., Boirin, L., & Parmar, A. 2012, A&A, 543, A50

Done, C., & Gierliński, M. 2003, MNRAS, 342, 1041

Done, C., Gierliński, M., & Kubota, A. 2007, Astronomy and Astrophysics Review, 15, 1

Done, C., & Jin, C. 2016, MNRAS, 460, 1716

Done, C., Sobolewska, M. A., Gierliński, M., & Schurch, N. J. 2007, MNRAS: Letters, 374, 15

Done, C., Tomaru, R., & Takahashi, T. 2018, MNRAS, 473, 838

Done, C., Wardziński, G., & Gierliński, M. 2004, MNRAS, 349, 393

Dyda, S., Dannen, R., Waters, T., & Proga, D. 2017, MNRAS, 467, 4161

Eggum, G. E., Coroniti, F. V., & Katz, J. I. 1988, ApJ, 330, 142

Fender, R. P., Belloni, T. M., & Gallo, E. 2004, MNRAS, 355, 1105

Ferland, G. J. 2003, ARA&A, 41, 517

Frank, J., King, A., & Lasota, J. 1987, A&A, 178, 137

Fukumura, K., Kazanas, D., Contopoulos, I., & Behar, E. 2010, ApJ, 715, 636

Fukumura, K., Kazanas, D., Shrader, C., Behar, E., Tombesi, F., & Contopoulos, I. 2017, Nature Astronomy, 1, 0062

Fukumura, K., Tombesi, F., Kazanas, D., Shrader, C., Behar, E., & Contopoulos, I. 2014, ApJ, 780, 120

Gardner, E., & Done, C. 2014, MNRAS, 442, 2456

Gavriil, F. P., Strohmayer, T. E., & Bhattacharyya, S. 2012, ApJ, 753, 2

George, I. M., & Fabian, A. C. 1991, MNRAS, 249, 352

Gierliński, M., & Done, C. 2002, MNRAS, 337, 1373

Gierliński, M., Done, C., & Page, K. 2008, MNRAS, 388, 753

Gierliński, M., Zdziarski, A. A., Poutanen, J., Coppi, P. S., Ebisawa, K., & Johnson, W. N. 1999, MNRAS, 309, 496

Gladstone, J., Done, C., & Gierliński, M. 2007, MNRAS, 378, 13

Hagino, K., Odaka, H., Done, C., Gandhi, P., Watanabe, S., Sako, M., & Takahashi, T. 2015, MNRAS, 446, 663

Hagino, K., Odaka, H., Done, C., Tomaru, R., Watanabe, S., & Takahashi, T. 2016, MNRAS, 461, 3954

Harten, A. 1983, Journal of Computational Physics, 49, 357

Hasinger, G., & van der Klis, M. 1989, A&A, 225, 79

Heckman, T. M., Armus, L., & Miley, G. K. 1990, The Astrophysical Journal Supplement Series, 74, 833

Higginbottom, N., Knigge, C., Long, K. S., Matthews, J. H., Sim, S. A., & Hewitt, H. A. 2018, MNRAS, 479, 3651

Higginbottom, N., & Proga, D. 2015, ApJ, 807, 107

Higginbottom, N., Proga, D., Knigge, C., & Long, K. S. 2017, ApJ, 836, 42

Higginbottom, N., Proga, D., Knigge, C., Long, K. S., Matthews, J. H., & Sim, S. A. 2014, ApJ, 789, 19

Homan, J., Neilsen, J., Allen, J. L., Chakrabarty, D., Fender, R., Fridriksson, J. K., Remillard, R. A., & Schulz, N. 2016, ApJ, 830, L5

Hynes, R. I., Brien, K. O., Mullally, F., & Ashcraft, T. 2009, MNRAS, 399, 281

Hynes, R. I., Haswell, C. A., Chaty, S., Shrader, C. R., & Cui, W. 2002, MNRAS, 331, 169

Hyodo, Y., Ueda, Y., Yuasa, T., Maeda, Y., Makishima, K., & Koyama, K. 2009, PASJ, 61, S99

Iaria, R., et al. 2013, A&A, 549, A33

Ichimaru, S. 1977, ApJ, 214, 840

Ingram, A., van der Klis, M., Middleton, M., Done, C., Altamirano, D., Heil, L., Uttley, P., & Axelsson, M. 2016, MNRAS, 461, 1967

Jimenez-Garate, M. A., Raymond, J. C., & Liedahl, D. A. 2002, ApJ, 581, 1297

Juett, A. M., & Chakrabarty, D. 2006, ApJ, 646, 493

Kaastra, J. S., Mewe, R., & Nieuwenhuijzen, H. 1996, 411

Kalberla, P. M. W., Burton, W. B., Hartmann, D., Arnal, E. M., Bajaja, E., Morras, R., & Pöppel, W. G. L. 2005, A&A, 440, 775

Kallman, T., Palmeri, P., Bautista, M., Mendoza, C., & Krolik, J. 2004, ApJS, 155, 675

Kallman, T. R., Bautista, M. A., Goriely, S., Mendoza, C., Miller, J. M., Palmeri, P., Quinet, P., & Raymond, J. 2009, ApJ, 701, 865

Kara, E., et al. 2019, Nature, 565, 198

Kato, Y., Mineshige, S., & Shibata, K. 2004, ApJ, 605, 307

Kimura, M., & Done, C. 2019, MNRAS, 482, 626

King, A. L., et al. 2012, ApJ, 746, L20

Knigge, C., Woods, J. A., & Drew, J. E. 1995, MNRAS, 273, 225

Kotani, T., Ebisawa, K., Dotani, T., Inoue, H., Nagase, F., Tanaka, Y., & Ueda, Y. 2000, ApJ, 539, 413

Krolik, J. H., McKee, C. F., & Tarter, C. B. 1981, ApJ, 249, 422

Kubota, A., et al. 2007, PASJ, 59, S185

Lasota, J.-P. 2001, \Nar, 45, 449

Lee, J. C., Reynolds, C. S., Remillard, R., Schulz, N. S., Blackman, E. G., & Fabian, A. C. 2002, ApJ, 567, 1102

Liffman, K. 2003, PASA, 20, 337

Lin, D., Remillard, R. A., & Homan, J. 2009, ApJ, 696, 1257

Liu, Q. Z., van Paradijs, J., & van den Heuvel, E. P. J. 2007, A&A, 469, 807

Livio, M., Ogilvie, G. I., & Pringle, J. E. 1999, ApJ, 512, 100

Lodders, K., Palme, H., & Gail, H. P. 2009, Landolt B&ouml;rnstein, 4B, 712

Long, K. S., & Knigge, C. 2002, ApJ, 579, 725

Luketic, S., Proga, D., Kallman, T. R., Raymond, J. C., & Miller, J. M. 2010, ApJ, 719, 515

Lynden-Bell, D. 1996, MNRAS, 279, 389

—. 2003, MNRAS, 341, 1360

Maccarone, T. J. 2003, A&A, 409, 697

Madej, O. K., Jonker, P. G., Díaz trigo, M., & Miškovičová, I. 2014, MNRAS, 438, 145

Marcel, G., et al. 2018a, A&A, 615, A57

—. 2018b, A&A, 617, A46

McKinney, J. C., & Gammie, C. F. 2004, ApJ, 611, 977

Migliari, S., & Fender, R. P. 2006, MNRAS, 366, 79

Miller, J. M., Fabian, A. C., Kaastra, J., Kallman, T., King, A. L., Proga, D., Raymond, J., & Reynolds, C. S. 2015, ApJ, 814, 87

Miller, J. M., Maitra, D., Cackett, E. M., Bhattacharyya, S., & Strohmayer, T. E. 2011, ApJ, 731, L7

Miller, J. M., Raymond, J., Fabian, A., Steeghs, D., Homan, J., Reynolds, C. S., van der Klis, M., & Wijnands, R. 2006, Nature, 441, 953

Miller, J. M., Raymond, J., Reynolds, C. S., Fabian, a. C., Kallman, T. R., & Homan, J. 2008, Astrophys. J, 680, 1359

Miller, J. M., et al. 2002, ApJ, 570, L69

—. 2004, ApJ, 601, 450

—. 2006, ApJ, 646, 394

—. 2012, ApJ, 759, L6

—. 2014, ApJ, 788, 53

Miller, J. M., et al. 2016, ApJ, 821, L9

Miller-Jones, J. C. A., et al. 2012, MNRAS, 421, 468

Mirabel, I. F., & Rodríguez, L. F. 1999, Annual Review of Astronomy and Astrophysics, 37, 409

Motta, S., Muñoz-Darias, T., & Belloni, T. 2010, MNRAS, 408, 1796

Muñoz-Darias, T., Casares, J., & Martínez-Pais, I. G. 2008, MNRAS, 385, 2205

Muñoz-Darias, T., Coriat, M., Plant, D. S., Ponti, G., Fender, R. P., & Dunn, R. J. H. 2013, MNRAS, 432, 1330

Narayan, R., & Yi, I. 1994, ApJ, 428, L13

Nayakshin, S., Kazanas, D., & Kallman, T. R. 2000, ApJ, 537, 833

Neilsen, J., & Homan, J. 2012, ApJ, 750, 27

Neilsen, J., & Lee, J. 2009, Nature, 458, 481

Neilsen, J., Rahoui, F., Homan, J., & Buxton, M. 2016, ApJ, 822, 20

Nomura, M., Ohsuga, K., Takahashi, H. R., Wada, K., & Yoshida, T. 2016, Publications of the Astronomical Society of Japan, 68, 16

O'Brien, K., Horne, K., Hynes, R. I., Chen, W., Haswell, C. A., & Still, M. D. 2002, MNRAS, 334, 426

Odaka, H., Aharonian, F., Watanabe, S., Tanaka, Y., Khangulyan, D., & Takahashi, T. 2011, ApJ, 740, 103

Odaka, H., Khangulyan, D., Tanaka, Y. T., Watanabe, S., Takahashi, T., & Makishima, K. 2014, ApJ, 780, 38

Odaka, H., Yoneda, H., Takahashi, T., & Fabian, A. 2016, MNRAS, 462, 2366

Ogilvie, G. I., & Dubus, G. 2001, MNRAS, 320, 485

Ohsuga, K., & Mineshige, S. 2011, ApJ, 736, 2

Ohsuga, K., Mineshige, S., Mori, M., & Kato, Y. 2009, PASJ, 61, L7

Ohsuga, K., Mori, M., Nakamoto, T., & Mineshige, S. 2005, ApJ, 628, 368

Osaki, Y. 1996, PASP, 108, 39

Ostriker, E., McKee, C., & Klein, R. 1991, ApJ, 377, 593

Paizis, A., et al. 2006, A&A, 459, 187

Papitto, A., D'Aì, A., Motta, S., Riggio, A., Burderi, L., di Salvo, T., Belloni, T., & Iaria, R. 2011, A&A, 526, L3

Parmar, A. N., Oosterbroek, T., Boirin, L., & Lumb, D. 2002, A&A, 386, 910

Ponti, G., Fender, R. P., Begelman, M. C., Dunn, R. J. H., Neilsen, J., & Coriat, M. 2012, MNRAS: Letters, 422, 11

Ponti, G., Muñoz-Darias, T., & Fender, R. P. 2014, MNRAS, 444, 1829

Ponti, G., et al. 2015, MNRAS, 446, 1536

Popham, R., & Sunyaev, R. 2001, ApJ, 547, 355

Press, W. H., Teukolsky, S. A., Vetterling, W. T., & Flannery, B. P. 1992, Numerical recipes in FORTRAN. The art of scientific computing

Proga, D. 2003, ApJ, 585, 406

Proga, D., & Kallman, T. R. 2002, ApJ, 20, 455

—. 2004, ApJ, 616, 688

Proga, D., Stone, J. M., & Kallman, T. R. 2000, ApJ, 543, 686

Rao, A., & Vadawale, S. V. 2012, ApJ, 757, L12

Reeves, J., Done, C., Pounds, K., Terashima, Y., Hayashida, K., Anabuki, N., Uchino, M., & Turner, M. 2008, MNRAS, 385, L108

Remillard, R. A., & McClintock, J. E. 2006, Annual Review of Astronomy and Astrophysics, 44, 49

Rybicki, G. B., & Lightman, A. P. 1979, Radiative processes in astrophysics

Saikia, P., Russell, D. M., Bramich, D. M., Miller-Jones, J. C. A., Baglio, M. C., & Degenaar, N. 2019, arXiv e-prints, arXiv:1910.01151

Schandl, S., & Meyer, F. 1994, A&A, 289, 149

Schulz, N. S., Cui, W., Canizares, C. R., Marshall, H. L., Lee, J. C., Miller, J. M., & Lewin, W. H. G. 2002, ApJ, 565, 1141

Shahbaz, T., Charles, P. A., & King, A. R. 1998, MNRAS, 301, 382

Shakura, N. I., & Sunyaev, R. a. 1973, A&A, 24, 337

Shapiro, S. L., & Teukolsky, S. A. 1983, Black holes, white dwarfs, and neutron stars: The physics of compact objects

Shibata, K., & Uchida, Y. 1985, PASJ, 37, 31

—. 1986, PASJ, 38, 631

Shidatsu, M., & Done, C. 2019, arXiv e-prints, arXiv:1906.02469

Shidatsu, M., Done, C., & Ueda, Y. 2016, ApJ, 823, 159

Shidatsu, M., et al. 2011, PASJ, 63, S785

—. 2013, ApJ, 779, 26

Sidoli, L., Oosterbroek, T., Parmar, A. N., Lumb, D., & Erd, C. 2001, A&A, 379, 540

Sim, S. a., Proga, D., Miller, L., Long, K. S., Turner, T. J., & Reeves, J. N. 2010, MNRAS, 408, 1369

Smak, J. 1970, Acta Astron., 20, 311

Smith, R. K., Edgar, R. J., & Shafer, R. A. 2002, ApJ, 581, 562

Steiner, J. F., McClintock, J. E., & Reid, M. J. 2012, ApJ, 745, L7

Stone, J. M., & Norman, M. L. 1992, ApJSupplement Series, 80, 753

Sunyaev, R. A., & Truemper, J. 1979, Nature, 279, 506

Takahashi, H. R., & Ohsuga, K. 2013, ApJ, 772, 127

Takeuchi, S., Ohsuga, K., & Mineshige, S. 2013, 11

Tanimoto, A., Ueda, Y., Odaka, H., Kawaguchi, T., Fukazawa, Y., & Kawamuro, T. 2019, ApJ, 877, 95

Tarter, C. B., & McKee, C. F. 1973, ApJ, 186, L63

Tarter, C. B., Tucker, W. H., & Salpeter, E. E. 1969, ApJ, 156, 943

Tchekhovskoy, A., Narayan, R., & McKinney, J. C. 2011, MNRAS, 418, L79

Tomaru, R., Done, C., Odaka, H., Watanabe, S., & Takahashi, T. 2018, MNRAS, 476, 1776

Tomaru, R., Done, C., Ohsuga, K., Nomura, M., & Takahashi, T. 2019a, MNRAS, 490, 3098

Tomaru, R., Done, C., Ohsuga, K., Odaka, H., & Takahashi, T. 2019b, arXiv e-prints, arXiv:1911.01660

Tombesi, F. 2010

Ueda, Y., Asai, K., Yamaoka, K., Dotani, T., & Inoue, H. 2001, ApJ, 556, L87

Ueda, Y., Murakami, H., Yamaoka, K., Dotani, T., & Ebisawa, K. 2004, ApJ, 609, 325

Ueda, Y., Yamaoka, K., & Remillard, R. 2009, ApJ, 695, 888

Uttley, P., & Klein-Wolt, M. 2015, MNRAS, 451, 475

van Paradijs, J. 1996, ApJ, 464, L139

van Peet, J. C. A., Costantini, E., Méndez, M., Paerels, F. B. S., & Cottam, J. 2009, A&A, 497, 805

Veledina, A., Gandhi, P., Hynes, R., Kajava, J. J. E., Tsygankov, S. S., Revnivtsev, M. G., Durant, M., & Poutanen, J. 2017, MNRAS, 470, 48

Walton, D. J., Miller, J. M., Harrison, F. A., Fabian, A. C., Roberts, T. P., Middleton, M. J., & Reis, R. C. 2013, ApJ, 773, L9

Watanabe, S., et al. 2006, ApJ, 651, 421

Waters, T. R., & Proga, D. 2012, MNRAS, 426, 2239

Wijnands, R., Yang, Y. J., & Altamirano, D. 2012, MNRAS, 422, L91

Woods, D. T., Klein, R. I., Castor, J. I., McKee, C. F., & Bell, J. B. 1996, ApJ, 461, 767

Yuan, F., & Narayan, R. 2014, ARA&A, 52, 529

Zdziarski, A. A., & Gierliński, M. 2004, Progress of Theoretical Physics Supplement, 155, 99

Zdziarski, A. A., Poutanen, J., Mikolajewska, J., Gierlinski, M., Ebisawa, K., & Johnson, W. N. 1998, MNRAS, 301, 435

Appendix A

Appendix

A.1 Geometry of thermal wind models

A.1.1 The rotation velocity for radial streamlines

Here we give details of how we calculate the rotation velocity of each element of the wind for radial streamlines (Section 3). We have a linear radial grid, with 20 points from R_{in} to R_{out}, so spaced by $dR = (R_{out} - R_{in})/20$. The inner shell has midpoint $R_0 = R_{in} + dR/2$. We inject all the mass loss rate into this radial shell, distributed as $(1 - \cos\theta)$, on a linear grid of 20 points in θ. Each point on this inner shell is at a horizontal distance of $R_0 \sin\theta$ from the black hole. We assume the material has the Keplarian velocity at this horizontal distance i.e. $v_\phi(R_0, \theta) = \sqrt{GM/(R_0 sin\theta)}$. Angular momentum conservation along each stream line (of constant θ for these radial streamlines) then gives $R_0 \sin\theta v_\phi(R_0, \theta) = R \sin\theta v_\phi(R, \theta)$ so $v_\phi(R, \theta) = (R/R_0) v_\phi(R_0, \theta)$

A.1.2 Density and velocity structure for the diverging streamlines

The diverging wind streamlines originate from the focal point which is a distance d below the black hole (see Fig 4). The innermost edge of the streamlines for the wind is at $\alpha_{min} = \arctan(R_{in}/d)$, and the outer edge is at $\alpha_{max} = \arctan(R_{out}/d)$. We make a linear grid so there are 40 angle elements in the wind, separated by $d\alpha = (\alpha_{max} - \alpha_{min})/40$ so that $\alpha_i = \alpha_0 + i d\alpha$ for $i = 0 \ldots 40$. We have α_0 as a free parameter, set by comparison to the results of W96 (see section 4)

The maximum 'streamline' length below the disc is from α_{max}, where $D = \sqrt{d^2 + R_{out}^2}$. We follow this for the same length above the disc. This defines the outer radius of the simulation box which is $R_{max} = 2\sqrt{d^2 + R_{out}^2}$. We take the inner edge at $R_{in} = 0.1R_{IC}$.

We superpose a standard θ grid on this (measuring down from the z-axis to radial lines from the centre: Fig.A.1). We set θ_0 to the point where the innermost streamline edge (at angle α_0) reaches R_{max} from the origin, and take 41 angles from this to $\pi/2$, giving $\theta_j (j = 0, 1..40)$. We make shells using the crossing points of these angles θ_j with the initial angles α_i (Fig.A.1). We also define the midpoint angles $A_i = (\alpha_i + \alpha_{i+1})/2$ and $\Theta_j = \frac{1}{2}(\theta_j + \theta_{j+1})$.

The velocity along each stream line at a distance l_{ij} from its launch point on the disc at radius $R_i = d \tan A_i$ is

$$v_l(R_i, l_{ij}) = f_v c_{ch}(R_i) \sqrt{\frac{l_{ij}}{R_i}} \tag{A.1}$$

where

$$l_{ij} = D_{ij} - d/\cos A_i, D_{ij} = d\frac{\sin \Theta_j}{\sin(\Theta_j - A_i)} \tag{A.2}$$

for a characteristic sound speed $c_{ch}(R_i) = \sqrt{\frac{kT_{ch}(R_i)}{\mu m_p}}$ defined from the characteristic temperature

$$T_{ch}(R_i) = \left(\frac{L}{L_{cr}}\right)^{2/3} (R_i/R_{IC})^{-2/3} \tag{A.3}$$

where the critical luminosity, L_{cr} is

$$L_{cr} = \frac{1}{8}\left(\frac{m_e}{\mu m_p}\right)^{1/2} \left(\frac{m_e c^2}{kT_{IC}}\right)^{1/2} L_{Edd} \tag{A.4}$$

(see Done et al., 2018) and f_v is free parameter which is determined by comparing with the results of W96.

We calculate the density of each shell n_{ij} assuming mass conservation along each streamline.

$$n_{ij} = \frac{\Delta \dot{M}_{wind}(R_i)}{m_I v_l(R_i, l_{ij}) 4\pi D_{ij}^2 (\cos \alpha_i - \cos \alpha_{i+1})} \tag{A.5}$$

where

$$\Delta \dot{M}_{wind}(R_i) = 2\pi \dot{m}(R_i) R_i \Delta R_i \times 2 = 4\pi \dot{m}(R_i) R_i d(\tan \alpha_{i+1} - \tan \alpha_i) \tag{A.6}$$

The total mass loss rate at a given luminosity L is $\dot{M}_{wind} = \sum_i \Delta \dot{M}_{wind}(R_i) = 2.0\times10^{19}$ g/s $(L/L_{edd} = 0.3)$, 8.0×10^{18} g/s $(L/L_{edd} = 0.08)$, 2.1×10^{18} g/s $(L/L_{edd} = 0.01)$.

Finally we, calculate the column density.

$$N_H(\Theta_j) = \sum_i n_{ij} \Delta h_{ij} \tag{A.7}$$

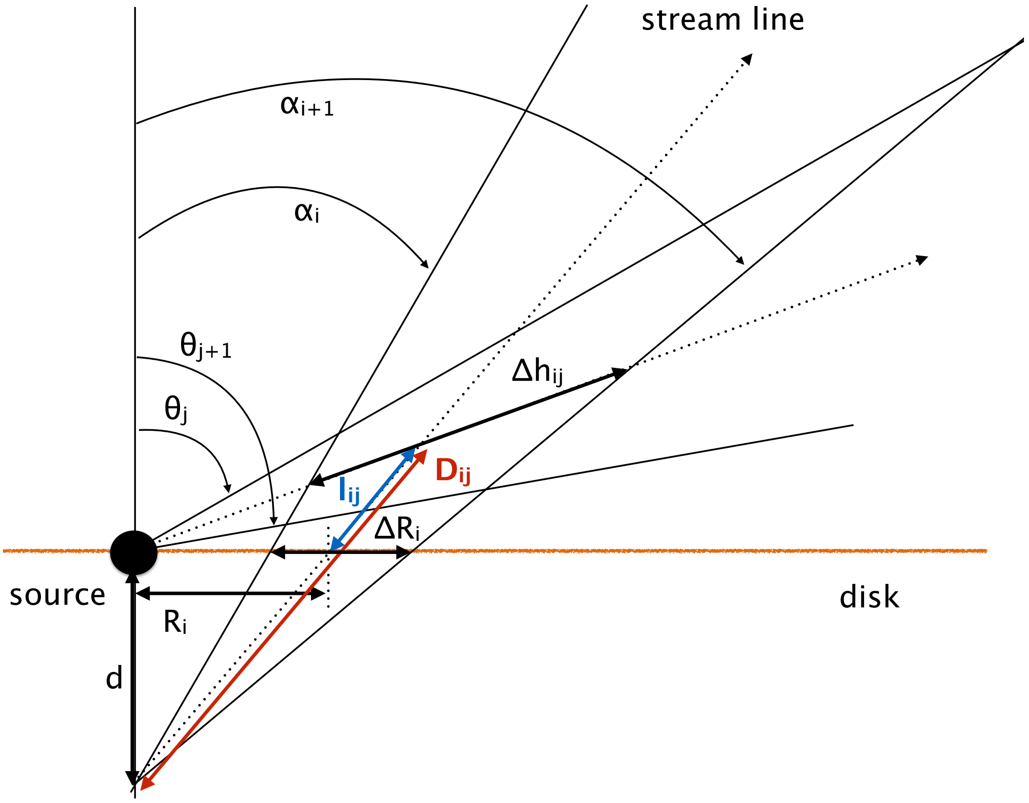

Figure A.1: Details of the model geometry for the diverging wind streamlines.

where

$$\Delta h_{ij} = d(\frac{\sin\alpha_{i+1}}{\sin(\Theta_j - \alpha_{i+1})} - \frac{\sin\alpha_i}{\sin(\Theta_j - \alpha_i)}) \tag{A.8}$$

We assume Keplerian velocity on the disc plane ($\theta = \pi/2$ which is at $j = 40$) so that

$$v_{\phi i,40} = \sqrt{\frac{GM}{D_{i,40}\sin A_i}} \tag{A.9}$$

and assume the angular momentum conversation along stream line so that

$$v_{\phi ij} = \frac{v_{\phi i,40} D_{i,40}\sin A_i}{D_{ij}\sin A_i} = \frac{v_{\phi i,40} D_{i,40}}{D_{ij}} \tag{A.10}$$

A.2 Numerical test II; the number of grid

We confirm whether the number of grid is enough for our simulations. We simulate same simulation as the fiducial run but changing the number of grid from $(N_R, N_\theta) = (120, 240)$ to (60, 120). The distribution of density and temperature shown in Fig. A.2. These distribution are same as the fiducial run (top left Fig.6.7). We also compare hydrogen column density (Fig.A.3). The column are same at high inclination angle. Thus we conclude the number of grid is enough.

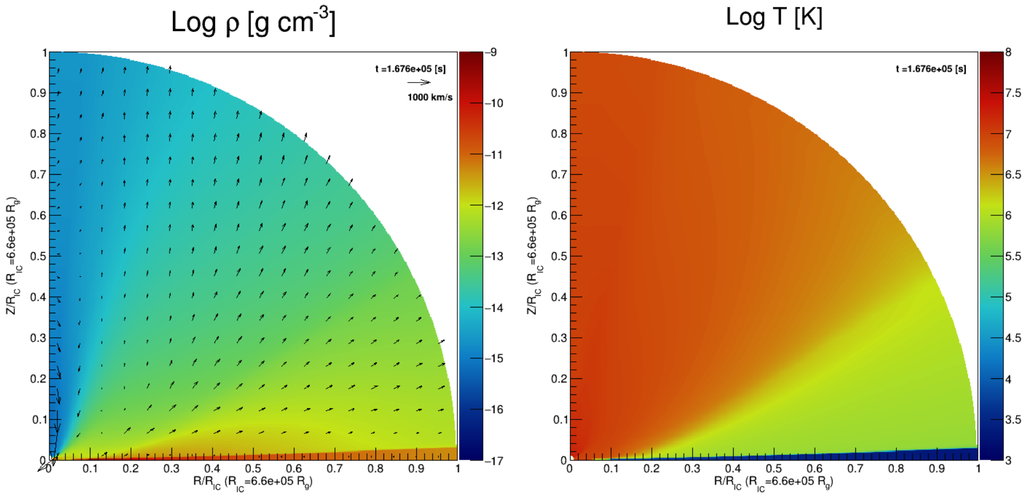

Figure A.2: The distribution of density

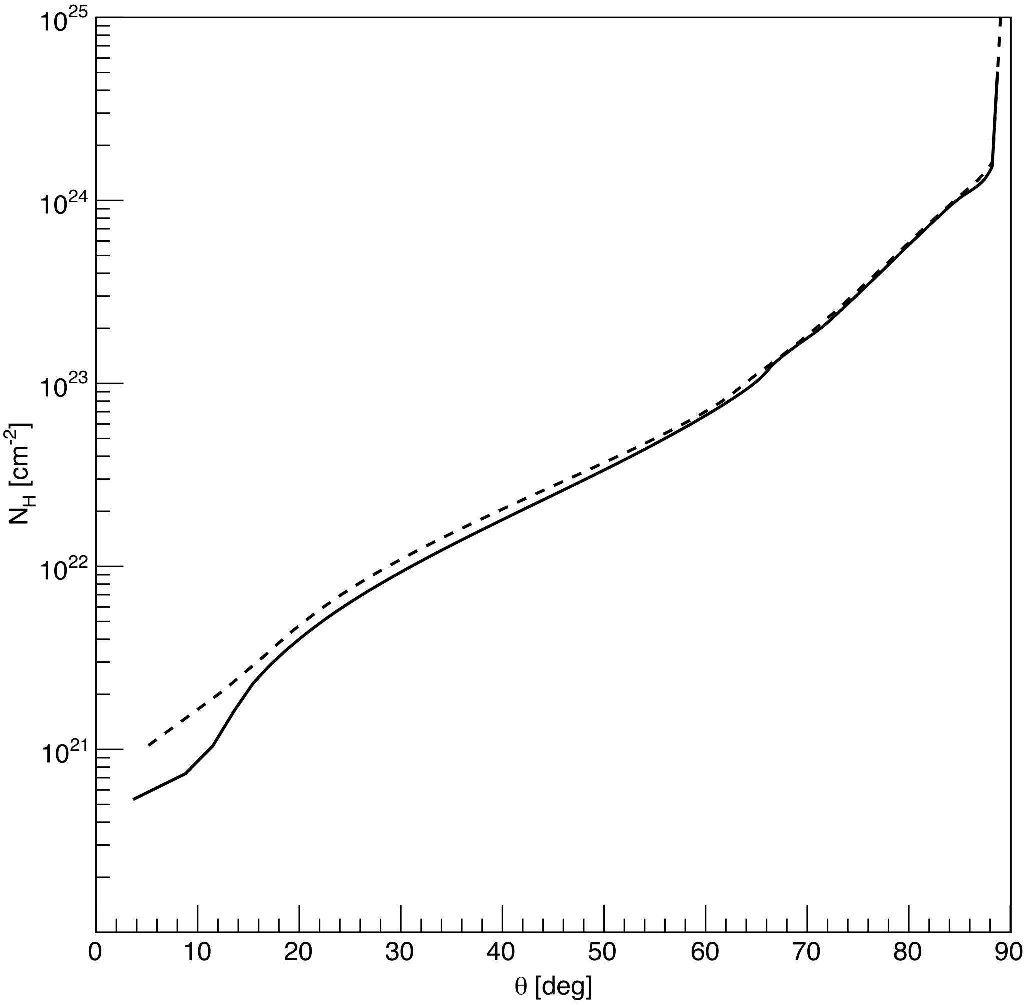

Figure A.3: Comparison of number of grid